UNIVERSITY COLLEGE LONDON

A rigorous treatment of excitation and quantum interference in laser-induced nonsequential double ionization of atoms and molecules

by

Tahir Shaaran
Under Supervision of Dr Carla Figueira de Morisson Faria
and Subsidiary Supervision of Professor Roy Newell

A thesis submitted in partial fulfillment for the
degree of Doctor of Philosophy

in the
UCL
Department of Physics and Astronomy

Examination committee:
Professor Jonathan Tennyson, Department of Physics and Astronomy (UCL)
Professor Mikhail Ivanov, Department of Physics (Imperial College London)

May 2011

Declaration of Authorship

I, Tahir Shaaran, declare that this thesis titled, 'A rigorous treatment of excitation and quantum interference in laser-induced nonsequential double ionization of atoms and molecules' and the work presented in it are my own. I confirm that:

- This work was done wholly or mainly while in candidature for a research degree at this University.
- Where any part of this thesis has previously been submitted for a degree or any other qualification at this University or any other institution, this has been clearly stated.
- Where I have consulted the published work of others, this is always clearly attributed.
- Where I have quoted from the work of others, the source is always given. With the exception of such quotations, this thesis is entirely my own work.
- I have acknowledged all main sources of help.
- Where the thesis is based on work done by myself jointly with others, I have made clear exactly what was done by others and what I have contributed myself.

Signed: _____

Date: _____

"I do not know what I may appear to the world; but to myself I seem to have been only like a boy playing on the sea-shore, and diverting myself in now and then finding a smoother pebble or a prettier shell than ordinary, whilst the great ocean of truth lay all undiscovered before me."

Isaac Newton

UNIVERSITY COLLEGE LONDON

Abstract

UCL
Department of Physics and Astronomy

Doctor of Philosophy

by Tahir Shaaran

Electron-electron correlation, excitation and quantum interference are generally important in attosecond physics, especially for imaging of atoms and molecules. These are the main topics addressed in this thesis, in the context of laser-induced nonsequential double ionization (NSDI). Excitation is the most extensive topic of this work and is addressed within a rigorous, semi-analytic study of the recollision-excitation with subsequent tunneling ionization (RESI) mechanism in laser-induced nonsequential double ionization (NSDI). This is the most comprehensive study of this mechanism performed in the context of the strong-field approximation to the preset date. Subsequently, we investigate potential imaging applications, by computing electron momentum distributions of atoms and molecules. For atoms, we show that the RESI electron momentum distributions depends very critically on the bound state wave function. For molecules, we address the influence of the molecular orbital geometry and of the molecular alignment with respect to the laser-field polarization, by computing the electron momentum distributions of N_2 and Li_2. We show that the electron-momentum distributions exhibit interference maxima and minima, either due to the electron emission at spatially separated centers, or to the orbital geometry, such as nodes of the atomic wavefunction. In this latter case, we do not restrict ourself only to RESI, and we also compute the electron momentum distributions of N_2 for electron-impact ionization, in which we also observe two-center interference patterns when the molecule is aligned along the laser-field polarization direction. The above-mentioned momentum constraints, together with the strong dependence of the distributions on the bound states involved, the molecular orbital geometry and the molecular alignment angle may be important for singling out the RESI mechanism in actual physical situations and using NSDI in ultra-fast imaging. In the final chapter, we present the first step taken by us in order to address the above-stated issues using an approach beyond the strong field approximation.

Acknowledgements

My thanks and appreciation for the accomplishment of this study goes to Dr Carla Figueira de Morisson Faria for her great supervision and support. Without her, this thesis would not have been possible. Also, a special thanks goes to the UK Engineering and Physical Sources Research Council (EPSRC) for funding my PhD. I am grateful to Prof. Maciej Lewenstein and Prof. Jens Biegert at Institute of Photonic Sciences in Barcelona for their kind hospitality. I also thank Dr Xiaojun Liu at Wuhan Institute of Physics and Mathematics (Chinese Academy of Sciences) for his collaboration. I also would like to thank Mr Tuomas Nygren for his invaluable help with the numerical work on RESI, and Mr Bradley Bernhard Augstein for the calculation of coefficients of the molecular wavefunctions using GAMESS-UK [1]. Furthermore, I am very grateful to my family and friends, especially to my mother and Fatima, for their emotional support and love. I am grateful to Tuomas Nygren and Bradley Bernhard Augstein for proof reading this thesis and correcting my English grammar.

Structure of this research

The work in this thesis was mainly performed at Physics and Astronomy department of University college London between October 2007 and 0ctober 2010, under the supervision of Dr Carla Figueira de Morisson Faria and the subsidiary supervision of Professor Roy Newell. It also includes collaborations with Prof. Maciej Lewenstein, from The Institute of Photonic Sciences (Barcelona), and Dr Xiaojun Liu, from the State Key Laboratory of Magnetic Resonance and Atomic and Molecular Physics(Wuhan Institute of Physics and Mathematics, Chinese Academy of Sciences). Parts of this thesis can be found in the following publications:

Paper 1: C. Figueira de Morisson Faria, T. Shaaran, X. Liu and W. Yang, "Quantum interference in laser-induced nonsequential double ionization in diatomic molecules: the role of alignment and orbital symmetry", Phys. Rev. A, **78**, 043407 (2008) (reference [2]).

Paper 2: T. Shaaran and C. Figueira de Morisson Faria, "Laser-induced nonsequential double ionization: Kinematic constraints for the recollision-excitation-tunneling mechanism", J. Mod. Opt., **57**, 11 (2010) (reference [3]).

Paper 3: T. Shaaran, M. T. Nygren and C. Figueira de Morisson Faria, "Laser-induced nonsequential double ionization at and above the recollision-excitation-tunneling threshold", Phys. Rev. A, **81**, 063413 (2010) (reference [4]).

Paper 4: T. Shaaran, B. B. Augstein and C. Figueira de Morisson Faria, "Excitation, two-center interference and the orbital geometry in Laser-induced nonsequential double ionization of diatomic molecules", under preparation (2010) (reference [5]).

Paper 5: T. Shaaran, C. Figueira de Morisson Faria and M. Lewenstein, "Coulomb corrections in above-threshold ionization: the influence of the tunnel exit, the binding potential and the dimensionality", under preparation (2010) (reference [6]).

In this thesis, paper 2 mainly appears in Chapters 3 and 5. Paper 3 mainly is presented in chapter 6 and partially in 5.2. Paper 1 and 4 appear in Chapters 7 and 8, respectively. Finally, Chapter 9 contains paper 5 [1]. I was the lead author in all publications apart from paper 1. In this latter paper I contributed to the investigation of the quantum-interference conditions and the numerical work.

[1]Thesis style is based on the ECS thesis style by Steve R. Gunn which was modified by Sunil Patel (www.sunilpatel.co.uk).

Contents

List of Figures

List of Tables

I dedicate this thesis to all children who have suffered in wars, especially to those who suffered the most under the brutal regime of Taliban in Afghanistan (1995-2001).

Chapter 1

Overview

This thesis brings together electron-electron correlation, excitation and quantum interference in the context of laser-induced nonsequential double ionization. This phenomenon occurs when atoms or molecules interact with very strong laser fields, whose intensities are of the order of 10^{13} W/cm^2 or higher.

The study of the interaction between matter and strong laser fields is one of the most prominent and active fields of research in atomic physics with a range of applications, such as solid-state physics [17–19], particle physics [20–22], novel X-ray sources [23–26], XUV [27–29], plasma physics (in laser fusion process) [30–32] and attosecond science [7, 33–35]. This field of research has posed a great challenge to theorists and experimentalists alike. This may be attributed to several reasons.

Firstly, at such high intensities the atomic binding forces are of the order of the laser fields involved. Thus, at these intensities, perturbation theory with respect to the field breaks down [36]. The breakdown of perturbation theory manifested itself as a series of counterintuitive features, such as the "plateau" in high-order above-threshold ionization (ATI)[1] and high-order harmonic generation (HHG)[2]. The plateau corresponds to a "flat" region in the HHG or ATI spectra, where harmonics or photoelectron peaks exhibit comparable intensities [37, 38], and it is followed by an abrupt decrease in the harmonic or photoelectron yield, whose energy position is dependent on the driving-field intensity [39]. These features have been observed since the early days of strong-field physics,

[1] Above-threshold ionization is a phenomenon in which matter absorbs more photons than the required number for ionization to take place.

[2] High-order harmonic generation is the highly nonlinear response of an atom or molecule to an intense driving field, emitting light whose frequency is a multiple of that of the driving field. For a typical, near infrared field, these harmonics can extend up to around the 300th order, i.e., to the extreme ultraviolet regime.

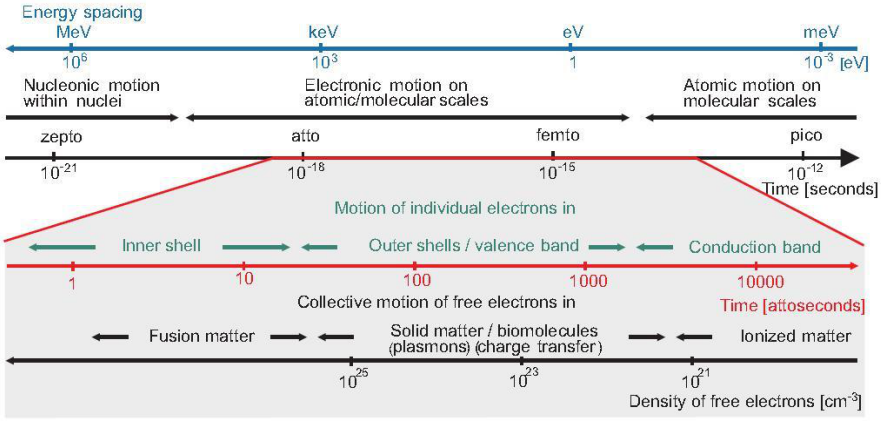

FIGURE 1.1: Schematic representation of the characteristic time scales for: (upper panel) microscopic motion and its connection with energy spacing between relevant stationary states; (lower panel) the motion of one or several electrons and the collective motion of an electronic ensemble (this is figure 2 in [7]).

when intense laser sources (10^{13} W/cm^2 and higher) became feasible [40]. Their presence completely contradicted the predictions of perturbation theory with respect to the field, in which one expects a monotonic decrease in the harmonic or ATI yield with increasing harmonic order or photoelectron energy, without any plateau. The above-stated features were highly counterintuitive findings and opened up a wide range of possibilities for studying new physics. For comparison, the observation of only second-harmonic generation in 1961 already revolutionized optical physics [41, 42].

Apart from that, at very high intensities relativistic effects start to play an important role. Indeed, since the mid-1990s laser technology has advanced further to construct lasers with intensities exceeding 10^{18} W/cm^2 [43]. At this intensity regime, when a laser interacts with an atomic system at a typical frequency range, it transfers kinetic energy which is of the same order as the rest mass of the electron in the system [44]. Therefore, the laser-atom interaction needs to be treated in a relativistic framework [45–51].

Secondly, this field of research deals not only with very strong fields, but also with some of the shortest timescales in nature. This has led to the birth of a highly interdisciplinary field of research in the past few years: attosecond science. This field, specifically, emerges from the fact that high-intensity optical phenomena owe their existence to the laser-induced rescattering or recombination of an electron with its parent ion. This process takes place within time intervals of hundreds of attoseconds (1 attosecond = 10^{-18} s), which is a fraction of a cycle of the laser field. This is the typical time scale of electron motion in atoms and molecules. This allows one, in principle, to resolve and control dynamic processes in matter with previously never-imagined precision.

In principle, attosecond physics studies microscopic motion of electrons in atoms, molecules, and nanoscale structures, the characteristic time scales of these microscopic motions is shown in figure 1.1 Thus, this field acts as a bridge to connect different disciplines such as physics, chemistry and biology [7]. Indeed, light including visible, x-ray and ultraviolet is emitted due to the motion of electrons inside atoms. On the molecular scale, electronic dynamics may change the biological function and initial chemical composition of a system. These subsequent changes, however, due to initial attosecond dynamics of valence electrons are not well understood. Apart from that, there are more open questions related to electronic dynamics in atoms, molecules and large systems (nanoscale materials) [7]. How does an electron migrate in a molecule, or a proton rearrange itself? What changes, physically speaking, occur in such short timescales? Can one steer electrons in chemical bonds in order to influence molecular structures or the function of biomolecules? How can one optimize charge transformations in molecules to produce solar cells with high efficiency? How can someone prevent radiation damage during biological imaging? Can someone create compact x-rays by exciting atoms in a more efficient way? These challenging questions can only be answered by studying, and even controlling, the microscopic electron motion.

In addition, the generation of extremely short attosecond XUV (Extreme Ultraviolet) pulses from high-order harmonics [52] has become possible. This has allowed even more control. For instant, by superposing the XUV pulses to the laser field, one can resolve dynamic processes in atom or molecule with precision of a few attoseconds [53]. In conclusion, attosecond science has a great potential to develop a new ultrasensitive molecular imaging and spectroscopic techniques [54]. Strong field phenomena can be used as a tool to retrieve information about the molecular or atomic structure of the sample. They also allow to study the quantum interference effects in molecules due to high-order harmonic or photoelectron emission at separated centers [55], as shown in figure.

Thirdly, in the context of the interaction of intense laser fields with a system with more than one active electron, electron-electron correlation becomes extremely important [56]. Specifically, in a complex system with many electrons such as a molecule or solid, the laser field interacts with many electrons as well as the electrons interacting with each other and the residual ions. Thus at such high intensities the multielectron effects are expected to play an important role. For example, multielectron effects shape the high-order harmonic polarization [57] and multiphoton ionization of diatomic molecules [58]. It is necessary to consider the electron-electron correlation for studying the underlying dynamics of a complex system. In particular, this correlation becomes very important for ultrafast imaging of matter, which is an important goal in strong laser field physics.

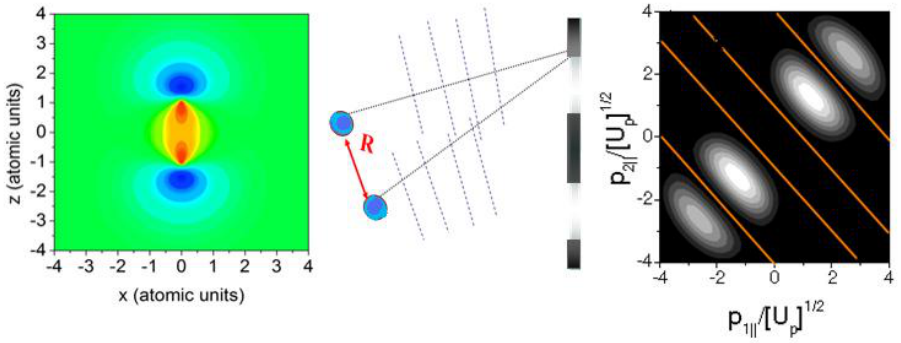

FIGURE 1.2: Schematic representation of the quantum interference effects in a molecule due to photoelectron emission at separated centers (similar to the double-slit experiment). Panel (a) represents geometry of the molecular orbitals; Panel (b) demonstrates the double slit behavior of a diatomic molecule; and panel (c) shows the electron momentum distributions as functions of the momentum components parallel to the laser field polarization with minima and maxima positions. I acknowledge Dr Carla Faria for providing me the figure in panel (a).

This is a great change from the early 1990s and 2000s, when most strong field phenomena could be explained by the Single Active Electron (SAE) approximation. In this approximation the motion of the electron, which is released either by tunneling through the atomic or molecular potential or multiphoton ionization, does not have any correlation with other electrons in the system. It means the outermost electron governs the ionization dynamics of the system while the other electrons are frozen in the core. Early calculations beyond the SAE approximation (see [59, 60]) showed that dynamical electron correlation is important for the increase in the high-order harmonics of He atoms, but it does not change the main features of HHG, such as the cutoff and plateau. Since the early days of strong-field and attosecond science, however, there is one phenomenon for which electron-electron correlation turns out to be very important: laser-induced nonsequential double ionization (NSDI) [14]. NSDI occurs due to the inelastic recollision of an electron with its parent ion [61]. In this recollision, the first electron interacts with a second electron by giving part of the kinetic energy it acquired from the driving field to it. As a result of this interaction, the second electron is freed. In this process the first electron can be ionized via several mechanisms (see detailed discussions in Chapter 2) depending on the laser field intensity, laser frequency and ionization potential of the matter. In this thesis, the tunnel ionization mechanism is considered for ionization of the first electron.

Nonsequential double ionization was first observed for Xe [62, 63], and then for noble-gas atoms [8–10, 64–71] and for some molecules [72, 73]. Since then, it has been a great challenge for theorists to develop a model to describe laser-induced nonsequential double ionization. Indeed, there is no analytical solution for NSDI even for a simple

system like helium and yet the numerical computation for such system is by no means easy. Apart from the theoretical challenge, nonsequential double ionization exhibits several advantages with regard to other strong field phenomena, such as ATI and HHG. In particular, it allows one to extract more dynamic information about the system, as the type of electron-electron interaction can be identified in the electron-momentum distributions [74–77][3]. Furthermore, events happening at different half cycles of the driving field can be mapped into different momentum regions [74, 78]. For instance, the theoretical investigation of NSDI with few-cycle pulses shows that the pulse envelope and its carrier oscillation highly influence the electron momentum distributions. Therefore this gives a great advantage to NSDI over HHG and ATI to delimit a confined phase space region. Furthermore, the study of two-centre interference in diatomic molecules shows that rescattering from a different molecular centre gives different electron momentum distributions [79]. In comparison to other strong field phenomena, NSDI has great potential in the study of excitation in atoms and molecules with attosecond time scales (see examples given in Chapter 6 and 8).

This thesis focuses on the the different rescattering mechanisms involved in the NSDI process by employing the strong-field approximation (SFA). In the SFA, the continuum is approximated by field-dressed plane waves, which are nonperturbative with respect to the laser field. In this method, in comparison to other available methods, the computation of NSDI transition amplitudes can, to a very large extent, be done analytically. Furthermore, this method provides a rigorous and transparent picture for NSDI mechanisms because the mechanisms involved can be defined clearly from the outset. Therefore, the strong-field approximation gives good physical insight into the space-time picture of the system.[4]

This thesis is structured as follows. Chapter 2 starts with a brief historical overview of NSDI, discussing the physical mechanisms behind it and going through some of the key features observed so far. It is followed by detailed discussions of two rescattering mechanisms: electron-impact ionization and recollision excitation with subsequential tunneling ionization (RESI). The former is a well studied mechanism and considerably easier to model in the context of semianalytical approaches [61, 74, 75, 81–83], while the latter is a less well studied mechanism and difficult to model. Therefore, the study of RESI is the main objective of this thesis. Electron-impact ionization happens when, at the time of the recollision, the first electron provides enough energy to the second electron to overcome the second ionization potential. On the other hand, for RESI, upon

[3] In principle for strong field approximation, one can easily turn the electron-electron interaction on and off or even defines different type of interactions.

[4] The coulomb potential, which is neglected in the SFA, affects the electron propagation in the continuum and causes a distortion in the electron momentum distributions as it was investigated for direct above-threshold ionization [80].

recollision the first electron does not have sufficient energy to directly ionize the second electron. Instead, the second electron is promoted to an excited state, from which, with laser assistance, it subsequently tunnels [84–86]. At the end of this chapter, the existing theoretical models of NSDI are investigated by going through their advantages, limitations and achievements.

Chapters 3 and 4 form the theoretical core of the thesis, the strong-field approximation, for the electron-impact ionization (3.3.1) and RESI (3.3.2) mechanisms. Chapter 3 shows how the SFA is applied to obtain the transition amplitude for electron-impact ionization and RESI. The former transition amplitude has been extensively studied in the early 2000s (e.g. see [75, 77, 81, 87–89]), while development of the latter one is part of my PhD work. Chapter 4 demonstrates how one can solve the multidimensional integral of the transition amplitudes derived in Chapter 3 by applying the saddle-point approximation. It is also shown when the saddle-point approximation needs to be replaced by the uniform approximation and how these two approximations relate to each other.

The saddle-point equations, which are derived in Chapter 4, provide useful information on the momentum-space regions populated by electron-impact ionization or RESI mechanisms as well as the shape of the electron momentum distributions. Chapter 5 shows how one may use the saddle-point equations to determine constraints for the parallel momentum components $p_{n||}(n = 1, 2)$ of electrons in the plane $p_{1\|}p_{2\|}$. These constraints will be discussed in this chapter for both electron-impact ionization and RESI mechanism. Furthermore, it is shown that these constraints can be used as a tool for sketching the approximate shapes of the electron-momentum distributions. It is demonstrated how the momentum-space constraints affect the electron momentum distributions for different driving-field intensities.

Subsequently, in Chapter 6, it is shown that the RESI mechanism developed provides information about the bound state with which the first electron collides, the bound state to which the second electron is excited, and the type of electron-electron interaction. In this chapter electron momentum distributions are computed for helium and argon in the threshold and above-threshold intensity regimes[5]. The computation for argon is compared with the existing experimental results [86]. The computations show that the momentum constraints, together with the strong dependence of the distributions on the bound states involved, may be important for singling out the RESI mechanism in actual physical situations and using NSDI in ultrafast imaging.

[5] At the threshold, the kinetic energy of the first electron, upon return, is just sufficient to excite the second electron.

Chapters 7 and 8 focus on the NSDI for diatomic molecules. The simplest targets for which the quantum interference effects due to photoelectron or high-harmonic emission at spatially separated centers can be studied are diatomic molecules. This can be viewed as as the microscopic counterpart of a double-slit experiment [90, 91][6]. Furthermore, NSDI experiments on diatomic molecules have shown that molecular orbital symmetry [84] and the alignment angle of the molecules with respect to the laser-field polarization [13] affect the shapes of the electron momentum distributions. In Chapters 7 and 8 these two properties are investigated, based on the electron-impact ionization and RESI mechanisms, respectively. The calculations demonstrate that the electron-momentum distributions exhibit interference maxima and minima due to the electron emission at spatially separated centers. Explicitly, in Chapter 8, we show that the electron-momentum distributions exhibit interference maxima and minima, due to the molecular orbital geometry, such as nodes of the atomic wavefunction. An analytical expression for such patterns is provided for both electron-impact ionization and RESI. For the former case, the classical limit of our model is employed.

Chapter 9 illustrates the Coulomb-corrected strong-field approximation. In the SFA, the effect of Coulomb potential is neglected when the electron is in the continuum, i.e. the ionized electron is propagating in the laser field. As a result, this approximation is not capable of describing sub-cycle features of strong field phenomena [93]. Furthermore, in some cases, it gives an incorrect qualitative picture (more details can be found in reference [94]). Therefore, one needs to move beyond the SFA to have a better description of strong field phenomena. The Coulomb-corrected strong-field approximation, however, is an alternative model, in which the the Coulomb potential is incorporated semi-analytically in the SFA. This chapter shows preliminary work on the Coulomb-corrected strong-field approximation for direct ATI. In this process an electron is tunnel ionized without any rescattering. In fact, this is the mechanism behind the dislodging of the second electron in RESI. The long-term goal of this work is to implement the Coulomb-corrected strong-field approximation to RESI. This approach yields identical working formulae to those in Smirnova et al. [95], but is developed from different starting points. In the last Chapter 9 a brief summary is provided with an illustration of some of the main results of my PhD work.

Topics of complementary and technical nature in the thesis are provided in the appendices. Derivation of the saddle-point approximation (SPA) and uniform approximation is presented in Appendices A and B, respectively. The derivations cover the SPA and uniform approximation of one-dimensional and multi-dimensional integrals in the real

[6]The role of entanglement and correlation between recollision of the first electron and ionization of the second electron is being currently investigated [92].

axis or the complex plane. Appendix C provides the general expressions for the prefactors employed in Chapter 6 related to hydrogenic states. In Appendix D, an argument is provided for neglecting the interference terms in electron momentum distributions of equations 3.49. Finally, Appendix E contains the definition of the atomic units, which are used throughout this thesis.

Chapter 2

Laser-induced Nonsequential Double Ionization

2.1 Historical Overview

In the context of the interaction of matter with a strong laser field, nonsequential double ionization occurs when there are at least two active electrons in the system. In this phenomenon, two electrons have a strong correlation at the time of ionization. The ionization may occur through several mechanisms.

For a high frequency laser, where individual photons have energy of the order of the ionization potential of the electron in matter (XUV and above), a one-photon absorption process can occur. For low frequency one-photon absorption does not lead to ionization. In this frequency regime, multiphoton ionization or tunneling ionization occur for low intensity laser and for a high intensity laser, respectively. In general, the adiabaticity parameter known as the Keldysh parameter $\gamma = \omega_l \sqrt{I_p}/E_l$ defines the limit in which the mentioned mechanisms occur. Respectively, ω_l, I_p and E_l give the frequency of the laser, ionization potential and laser field intensity. If $\gamma \ll 1$ tunneling ionization takes place and if $\gamma \gg 1$ multiphoton ionization happens.

In the early 1980s, the existence of NSDI was predicted for the first time, when the cross section of multiphoton ionization ($\gamma \gg 1$) of Xe atoms was investigated [62], based on the rate of ionization against the intensity of an external laser field. In this work, two cases of ionization were studied: 1) simultaneous ionization of two electrons from the ground state of Xe atoms; and 2) ionization of a single electron from the ground state of atoms and ground state of ions. In comparison with experimental results, the calculation

showed that at low intensities doubly charged ions are mainly produced by the simultaneous removal of two electrons from the ground state of Xe. At high intensities they are produced by a stepwise process via a singly charged ion. The former process corresponds to nonsequential double ionization and the latter process to sequential double ionization with no electron-electron correlation.

This existence of NSDI is not just limited to the multiphoton ionization mechanism. Indeed, several experimental observations confirmed the existence of nonsequential double ionization in the tunneling regime ($\gamma \ll 1$) [8, 64]. The experiments showed an enhancement, known as "the knee", in the double ionization yield of both He and Ne as a function of the driving field intensity, which deviated by several orders of magnitude from predictions of sequential double ionization models. The experimental results which show the knee for He are shown in figure (2.1). "The knee" has also been observed in interaction of intense laser fields with molecules [72, 73, 96, 97].

The observation of "the knee" in the double ionization yield of several species made it clear that correlated electron-electron dynamics is responsible for NSDI [98]. However, it opened the debate about the physical mechanism responsible for nonsequential double ionization in the low-frequency (near infrared), high-intensity ($10^{13} - 10^{15}$ W/cm^2) regime. Since then, many mechanisms have been proposed to explain the NSDI for a low-frequency, high-intensity laser field, such as collective tunneling [99], a shake-off process [64] and rescattering [61, 100, 101]. For the collective tunneling, it was suggested that in laser-matter interaction both electrons reach the continuum simultaneously by tunneling ionization. For the shake-off process, it was suggested that the first electron at the time of tunneling leaves the atom so quickly, that due to the very fast rearrangement of the core, the second electron is promoted to an excited state, from which it immediately ionizes. According to these mechanisms one would expect that both electrons tunnel at the maxima of the external laser field, when the tunneling probability maximizes. This happens due to the fact that at the field maxima the potential well of the system is distorted the most. Thus, the electrons most probably leave the system with zero momentum (for detailed discussion see reference [9]). On the other hand, the scattering mechanism postulates a three-step physical process to explain NSDI: 1) Near the maxima of the external laser field, the first electron is ionized by tunneling through potential barrier of the atom, and subsequently accelerated in the continuum by the laser field; 2) Later on when the phase of the field reverses, it is driven back towards its parent ion by gaining some additional energy from the laser field; 3) Upon its return to the core (most effectively with a linearly polarized field), the first electron collides with the parent ion and releases the second electron by transmitting part of its kinetic energy

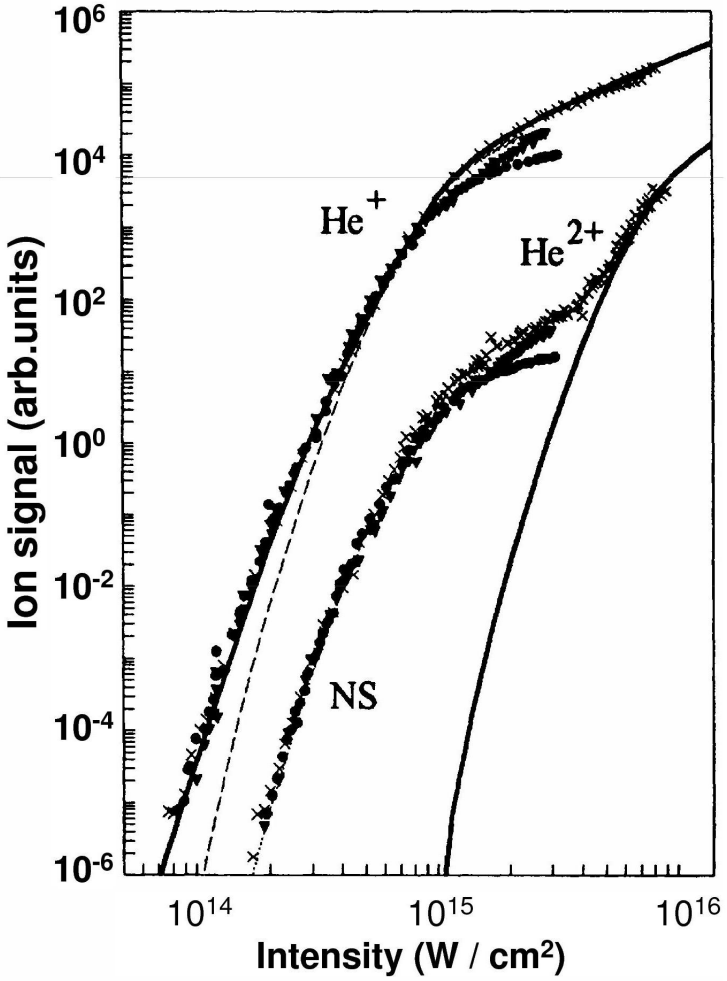

FIGURE 2.1: Measured ionization yields as functions of the laser intensity for double ionization of helium at 780 nm. The crosses represent the experimental results and the rest theoretical calculations. For He^{2+} the solid and dot lines show the calculations for sequential and nonsequential (NS) double ionization, respectively (figure 1 in [8]).

to the core. The first evidence that a laser-induced rescattering mechanism was responsible for NSDI was a decrease in the double ionization yield with increasing driving-field elipticity, whose physical explanation was consistent with the rescattering mechanism [100][1].

However, up to one decade ago, the debate on the physical mechanism behind NSDI was solely based on total multiple ionization rate measurements. New experimental evidence in support of the rescattering mechanism, however, emerged when the ion momentum distributions of neon [9] and helium [67], as functions of the ion momentum components

[1]With elliptical polarization the released electron does not have a chance to return to the core to collide with it.

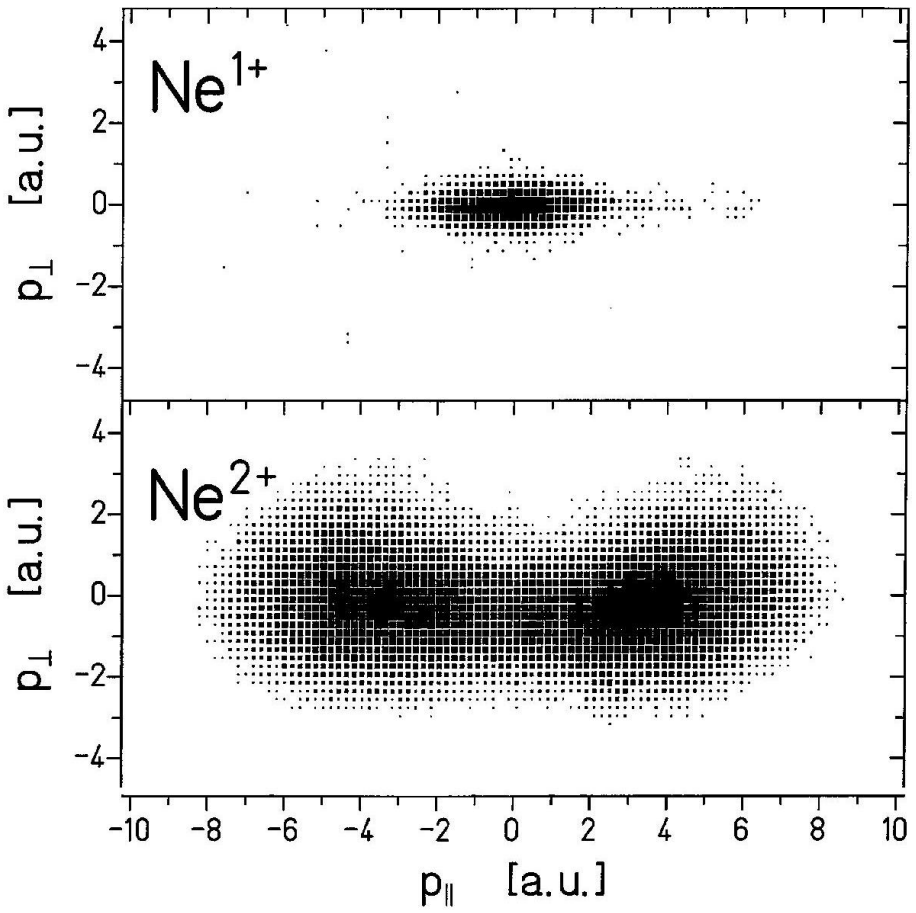

FIGURE 2.2: Two-dimensional momentum distributions of single and double ionization of Neon $(p_\perp, p_{||})$, in which distributions are integrated over the third Cartesian coordinate (upper and middle panels of figure 2 in [9]).

parallel and perpendicular to the laser-field polarization, were measured using recoil-ion momentum spectroscopy [102]. It was found that for doubly charged ions the electron momentum distributions peaked at nonvanishing parallel momenta (for neon it was more obvious), while for singly charged ions the electron momentum distributions peaked at vanishing parallel momenta. The former process shows that both electrons prefer to leave the atom when the laser field is at any local crossing, while the latter process indicates that an electron leaves the atom at the the field maxima. Experimental results which show the peaks for NSDI of neon are given in figure 2.2. Therefore, the observation of peaks at nonvanishing parallel momenta are in favor of the rescattering mechanism for NSDI in the low-frequency, high-intensity regime. In addition, coincident momentum distributions of two electrons as functions of the electron momentum components parallel to the laser-field polarization were measured for different atoms [9, 67, 86, 88, 103] and molecules [13, 84]. NSDI can be studied in more detail using this technique, since it provides a better picture for the correlation of the electrons at the time of recollision. Like in the previous experiments, the electron momentum distributions show peaks at

at nonvanishing parallel momenta, more astonishing evidence in favor of rescattering mechanism for NSDI. Today, there is a general consensus that for infrared frequencies at high intensities, i.e. $10^{13} - 10^{15}$ W/cm^2, the emission of more than one electron from an atom or molecules occurs via rescattering [10].

Numerical calculations of NSDI, based on solving the time dependent Schrödinger equation (TDSE) in one dimension [104], predicted a V-shaped structure for the electron momentum distributions as functions of the parallel momentum components. At the beginning, there was some doubt about their physical presence due to reduced dimensionality in the model. A few years later, this feature was also predicted by semi-analytical models [74, 75, 105]. In 2007, two groups [10, 71] reported the V-shaped or finger-print-like structure experimentally. In addition, this feature was identified in the computations of NSDI of helium with the time dependent Schrödinger equation in three-dimensional [11] and classical models [76, 77, 83]. Figure 2.3 demonstrates the finger-like structure both theoretically and experimentally. One should note, however, that early calculations and observations of NSDI suggested that the electrons left the system with the same energy, and that the V-shaped structure was not present. This was due to the fact that these early measurements did not have enough resolution to resolve this structure. The finger-like structure may occur due to the long-range Coulomb interaction of the first electron with the core at the time of the rescattering and the electron-electron repulsion after simultaneous release of both electrons [75, 83, 105]. This causes the electrons to have unequal momentum.

Electron correlation in NSDI has also been investigated in the near-infrared wavelength (800 nm), low laser intensity regime. This is the intensity regime in which the maximal energy of the first electron, upon its return to the core, is below the ionization potential of the second electron. To my knowledge, in 2003 Eremina et al. for the first time measured the electron momentum distributions of argon at such low intensities [86]. Recently, Liu et al. investigated this mechanism measuring electron momentum distributions of Ar and Ne [12, 85] at the lowest intensities ever addressed. Figure 2.4 shows the experimental results of these studies. Apart from experimental observation, several theoretical groups have attempted to investigate this mechanism using different theoretical methods, such as quantum mechanical approaches [106–108], classical [109–117] and semi-classical approaches [118]. However, the underlying mechanisms for NSDI in this low laser intensity regime are not yet understood to a great extent. The main part of this thesis is dedicated to developing a semi-classical model for understanding this phenomenon.

As discussed above, several measurements have been carried out for the total ionization yields of molecules, while (to my knowledge) just two experiments have measured the

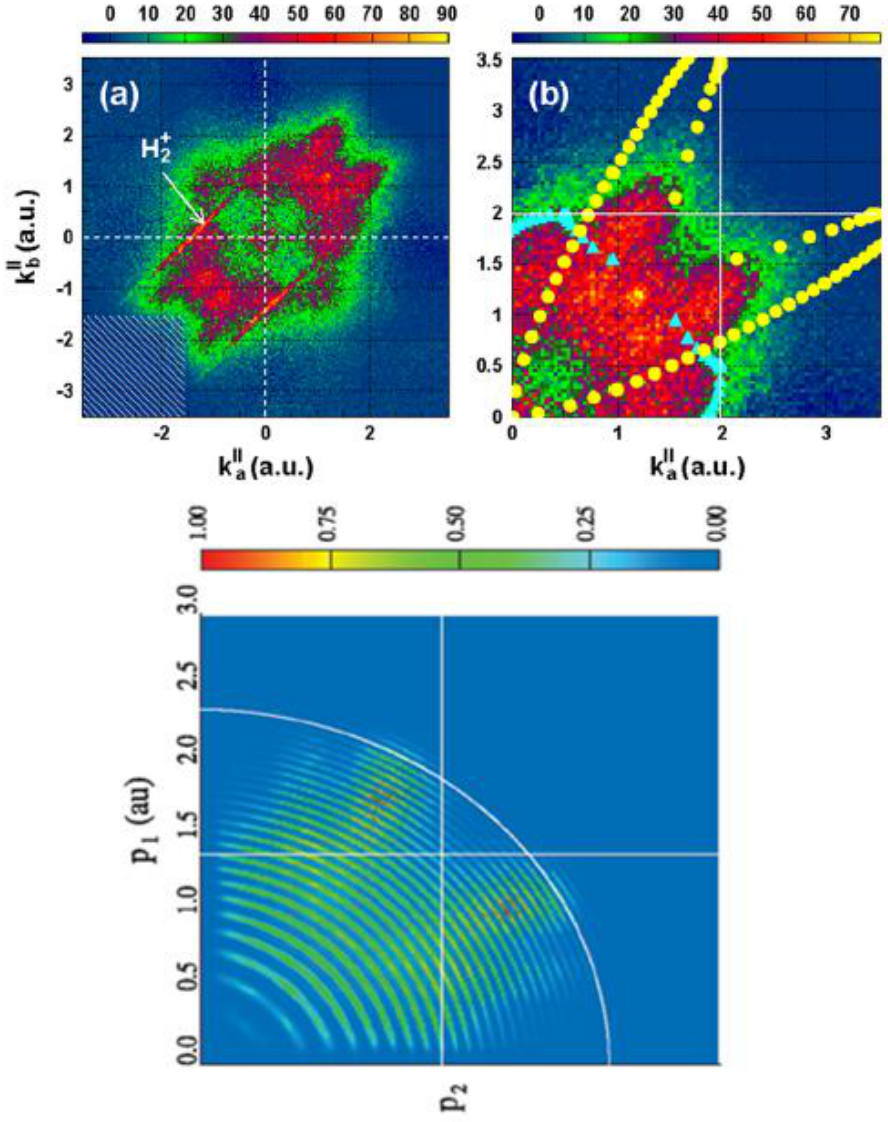

FIGURE 2.3: The upper panels (a) and (b) show the experimentally measured correlated electron momenta for double ionization of helium at 800 nm, 4.5×10^{14} W/cm^2, where $k_{a,b}^{\parallel}$ are the electron momentum components along the polarization direction [10]. Panel (a) corresponds to first quadrant and panel (b) to all quadrants. The lower panel corresponds to the fully numerical solution of the time-dependent Schrödinger equation [11]. The driving-field intensity and frequency were taken as $I = 1.0$ PW/cm^2 and $I_p = 0.057$ a.u., respectively. The vertical line constrains the kinetic energy of electron 1 to 1.9 U_p and the white circular arc indicates when the total kinetic energy equals 5.3 Up. One can clearly see the finger-like or V-shaped structure in the numerical calculations and the experimentally observation.

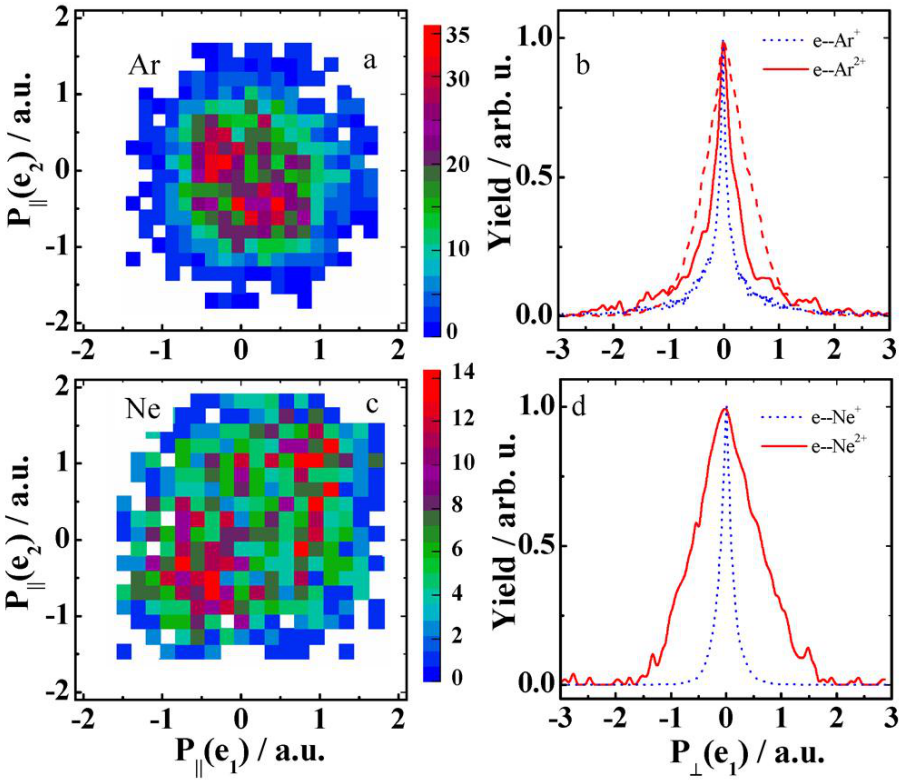

FIGURE 2.4: Electron momentum distribution parallel to the laser field polarization for argon (a) at intensity 3×10^{13} W/cm^2) and neon (c) at intensity 1.5×10^{14} W/cm^2). Electron transverse momentum ($p_\perp$) distributions for argon (b) and neon (d) with the same intensity as their left column. (figure 1 in [12]).

electron momentum distributions as functions of the electron momentum parallel to the laser-field polarization for NSDI of molecules. Experiments (reference [84]) studied the effect of the molecular orbital symmetry by looking at electron momentum distributions of N_2 and O_2, while the role of alignment angle of the molecules with respect to the laser-field polarization on electron momentum distributions was investigated in reference [13]. The former experiment was performed using the optical spectroscopic method. With this method a molecule can be excited, oriented, or aligned before the recollision process occurs (for more details see [13]). Consequently, this allows us to measure the influence of molecular excitation or geometry on attosecond multielectron dynamics. The result of the molecular alignment experiment is shown in figure 2.5. Since then, many theoretical studies have also been performed via different approaches, such as the numerical solution of the TDSE in reduced dimensionally [106–108], semi-analytical methods based on the S-Matrix formalism [2] and classical methods [112, 119]. However, NSDI in molecules has been considerably less well studied since it is far more difficult to measure and model (see, e.g. [120]). The difficulty comes from the fact that molecules have more degrees of freedom than atoms. Thus, one needs to consider many related problems such as the effect of the alignment on ionization. On the other hand, understanding of these effects

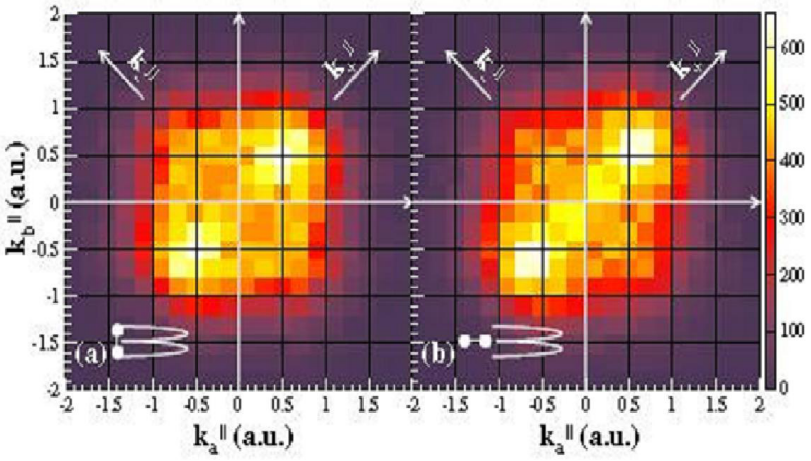

FIGURE 2.5: Electron correlation for the double ionization of N_2 at 1.2×10^{14} W/cm^2, 800 nm, 40 fs. (a) N_2 molecules oriented perpendicular, (b) parallel to the probe laser polarization ([13]).

is essential for the attosecond imaging of molecules.

In comparison to NSDI in the tunneling regime (where $\gamma \ll 1$), fewer studies have been carried on the mechanisms behind NSDI in the multiphoton ionization regime (where $\gamma \gg 1$) due to the experimental difficulties [121]. Just recently, high order harmonics generated with femtosecond laser pulses and vacuum ultraviolet (VUV) photons generated by a free-electron laser have allowed one to study double ionization in the multiphoton ionization regime [2]. The experiments were performed using either former source [124] or latter source [125, 126] confirming that the two-photon absorption double ionization leads to NSDI. In [125], the study of few-photon multiple ionization of neon and argon showed that at low intensities ($I < 6 \times 10^{13}$ W/cm^2) two-photon absorption leads to nonsequential ionization, while at higher intensities sequential ionization dominates because of the involvement of multiphoton processes. In [126], in which sequential and nonsequential mechanisms were clearly disentangled, the recoil-ion momentum distributions of helium clearly show that both electrons share the two observed photons, ionize simultaneously and reach the detector with same energy.

[2] Compared to HHG, a free-electron laser (FEL) is more reliable source for generating coherent short-wavelength light [122]. With recent advances in the free-electron laser, it has become possible to produce vacuum ultraviolet (VUV) photons at unprecedented intensities [123].

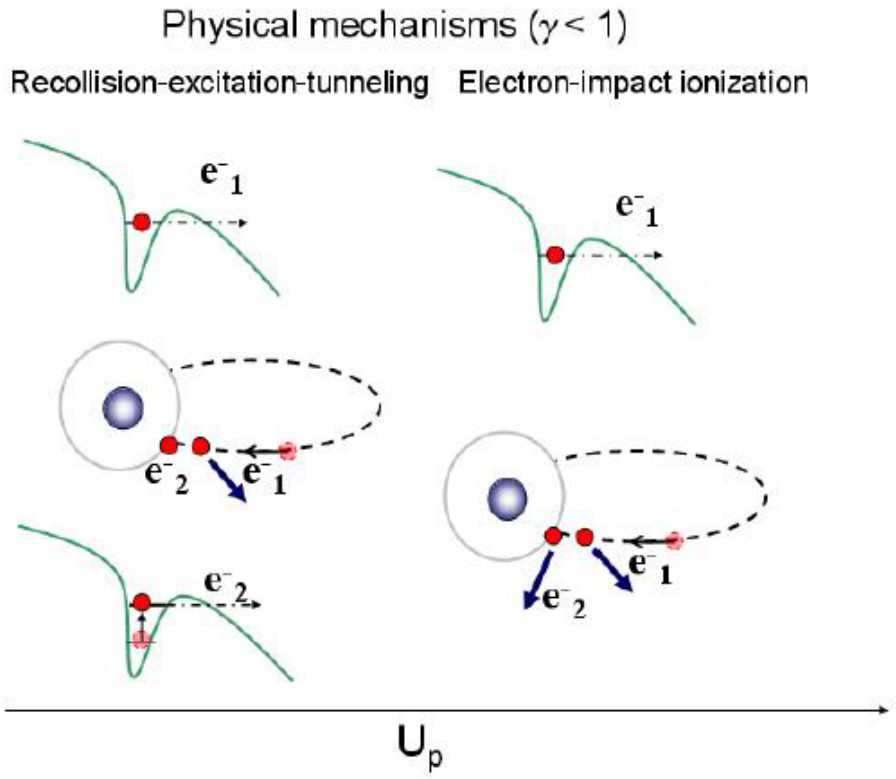

FIGURE 2.6: Schematic representation of the RESI dominant physical mechanisms behind laser-induced double ionization for driving field of high intensities and low frequencies (tunneling regime), as functions of increasing pondermotive energy (modified version of figure 2 in [14]).

2.2 Rescattering Mechanisms

As it was discussed earlier, the NSDI occurs in the tunneling regime by rescattering. There have been, however, different proposed mechanisms for the dislodging of the second electron, depending on the intensity of the field and ionization potential of the target. Below we will discuss two main mechanisms responsible for releasing of the second electron into the continuum. In figure 2.6 we present a schematic representation of these mechanisms as functions of ponderomotive energy.

2.2.1 Electron-impact Ionization

The most simple and well-studied rescattering mechanism is electron-impact ionization in which the first electron, during the accelerating in the field, gains enough kinetic energy to provide to the second electron the energy necessary to overcome the second ionization potential of the target. In this process, both electrons leave simultaneously to reach the detector. In fact, the first cold-target recoil ion momentum spectroscopy

(COLTRIMS) experiments carried out on helium [67] and neon [9], reported a double-peak structure near $p_{1\parallel} = p_{2\parallel} = \pm 2\sqrt{U_p}$, where U_p is the pondermotive energy, i.e. the average energy of a free electron in the laser field, and $p_{1\parallel}$ and $p_{2\parallel}$ denote the electron momentum components parallel to the laser-field polarization for the first and second electron, respectively. The ponderomotive energy depends on the electric field intensity E_l and wavelength ω_l of the laser-field and is defined as $U_p = E_l^2/4\omega_l^2$.

With the intensity used in above-cited experiments, the rescattering process is electron-impact ionization because both electrons share the same amount of energy with double-peak structure close to $\pm 2\sqrt{U_p}$, when they reach the detector. Furthermore, the first electron can gain the maximum kinetic energy of $3.17U_p$ by the time it returns to the core [127]. As result, it has sufficient energy to ionize the second electron directly with impact collision. If the energy of the first electron is at least of the order of ionization potential of the second electron of the target, then electron-impact ionization most probably will be the dominant rescattering mechanism, as was the case for neon experiment in [9].

The peaks at $2\sqrt{U_p}$ correspond to the most probable momentum the electrons may have in this process which depends on the driving-field intensity[3]. However, the electron-momentum distributions can extend far beyond this specific momentum. This has been demonstrated experimentally (for the first time in [88]) and theoretically, by applying classical-trajectory methods [77, 87], the strong-field approximation [75] and the time-dependent Schrödinger equation [11].

For the electron-impact mechanism, the main body of theoretical analysis has suggested that after recollision, most ionized electrons pairs should emerge together in the first and third quadrant (i.e. $p_{1\parallel} > 0$ and $p_{2\parallel} > 0$ or $p_{1\parallel} < 0$ and $p_{2\parallel} < 0$) of the plane spanned by the electron-momentum components parallel to the laser-field polarization [75, 81, 82, 89, 129–131]. In all NSDI experiments, however, there are always some signals in the second and fourth quadrant of the electron momentum distributions and these signals become stronger as the laser intensity decreases. Nevertheless, until now, the key features of most NSDI experiments, such as the peaks at nonvanishing momenta and V-shaped structure (discussed in the previous section 2.1) could be explained sufficiently by the electron-impact ionization mechanism. Furthermore, this mechanism has predicted the existence of two-center interference due to photoelectron emission at spatially separated centers in diatomic molecules, a feature which is observed in other strong-field phenomena, such as high order harmonic generation and above threshold ionization [2]. However, it becomes necessary to move beyond electron-impact ionization when we are dealing with NSDI

[3]The original of the cutoffs for laser-induced nonsequential double ionization was classically explained in [128]

experiments at these intensities, in which the energy of the first electron is not sufficient to directly, on recollision, free the second electron.

2.2.2 RESI

Recollision excitation with subsequential tunneling ionization happens when the first electron, upon its return to the core, promotes the second electron to an excited bound state, from which, with laser assistance, it subsequently tunnels [69]. This mechanism becomes important when the first electron at the time of the recollision does not have sufficient energy to directly ionize the second electron. In 2000, the existence of this mechanism was proposed by experimentalists and theorists [68, 118, 132]. A year later, Feuerstein et el. [69] managed to separate the electron-impact ionization and the RESI mechanism in argon. This study confirmed the existence of RESI mechanism in the rescattering process of NSDI. The observation of NDSI at laser intensities below the ionization threshold of the second electron motivated several groups to study the RESI mechanism [84, 86]. In this intensity regime the energy of the first electron, upon return, is not sufficient to overcome the ionization potential of the second electron to release it to continuum. Thus in this case the electron-impact ionization does not occur and RESI becomes the predominant process for release of the second electron[4].

For RESI, the first electron rescatters and immediately leaves, almost at the crossing of the driving field, while the second electron tunnels slightly later at a field maximum. Hence, there is a time delay between rescattering of the first electron and tunnel ionization of the second electron. In this mechanism, the electron momentum distributions are mainly populated at around $p_{1\parallel} = p_{2\parallel} = 0$, whereas in the impact-ionization the peaks are at $p_{1\parallel} = p_{2\parallel} = \pm 2\sqrt{U_p}$. Furthermore, the classical study of RESI suggests (for instance [77, 109]) that both electrons leave with opposite momenta and fill the valley in between double peak of the impact-ionization. According to these models, the second and fourth quadrants are populated due to a time lag between the rescattering of the first electron and ionization of the second electron. As a result, some (like the authors of [117]) may argue that main features of NSDI can be explained fully by classical physics without considering the quantum effects including excitation tunneling of the second electron. However, they have not shown how this time delay may relate to excitation. In fact, electron-impact ionization with a time delay also populates the low regions of electron momentum distributions (for more details see the review article [14]). On the other hand, a newly developed, semi-classical model for RESI, which rigorously incorporates the excitation of the second electron, shows that electron momentum distributions

[4]For SFA the ionization potential of the electron does not change while in reality the boundary is a bit fuzzy due to present of stark shifts.

occupy all four quadrants, not just the second and the fourth quadrants. Development of this model was part of my PhD work and will be explained in more detail in Chapter 5.

So far, substantially less attention has been paid to the recollision excitation with subsequent tunneling ionization than the electron-impact ionization mechanism. One can find two main reasons for the popularity of the latter mechanism. Firstly, in most experiments, the key features of NSDI occur at large momenta. For example, the peaks appear near $2\sqrt{U_p}$ and the V-shape structure appears beyond $2\sqrt{U_p}$. On the other hand, the key features of RESI mechanism appears at lower momenta, around $p_{2\parallel} = 0$ and $p_{1\parallel} = 2\sqrt{U_p}$. Hence, according to the present observations, RESI corresponds to the less stunning features of NSDI [69, 70, 118]. Secondly, the theoretical model for electron-impact ionization is simpler than that for RESI. For example, in the strong-field approximation (SFA), the electron-impact ionization can be modeled by using a simple Feynman diagram, while for RESI one needs to incorporate the excitation and the time delay into this framework, which is not an easy task. Furthermore, for electron-impact ionization, a classical counterpart exists which helps us to define a classical limit for the SFA-based approaches, while defining a quantum-classical counterpart for RESI may not be possible as it occurs by tunneling and excitation processes.

Up to now, most of the NSDI ionization experiments for atoms and simple molecules have been carried out for atoms in the tunneling regime with high-intensity lasers. However, for studying a more complex system one needs to deal with the intensities that are sufficiently low to prevent molecular bonding breaks as well as having a chance to probe the structure of the target. For example, the study of NSDI of N_2, using electron-impact ionization, showed that the interference maxima and minima due to electron emission at spatially separated centres can only be observed if we have an intensity which is almost one order of magnitude greater than the experimental intensity (this is discussed in Chapter 8). However, one may examine the two-centre interference of N_2 at low intensity by using the RESI mechanism [4]. Thus this mechanism plays an important role when we are dealing with NSDI experiments at intensities below which electron-impact ionization occurs or when we investigate more complex system such as molecules. As a direct consequence, the RESI mechanism has got great potential for ultrafast imaging.

Recently, more obvious experimental evidence has emerged that confirms the existence of RESI for molecules [13]. The observation showed that during double ionization of N_2 electrons leave with anti-correlation momenta. For molecules aligned parallel to the

laser-field polarization, the electrons were mainly ejected in the same direction within a few hundred attosecond of each other. For molecules aligned perpendicular to the laser-field polarization, double ionization takes longer with less probability. The result of this experiment is shown in figure 2.5. Apart from experimental observation, several theoretical groups have attempted to investigate this mechanism using different theoretical methods, such as quantum mechanical approaches [106–108], classical [109–117] and semi-classical approaches [118]. In all these methods, with the exception of the semi-classical approach in [133], one cannot easily disentangle the different rescattering mechanisms from each other. Furthermore, in the calculations RESI is almost masked by multiple collisions or electron-impact ionization. In the next chapters, we will discuss how for the first time we could disentangle RESI from other rescattering mechanisms using the strong-field approximation.

Apart from the above-stated rescattering mechanisms, a multi-recollision mechanism has been proposed for NSDI at recollision threshold intensities [83, 134, 135]. This is the intensity regime in which the maximum kinetic energy acquired by the first electron is not even sufficient to promote the second electron to an real excited state. Thus, the second electron can not be released through the excitation-tunneling channel. However, one might consider a victual excited state to explain the excitation-tunneling channel in this intensity regime [5]. In fact, a recent experiment on argon [136] confirms the existence of NSDI at such low intensities, in which strongly correlated back-to-back emission of the electrons along the polarization of the laser field was observed. It was suggested that multiple, inelastic field-assisted recollision induced direct-ionization was the cause. However, the existence of this back-to-back emission (anticorrelation) depends on the target structure and may always not be present as demonstrated in the most recent experiment [12]. As is hinted in [137], a combination of rescattering for the first electron and multiphoton ionization for the second electron may be responsible for this feature. However, the underlying mechanism responsible for NSDI process at the intensities far below the threshold ionization is still not clear.

2.3 Existing Theoretical Approaches

Interaction of the strong laser field with a system having more than one active electron is challenging as far as theoretical modeling is concerned. Developing a theoretical model which can describe laser-induced nonsequential double ionization, in which electron-electron correlation plays a key role, is not an easy task. Indeed, even for NSDI of a simple system like helium one cannot find an analytical solution and, even the numerical

[5] In this thesis the excited state is considered to be real.

computation of NSDI in this system is by no means easy. For example, for the simple case of the helium atom one needs to deal with solving the time-dependent Schrödinger equation in six spatial dimensions, which requires a great deal of computer power and immense technical tricks. In fact, just recently has the TDSE been solved for a realistic, three-dimensional model of helium, after a continuous effort of over 10 years [11]. However, since observation of NSDI, different theoretical models have been applied to describe this phenomenon. These models can be categorized in three mean approaches; whose overview is provided below.

2.3.1 Classical Approaches

The main idea behind all classical models developed for laser-induced nonsequential double ionization is that one can imitate the behaviour of the quantum-mechanical wavefunction by means of an ensemble of classical electron trajectories. Classical models consists of many electrons each of which has certain probability to be released into the continuum. Then their classical equations of motion, which include the external laser field, electron-electron correlation and the residual binding potentials, are applied to describe the electron motion in the field. Taking into account all of these effects in the computations gives a great advantage to this theoretical approach, whereas including them in the computation of time-dependent Schrödinger equation is extremely challenging.

On the other hand, laser-induced nonsequential ionization can be considered as a quantum mechanical phenomenon, due to involvement of tunneling and, in case of RESI, excitation. Hence, classical approaches lack the ability to reproduce the full dynamics of NSDI. As a direct consequence, this method has some disadvantages in comparison to ab initio computations of NSDI. The disadvantages arise from the fact that by using this method one cannot easily take into account the quantum interference effects, the spreading of electron wavepacket in the continuum, the Heisenberg uncertainty relation or the Pauli Exclusion Principle. In the classical method, the spreading of quantum mechanical wavepacket can be mimicked to some extent. However, in the quantum mechanical transition amplitude, there is an extra time factor related to the spread of the wave, which cannot appropriately be included in the classical models [14]. In addition, this method does not include the atomic bound states (ground or excited) in an appropriate way.

As far as existing experiments on NSDI are concerned, the quantum interference effects are not required in the theoretical models to reproduce the experimental results. Indeed,

NSDI computations require integration over several degrees of freedom, such as the momentum components perpendicular to the laser-filed polarization. This integration, however, washes out interference effects. On the other hand, the Heisenberg uncertainty relation and Pauli Exclusion Principle have been handled by treating them as effective forces [138, 139]. Recently, in the classical models a time dependent "fudge" factor has been included to take care of spreading of electron wavepacket in the continuum [140, 141].

Incorporating excitation in classical models of RESI is a challenging task. In this mechanism, from a classical point of view, the first electron, upon its return to the core, may not have sufficient energy to directly ionize the second electron. Instead the second electron is released through excitation-tunneling, which is a quantum mechanical process[6]. On the other hand, one could argue that, as long as the excited states are close to the threshold, they form a quasi-continuum and hence have a classical counterpart. Recently, however, in order to describe RESI in the framework of classical models it was necessary to incorporate several quantum mechanical features. This resulted in a WKB-like, semiclassical approach [135]. As was discussed in the previous section 2.2.2, in classical models the time delay between the rescattering of the first electron and the release of the second electron is incorporated in the electron-impact ionization mechanism of NSDI [13, 109, 112–117]. As is shown in Chapter 7, this time delay corresponds to different kinematic constraints than those which include excitation. Furthermore, the computations based on this approach includes both electron-impact ionization and RESI mechanisms. Thus, the absence of excitation as well as the difficulty of disentangling the embedded-rescattering mechanisms are the key weaknesses of the classical models.

It has, however, been proved that semiclassical methods are very powerful as they have explained the main features of NSDI in the last two decades. For example, they reproduced "the knee"observed in the total double ionization yield [130], the peaks at nonvanishing momenta for the ion and electron momentum distributions [89], the V-shaped structure for the electron momentum distributions beyond $2\sqrt{U_p}$ [77] and, more recently, the finger-like structure, which observed in the TDSE computation and in experiments [76, 77].

[6] Apart from excitation-tunneling the second electron can be released by other possible physical mechanisms, such as over-the-barrier ionization [111] and multiple field-assisted recollisions with the trapping potential [85].

2.3.2 Quantum Mechanical Approaches

Classical and semi-classical (see 2.3.3) models provide the key features of laser-induced nonsequentail double ionization as far as the existent experiments are concerned. However, these approaches are based on certain approximations, as a result of which some physics may be lost. On the other hand, the numerical solution of time dependent Schrödinger equation for a two-electron system in a strong field is free of any physical approximations. Thus, the calculations based on this method can be used as a benchmark for testing and improving other NSDI models. However, this theoretical approach has two main disadvantages: 1) solving the TDSE for NSDI is very complicated; 2) extracting physical mechanisms from the results of such computations is difficult, since all the existing mechanisms of NSDI are embedded in the computations. Hence, electron momentum distributions computed with the TDSE can be viewed as the outcome of numerical experiments, which albeit accurate, does not provide a transparent physical interpretation.

In the past two decades, enormous efforts have been made for solving the TDSE for NSDI phenomenon. The early models dealt with solving the TDSE for two-electron systems in one dimension for high frequency lasers, in which active electrons in the continuum have small excursion amplitude, in order to avoid divergence problems [142, 143]. After further improvements to the one dimensional models, in late 1990s, "the knee" observed in NSDI experiments was reproduced, since the new models were extended to low-frequency lasers in the tunneling regime [98, 144]. The one-dimensional model for electron momentum distributions of NSDI reproduced the V-shaped structure [104] observed in the experiments [10, 71] and predicted by other theoretical approaches. Furthermore, apart from electron-impact ionization, the computations confirmed the existence of other mechanisms such as RESI and over-the-barrier [11, 104] ionizations.

Recently, Parker et al. have managed to solve the time-dependent Schrödinger equation for NSDI of Helium in three spatial dimensions [11]. In agreement with experimental results [10, 71], the results of their computation show a finger-like structure in the electron momentum distributions. Furthermore, the results show a cutoff at around $5\sqrt{U_p}$, similar to what is predicted by strong-field approximation [75] and classical-trajectory methods [77, 87] (it is discussed in Chapter 5). The boundary between classical allowed and forbidden regimes causes a cutoff in the energy spectrum (for more details see Chapter 5). The lower panel in figure 2.3 shows the electron momentum distributions obtained. Despite the astonishing results obtained in ab initio models, one still cannot disentangle the NSDI physical mechanisms present in the computation.

2.3.3 Semi-classical Approaches

Semi-classical approach for NSDI are based on a nonperturbative (with respect to the external field) analytical approximation method called the strong-field approximation (SFA) [7]. Since the early days of strong field physics, this method has been applied to many strong-field phenomena. There are two main assumptions behind this approach: 1) the influence of laser field is neglected when the electrons are bound to the atoms or molecules; 2) the binding ionic potential is neglected when the electrons are in the continuum. The free electrons in the continuum are described by field-dressed plane waves, which are known as Volkov states [146, 147]. The Volkov wave function has been used in many approximative procedures for calculating the ionization of atoms in a strong field since it has an analytical solution [145, 148]. This approach is very frequently combined with saddle-point methods, which lead to equations that can be directly related to the classical equation of motion of an electron in a laser field. Yet, the SFA transition amplitude retains several quantum mechanical features such as quantum interference. For this reason, the SFA is in many situations viewed as semi-classical.

The assumptions made in the strong-field approximation may lead to the loss of some important physics. For example, distortion of the bound states by the laser or the Coulomb effect on the electron in the continuum may have a big contribution. In fact, there are some groups [95, 149] that have already started to study the effect of the Coulomb potential in NSDI, as will be discussed in Chapter 9. Within the SFA framework, computations of strong-field phenomenon give different results in different gauges. This problem also arises because of the assumptions made in this method. From the start, there has been some dispute among the strong-field community on the validity of gauges (see e.g. [150]). Nonetheless, there is almost a general consensus that the physical gauge can be chosen by comparing different methods and experiments.

In comparison to previous methods, however, this approach has several advantages. The computation of NSDI, to a very large extent, can be done analytically as far as field-dressed plane waves are concerned. Furthermore, this method provides a transparent picture for NSDI mechanisms because the mechanisms involved such as electron-impact ionization and RESI can be defined clearly from the outset. In addition, the classical trajectory of an electron in an external laser field can be directly connected with this method without loss of quantum-interference effects. These advantages make the SFA a powerful semi-analytic method for describing NSDI, or strong field phenomena in general. In fact, it gives good physical insight into the space-time picture of the system.

[7] The SFA, however, as pointed out in [145] is, in fact, perturbation theory with a modified basis, in which field free plane waves have been replaced by Volkov states.

Within the SFA framework, the scattering matrix (or the S-matrix) approach can be used to relate the initial state and the final state of the system, like the bound state and continuum state of electrons in NSDI [151]. In addition, for a given NSDI process one can identify the most relevant Feynman diagrams that contribute to the transition amplitude [152]. For example, for RESI and electron-impact ionization one can define different Feynman diagrams to compute the related transition amplitude. This approach provides a platform to disentangle NSDI mechanisms. This is explained in more details in Chapter 3. As a direct consequence of this technique, the SFA successfully reproduces the key features of NDSI which have been observed experimentally or by ab initio methods, such as the knee in the NSDI yield [152, 153] and peaks at nonvanishing momenta [118]. Furthermore, the SFA enables us to examine the influence of different type of electron-electron interaction on the NSDI electron momentum distributions [82, 154]. The above studies have showed that for contact-type interaction at the position of the ion, the electron momentum distribution peaked at $p_{1\parallel} = p_{2\parallel} = \pm 2\sqrt{U_p}$, while for Coulomb interaction they peaked at unequal momenta. Above all, the calculation using this method showed that the shape and centre of the electron momentum distributions may be influenced by several physical features, such as the initial bound states of the first and second electron [8], the final state electron-electron repulsion [75, 105] and two-centre interference in diatomic molecules [2, 5].

So far, little attention has been paid to studying RESI in the framework of strong-field approximation. In fact, there is only one early work addressing this mechanism [118]. Thus, it is a less-well understood mechanism which needs to be addressed. This was the main motivation behind our detailed study of RESI.

Methods	**Advantages**	**Drawbacks**
Classical models	• Can mimic the evolution of the quantum-mechanical wavepacket • Take into account the external laser field, electron-electron correlation and residual binding potentials • Have predicted main features of NSDI, like "the knee" and V- shaped/finger like structures	Cannot take into account: • quantum interference effects • Pauli exclusion principle and Heisenberg uncertainty relation • spread of electron wavepacket in the continuum • atomic bound states (excitations)
Strong-field approximation	• Can compute analytically to a very large extent • Gives a rigorous and transparent picture for NSDI • Provides a platform to disentangle NSDI mechanisms • Includes atomic bound states such as excitations • can define a classical counterpart • No loss of quantum interference effects	• Neglects the influence of laser field for the bound electrons • Neglects the binding ionic potential for the electrons in the continuum
TDSE	• Ab initio calculation without any approximation • A benchmark for testing and improving other NSDI models	• Computation is very complicated • Difficult to extract different physical mechanisms of NSDI

TABLE 2.1: Comparing different theoretical methods for nonsequential double ionization by going through their advantages and disadvantages

Chapter 3

The Strong-field Approximation

This chapter focuses on the theoretical aspects of the strong-field approximation, with the purpose of deriving the transition amplitude for nonsequential double ionization. First, it provides a brief historical overview of the SFA including its implementation for describing strong field phenomena. In section 3.2, for the sake of simplicity, we will first discuss the strong-field approximation in a single active electron context and derive the ionization amplitude for direct and rescattered ionization. Finally, in section 3.3 we illustrate the SFA for NSDI and provide a general transition amplitude for both electron-impact ionization and RESI mechanisms.

3.1 Historical Overview

In 1964, Keldysh proposed the strong-field approximation (SFA) to investigate ionization processes in the context of the interaction of atoms with an electric field [145]. As discussed in the previous chapter, this approximation neglects the effect of the atomic binding potential, when the electron is in the continuum, and the laser field, when the electron is bound to the atom. Based on this approximation, Keldysh used the adiabaticity parameter (γ) to define the limits for the occurrence of multiphoton ionization and tunnel ionization processes. Furthermore, Keldysh [145] and Perelomov et al. [155] determined the transition amplitude for direct ionization of the hydrogen atom in the length gauge. Subsequently, they were followed by Faisal [156] and Reiss [148] who employed the velocity gauge for describing atom-laser interaction. The method developed by these three people is also known as Keldysh-Faisal-Reiss theory. This theory is not limited to the hydrogen atom, which has one active electron. In fact, it can been applied to other systems by considering the single active electron approximation (for e.g. see [157, 158]), or even extended to multielectron systems.

Lewenstein et al. applied the SFA to model high order harmonic generation [159]. They derived the time dependent atomic dipole moment and showed that the Fourier transform of this dipole momentum gives the harmonic spectrum. Shortly thereafter, more general equations for HHG were derived, in close analogy to the Keldysh-Faisal-Reiss theory [160]. This generalized theory unified the effective-dipole model of Lewinstein [159] and the zero-range potential model, in which had been developed independently by Becker and co-workers [161]. In addition, the Keldysh-Faisal-Reiss model was improved further by incorporating an additional interaction with the core to take care of the rescattering process in above threshold ionization [162]. It was claimed that this model works for arbitrary binding potentials, but works better with shorter range potentials and higher laser intensities. In fact, this is true for all ordinary Keldysh-type amplitudes, in which the shorter range potential justifies ignoring the binding potential when the electron propagates in the field and the high intensity allows one to consider only the contribution of the ground state of the atom (neglecting the effect of the laser when the electron is bound to the atom) [159, 162].

The above-stated formulations of the strong-field approximation were developed considering a system with just one active electron. Under the single active electron approximation one can describe HHG and ATI. This approximation, however, fails for nonsequential double ionization, in which a correlated energy-sharing process exists between the two electrons at the time of recollision. Nonetheless, in the context of the strong-field approximation, several scattering matrix (S-matrix) models have been formulated to include the intermediate electron-electron interaction, considering it either as an instantaneous Coulomb interaction [129, 163, 164] or as a contact interaction [118]. In all these models, the second electron stays inactive in its bound state until the recollision happens. Faisal and A. Becker have developed a model for NSDI based on their intense-field many-body S-matrix (IMSM) theory [152, 165, 166], while others have followed the Keldysh-Faisal-Reiss approach. IMSM is an asymptotic and probability series, in which by rearranging the S-matrix series the desired transition process appears in the first few leading terms of series. The leading terms of the series provide a Feynman diagram that contributes to the transition amplitude [167]. As a result, by analyzing the Feynman diagram one can identify the possible mechanisms involved in the process of interest. A more detailed discussion of this theory is presented in the review [168].

Up to now, several groups have managed to evaluate the Feynman diagram of electron-impact ionization of NSDI in the context of the SFA [81, 105, 118, 129, 163, 164]. Furthermore, the Feynman diagram of the RESI mechanism has been evaluated as part of my PhD work. These Feynman diagrams are illustrated in section 3.3.1.

3.2 Direct and Rescattered Ionization Amplitude of One-electron Processes

In this section we employ the strong-field approximation to derive the ionization amplitude for both direct and rescattered processes when considering a system with just one active electron[1].

With the presence of an external field the full Hamiltonian of an atom is

$$H = H_0 + H_{int}(t) \tag{3.1}$$

which satisfies the Schrödinger equation

$$i\frac{\partial}{\partial t}\left|\psi(t)\right\rangle = H\left|\psi(t)\right\rangle \tag{3.2}$$

Here H_0 is the Hamiltonian of the unperturbed atom and H_{int} represents the atom-laser interaction Hamiltonian.

The field-free or the unperturbed atomic Hamiltonian is

$$H_0 = \frac{\widehat{\mathbf{p}}^2}{2} + V(\widehat{r}) \tag{3.3}$$

which satisfies

$$i\frac{\partial}{\partial t}\left|\psi(t)\right\rangle = H_0\left|\psi(t)\right\rangle \tag{3.4}$$

Here $\widehat{\mathbf{p}}^2/2$ and $V(r)$ represent the kinetic energy of the free electron and the Coulomb potential of the system, respectively. In the above equations, the hat denotes operators.

By ignoring the Coulomb potential $V(\widehat{r})$ in equation (3.1), we will have the Gordon-Volkov Hamiltonian

$$H_v = \frac{\widehat{\mathbf{p}}^2}{2} + H_{int}(t) \tag{3.5}$$

[1]The derivation in this section is based mainly on lectures that have been given by Dr Carla Figueira de Morisson Faria and reference [160].

which satisfies

$$i\frac{\partial}{\partial t}\left|\psi^{v}(t)\right\rangle = H_{v}\left|\psi^{v}(t)\right\rangle \tag{3.6}$$

The time evolution operator associated with the full Hamiltonian of the system, which includes the binding potential and the laser field, is defined as $U(t,t') = \mathcal{T}exp[-i\int_{t'}^{t} H(s)ds]$, where $\mathcal{T}$ denotes the time ordering.

By using the Dyson equation, we define the time-evolution operator $U(t,t')$ of the system, as

$$U(t,t') = U_0(t,t') - i\int_{t'}^{t} dt'' U(t,t'')H_{int}(t'')U_0(t'',t') \tag{3.7}$$

where $U_0(t,t') = e^{-iH(t-t')}$ is the field-free time-evolution operator for an electron interacting with the core, for which (3.3) is the corresponding Hamiltonian. This time evolution operator satisfies

$$\begin{aligned} i\frac{\partial}{\partial t}U_{(0)}(t,t') &= H_0(t)U_{(0)}(t,t') \\ -i\frac{\partial}{\partial t'}U_{(0)}(t,t') &= U_{(0)}(t,t')H_0(t') \end{aligned} \tag{3.8}$$

In (3.7), the Hamiltonian H_{int} will have different forms depending on the gauge one uses. In the length gauge, it reads:

$$H_{int}(t'') = \mathbf{E}(t'').\mathbf{r}$$

and in the velocity gauge

$$H_{int}(t'') = -i\nabla.\mathbf{A}(t'') + \frac{\mathbf{A}^2(t'')}{2}.$$

In addition, the time-evolution operator $U(t,t')$ can have another integral form if written in terms of the binding potential V:

$$U(t,t') = U^{(v)}(t,t') - i\int_{t'}^{t} dt'' U(t,t'')VU^{(v)}(t'',t') \tag{3.9}$$

where $U^{(v)}(t,t')$ is the Gordon-Volkov time evolution operator [146, 147]. This is the time-evolution operator for a free electron in an external field and its corresponding Hamiltonian is (3.5). This time evolution operator satisfies

$$\begin{aligned} i\frac{\partial}{\partial t}U^{(v)}(t,t') &= H_v(t)U^{(v)}(t,t') \\ -i\frac{\partial}{\partial t'}U^{(v)}(t,t') &= U^{(v)}(t,t')H_v(t') \end{aligned} \tag{3.10}$$

In standard ("weak field ") perturbation theory we iterate (3.7), while in the Gordon-Volkov series we iterate (3.9). In the strong-field approximation we mix these two series as will be demonstrated.

If a system is in the initial state $|\psi(t')\rangle$, then under the time evolution operator $U(t,t')$ it evolves from t' to t , i.e.

$$|\psi(t)\rangle = U(t,t')\left|\psi(t')\right\rangle, \tag{3.11}$$

The transition amplitude for ionization from the the ground state of an atom $|\psi_g(t')\rangle$ into a scattering state $|\psi_p(t)\rangle$ is

$$M_p = \lim_{t\to\infty,t'\to-\infty} \langle\psi_p(t)|\, U(t,t')\left|\psi_g(t')\right\rangle, \tag{3.12}$$

where p is the asymptotic momentum of the scattering state.

By substituting Dyson equation (3.7) into (3.12) we have

$$M_p = \lim_{t\to\infty,t'\to-\infty} < \psi_p(t)U_0(t,t')|\psi_g(t') > -i\lim_{t\to\infty,t'\to-\infty}\int_{t'}^{t} dt' \left\langle\psi_p(t)\right| U(t,t')H_{int}(t')\left|\psi_g(t')\right\rangle, \tag{3.13}$$

The first term is zero since the ground state and the scattering state are orthogonal. Thus,

$$M_p = -i\lim_{t\to\infty}\int_{-\infty}^{t} dt' \left\langle\psi_p(t)\right| U(t,t')H_{int}(t')\left|\psi_g(t')\right\rangle. \tag{3.14}$$

Equation (3.14) gives the matrix element without any approximation. We now employ the strong-field approximation. We take the zeroth order of (3.9) and insert it into (3.7).

Equation (3.14) now becomes

$$M_p^{(1)} = -i \lim_{t\to\infty} \int_{-\infty}^{t} dt' \, \langle \psi_p(t)| \, U^{(v)}(t,t') H_{int}(t') \, |\psi_g(t')\rangle \, . \tag{3.15}$$

The $H_{int}(t')$ in equation (3.15) can be replaced by the binding potential V, if we write $H_{int}(t')$ as

$$H_{int}(t') + H_0 = H_v + V,$$

and using equations (3.4) and (3.10) we will have

$$\begin{aligned} M_p^{(1)} &= -i \lim_{t\to\infty} \int_{-\infty}^{t} dt' \, \langle \psi_p(t)| \, U^{(v)}(t,t')(H_v(t') - H_0 + V) \, |\psi_g(t')\rangle \\ &= -i \lim_{t\to\infty} \int_{-\infty}^{t} dt' \, \langle \psi_p(t)| \, \{-i\frac{\partial}{\partial t'} U^{(v)}(t,t') - U^{(v)}(t,t') i\frac{\partial}{\partial t'} \\ &\qquad + U^{(v)}(t,t')V\} \, |\psi_g(t')\rangle \, . \end{aligned} \tag{3.16}$$

The second term in the bracket cancels if we integrate the first term in the bracket using integration by parts with respect to t'. As a result, we have

$$\begin{aligned} M_p^{(1)} &= -\lim_{t\to\infty} \langle \psi_p(t)| \, U^{(v)}(t,t') \, |\psi_g(t')\rangle \\ &\quad -i \lim_{t\to\infty} \int_{-\infty}^{t} dt' \, \langle \psi_p(t)| \, U^{(v)}(t,t')V \, |\psi_g(t')\rangle \, . \end{aligned} \tag{3.17}$$

This first term in (3.17) vanishes due to the orthogonality of the initial state and the final scattering state. Thus we end up with the same equation as (3.15), just having V instead of H_{int}, i.e.

$$M_p^{(1)} = -i \lim_{t\to\infty} \int_{-\infty}^{t} dt' \, \langle \psi_p(t)| \, U^{(v)}(t,t')V \, |\psi_g(t')\rangle \, . \tag{3.18}$$

Equations (3.15) and (3.18) represent the SFA transition amplitude of direct ionization of a system with just one active electron.

If we insert the first order of (3.9) into (3.7) and replace its result with $U(t,t')$ in (3.14), then we obtain

$$\begin{aligned} M_p^{(1,2)} &= -i\lim_{t\to\infty}\int_{-\infty}^{t} dt' \left\langle \psi_p(t)\right| U^{(v)}(t,t')H_{int}(t') \left|\psi_g(t')\right\rangle \\ &+ \lim_{t\to\infty}\int_{-\infty}^{t} dt''\int_{-\infty}^{t''} dt' \left\langle \psi_p(t)\right| U^{(v)}(t,t'')VU^{(v)}(t'',t')H_{int}(t') \left|\psi_g(t')\right\rangle \end{aligned} \tag{3.19}$$

The first term in (3.19) corresponds to direct ionization, while the second terms gives the scattered ATI transition amplitude. Following the same argument as above the scattered part in (3.19) can be written in terms of the binding potential V. Thus

$$M_p^{(2)} = -\lim_{t\to\infty}\int_{-\infty}^{t} dt'' \int_{-\infty}^{t''} dt' \left\langle \psi_p(t)\right| U^{(v)}(t,t'')VU^{(v)}(t'',t')V \left|\psi_g(t')\right\rangle \tag{3.20}$$

Performing this integral in the limit $t \to \infty$ is awkward. However, one can overcome this problem by replacing the scattering state $\langle\psi_p(t)|$ with a field-dressed plane wave (Volkov state $\left\langle\psi_p^{(v)}(t)\right|$).

$$M_p^{(2)} = -\int_{-\infty}^{\infty} dt \int_{-\infty}^{t} dt' \left\langle \psi_p^{(v)}(t)\right| VU^{(v)}(t,t')V \left|\psi_g(t')\right\rangle \tag{3.21}$$

The use of Volkov wavefunction for the final state makes the calculation of matrix element much easier but it destroys the orthogonality of the initial and the final states.

The equation we derived in (3.21) describes the physical process in which an electron, initially, is in a bound state $|\psi_g\rangle$. Then at a time t', this electron is freed by tunneling ionization and propagates in the continuum. Later on at a time t, it interacts with parent ion and rescatters to a Volkov state. Equation (3.21) is very general and under the single active electron approximation can be applied to any system. Furthermore, it can be modified to in order to take care of a system with two correlated electrons. In the next section we discuss how it can be modified for NSDI.

3.3 Transition Amplitudes for NSDI

In the rescattering mechanism, nonsequential double ionization is initiated by tunneling of the first electron through the potential barrier of the system. Subsequently, the

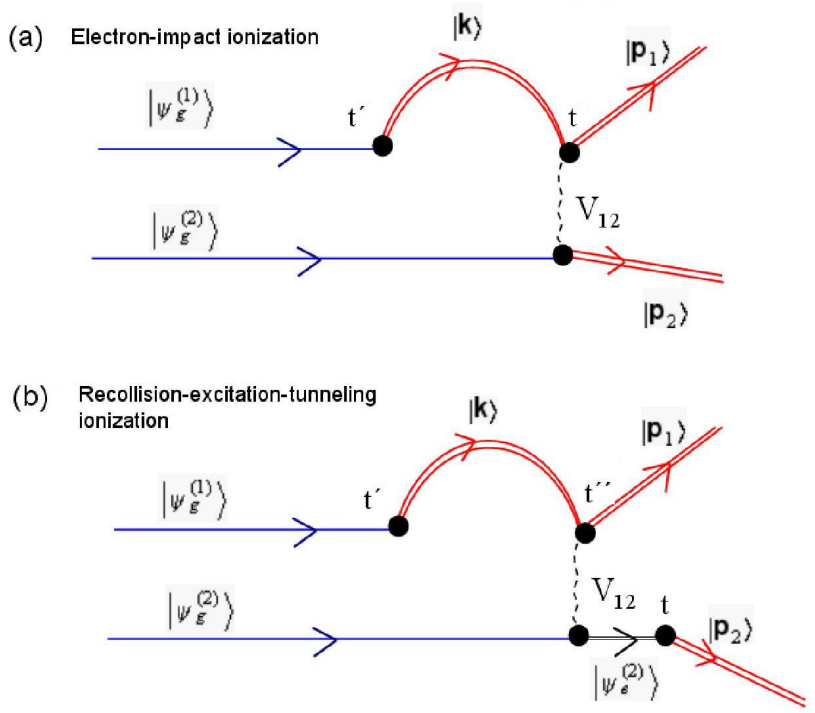

FIGURE 3.1: (Modified version of figure 16 in [14]) Feynman diagram of the dominant rescattering mechanisms of NSDI in the tunneling regime. Diagram (a) represents electron-impact ionization, in which an electron initially in a bound state $|\psi_{1g}>$, is released by tunneling ionization into a Volkov state at a time t', returns at a time t and releases the second electron by giving enough energy to make it overcome the second ionization potential. Diagram (b) corresponds to RESI, in which an electron, initially in a bound state $|\psi_g^{(1)}>$, is released by tunneling ionization into a Volkov state at a time t', returns at a time t'' and excites a second electron from the initial bound state $|\psi_{2g}>$ to the bound state $|\psi_{2e}>$, which it subsequently tunnels at a later time t, reaching a Volkov state. The electron-electron interaction is indicated in the figure by V_{12}, the initial bound states by the dark blue lines, the excited bound state of the second electron by the thick black line and the Volkov states by the double red lines.

released electron is driven back toward its parent ion, with which it collides. In the recollision process, the second electron may be dislodged by impact ionization or it may be promoted to an excited state, from which it subsequently tunnels. The Feynman diagram that describes these two rescattering mechanisms is shown in Figure 3.1. In this diagram, panel (a) represents the impact-ionization rescattering process of NSDI, while panel (b) shows the RESI mechanism. Here, we do not consider electron-electron interaction in the continuum, i.e. when both electrons are released [75, 169]. Now, based on the transition amplitude we derived in (3.21), we define the transition amplitudes of electron-impact ionization and RESI. The former transition amplitude has mainly been developed by Faria et al. [75, 105], while the latter has been developed during my PhD.

3.3.1 Electron-impact Ionization

In NSDI, we are dealing with two active electrons, Thus, we need to incorporate the wave function of these two electrons into the transition amplitude (3.21). For the sake of simplicity in analytical calculation we approximate the ground state of the two-electron system by a product of one-electron states

$$\left|\psi_g(t^{'})\right\rangle = \left|\psi_g^{(2)}(t^{'})\right\rangle \otimes \left|\psi_g^{(1)}(t^{'})\right\rangle \tag{3.22}$$

where $|\psi_g^{(n)}(t') > = \exp[iE_{ng}t']|\varphi_g^{(n)} >$, and $n = 1, 2$. The ionization potential of the first and the second electron is given by E_{ng}.

The final state of the two-electron system can be chosen either as a two-electron Volkov state, with correlation via electron-electron repulsion, or the product of one-electron Volkov states:

$$\left|\psi_p^{(v)}(t)\right\rangle = \left|\psi_{\mathbf{p}_2}^{(v)}(t)\right\rangle \otimes \left|\psi_{\mathbf{p}_1}^{(v)}(t)\right\rangle \tag{3.23}$$

with asymptotic momenta $\mathbf{p}_{1'}\mathbf{p}_2$,

By considering the initial state (3.22) and the final state (3.23), the S-matrix in (3.21) can be written as

$$M_{EI} = -\int_{-\infty}^{\infty} dt \int_{-\infty}^{t} dt' < \psi_{p_1}^{(v)}(t), \psi_{p_2}^{(v)}(t)|\tilde{V}_{12}U_1^{(v)}(t,t')U_2(t,t')\tilde{V}_1|\psi_g^{(1)}(t'), \psi_g^{(2)}(t') > \tag{3.24}$$

where $U_1^{(v)}(t,t')$ is the Gordon-Volkov time-evolution operator for the first electron and $U_2(t,t')$ is the field-free time evolution operator for the second electron. The interactions $\tilde{V}_1 = P_{cg}V_1P_{gg}$ corresponds to the atomic binding potential acting on the first electron and $\tilde{V}_{12} = P_{cc}V_{12}P_{cg}$ to the electron-electron interaction. Unless otherwise stated, we consider the length gauge and atomic units throughout.

The operators $P_{\mu\nu}$ are projectors onto the bound or continuum subspaces. Specifically,

$$P_{gg} = \left|\varphi_g^{(1)}, \varphi_g^{(2)}\right\rangle \left\langle\varphi_g^{(1)}, \varphi_g^{(2)}\right| \tag{3.25}$$

is the projector onto the two-electron field-free ground state,

$$P_{cg} = \left|\mathbf{k}, \varphi_g^{(2)}\right\rangle \left\langle\mathbf{k}, \varphi_g^{(2)}\right| \tag{3.26}$$

projects the first electron onto the continuum state $|\mathbf{k}\rangle$, and keeps the second electron in the ground state $\left|\varphi_g^{(2)}\right\rangle$, and

$$P_{cc} = |\mathbf{p}_1, \mathbf{p}_2\rangle \langle \mathbf{p}_1, \mathbf{p}_2| \,. \tag{3.27}$$

is the projector onto the two-electron state in the field-free continuum.

These projectors guarantee that the continuum and bound states remain orthogonal. For the exact time evolution operators, the orthogonality property holds, while it is lost if the continuum states are approximated by Volkov states (for details see [170]). However, we apply projector operators to force the orthogonality relationship in the Volkov state. Then, equation (3.24) becomes

$$\begin{aligned} M_{EI} &= -\int_{-\infty}^{\infty} dt \int_{-\infty}^{t} dt' < \psi_{p_1}^{(v)}(t), \psi_{p_2}^{(v)}(t)|V_{12}U_1^{(v)}(t,t')U_2(t,t')|\mathbf{k}, \psi_g^{(2)}(t') > \\ &\quad < \mathbf{k}|V_1|\psi_g^{(1)}(t') > . \end{aligned} \tag{3.28}$$

We expand the Volkov propagator in terms of Volkov states

$$U^{(v)}(t,t') = \int d^3k |\psi_{\mathbf{k}}^{(v)}(t) >< \psi_{\mathbf{k}}^{(v)}(t')|,$$

then we obtain

$$\begin{aligned} M_{EI} &= -\int_{-\infty}^{\infty} dt \int_{-\infty}^{t} dt' \int d^3k < \psi_{p_1}^{(v)}(t), \psi_{p_2}^{(v)}(t)|V_{12}|\psi_{\mathbf{k}}^{(v)}(t) > \\ &\quad U_2(t,t')\psi_g^{(2)}(t') >< \psi_{\mathbf{k}}^{(v)}(t')|\mathbf{k} >< \mathbf{k}|V_1|\psi_g^{(1)}(t') > . \end{aligned} \tag{3.29}$$

We write the field-free time evolution operator as

$$U_n(t,t') = \exp[i \int_{t'}^{t} \widehat{H}(\tau) d\tau] = \exp[iE_{ng}(t-t')] \tag{3.30}$$

where $\widehat{H}(\tau)$ is the Hamiltonian of the bound-electron and E_{ng} is its ionization potential.

The bound state wavefunction and the Volkov state wavefunction are given by

$$< \mathbf{r}_i|\psi_g^{(n)}(t') >= \exp[iE_{ng}t']\varphi_g^{(n)}(\mathbf{r}_i) \tag{3.31}$$

and

$$< \mathbf{r}_i|\psi_p^{(v)}(t') >= (2\pi)^{-3/2}\exp[i(\mathbf{p}+\mathbf{A}(t)\cdot\mathbf{r}_i]\exp[-\frac{i}{2}\int^t d\tau(\mathbf{p}+\mathbf{A}(t))^2], \tag{3.32}$$

respectively.

By using (3.30)-(3.32) in equation (3.29) and applying closure relations $\int d^3p_i|\mathbf{p}_i >< \mathbf{p}_i|$ and $\int d^3r_i|\mathbf{r}_i >< \mathbf{r}_i|$, we obtain

$$M_{EI} = \int_{-\infty}^{\infty} dt \int_{-\infty}^{t} dt' \int d^3k V_{\mathbf{p}_n,\mathbf{k}} V_{\mathbf{k}0} \exp[iS_{EI}(\mathbf{p}_n,\mathbf{k},t,t')] \tag{3.33}$$

with the action

$$\begin{aligned} S_{EI}(\mathbf{p}_n,\mathbf{k},t,t') &= -\sum_{n=1}^{2}\int_t^{\infty} d\tau \frac{[\mathbf{p}_n+\mathbf{A}(\tau)]^2}{2} \\ &\quad -\int_{t'}^{t} d\tau \frac{[\mathbf{k}+\mathbf{A}(\tau)]^2}{2} + E_{2g}t + E_{1g}t' \end{aligned} \tag{3.34}$$

Here, $\mathbf{A}(\tau)$ is the vector potential. The energies E_{1g} and E_{2g} denote the first ionization potential and the ground-state energy of the singly ionized atom, respectively. The drift momentum of the first electron, between ionization and recollision, is given by $\mathbf{k}$ and the final momenta of both electrons by $\mathbf{p}_n(n=1,2)$.

Equation (3.33) describes a physical process in which at time t' the first electron leaves the atom by tunneling from a ground state $\left|\varphi_g^{(1)}\right\rangle$. From t' to t, it propagates in the continuum with momentum $\mathbf{k}$. Upon its return, through the interaction V_{12}, the first electron releases the second electron into the continuum. Finally, both electrons reach the detector with momenta $\mathbf{p}_n(n=1,2)$.

Here, the influence of the binding potentials and the electron-electron interaction is embedded in the prefactors $V_{\mathbf{k}0}$ and $V_{\mathbf{p}_n,\mathbf{k}}$. Explicitly, they read

$$V_{\mathbf{k}0} =< \widetilde{\mathbf{k}}(\mathbf{t}')|V_1|\varphi_g^{(1)} >= \frac{1}{(2\pi)^{3/2}}\int d^3r_1 \exp[-i\widetilde{\mathbf{k}}(t')\cdot\mathbf{r}_1]V(\mathbf{r}_1)\varphi_g^{(1)}(\mathbf{r}_1), \tag{3.35}$$

and

$$V_{\mathbf{p}_n,\mathbf{k}} = \langle \widetilde{\mathbf{p}}_1(t), \widetilde{\mathbf{p}}_2 |\, V_{12} \left| \widetilde{\mathbf{k}}(t), \varphi_g^{(2)} \right\rangle = \frac{1}{(2\pi)^{9/2}} \iint d^3r_2 d^3r_1 \exp[i\widetilde{\mathbf{k}}(t)\cdot\mathbf{r}_1] \exp[-i\sum_n^2 \widetilde{\mathbf{p}}_n(t)\cdot\mathbf{r}_n] \varphi_g^{(2)}(\mathbf{r}_2) V_{12}(\mathbf{r}_1,\mathbf{r}_2) \quad (3.36)$$

where in length gauge $\widetilde{\mathbf{k}}(\tau) = \mathbf{k} + \mathbf{A}(\tau)$ and $\widetilde{\mathbf{p}}_n(\tau) = \mathbf{p}_n + \mathbf{A}(\tau)$ ($\tau = t, t'$) and in velocity gauge $\widetilde{\mathbf{k}}(\tau) = \mathbf{k}$ and $\widetilde{\mathbf{p}}_n(\tau) = \mathbf{p}_n$. In the above equations, $\varphi_g^{(1)}(\mathbf{r}_1)$ and $\varphi_g^{(2)}(\mathbf{r}_2)$ denote the initial position-space wave functions of the first and the second electrons in the ground states, respectively. The potential $V(\mathbf{r}_1)$ corresponds to the atomic binding potential as seen by the first electron and $V_{12}(\mathbf{r}_1,\mathbf{r}_2)$ corresponds to the electron-electron interaction at the time of the recollision[2].

One can choose different kinds of binding potential $V(\mathbf{r}_1)$, wavefunction $\varphi_g^{(n)}(\mathbf{r}_n)$ and interaction $V_{12}(\mathbf{r}_1,\mathbf{r}_2)$ processes for the prefactors. For atoms, it is more convenient to use ground state hydrogenic-wavefunction for $\varphi_g^{(n)}(\mathbf{r}_n)$. In the length gauge, for some cases, this assumption causes a singularity in the computation of the prefactors. In Chapter 6, I illustrate this issue in more detail. The binding potential $V(\mathbf{r}_1)$ and the type of the electron-electron interaction $V_{12}(\mathbf{r}_1,\mathbf{r}_2)$ affect the computation of the electron momentum distributions in (3.33). For instance, if $V(\mathbf{r}_1)$ is considered as a zero-range potential and $V_{12}(\mathbf{r}_1,\mathbf{r}_2)$ as a three-body contact type interaction ($V(\mathbf{r}_1,\mathbf{r}_2) \sim \delta(\mathbf{r}_1-\mathbf{r}_2)\delta(\mathbf{r}_2)$), the five dimension transition amplitude in (3.33) can be expressed by one-dimensional quadrature in terms of Bessel functions [151]. This thesis examines the NSDI process in the tunneling regime with long and short range potentials. The effect of the electron-electron interaction and the initial electron bound states are illustrated in Chapter (6).

Under the additional assumption, that the electron-electron interaction depends only on the difference between the two electron coordinates, we obtain

$$V_{12}(\mathbf{r}_1,\mathbf{r}_2) = V_{12}(\mathbf{r}_1-\mathbf{r}_2) \quad (3.37)$$

By using (3.37) the form factor in (3.36) becomes

$$V_{\mathbf{p}_n,\mathbf{k}} = \frac{1}{(2\pi)^{9/2}} \widetilde{\mathbf{V}}_{12}(\mathbf{p}_n-\mathbf{k}) \int d^3r_2 \exp[-i\sum_n^2 (\widetilde{\mathbf{p}}_n(t) - \widetilde{\mathbf{k}}(t))\cdot\mathbf{r}_2] \varphi_g^{(2)}(\mathbf{r}_2)$$

[2] One can show that the gauge transformation $e^{i\mathbf{r}\cdot\mathbf{A}(\tau)}$, where $\tau = t, t'$, from the length gauge to velocity gauge causes a shift $\mathbf{p} \to \mathbf{p} - \mathbf{A}(\mathbf{t})$ in a ket $|\mathbf{p}\rangle$. In our framework, this shift cancels the time dependence of the Volkov states. This will held for the RESI transition amplitude.

where

$$\widetilde{\mathbf{V}}_{12}(\mathbf{p}_1 - \mathbf{k}) = \int d^3r \exp[-i(\mathbf{p}_1(t) - \mathbf{k}(t)) \cdot \mathbf{r}] V_{12}(\mathbf{r}) \tag{3.38}$$

and $\mathbf{r} = \mathbf{r}_1 - \mathbf{r}_2$.

3.3.2 Recollision-excitation with Subsequent Tunneling Ionization

In the RESI mechanism, the second electron is released by excitation with subsequent tunneling instead of direct ionization, as is the case for electron-impact ionization mechanism of NSDI. Therefore, we need to incorporate this process in (3.24). As a result, the transition amplitude describing the recollision-excitation-tunneling ionization (RESI) physical mechanism reads

$$\begin{aligned} M_{RESI} \;=\; & \int_{-\infty}^{\infty} dt \int_{-\infty}^{t} dt'' \int_{-\infty}^{t''} dt' \\ & < \mathbf{p}_1(t), \mathbf{p}_2(t) | \tilde{V}_{\text{ion}} \tilde{U}(t, t'') V_{12} U(t'', t') \tilde{V} | \psi_g^{(1)}(t'), \psi_g^{(2)}(t') >, \end{aligned} \tag{3.39}$$

where $U(t'', t')$ and $\tilde{U}(t, t'')$ denote the time evolution operator of the two-electron system. Like in the previous case, $|\psi_g^{(1)}(t'), \psi_g^{(2)}(t') >$ is the two-electron initial state, and $|\mathbf{p}_1(t), \mathbf{p}_2(t)\rangle$ the final two-electron continuum state. The interactions $\tilde{V} = P_{cg} V_1 P_{gg}$ and V_{12} correspond to the atomic binding potential and the electron-electron interaction, respectively. Here, in comparison to electron-impact ionization, we have one extra interaction, due to the ionization of the second electron from an excited state. Therefore, $\tilde{V}_{\text{ion}} = P_{cc} V_{\text{ion}} P_{ce}$ corresponds to the binding potential of the singly ionized core. Also, similar to electron-impact ionization, we assume the initial state of the system is a product state of one-electron ground states, i.e., $|\psi_g^{(1)}(t'), \psi_g^{(2)}(t') >= |\psi_g^{(1)}(t') > \otimes |\psi_g^{(2)}(t') >$, with $|\psi_g^{(n)}(t') >= \exp[iE_{ng}t']|\varphi_g^{(2)} >$.

The operators $P_{\mu\nu}$, which project electrons onto the bound or continuum subspaces, stay the same as for electron-impact ionization. In addition to those operators, we have one extra operator to project the first electron onto the continuum state $|\mathbf{k}\rangle$, and the second electron onto the excited state $\left|\varphi_e^{(2)}\right\rangle$.

$$P_{ce} = \left|\mathbf{k}, \varphi_e^{(2)}\right\rangle \left\langle \mathbf{k}, \varphi_e^{(2)}\right| \tag{3.40}$$

The time-evolution operator of the system from the tunneling time t' of the first electron to the recollision time t'' was approximated by $U(t'', t') = U_V^{(1)}(t'', t') \otimes U_g^{(2)}(t'', t')$, where $U_V^{(1)}$ is the Gordon-Volkov time-evolution operator for the first electron and $U_g^{(2)}$ is the

field-free time evolution operator for the second electron in the ground state. Subsequent to the recollision, the time evolution operator of the system was taken to be $\tilde{U}(t,t'') = U_V^{(1)}(t,t'') \otimes U_e^{(2)}(t,t'')$. Here, $U_V^{(1)}$ is the Gordon-Volkov time-evolution operator for the first electron and $U_e^{(2)}$ is the field-free time evolution operator for the second electron in the excited state of the singly ionized ion.

Similar to the electron-impact ionization mechanism, we employ the closure relations and the explicit expressions for the Gordon-Volkov time-evolution operators. Thus, the equation (3.39) can be written as

$$M_{RESI} = \int_{-\infty}^{\infty} dt \int_{-\infty}^{t} dt'' \int_{-\infty}^{t''} dt' \int d^3k V_{\mathbf{p}_2 e} V_{\mathbf{p}_1 e,\mathbf{k}g} V_{\mathbf{k}g} \exp[iS(\mathbf{p}_n, \mathbf{k}, t, t', t'')] \quad (3.41)$$

with the action

$$\begin{aligned} S_{RESI}(\mathbf{p}_n, \mathbf{k}, t, t', t'') \;=\; & -\int_t^{\infty} d\tau \frac{[\mathbf{p}_2 + \mathbf{A}(\tau)]^2}{2} - \int_{t''}^{\infty} d\tau \frac{[\mathbf{p}_1 + \mathbf{A}(\tau)]^2}{2} \\ & - \int_{t'}^{t''} d\tau \frac{[\mathbf{k} + \mathbf{A}(\tau)]^2}{2} + E_{2e}(t - t'') \\ & + E_{2g} t'' + E_{1g} t'. \end{aligned} \quad (3.42)$$

Thereby, $\mathbf{A}(\tau)$ is the vector potential, the energy E_{1g} denotes the first ionization potential, E_{2g} the ground-state energy of the singly ionized atom and E_{2e} the ionization potential energy of the state to which the second electron is excited[3]. The intermediate momentum of the first electron is given by $\mathbf{k}$ and the final momenta of both electrons by $\mathbf{p}_n (n = 1, 2)$. Equation (3.41) describes a physical process in which the first electron leaves the atom at a time t', propagates in the continuum with momentum $\mathbf{k}$ from t' to t'', and upon returning, gives part of its kinetic energy to the core so that a second electron is promoted from a state with energy E_{2g} to an excited state with energy E_{2e}. This electron then reaches the detector with momentum $\mathbf{p}_1$. At a subsequent time t, the second electron tunnels from the excited state, reaching the detector with momentum $\mathbf{p}_2$.

Within our framework, all influence of the electron-electron interaction and of the binding potential is contained in the prefactors $V_{\mathbf{p}_2 e}, V_{\mathbf{p}_1 e,\mathbf{k}g}$ and $V_{\mathbf{k}g}$. Explicitly, they read

$$V_{\mathbf{p}_2 e} = < \mathbf{p}_2(t) | V_{\text{ion}} | \varphi_e^{(2)} > = \frac{1}{(2\pi)^{3/2}} \int d^3 r_2 V_{\text{ion}}(\mathbf{r}_2) e^{-i\mathbf{p}_2(t)\cdot\mathbf{r}_2} \varphi_e^{(2)}(\mathbf{r}_2), \quad (3.43)$$

[3]This energy is postulated according to the problem at hand.

$$V_{\mathbf{p}_1 e,\mathbf{k}g} = \left\langle \mathbf{p}_1(t''), \varphi_e^{(2)} \right| V_{12} \left| \mathbf{k}(t''), \varphi_g^{(2)} \right\rangle = \frac{1}{(2\pi)^3} \int\int d^3r_2 d^3r_1 e^{-i(\mathbf{p}_1-\mathbf{k})\cdot\mathbf{r}_1} \left[\varphi_e^{(2)}(\mathbf{r}_2)\right]^* \varphi_g^{(2)}(\mathbf{r}_2) V_{12}(\mathbf{r}_1,\mathbf{r}_2) \quad (3.44)$$

and

$$V_{\mathbf{k}g} = < \mathbf{k}(t')|V|\varphi_g^{(1)} > = \frac{1}{(2\pi)^{3/2}} \int d^3r_1 e^{-i\mathbf{k}(t')\cdot\mathbf{r}_1} V(\mathbf{r}_1)\varphi_g^{(1)}(\mathbf{r}_1), \quad (3.45)$$

where in the length gauge $\mathbf{k}(\tau) = \mathbf{k} + \mathbf{A}(\tau)$ and $\mathbf{p}_n(\tau) = \mathbf{p}_n + \mathbf{A}(\tau)$ ($\tau = t, t', t''$ and in the velocity gauge $\mathbf{k}(\tau) = \mathbf{k}$) and $\mathbf{p}_n(\tau) = \mathbf{p}_n$. In the above equations, $\varphi_e^{(2)}(\mathbf{r}_2), \varphi_g^{(2)}(\mathbf{r}_2)$, and $\varphi_g^{(1)}(\mathbf{r}_1)$ denote the initial position-space wave functions of the second electron in the excited state, of the second electron in the ground state and of the first electron in the ground state, respectively. The potentials $V(\mathbf{r}_1)$ and $V_{\text{ion}}(\mathbf{r}_2)$ correspond to the atomic binding potential as seen by the first and second electron, respectively. One should note that the form factor $V_{\mathbf{p}_2 e}$ is similar to that obtained for direct above-threshold ionization, in which an electron, initially bound, reaches the detector without rescattering [160].

By applying the assumption in (3.37), equation (3.44) may be written as

$$V_{\mathbf{p}_1 e,\mathbf{k}g} = \frac{V_{12}(\mathbf{p}_1-\mathbf{k})}{(2\pi)^3} \int d^3r_2 e^{-i(\mathbf{p}_1-\mathbf{k})\cdot\mathbf{r}_2} \left[\varphi_e^{(2)}(\mathbf{r}_2)\right]^* \varphi_g^{(2)}(\mathbf{r}_2), \quad (3.46)$$

with

$$V_{12}(\mathbf{p}_1-\mathbf{k}) = \int d^3r V_{12}(\mathbf{r}) \exp[-i(\mathbf{p}_1-\mathbf{k})\cdot\mathbf{r}] \quad (3.47)$$

and $\mathbf{r} = \mathbf{r}_1 - \mathbf{r}_2$. One should note that the prefactor (3.46) resembles that obtained for high-order above-threshold ionization, in which an electron reaches the detector after experiencing a single rescattering [160].

3.3.3 Electron Momentum Distributions

In this thesis the electron momentum distributions are computed as functions of the momentum components $(p_{1\parallel}, p_{2\parallel})$ parallel to the laser-field polarization, in order to compare with existing experiments. Throughout this thesis, we approximate the external laser field by a monochromatic wave

$$E(t) = -dA(t)/dt = 2\omega\sqrt{U_p}\sin\omega t \quad (3.48)$$

This is a reasonable approximation for pulses whose duration is of the order of ten cycles or longer (see, e.g. [78, 171] for a more detailed discussion). In this case, the electron momentum distributions, when integrated either partially or fully over the transverse momentum components, read

$$F(p_{1\parallel}, p_{2\parallel}) = \iint d^2p_{1\perp} d^2p_{2\perp} |M_R(\mathbf{p}_1, \mathbf{p}_2) \tag{3.49}$$

$$+ \quad M_L(\mathbf{p}_1, \mathbf{p}_2) + \mathbf{p}_1 \leftrightarrow \mathbf{p}_2|^2, \tag{3.50}$$

where $M_R(\mathbf{p}_1, \mathbf{p}_2)$ is given by equations (3.33) (electron impact ionization) or (3.41) (RESI) and $d^2p_{n\perp} = p_{n\perp} dp_{n\perp} d\varphi_{p_n}$. The amplitudes $M_R(\mathbf{p}_1, \mathbf{p}_2)$ and $M_L(\mathbf{p}_1, \mathbf{p}_2)$ are related to the right and the left peaks in the electron momentum distributions, respectively We employ symmetry $\mathbf{A}(t \pm T/2) = -\mathbf{A}(t)$, where $T = 2\pi/\omega$ denotes a field cycle, to compute left peak $M_L(\mathbf{p}_1, \mathbf{p}_2)$ from the right peak. The symmetry works for monochromatic laser fields, while for few-cycle pulses it does not and one needs to computes each peak separately.

For electron-impact ionization, we have $M_L(\mathbf{p}_1, \mathbf{p}_2, t, t') = M_R(-\mathbf{p}_1, -\mathbf{p}_2)$, where the momentum signs must be changed simultaneously. This implies that there is a symmetry upon the reflection $(\mathbf{p}_1, \mathbf{p}_2) \to (-\mathbf{p}_1, -\mathbf{p}_2)$, which comes from the fact that the action corresponding to M_L and M_R are given by $S_R(\mathbf{p}_1, \mathbf{p}_2, \mathbf{k}, t, t') = S_{EI}(\mathbf{p}_1, \mathbf{p}_2, \mathbf{k}, t, t')$ and $S_L(\mathbf{p}_1, \mathbf{p}_2, \mathbf{k}, t, t', t'') = S_{EI}(-\mathbf{p}_1, -\mathbf{p}_2, \mathbf{k}, t \pm T/2, t' \pm T/2)$. For RESI, the actions corresponding to the transition amplitudes M_L and M_R are given by $S_R(\mathbf{p}_1, \mathbf{p}_2, \mathbf{k}, t, t', t'') = S_{RESI}(\mathbf{p}_1, \mathbf{p}_2, \mathbf{k}, t, t', t'')$ and $S_L(\mathbf{p}_1, \mathbf{p}_2, \mathbf{k}, t, t', t'') = S_{RESI}(\mathbf{p}_1, \mathbf{p}_2, \mathbf{k}, t \pm T/2, t' \pm T/2, t'' \pm T/2)$. They also obey the symmetry $|S_{RESI}(\mathbf{p}_1, \mathbf{p}_2, t, t', t'')| = |S_{RESI}(-\mathbf{p}_1, -\mathbf{p}_2, t \pm T/2, t' \pm T/2, t'' \pm T/2)|$. In our computation the distributions have also been symmetrized with respect to the exchange $\mathbf{p}_1 \leftrightarrow \mathbf{p}_2$. To a good approximation, the quantum-interference terms $[M_\nu(\mathbf{p}_1, \mathbf{p}_2)]^* M_\mu(\mathbf{p}_1, \mathbf{p}_2), \nu \neq \mu$, get washed out upon the transverse-momentum integration, so that it is sufficient to add the above-stated amplitudes incoherently. In Appendix D, we provide details on why the interference terms can be neglected. A similar argument can be applied to electron-impact ionization.

Chapter 4

The Saddle-point and the Uniform Approximations

The transition amplitude of the nonsequential double ionization in (3.33) and (3.41) has the exponential integral format with a coefficient. The exponential part, the action of the integral, describes the motion of the electron in the laser field. The coefficient of the integral, the prefactors, contain the target structure. However, numerically, it is not easy to solve the multidimensional integral of the transition amplitude. Therefore, one needs to apply some integral transform techniques, such as asymptotic expansions of integrals, to approximate this integral. In the asymptotic expansions of integrals technique, one needs to find a series representation of the integral, and then obtain the desired approximation, by using the appropriate partial sums. Within this technique, the transition amplitude for the strong laser field phenomena such as HHG, ATI and NSDI can be easily computed via the method of steepest descent. In this method, the entire integral is approximated by contribution from the vicinity of the points on the integration contour where the partial derivatives of the action with respect to the integration variables vanish [172]. This approximation works well as long as the action varies much faster than the prefactors. In fact, this is the case for the external laser field in question, which is near-infrared high-intensity. This chapter illustrates how we solve the transition amplitude (3.33) and (3.41) employing saddle-point methods. In section 4.1 it is shown how the saddle-point equations are derived from actions (3.34) and (3.42). Furthermore, it is explained how we use the solution of the the saddle-point equations to approximate the transition amplitudes, using the standard saddle-point approximation (section 4.2) or the uniform approximation (section 4.3).

4.1 The Saddle-point Equations

In the steepest descent method, first, one needs to determine the values of the integration variables t, t', t'' and $\mathbf{k}$ for which the action in (3.34) and (3.42) is stationary. For electron impact ionization mechanism (3.33), these equations are obtained from $\partial S_{EI}(\mathbf{k}, t, t')/\partial t' = 0, \partial S_{EI}(\mathbf{k}, t, t')/\partial t = 0$ and $\partial S_{EI}(\mathbf{k}, t, t')/\partial \mathbf{k} = \mathbf{0}$. This leads to the saddle-point equations

$$[\mathbf{k} + \mathbf{A}(t')]^2 = -2E_{1g}, \tag{4.1}$$

$$\mathbf{k} = -\frac{1}{t - t'} \int_{t'}^{t} \mathbf{A}(\tau) d\tau, \tag{4.2}$$

and

$$\sum_{n=1}^{2} [\mathbf{p}_n + \mathbf{A}(t)]^2 = [\mathbf{k} + \mathbf{A}(t')]^2 - 2E_{2g} \tag{4.3}$$

The saddle-point equation (4.1) gives the conservation of energy at the time t', when the first electron is ionized by tunneling. The solution of this equation is complex. This is a consequence of the fact that one can not define a classical counterpart for the tunneling process. The imaginary part of t' can be related to the width of the potential barrier through which the electron tunnels. Equation (4.2) constrains the intermediate momentum $\mathbf{k}$ of the first electron and ensures that it returns to its parent ion. By assuming $E_g \to 0$, loosely speaking, the potential barrier becomes infinitely thin. Thus, the electron leaves the atom with zero imaginary t'. Upon this assumption, equation (4.2) can be related to the classical equations of motion of an electron in the presence of the driving field. Equation (4.3) gives the conservation of energy at the instant t. At this time, the first electron returns to its parent ion with a kinetic energy $E_{\text{res}}(t') = [\mathbf{k} + \mathbf{A}(t')]^2/2 \geq E_{2g}$ and releases the second electron. Later on, both of the electrons reach the detector with momenta $\mathbf{p}_n (n = 1, 2)$. For the electron-impact ionization, there is a classically allowed region, since $E_{\text{res}}(t') > 2E_{2g}$.

For the RESI mechanism, these equations are obtained from the conditions $\partial S_{RESI}(\mathbf{k}, t, t'', t')/\partial t' = 0, \partial S_{RESI}(\mathbf{k}, t, t'', t')/\partial t'' = 0, \partial S_{RESI}(\mathbf{k}, t, t'', t')/\partial t = 0$ and $\partial S_{RESI}(\mathbf{k}, t, t'', t')/\partial \mathbf{k} = \mathbf{0}$. This gives

$$[\mathbf{k} + \mathbf{A}(t')]^2 = -2E_{1g}, \tag{4.4}$$

$$\mathbf{k} = -\frac{1}{t'' - t'} \int_{t'}^{t''} \mathbf{A}(\tau) d\tau, \tag{4.5}$$

$$[\mathbf{p}_1 + \mathbf{A}(t'')]^2 = [\mathbf{k} + \mathbf{A}(t'')]^2 - 2(E_{2g} - E_{2e}) \tag{4.6}$$

and

$$[\mathbf{p}_2 + \mathbf{A}(t)]^2 = -2E_{2e}. \tag{4.7}$$

The saddle-point equation (4.4) gives the conservation of energy at the instant t'. Physically, it corresponds to tunneling ionization of the first electron. Equation (4.5) constrains the intermediate momentum $\mathbf{k}$ of this electron so that it can return to its parent ion. Equation (4.6) expresses the fact that the first electron returns at a time t'' and gives part of its kinetic energy $E_{\text{ret}}(t'') = [\mathbf{k} + \mathbf{A}(t'')]^2/2$ to the core, which is excited from a state with energy E_{2g} to a state with energy E_{2e}. This electron then reaches the detector with final momentum $\mathbf{p}_1$. Finally, a second electron tunnels from the excited state at a subsequent time t, and reaches the detector with final momentum $\mathbf{p}_2$. The conservation of energy at this instant is given by the saddle-point equation (4.7). One should note that the saddle-point equations (4.4) and (4.7) have no purely real solution. In both cases, Im$[t']$ and Im$[t]$ give a rough idea of the width of the barrier and of the ionization probability for the first and the second electron, respectively. The larger this quantity is, the wider the barrier through which they must tunnel. From the saddle-point equations, one can see that both electrons are decoupled in RESI while in electron-impact ionization they are coupled. Thus this will simplify the problem as we have inelastic scattering for the first electron and direct ionization for the second one.

4.2 The Saddle-point Approximation

In the context of the saddle-point approximation (SPA), first we need to find solutions of the saddle-point equations in order to compute the transition amplitudes in (3.33) and (3.41). For that, the monochromatic linearly polarized field defined in (3.48) is used for the saddle-point equations, i.e equations (4.1)-(4.3) (for electron-impact ionization) and (4.4)-(4.7) (for RESI). Furthermore, we write the final momenta in terms of their components $\mathbf{p}_{n\perp}$ and $p_{n||}$ perpendicular and parallel to the polarization of the laser field, similar to equations (5.1) and (5.5). For a given asymptotic momentum p_n there are infinite number of pair solutions for (t'', t', t) [154, 173]. However, for the first electron, pairs of solutions which have the shortest travel time $Re(t' - t'')$ are taken, since their

contribution dominates [154]. For pairs of solutions which have longer travel time, the wave function spreads considerably. As a result, their contributions to the transition amplitude become small. The saddle-point equations are non-linear, and do not have any analytical solutions. Thus one needs to solve them numerically, which requires a good initial guess value for finding the exact solution. On the other hand, proposing a good initial guess value is not an easy task since solutions lie in a complex plan and have many close branches. To overcome this problem, we choose the ionization potential to be zero so that the variables become real (as in the classical simpleman's model [39]). These solutions help us to come up with a good guess value, but they do not solve the problem completely. Therefore, one needs to use trial and error method to find the right solutions (this is discussed in more details in section 4.4). It is always good to graphically visualize the solutions to see if they make sense physically (see Chapter 5).

Once these solutions are obtained then one can determine the transition amplitudes (for a full derivation see Appendix A)

$$M = \sum_s A_s \exp(iS_s) \tag{4.8}$$

where for the electron-impact ionization

$$S_s = S_{EI}(t_s, t'_s, \mathbf{k}_s) \tag{4.9}$$

$$A_s = (2\pi)^{5/2} \frac{V_{\mathbf{k}0} V_{\mathbf{p}_n,\mathbf{k}}}{\sqrt{\det S''_{EI}(t_s, t'_s, \mathbf{k}_s)}} \tag{4.10}$$

and for the RESI

$$S_s = S_{RESI}(t_s, t'_s, t''_s, \mathbf{k}_s) \tag{4.11}$$

$$A_s = (2\pi)^3 \frac{V_{\mathbf{p}_2 e} V_{\mathbf{p}_1 e,\mathbf{k}g} V_{\mathbf{k}g}}{\sqrt{\det S''_{RESI}(t_s, t'_s, t''_s, \mathbf{k}_s)}} \tag{4.12}$$

Here, the index s runs over the relevant saddle points. $\det S''_{EI}(t_s, t'_s, \mathbf{k}_s)$ denotes the determinant of the 5×5 matrix of the second derivatives of the action (3.34) with respect to t, t' and $\mathbf{k}$ and $\det S''_{RESI}(t_s, t'_s, t''_s, \mathbf{k}_s)$ denotes the determinant of the 6×6 matrix of the second derivative of the action (3.42) with respect to t, t', t'' and $\mathbf{k}$.

For the electron impact ionization mechanism, the intermediate $\mathbf{k}$ in the saddle-point equation (4.2) can be replaced by

$$\mathbf{k} \longrightarrow \mathbf{k}(t,t') = -\frac{1}{t-t'}\int_{t'}^{t}\mathbf{A}(\tau)d\tau \tag{4.13}$$

and $S_{EI}(t,t') \longrightarrow S_{EI}(t,t',\mathbf{k}(t,t'))$.

As a direct consequence, the transition amplitude (3.33) can first be evaluated over $\mathbf{k}$ (a three-dimension integral), by applying the saddle-point approximation. Once the three-dimension integral over $\mathbf{k}$ is solved, we again apply the saddle-point approximation to compute the two-dimensional integral over t and t'. As a result, the action and amplitude in (4.9) become

$$S_s = S_{EI}(t_s, t'_s) \tag{4.14}$$

$$A_s = (2\pi)^{5/2}\frac{V_{\mathbf{k}(t_s,t'_s)0}V_{p_n,\mathbf{k}(t_s,t'_s)}}{\sqrt{(t_s-t'_s)^3\det S''_{EI}(t_s,t'_s)}} \tag{4.15}$$

where $\det S''_{EI}(t_s,t'_s)$ is 2×2 the determinant of the second derivatives of the action with respect to t and t'.

A similar approximation can be performed for RESI, giving

$$S_s = S_{RESI}(t_s, t'_s, t''_s) \tag{4.16}$$

$$A_s = (2\pi)^{3}\frac{V_{\mathbf{k}(t''_s,t'_s)0}V_{p_n,\mathbf{k}(t''_s t'_s)}}{\sqrt{(t'_s-t''_s)^3\det S''_{RESI}(t_s,t'_s,t''_s)}} \tag{4.17}$$

where $\det S''_{RESI}(t_s,t'_s,t''_s)$ is 3×3 the determinant of the second derivatives of the action with respect to t , $t'$and t''

The concept of "quantum orbits" has emerged from the saddle-point method in relation to the classical trajectories. The classical orbits describe the motion of an electron from the time it tunnels into the continuum to the time it returns to the core in real space, while the "quantum orbits" deal with its motion in the complex plane. In strong laser field phenomena, the "quantum orbits" come in pairs composed of a short and a long orbit. For the short orbit, the first electron tunnels late and returns to its parent

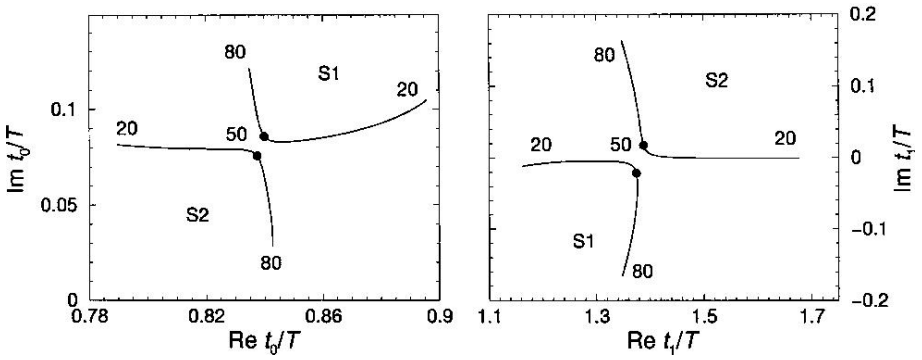

FIGURE 4.1: Schematic representation of the quantum orbits, which are solutions of the saddle-point equations and come in pairs ($S1$ and $S2$). The cutoffs appear at the points where curves $S1$ and $S2$ are very close to each other (in here quantum orbits 50). This figure corresponds to tunneling t_0 and return time t_1 of the electron in HHG process (lower panel of figure 2 in [15])

ion earlier. For the long orbit, the first electron tunnels early and rescatters at a later time. The saddle-point approximation (SPA) picks the relevant "quantum orbits", those that contribute to the final state of the electron after rescattering. There are several quantum orbits that contribute to a given final state but the pair with shortest real time interval $Re(t - t')$ is the dominant one. These two dominated orbits are sufficient for simulating electron momentum distributions because in the present problem the transverse momentum is being integrated over. By adding their contribution coherently, we get quantum interference in the photoelectron spectra, a feature which can not be produced by the classical trajectory method. At a certain final momentum, short and a long orbits approach each other very closely and reach what is called the classical cutoff (this is illustrated in figure 4.1). The electrons with final momentum beyond the cutoff do not have an associated classical counterpart.

The classically allowed region can be better understood in terms of the six-dimensional final momentum space ($\mathbf{p} = (\mathbf{p}_1, \mathbf{p}_2)$). For equation (4.1), it is related to the solutions in which $\mathbf{k}$ and t' are real. The real solutions occur if we ignore the ionization potential of the first electron E_{1g}, if the classical limit of the saddle-point equations is taken. For instance, for the electron-impact ionization the momentum space $p = (p_1, p_2)$, equation (4.2) represents the surface equation of a six-dimensional sphere. The centre of this sphere is at $(-A(t), -A(t))$, and its radius is given by $\sqrt{[k + A(t)]^2 - 2E_{2g}}$. For an electron that tunnels at time t', the classically allowed region is defined by the electron momenta p located on the surface of this sphere. However, quantum mechanics allows a nonzero yield beyond the classically allowed region. The saddle-point approximation deforms the original integration contour of the transition amplitude into a complex

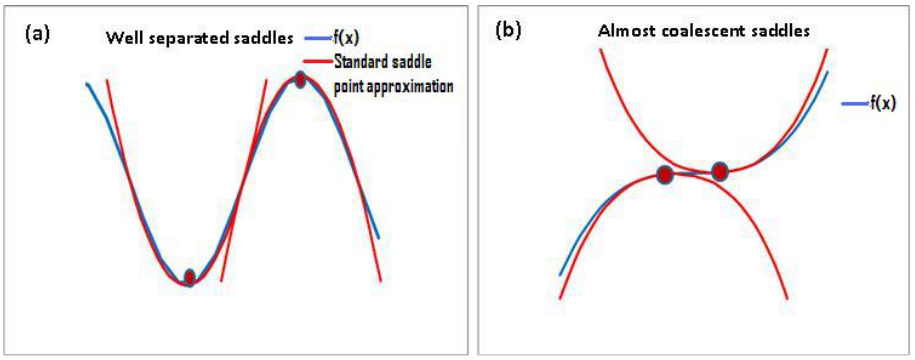

.

FIGURE 4.2: Schematic representation of the two saddle-points. In (a) two saddles are well separated, thus standard saddle point approximation works well, while in (b) two saddles are very close to each other, therefore one needs to apply uniform approximation

hyperplane, in order to encompass the relevant complex saddle points. The constraints are explained in more details in Chapter 5.

Within the classically allowed region, the standard saddle-point approximation works well, while at and beyond the cutoff it breaks down. At the cutoff, the real part of the short and long orbits almost coalesce. Thus, the two saddle points are not well separated and their second derivative is zero, as is illustrated in figure 4.2. In this case, the standard saddle-point approximation becomes unsuitable. Furthermore, outside the cutoff, there is a classically forbidden regime. In this region, the imaginary part of the solutions rapidly increases and the asymptotic expansion must change. Therefore, the contribution from one of the orbits should be dropped, in order to prevent the divergence of the transition amplitude [173]. At some points beyond the classically allowed region a quantitative change in the contour of the integral occurs so that the asymptotic expansion still describes the function well. This change is known as "Stokes transition" [174]. If i and j denote a pair of trajectories, the Stokes transition corresponds to a value of p, such that $ReS(t_i, t_i', k_i) = ReS(t_j, t_j', k_j)$.

However, the standard SPA can be replaced by a more general method called the uniform approximation (4.3). This method works at the Stokes transition, and allows a smooth transition from the classically allowed region to the classically forbidden region. One should note that, both standard SPA and uniform approximations are valid if the expansion of the action holds until the integrand has become much smaller than it was at the saddle point. This is the limit in which the integration contour can be extended to infinity.

4.3 The Uniform Approximation

In the standard saddle-point approximation, the multidimensional integral to the transition amplitude is estimated by second-order expansion of the action around the saddle points. However, the expansion becomes inaccurate when the saddle points of two quantum orbits composing a pair are too close to each other. For NSDI the failure occurs near the classical cutoff. The uniform approximation has been developed to improve the expansion of the action around the two coalescent saddle points by including a higher-order expansion and taking the resulting approximate integral as a collective contribution of both saddle points [172]. In the uniform approximation, a pair of orbits (well separated or close to each other) is defined by a diffraction integral. Then, the parameters of the formal expansion are determined in terms of the quantities that enter the standard saddle-point approximation. This method makes sure that the conventional saddle-point approximation is recovered when two saddle points are well separated. The derivation of this method, with a more detailed discussion, is provided in Appendix B.

In the classically allowed region, we consider any pair of trajectories denoted by i and j. Then, within the uniform approximation, the contribution of this pair to the transition amplitude of NSDI is given by

$$\begin{aligned} M_{i+j} &= \sqrt{2\pi\Delta S/3}\exp(i\overline{S}+i\pi/4) \\ &\quad \times\overline{A}[J_{1/3}(\Delta S)+J_{-1/3}(\Delta S)]+\Delta A[J_{2/3}(\Delta S)-J_{-2/3}(\Delta S)], \end{aligned} \tag{4.18}$$

where

$$\begin{aligned} \Delta S &= (S_i-S_j)/2,\ \overline{S}=(S_i+S_j)/2 \\ \Delta A &= (A_i-iA_j)/2,\ \overline{A}=(iA_i-A_j)/2. \end{aligned} \tag{4.19}$$

By using the asymptotic behavior of the Bessel functions for large z, i.e.

$$J_{\pm\nu}(z)\sim(2/z\pi)^1/2\cos(z\mp\upsilon\pi/2-\pi/4), \tag{4.20}$$

one can show that the saddle-point approximation (4.8) is recovered from the uniform approximation (4.18) when the saddle points are well separated.

In the uniform approximation (4.18) we do not need any special information, such as higher derivatives of the action. We just need to compute the actions S_i and their

associated prefactors A_i, by using the solution of the saddle-point equations, and then enter them into (4.18).

In addition, on can modify the uniform approximation, so that it works when one of the two saddle points is bypassed by the contour in the classically forbidden region. In here, we require a smooth functional behavior to select the branches of the function automatically. Beyond the Stokes transition, these branches can be selected if we replace the Bessel J functions by Bessel K functions [174]. Thus, in the classically forbidden region, the transition amplitude will be

$$\begin{aligned} M_{i+j} &= \sqrt{2i\Delta S/\pi}\exp(i\overline{S}) \\ &\quad \times[\overline{A}K_{1/3}(-i\Delta S) + i\Delta A K_{2/3}(-i\Delta S)] \end{aligned} \tag{4.21}$$

Like the previous case, for a large ΔS, the saddle-point approximation (4.8) can be recovered from the uniform approximation (4.21). This can be checked by using the asymptotic expansion

$$J_{\pm\nu}(z) \sim (\pi/2z)^1/2\exp(-z) \tag{4.22}$$

Furthermore, the uniform approximations at the cutoff (4.18) and beyond the classically allowed region (4.21) match at Stoke transitions. In nonsequential double ionization, there are two cutoffs with two different energies. The position of these energies coincides with minimum and maximum classically allowed momenta, and they create the boundary between the classically allowed and forbidden regions.

4.4 Practical Issues

There are many branches for the saddle-point equations, both in the uniform approximation and standard saddle-point approximation since their solutions are complex. As was discussed above, for numerical solutions one needs to use trial and error to find the appropriated solutions. For the short orbit the guess values can be chosen based on the assumptions that the electron tunnels just after field maxima and returns just before field crossing. For the long orbit the guess values are chosen such that the electron tunnels just after field maxima but a bit earlier than the tunneling time of the short orbit and returns just after field crossing. Furthermore, an imaginary part is associated with the time the electron is born in the continuum through tunneling. For the classically allowed region this imaginary part vanishes when the first electron returns to the core.

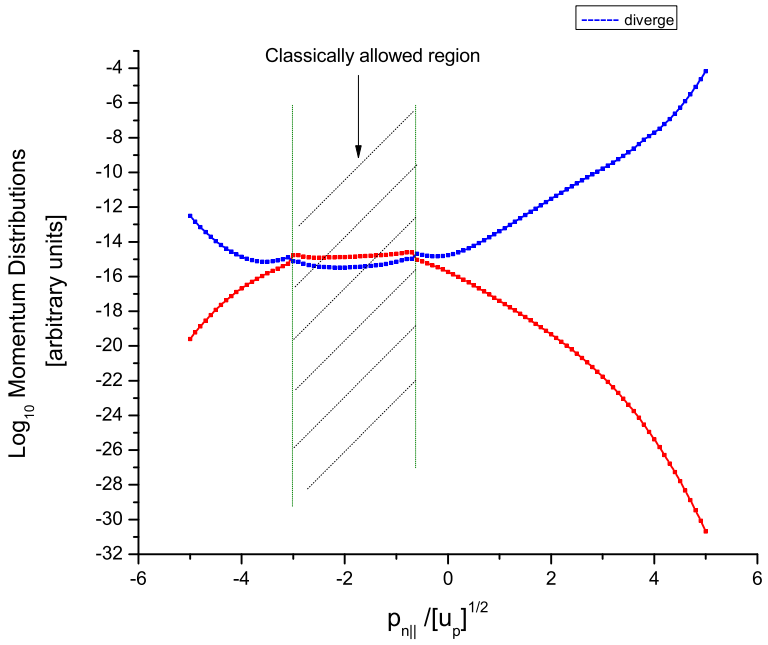

.

FIGURE 4.3: Schematic representation of the divergency at the Stokes transition. In order to prevent divergency we take those solutions which decay exponentially at Stokes transition (red line).

In addition, complex solutions always come in a complex conjugate pairs. Thus the complex conjugate of the solutions of the saddle-point equations will also be solutions.

Generally, physically relevant solutions have the following properties: 1) the real part of the solutions is associated to the classical orbits; 2) their imaginary part decays beyond the classical cutoff and does not increase exponentially for avoiding divergency (This is illustrated in figure 4.3); 3) for the classically allowed region the imaginary part of the return times is much smaller than unity $Im[\omega t] << 1$; 4) the imaginary part of the tunneling time should be greater than zero $Im[\omega t] > 0$, otherwise the barrier is unphysical.

As far as the computation is concerned, the saddle-point equations of NSDI can be further simplified due to symmetry consideration. This simplification become very important when we compute the electron momentum distributions. For both electron-impact ionization and RESI the final momenta $\mathbf{p}_n$ are written in terms of their components parallel $\mathbf{p}_{n||}$ and perpendicular $\mathbf{p}_{n\perp}$ to the the laser polarization. For the electron-impact ionization we expand the quadratic terms of the action (3.34). Then we write them in the following format:

$$p_{||} = p_{1||} + p_{2||}$$

$$\epsilon = p_{1||}^2 + p_{2||}^2 + p_{1\perp}^2 + p_{2\perp}^2 + E_{2g}$$

As a result, the saddle point reads

$$\begin{aligned} S_{EI}(\mathbf{p}_n, \mathbf{k}, t, t') &= \frac{1}{2}\epsilon t - \mathbf{p}_{||}\int_0^t \mathbf{A}(\tau)d\tau + \int_0^t \frac{\mathbf{A}^2(\tau)}{2}d\tau \\ &+ \frac{[\int_{t'}^t d\tau \mathbf{A}(\tau)]^2}{2(t-t')} - \int_{t'}^t \frac{\mathbf{A}^2(\tau)}{2}d\tau + E_{1g}t' \end{aligned} \tag{4.23}$$

In order to find the solution of the saddle-point equations we start from the middle of the classical region and move away from it.

For RESI, the solutions of the saddle-point equations for $\mathbf{p}_1$ and $\mathbf{p}_2$ are decoupled. The first three saddle-point equations, i.e. (4.4)-(4.6) give the tunneling t' and return t" time and the drift momentum $\mathbf{k}$ of the first electron independent from the momentum of the second electron. The fourth equation (4.7) corresponds to the tunneling of the second electron without having any coupling with the first electron. As a result, it becomes easier to solve the saddle-point equations. There are, however, some problems in defining the pair of saddles in the uniform approximation. Thus we use the standard saddle-point approximation and take the appropriate solutions, i.e. those make physically sense, at the cutoff and beyond. Work in this direction, however, is in preparation.

Chapter 5

Constraints in Momentum Space

From the saddle-point equations in the previous section, one may determine constraints for the parallel momentum components $p_{n||}(n = 1, 2)$ in the plane $p_{1\parallel}p_{2\parallel}$. This can be done by writing the saddle-point equations in terms of the electron-momentum components parallel and perpendicular to the laser field polarization.These constraints will be discussed here for both the electron-impact ionization and RESI mechanisms, and will serve as a tool for sketching an approximate shapes for the electron-momentum distributions [78, 171].

For simplicity, we will consider a monochromatic field in equation (3.48) of frequency ω [78, 171]. The momentum constraints for electron-impact ionization have been discussed by Faria et al. in [16], and will be briefly summarised here for the sake of self-consistency. The momentum constraints for RESI are part of my PhD work and have been published in [3].

5.1 Electron-impact Ionization

We write equation (4.3) in terms of the electron-momentum components parallel and perpendicular to the laser-field polarization

$$\sum_{n=1}^{2}[p_{n||} + A(t)]^2 + \mathbf{p}_{n\perp}^2 = \left[\mathbf{k} + \mathbf{A}(t')\right]^2 - 2E_{2g}. \tag{5.1}$$

In momentum space, this equation represents a six-dimensional hypersphere with a center at $\mathbf{p}_{n\perp} = \mathbf{0}, p_{n||} = -A(t)$, $(n = 1, 2)$. As discussed in the previous chapter, the hypersphere equation (5.1) describes the classically allowed region. The shape of this region is determined by $A(t)$, which can have different values, depending on the tunneling

time of the electron as well as its time of return to the parent ion. Therefore, the union of all the possible hyperspheres defined by equation (5.1) will determine the classically allowed region [175]. However, the electron-impact ionization constraints can roughly be determined if one assume the that the first electron returns around a crossing of the laser driving field. For the monochromatic field (3.48), this estimation leads to a center at approximately $p_{n||} = \pm 2\sqrt{U_p}$, for the parallel component of the electron momentum. For electron-impact ionization, this is the most probable parallel momentum rather than the maximum momentum value. The right-hand side of equation (5.1) defines the radius of the hypersphere, which is a function of driving-field intensities. For high driving-field intensity, the radius may extend far beyond $2\sqrt{U_p}$. The increase in radius has been demonstrated by different theoretical approaches, such as the SFA [75], classical models [77] and the time-dependent Schrödinger equation [11]. As the driving-field intensity decreases, the radius of the hypersphere becomes smaller and smaller until the classically allowed region collapses. Equation (5.1) can be further examined by considering a fixed value for the transverse momentum. If the transverse momentum is kept fixed, then equation (5.1) can be written as

$$\sum_{n=1}^{2}[p_{n||} + A(t)]^2 = \left[\mathbf{k} + \mathbf{A}(t')\right]^2 - 2\widetilde{E}_{2g}, \tag{5.2}$$

with an effective ionization potential

$$\widetilde{E}_{2g} = \sum_{n=1}^{2} \mathbf{p}_{n\perp}^2/2 + E_{2g} \tag{5.3}$$

Here, the kinematic constraints are defined by equation (5.2), which is the equation of a circle in the parallel-momentum plane. The right-hand side of equation (5.2) gives the radius of the circle. It shows that the parallel-momentum plane will become more localized around $p_{n||} = \pm 2\sqrt{U_p}$, as the transverse momenta become larger. Equation (5.3) shows that the effective potential energy increases as the transverse momentum of the electrons increases. Therefore, for non-vanishing momenta, the second electron needs to overcome a larger second ionization potential. In addition, according to equation (5.2), the electron momentum distribution will populate the first and third quadrants of the parallel momentum plane, which is the key feature of electron-impact ionization mechanism. This emerges from the fact that $p_{n||}$ have the same centre, hence at the maximum they have the same signs. For a monochromatic field $\mathbf{A}(t) = \mathbf{A}(t \pm T/2)$ with the laser field cycle of $T = 2\pi/\omega$, the electron momentum distributions are symmetric with respect to the reflection $(p_{1||}, p_{2||}) \rightarrow (-p_{1||}, -p_{2||})$. However, it has been shown that this

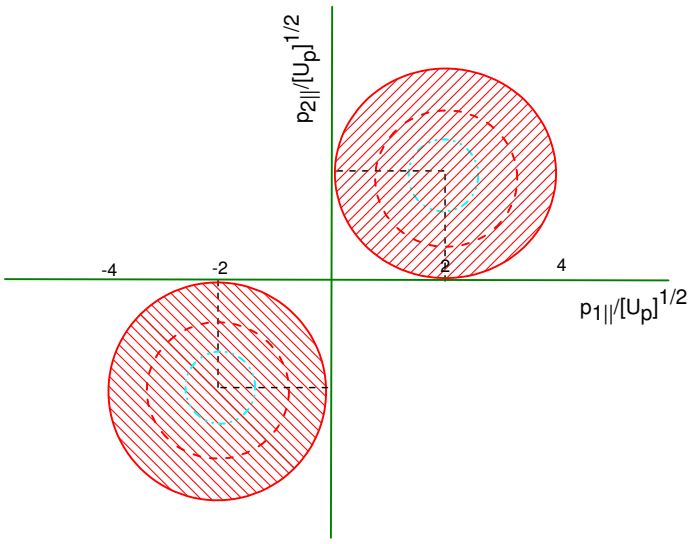

FIGURE 5.1: Schematic representation of the classically allowed region for electron-impact ionization, as a function of the electron momentum components $p_{n\parallel}(n = 1, 2)$ parallel to the laser-field polarization. The different fixed transverse momenta $\mathbf{p}_{n\perp}(n = 1, 2)$ correspond to the different concentric circles. The picture is simplified as we assumed a monochromatic driving field and $A(t) = \pm 2\sqrt{U_p}$ (figure 17 of [14]).

symmetry breaks down for few-cycle pulses [78, 171]. A schematic representation of the discussed classically allowed region is shown in figure 5.1.

Now, one needs to see how this estimate agrees with the solutions of the saddle-point equations, in terms of the start time t' and the return time t. Only those solutions which correspond to the shortest pair of orbits are considered, as they provide the dominant contributions to the NSDI distributions. The imaginary part of these solutions shows if a process is classically allowed or forbidden, and the real parts are related to the classical start and return times of both electrons. Figure 5.2 shows a plot of real and imaginary time of t' and t against the equal parallel momenta for both particles $p_{1\parallel} = p_{2\parallel} = p_{\parallel}$. The plot shows that the return time t has almost zero imaginary part just before the cutoffs. This means the recollision dynamics can be visualized classically. As the transverse momentum increases, the classically allowed region becomes more concentrated around $p_{n||} = \pm 2\sqrt{U_p}$ and eventually it collapses, as we expect according to our rough estimation. When the classical allowed region collapses, the imaginary part of t increases rapidly. On the other hand, for the tunneling time t', the imaginary part is nonzero. The nonzero imaginary part indicates that tunneling does not have a classical counterpart. Furthermore, from panel (a) we can see the electron tunnels earlier with small $\mathrm{Im}[t']$ on the long orbits, while it tunnels later with large $\mathrm{Im}[t']$ on the short orbits. This happens because, for the long orbit, the field is close to its maximum.

The long orbit indicates that the electron tunnels easily when the laser field is at its maximum. A more detailed discussion can be found in reference [16].

Apart from that, figure 5.2 also shows two momentum for the real part of the start and return times almost coalesce. These momenta corresponds to the classical cutoffs, for constant transverse momenta. They delimit a region centred at roughly $2\sqrt{U_p}$. This region collapses for increasing transverse momenta. Furthermore, we include electron-momentum distribution computed with equation (3.50) for three different driving-field intensities in figure 5.3. We consider the prefactor $V_{\mathbf{p}_n,\mathbf{k}} = constant$, in order to single-out the influence of the momentum-space constraints. For effect of the different type of the interactions the reader is refered you to [75, 105]. The figure clearly reflect the previously estimated constrains. Indeed, the electron momentum distributions are centered around $\pm 2\sqrt{U_p}$, whose radius increases with the driving field intensity.

5.2 RESI

The saddle-point equations (4.6) and (4.7) provide useful information on the momentum-space regions populated by the RESI mechanism, and on the shapes of the electron-momentum distributions. Equation (4.7), which corresponds to the tunneling of the second electron, is formally identical to the saddle-point equation describing the low-energy electrons in above-threshold ionization (ATI), the so-called "direct electrons". In this case, an electron tunnels from a bound state and reaches the detector without rescattering with its parent ion [176].

Physically, this is exactly the situation encountered for the second electron, and will have two main consequences. Firstly, the solutions of the saddle-point equations will be identical to those for the direct ATI electrons [176]. For vanishing electron drift momenta, these solutions are displaced by half a cycle, and are located at a maximum of the field. As the momentum increases, the solutions approach each other and move away from the maximum. Secondly, the maximal kinetic energy for the direct ATI electrons, if the field is approximated by a monochromatic wave, is $2U_p$ [177]. Hence, in RESI, the second electron leaves the excited state with largest probability when the electric field $E(t) = -dA(t)/dt$ is at its maximum. If the time dependence of the laser field is such that $A(t)$ vanishes when $E(t)$ is at its peak (for instance, monochromatic fields), then

$$-2\sqrt{U_p} \leq p_2 \leq 2\sqrt{U_p}. \tag{5.4}$$

If, to first approximation, we neglect the momentum components perpendicular to the laser-field polarization, one can see that the momentum of the second electron, in the

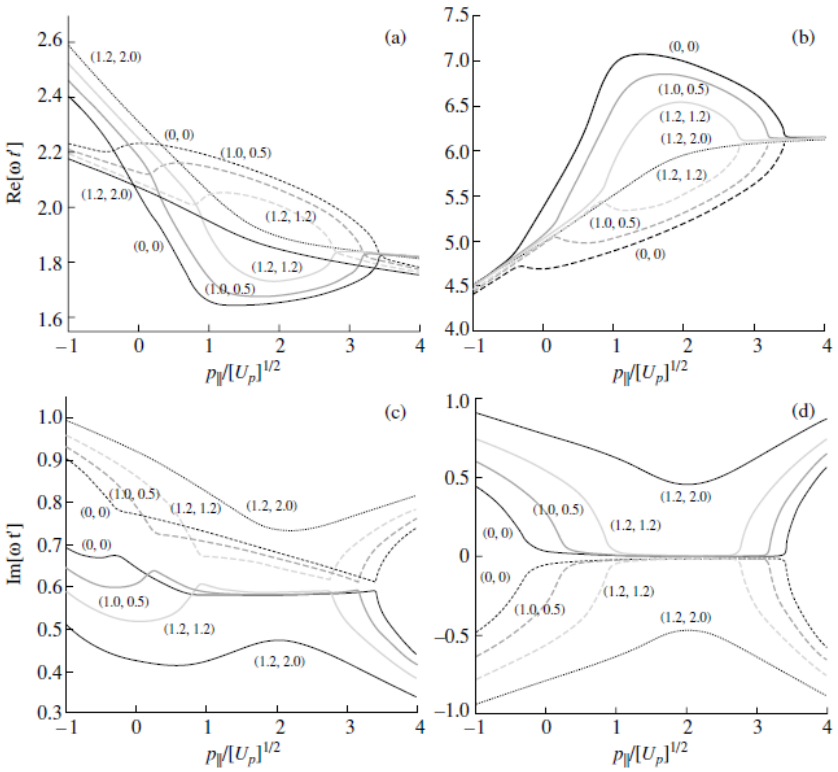

FIGURE 5.2: Real and imaginary parts of the start and return times, obtained by solving the saddle-point equations (4.1)-(4.3) for a monochromatic linearly polarized field of frequency $\omega = 0.0551$ a.u. and pondermotive energy $U_p = 1.2$ a.u. The ionization potential for neon atom were taken ($E_{2g} = 1.51$ a.u. and $E_{1g} = 0.9$ a.u.). Panels (a) and (c) give the real and imaginary parts of the start time, respectively, while panels (b) and (d) depict the real and imaginary parts of the return time. The transverse momenta $(p_{1\perp}, p_{2\perp})$ is given by numbers in the curves in units of $\sqrt{U_p}$. (upper and middle panels of figure 1 in [16])

parallel momentum plane, is expected to be centered around vanishing momentum $p_{2\parallel}$ and be limited by the bounds $p_{2\parallel} = \pm 2\sqrt{U_p}$. One should note that this is in contrast to the situation discussed in the previous section, in which the second electron is dislodged by electron-impact ionization. In the electron-impact ionization mechanism, $\pm 2\sqrt{U_p}$ is the *most probable* momentum $p_{2\parallel}$ with which the second electron may leave. In the present scenario, this is the *maximum* value for this quantity.

Furthermore, due to the fact that equation (4.7) describes a tunneling process, there is no classically allowed region for the second electron. For nonvanishing transverse momenta, this region will remain the same. We expect, however, that there will be a large drop in the yield. This is due to the fact that there will be an effective increase in the potential barrier through which the electron tunnels. This can be readily verified

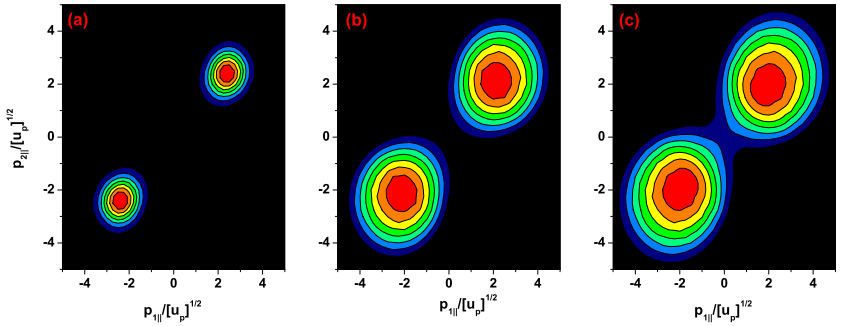

FIGURE 5.3: Electron momentum distributions as functions of the momentum components $(p_{1\|}, p_{2\|})$ parallel to the laser-field polarization, computed with constant prefactors and integrated over transverse momenta. This figure demonstrate how the classical allowed region increases with intensity. The driving field frequency has been taken as $\omega = 0.057$ a.u. The ionization potentials $E_{01} = 0.573$ a.u. and $E_{02} = 0.997$ a.u. correspond to N_2 at the equilibrium internuclear distance $R = 2.068$ a.u. Panels (a) correspond to the laser field intensity of $I = 1\times10^{14}$ W/cm^2, and (b) and (c) correspond to $I = 3 \times 10^{14}$ W/cm^2 and $I = 5 \times 10^{14}$ W/cm^2, respectively.

by writing the saddle-point equation (4.7) as

$$[p_{2\|} + A(t)]^2 = -2\tilde{E}_{2e}, \tag{5.5}$$

with an effective ionization potential $\tilde{E}_{2e} = E_{2e} + \mathbf{p}_{2\perp}^2/2$.

Equation (4.6), on the other hand, has a similar form to the saddle-point equation describing the rescattered electrons in ATI [172], apart from the energy difference $E_{2g} - E_{2e}$ on the right-hand side. Physically, this is expected, as in both cases the first electron leaves immediately after rescattering. The difference is that, while in ATI the rescattering is elastic, in NSDI part of the electron's kinetic energy is used to excite the core. Explicitly, the momentum component of the first electron parallel to the laser-field polarization is given by

$$-A(t) - \sqrt{2E_{\text{diff}}} \leq p_{1\|} \leq -A(t) + \sqrt{2E_{\text{diff}}}, \tag{5.6}$$

where $E_{\text{diff}} = E_{\text{kin}}(t', t'') - (E_{2g} - E_{2e}) - \mathbf{p}_{1\perp}^2/2$ and $E_{\text{kin}}(t', t'')$ denotes the kinetic energy of the first electron upon return. For a monochromatic field, the electron returns most probably near a crossing of the laser field; one may use the approximation $A(t) \simeq 2\sqrt{U_p}$ in the above-stated equation. In this case, we also know that the kinetic energy $E_{\text{kin}}(t', t'') \leq 3.17U_p$. Hence, $E_{\text{diff}}^{(\max)} \leq 3.17U_p - (E_{2g} - E_{2e}) - \mathbf{p}_{1\perp}^2/2$ and

$$-2\sqrt{U_p} - \sqrt{2E_{\text{diff}}^{(\max)}} \leq p_{1\|} \leq -2\sqrt{U_p} + \sqrt{2E_{\text{diff}}^{(\max)}}. \tag{5.7}$$

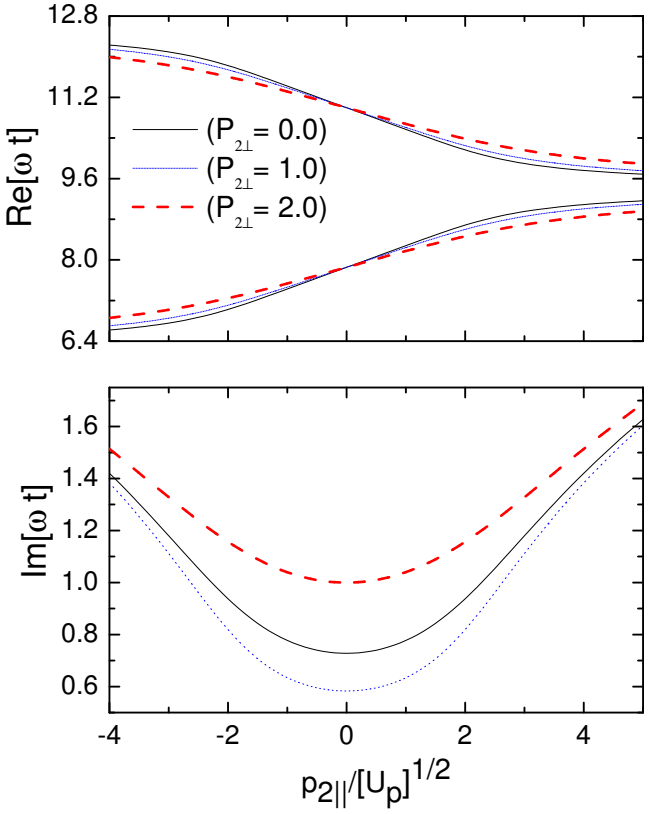

FIGURE 5.4: Tunneling time t for the second electron, as functions of its parallel momentum $p_{2||}$, for a monochromatic field of intensity $I = 1.5 \times 10^{14}$ W/cm^2 and frequency $\omega = 0.057$ a.u, for several transverse momenta $p_{2\perp}$. The upper and lower panel give the real and imaginary parts of such times, respectively. We consider a model atom for which the excited-state energy is, $E_{2e} = 0.25$ a.u. and $E_{2g} = 1$ a.u.

Equation (5.7) allows one to delimit a region in momentum space for $p_{1\parallel}$ centered around $-2\sqrt{U_p}$ and bounded by $2E_{\rm diff}^{(\rm max)}$. In contrast to the previous case, there may be a classically allowed region for the momentum of the first electron if the parameters inside the square root are positive, i.e., if $3.17U_p \geq (E_{2g} - E_{2e}) + \mathbf{p}_{1\perp}^2/2$. For increasing perpendicular momentum and/or bound-state energy difference, this region will become more and more localized around $-2\sqrt{U_p}$ until it collapses. Therefore, it is also possible to distinguish between threshold and above-threshold behavior in the context of recollision-excitation-tunneling. One should note, however, that intensities below the recollision-excitation threshold $(E_{2g} - E_{2e}) = 3.17U_p$ do not make physical sense, as the energy of the returning electron would not be sufficient to promote the bound electron to an real excited state. However, for this intensity one may describe recollision-excitation-tunneling by considering victual excited state for the second electron. If $(E_{2g} - E_{2e}) \ll 3.17U_p$ the well-known cutoff of $10U_p$ for rescattered above-threshold ionization is recovered. Based on ATI kinetic energy values, the upper bound for the parallel electron momentum $p_{1\parallel}$ can be estimated as $-2\sqrt{U_p} \lesssim p_{1\parallel} \lesssim 4\sqrt{U_p}$. For the orbits leading to the mirror image of the distribution with respect to the reflection ($p_{1\parallel}$,

$p_{2\parallel}) \to (-p_{1\parallel}, -p_{2\parallel})$, the constraint upon the parallel momentum of the first electron will be $-4\sqrt{U_p} \lesssim p_{1\parallel} \lesssim 2\sqrt{U_p}$. For these latter orbits, the times t', t'' and t are displaced by half a cycle. A nonvanishing transverse momentum component $\mathbf{p}_{1\perp}$ will lead to lower maximal and minimal momenta.

In view of the above-mentioned constraints, the expected maxima of the electron momentum distribution are located at the most probable momenta $(p_{1||}, p_{2||}) = (\pm 2\sqrt{U_p}, 0)$, and, after symmetrizing with respect to the exchange $\mathbf{p}_1 \leftrightarrow \mathbf{p}_2$, at $(p_{1||}, p_{2||}) = (0, \pm 2\sqrt{U_p})$. This implies that, if the field can be approximately described by a monochromatic wave, the outcome of our model should have distributions in the $p_{1\parallel}p_{2\parallel}$ plane, which are symmetric upon $\mathbf{p}_n \to -\mathbf{p}_n$, $n = 1, 2$ and upon $\mathbf{p}_1 \leftrightarrow \mathbf{p}_2$, and which equally occupy the four quadrants of the parallel momentum plane. The width of such distributions will remain constant around $-2\sqrt{U_p} \lesssim p_{n\parallel} \lesssim 2\sqrt{U_p}$ and their length will increases from a small region around $\pm 2\sqrt{U_p}$ to a momentum region comparable to that defined by the rescattered ATI plateau. Summarizing, as the intensity of the driving field increases, the shape of the distributions will become more elongated. In other words, they will change from ring-shaped to cross-shaped distributions (see subsection 5.2.1).

In figure 5.4, we plot the real and imaginary parts of the ionization times t for the second electron, as functions of the electron momentum $p_{2\parallel}$, for several transverse momenta (upper and lower panel, respectively). In all cases, the imaginary parts of each time t in a pair are identical and exhibit a minimum at the peak-field times $\omega t = \pi/2$. This is expected, as i) the two orbits behave symmetrically with respect to the laser field, and ii) the effective potential barrier through which the electron tunnels is narrowest for these times. As the transverse momentum $\mathbf{p}_{2\perp}$ becomes larger in absolute terms, we see an increase in $\mathrm{Im}[t]$. This is consistent with the fact that the potential barrier widens in this case.

In figure 5.5, we display the real and imaginary part of the ionization [panels (a) and (b), respectively] and rescattering times [panels (c) and (d), respectively] for the first electron. We consider the shortest orbits for the returning electron. The remaining sets of orbits are strongly suppressed due to wave-packet spreading. By associating the real parts of t' and t'' with the classical trajectories of an electron in a laser field, one may identify a longer and a shorter orbit, along which the first electron returns. These orbits practically coalesce for two specific values of $p_{1\parallel}$, namely the minimum and the maximum momenta for which the rescattering process described by the saddle-point equation (4.6) has a classical counterpart. Beyond these momenta, the yield decays exponentially. For vanishing transverse momentum $p_{1\perp}$, these cutoffs are near $-4\sqrt{U_p}$ and $2\sqrt{U_p}$, as predicted by our estimates. As $p_{1\perp}$ increases, the classically allowed region shrinks and gets very localized near $p_{1\parallel} = -2\sqrt{U_p}$. For the parameters considered here,

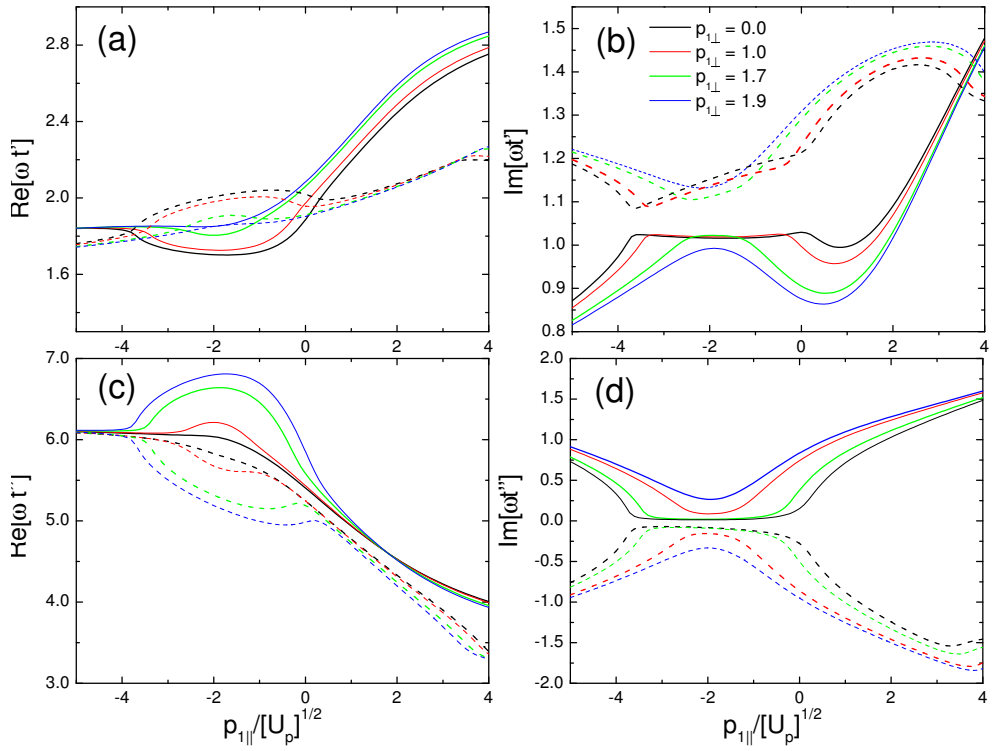

FIGURE 5.5: Tunneling and rescattering times for the first electron, as functions of its parallel momentum $p_{1||}$ (with the same driving filed as figure 5.4). Panels (a) and (b) give the real and imaginary parts of the tunneling time t', respectively, and panels (c) and (d) depict the real and imaginary parts of the rescattering time t''. We consider a model atom for which the first electron tunnels from a ground state of energy $E_{1g} = 0.92$ a.u., and rescatters with a ground ionic state of energy $E_{2g} = 1$ a.u. Thereby the returning electron gives part of its kinetic energy to excite a second electron to the state $E_{2e} = 0.25$ a.u. The dashed and solid lines correspond to the short and long orbits, respectively.

this corresponds to the situation in which the electron returns at a crossing of the field. Finally, for very large transverse momenta, this region disappears.

The imaginary parts of the times t' and t'', displayed in figures 5.5.(b) and 5.5.(d), confirm this physical interpretation. In fact, they show that, for the rescattering times, $\mathrm{Im}[t'']$ essentially vanishes between the momenta for which the real parts $\mathrm{Re}[t'']$ coalesce. Physically, this means that, in this region, rescattering is classically allowed. Beyond this region, $\mathrm{Im}[t'']$ increases abruptly, which indicates that the classically forbidden region has been reached. In this context, it is worth mentioning that, even if there is no classically allowed region, $\mathrm{Im}[t'']$ exhibits a minimum near $p_{1\|} = -2\sqrt{U_p}$. This is due to the fact that rescattering is most probable for this specific momentum. A similar behavior has been observed in [16] for electron-impact ionization. These findings have been briefly summarized in the previous section.

The imaginary part $\mathrm{Im}[t']$ of the start time of the first electron, on the other hand,

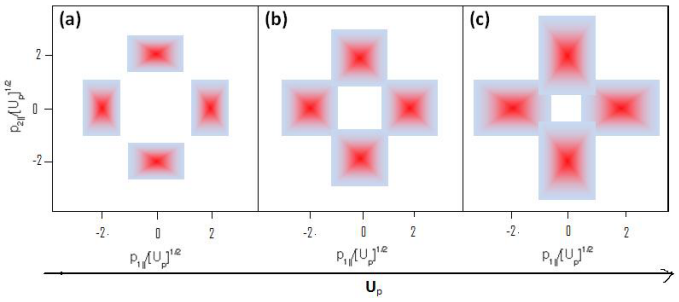

FIGURE 5.6: Schematic representation of the regions of the parallel momentum plane populated by the recollision-excitation-tunneling ionization mechanism, highlighted as the rectangles in the figure. The shape of electron momentum distributions change with intensity from ring-shaped (a) to cross-shaped (c) by increasing of intensity, while the maxima of the electron momentum distributions are around $p_{n\parallel} = \pm 2\sqrt{U_p}$. We consider different sets of trajectories, whose start and recollision times are separated by half a cycle of the field, and the symmetrization $\mathbf{p}_1 \leftrightarrow \mathbf{p}_2$ with respect to the indistinguishability of the two electrons. In our estimates, we considered vanishing transverse momenta, so that the constraints provided constitute an upper bound for this region.

is always non-vanishing. This is not surprising, as tunneling has no classical counterpart. They are, however, approximately constant between the lower and upper cutoff momenta.

In figure 5.6, we summarize the information discussed above, and provide a schematic representation of the momentum regions occupied in the RESI process in three different intensities. In particular, we expect the distributions to exhibit maxima near the points $(p_{1||}, p_{2||}) = (\pm 2\sqrt{U_p}, 0)$. In a real-life situation, since both electrons are indistinguishable, one would expect maxima also at $(p_{1||}, p_{2||}) = (0, \pm 2\sqrt{U_p})$.

In the following figure (i.e. figure 5.7), we present electron momentum distributions computed employing equation (3.50) (as discussed in section 3.3.3) under the assumption that the prefactors $V_{\mathbf{p}_2 e}, V_{\mathbf{p}_1 e, \mathbf{k}g}$ and $V_{\mathbf{k}g}$ are constant. This removes any momentum bias that may arise from such prefactors, and therefore provides a clearer picture of how the momentum-space constraints affect such distributions. The transverse momentum components $d^2p_{1\perp} d^2p_{2\perp}$ are integrated over.

In panel (a), we consider only that the first electron is released in $0 < t' < T/2$, where $T = 2\pi/\omega$ denotes a cycle of the external driving field, while in panel (b) we also consider the contributions from $t' \to t' \pm T/2$, $t'' \to t'' \pm T/2$ and $t \to t \pm T/2$. Furthermore, in the latter case, we also symmetrize the distributions with respect to $\mathbf{p}_1 \leftrightarrow \mathbf{p}_2$, as the two electrons are indistinguishable. We have considered the parameters for a model atom, corresponding to the situation in which an electron initially in $1s$ was released and promoted a second electron to the $2p$ state.

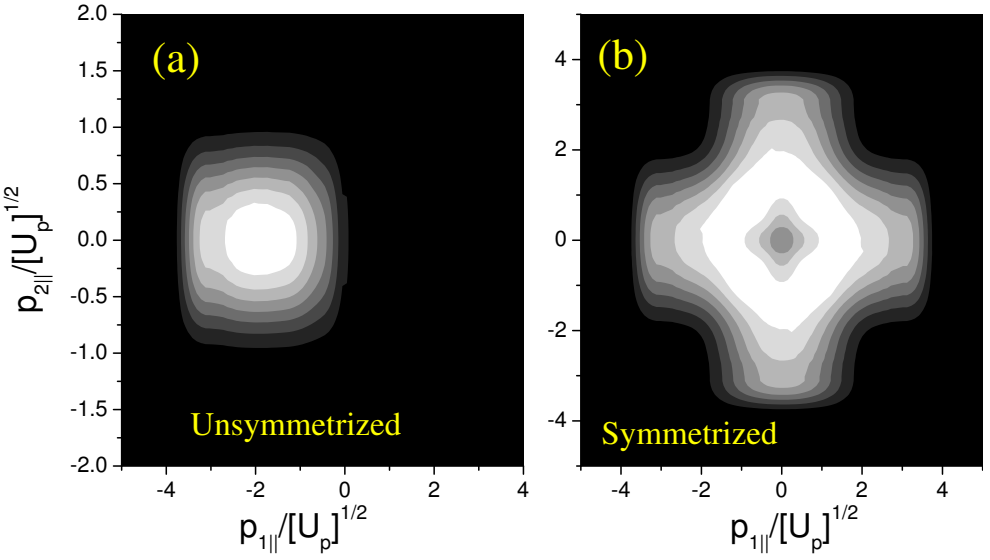

FIGURE 5.7: Electron momentum distributions for a model atom ($E_{1g} = 0.92$ a.u., $E_{2g} = 1$ a.u. and $E_{2e} = 0.25$) in a linearly polarized, monochromatic field of frequency $\omega = 0.057$ a.u. and intensity $I = 1.5 \times 10^{14}$ W/cm^2. Panel (a) displays only the contributions from the sets of orbits starting at $0 < t' < T/2$, while panel (b) depicts also the contributions from the other half-cycle of the field. In panel (b), the distributions have also been symmetrized with respect to the exchange $\mathbf{p}_1 \leftrightarrow \mathbf{p}_2$

In figure 5.7.(a), one clearly sees that the distributions are brightest along the axis $p_{2||} = 0$. This is expected, as the emission of the second electron is most probable at a field maximum. For this time, the electron momentum vanishes. Apart from that, the distribution is longer in the $p_{1||}$ direction. This is expected, as the cutoff momenta is higher in this case. Finally, the distributions also exhibit a maximum at $p_{1||} = -2\sqrt{U_p}$, in agreement with the RESI constraints defined earlier (see 5.2). Upon symmetrization (figure 5.7.(b)), we obtain distributions highly concentrated along the momentum axis $p_{1||} = 0$ and $p_{2||} = 0$. These distributions also exhibit a ring-shaped maximum around the origin of the $p_{1||}p_{2||}$ plane. These results show that the momentum regions populated by the RESI mechanism are much lower than those populated if the second electron is released by electron-impact ionization, in agreement with other results reported in the literature [70, 118].[1]

5.2.1 Intensity Dependence

We will now have a closer look at how the momentum-space constraints affect the electron momentum distributions for different driving-field intensities. For that purpose, we will once more assume that the prefactors $V_{\mathbf{p}_1 e,\mathbf{k}g}$ and $V_{\mathbf{p}_2 e}$ are constant, and vary

[1] The ionization potential of the second electron is small with respect to the external field, hence, one needs to include the saturation. However, for the problem we are considering in here, this saturation is ignored.

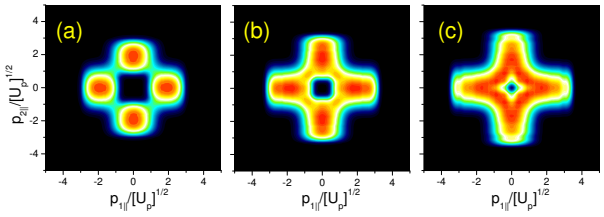

FIGURE 5.8: Electron momentum distributions for Helium ($E_{1g} = 0.97$ a.u., $E_{2g} = 2$ a.u. and $E_{2e} = 0.5$ a.u.) in a linearly polarized, monochromatic field of frequency $\omega = 0.057$ a.u.. In the picture, we considered all prefactors to be constant. Panels (a), (b) and (c) correspond to a driving-field intensity $I = 2.16\times10^{14}$ W/cm^2, $I = 2.5\times10^{14}$ W/cm^2 and $I = 3\times10^{14}$ W/cm^2, respectively. The contour plots have been normalized to the maximum probability in each panel.

the laser-field intensity. For the lowest intensity, the kinetic energy of the returning electron is just enough to promote the second electron to an excited state, i.e., we are considering the recollision excitation (RESI) threshold $E_{2g} - E_{2e} \simeq 3.17U_p$. This intensity, however, is below the electron-impact ionization threshold, i.e., $E_{2g} > 3.17U_p$. The intermediate intensity has been chosen such that $E_{2g} - E_{2e} < 3.17U_p$, i.e., above the threshold for recollision-excitation. Nevertheless, this intensity is not sufficient to make the second electron overcome the ionization potential and be freed by electron-impact ionization. Finally, the highest driving-field intensity considered in this section is far above the recollision-excitation threshold, and slightly above the electron-impact ionization threshold. This implies that rescattering is classically allowed for both physical mechanisms. The computations in this section have been performed for helium, and the results are presented in figure 5.8.

As an overall feature, the distributions exhibit four peaks at $(p_{j||}, p_{\nu||}) = (\pm2\sqrt{U_p}, 0)$, with $j, \nu = 1, 2$ and $j \neq \nu$. These peaks agree well with the constraints discussed in the previous sections, and exhibit a striking resemblance with the schematic representation of such constraints, displayed in figure 5.6. This holds even if the driving-field intensity is just enough to excite the second electron and the only allowed momenta are $\pm2\sqrt{U_p}$ [figure 5.8.(a)]. Physically, this means that the first electron will reach its parent ion most probably at a crossing of the driving field, reaching the detector with the most probable momenta of $\pm2\sqrt{U_p}$, while the second electron will reach it with vanishing momentum.

The shapes of the distributions, however, differ considerably. Indeed, at the RESI threshold intensity [figure 5.8.(a)], one observes ring-shaped distributions. As the intensity

increases, this distributions become more and more elongated along the $p_{n\parallel}$ axis [figure 5.8.(b)], until the maxima merge and cross-shaped distributions are observed [figure 5.8.(c)].

This change of shape may be understood by analyzing the momentum-space constraints. The widths of the distributions are determined by the tunnel ionization of the second electron from an excited state. This process has no classical counterpart and leads to distributions peaked at $p_{2\parallel} = 0$ and which vanish at $p_{2\parallel} = \pm 2\sqrt{U_p}$, i.e., at the direct ATI cutoff. Increasing the intensity will only make the effective potential barrier smaller or wider, and thus affect the overall yield, but will not change such constraints.

The elongations in the distributions are determined by the rescattering of the first electron. This rescattering, in contrast, delimits a momentum region which is highly dependent on the driving-field intensity. Therefore, its width in momentum space will vary. Specifically, at the RESI threshold, there will be maxima in the distributions at $p_{1\parallel} = \pm 2\sqrt{U_p}$ due to the fact that the first electron rescatters most probably at a field crossing. However, as these are the only classically allowed momenta, the distributions will be fairly narrow around this value. With increasing driving-field intensity, the classically allowed region defined by equation (5.7) will become more and more extensive and this will cause the elongation.

Note that the electrons are indistinguishable so that the above arguments hold upon the exchange $p_{1\parallel} \leftrightarrow p_{2\parallel}$. Hence, the horizontal and vertical axis in the parallel momentum plane will be equally affected.

5.2.2 Conclusions

The main conclusion to be inferred from this work is that the recollision-excitation-ionization mechanism, which is becoming increasingly studied due to its importance for NSDI of molecules and at threshold intensities, can be understood as a rescattered above-threshold ionization-like process (ATI) for the first electron, followed by direct ATI for the second electron.

The shapes of the electron momentum distributions, are determined by the interplay between two different behaviours, associated with the collision of the first electron and the tunneling of the second electron. The momentum region determined by the tunnel ionization of the second electron from an excited state will always be restricted by the direct ATI cutoff. The relevant momentum region will not change regardless of the driving-field intensity, as this will always be a classically forbidden process.

The first electron, on the other hand, rescatters inelastically with its parent ion, giving part of its kinetic energy upon return to excite the second electron. Hence, if its maximum return energy is larger than the energy difference $E_{2g} - E_{2e}$, rescattering has a classical counterpart. This implies that there will be a classically allowed region in momentum space. If, however, this energy is just enough to excite the second electron, the classical region will collapse. Hence, the extension of the relevant region in momentum space related to the rescattering of the first electron will depend on the driving-field intensity. Hence, the distributions become increasingly elongated as the intensity increases.

This also implies that one may define a threshold driving-field intensity for the RESI mechanism. This intensity is considerably lower than that necessary for the second ionization potential to be overcome by the second electron, i.e., for electron-impact ionization to occur.

Chapter 6

Bound-state Signature in RESI in Atoms

This chapter illustrates how we performed a rigorous, semi-analytic study of the recollision excitation with subsequent tunneling ionization (RESI) mechanism in laser-induced nonsequential double ionization (NSDI), based on the strong-field approximation. This work is part of my PhD work and has been published in [4]. This study shows how the shapes of the electron momentum distributions carry information about the bound state with which the first electron collides, the bound state to which the second electron is excited, and the type of electron-electron interaction. Electron momentum distributions are computed for helium and argon in the threshold and above-threshold intensity regimes. In the latter case, our findings are related to existing experiments [86]. The electron momentum distributions encountered are symmetric with respect to all quadrants of the plane spanned by the momentum components parallel to the laser-field polarization, instead of concentrating on only the second and fourth quadrants. The above-mentioned momentum constraints, together with the strong dependence of the distributions on the bound states involved, may be important for singling out the RESI mechanism in actual physical situations and using NSDI in ultrafast imaging.

The prefactors of the transition amplitude contain all the information about the target structure. In this chapter, an investigation is carried out to see how the initial and excited states and the electron-electron interaction affect the electron momentum distributions of NSDI in the RESI mechanism. In section 6.1, the specific prefactors are provided for the hydrogenic systems to be investigated in this work. This approach is employed to compute electron momentum distributions for helium and argon in section 6.2. For the latter species, an explicit comparison with the results in reference [86] is performed. Finally, in section 6.3, we bring the main conclusions from this chapter.

6.1 Prefactors

In this work, we are particularly interested in exponentially decaying, hydrogenic bound states. This means that, in general, the bound-state wavefunction reads

$$\psi^{(nlm)}(\mathbf{r}_\alpha) = R_{nl}(r_n)Y_l^m(\theta_\alpha, \varphi_\alpha), \tag{6.1}$$

where n, l and m denote the principal, orbital and magnetic quantum numbers, the index α refers to the electron in question, and the angular coordinates are given by θ_α and φ_α. In this case, the binding potentials $V(r_1)$ and $V_{\text{ion}}(r_2)$ will be given by

$$V_\alpha(r_\alpha) = -\frac{Z_{\text{eff}}}{r_\alpha}, \tag{6.2}$$

where V_α yields either V or V_{ion}, and Z_{eff} corresponds to the effective electronic charge. The general expressions for the prefactors in this work are provided in the Appendix C.

Below, we state the specific prefactors to be employed for helium and argon. In the former case, upon collision, the second electron may be excited from the $1s$ state to either the $2s$ or the $2p$ state, while in the latter species it may undergo a transition from the $3p$ state to the $4s$ or the $4p$ state. One should note that the prefactor $V_{\mathbf{p}_2 e}$ is gauge dependent. In the length gauge, $\tilde{\mathbf{p}}_2(t) = \mathbf{p}_2 + \mathbf{A}(t)$, and $\tilde{p}_2(t)_\parallel = p_{2\parallel} + A(t)$ while, in the velocity gauge, $\tilde{\mathbf{p}}_2(t) = \mathbf{p}_2$ and $\tilde{p}_2(t)_\parallel = p_{2\parallel}$. The prefactor $V_{\mathbf{p}_1 e, \mathbf{k} g}$, on the other hand, is gauge invariant because phases cancel out(

6.1.1 Excitation $1s \to 2s$

Let us first consider the simplest case, in which the second electron is excited to $2s$. This gives the prefactors

$$V_{\mathbf{p}_2 e}^{(2s)} \sim \frac{[\tilde{p}_2(t)]^2 - 2E_{2e}}{[[\tilde{p}_2(t)]^2 + 2E_{2e}]^2} \tag{6.3}$$

and

$$V_{\mathbf{p}_1 e, \mathbf{k} g}^{(1s \to 2s)} \sim V_{12}(\mathbf{p}_1 - \mathbf{k}) \frac{\eta_1(\kappa^2, E_{2g}, E_{2e})}{[\kappa^2 + \zeta^2(E_{2g}, E_{2e})]^3}, \tag{6.4}$$

with

$$\begin{aligned} \eta_1(\kappa^2, E_{2g}, E_{2e}) \quad = \quad & \kappa^2(\sqrt{2E_{2g}} + 2\sqrt{2E_{2e}}) + (2E_{2g})^{3/2} \\ & -2(2E_{2e})^{3/2} - 6E_{2e}\sqrt{2E_{2g}}. \end{aligned} \tag{6.5}$$

and

$$\zeta(E_{2g}, E_{2e}) = \sqrt{2E_{2e}} + \sqrt{2E_{2g}}. \tag{6.6}$$

The above-stated equations can also be written in terms of the momentum components parallel and perpendicular to the laser field polarization, denoted by $p_{\alpha||}$ and $p_{\alpha\perp}$, ($\alpha = 1, 2$), respectively. In this case,

$$V_{\mathbf{p}_2 e}^{(2s)} \sim \frac{\left[\tilde{p}_2(t)_{\|}\right]^2 + \mathbf{p}_{2\perp}^2 - 2E_{2e}}{[\left[\tilde{p}_2(t)_{\|}\right]^2 + \mathbf{p}_{2\perp}^2 + 2E_{2e}]^2} \tag{6.7}$$

$$V_{\mathbf{p}_1 e,\mathbf{k}g}^{(1s\to 2s)} \sim V_{12}(\mathbf{p}_1 - \mathbf{k}) \frac{\eta_1 \left[\left(k - p_{1\|}\right)^2 + \mathbf{p}_{1\perp}^2, E_{2g}, E_{2e}\right]}{[\left(k - p_{1\|}\right)^2 + \mathbf{p}_{1\perp}^2 + \zeta^2(E_{2g}, E_{2e})]^3}, \tag{6.8}$$

6.1.2 Excitation $1s \to 2p$

If, on the other hand, the second electron is excited to $2p$, one must consider three degenerate states, corresponding to the magnetic quantum numbers $m = \pm 1, 0$.

This yields

$$V_{\mathbf{p}_2 e}^{(2p)} \sim \frac{\sqrt{\left[\tilde{p}_2(t)\right]^2}}{\left(2E_{2e} + \left[\tilde{p}_2(t)\right]^2\right)^2} \left[Y_1^m(\theta_{\tilde{p}_2}, \varphi_{\tilde{p}_2})\right]^* \tag{6.9}$$

and

$$V_{\mathbf{p}_1 e,\mathbf{k}g}^{(1s\to 2p)} \sim V_{12}(\mathbf{p}_1 - \mathbf{k}) \eta_2(\kappa^2, E_{2g}, E_{2e}) \left[Y_1^m(\theta_\kappa, \varphi_\kappa)\right]^*, \tag{6.10}$$

with

$$\eta_2(\kappa^2, E_{2g}, E_{2e}) = \frac{\zeta(E_{2g}, E_{2e})\sqrt{\kappa^2}}{\left(\zeta^2(E_{2g}, E_{2e}) + \kappa^2\right)^3}. \tag{6.11}$$

Since the electron may be excited to any of the $2p$ states, we will consider the coherent superposition

$$\left|\psi_{2p}^{(2)}\right\rangle = \frac{1}{\sqrt{3}} \left(\left|\psi_{2p_x}^{(2)}\right\rangle + \left|\psi_{2p_y}^{(2)}\right\rangle + \left|\psi_{2p_z}^{(2)}\right\rangle\right), \tag{6.12}$$

where $\langle \mathbf{r}_2 \left|\psi_{2p_j}^{(2)}\right\rangle = \psi_{2p_j}^{(2)}(\mathbf{r}_2)$, with $j = x, y, z$. This implies that

$$V_{\mathbf{p}_2 e}^{(2p)} \sim \frac{\sqrt{\left[\tilde{p}_2(t)\right]^2}}{\left(2E_{2e} + \left[\tilde{p}_2(t)\right]^2\right)^2} \beta(\tilde{\mathbf{p}}_2(t)) \tag{6.13}$$

and

$$V_{\mathbf{p}_1 e,\mathbf{k}g}^{(1s\to 2p)} \sim V_{12}(\mathbf{p}_1 - \mathbf{k}) \eta_2(\kappa^2, E_{2g}, E_{2e}) \beta(\kappa), \tag{6.14}$$

where the angular dependency is given by

$$\beta(\mathbf{q}) = (\sin\theta_q \cos\varphi_q + \sin\theta_q \sin\varphi_q + \cos\theta_q). \tag{6.15}$$

Thereby, we employed the usual relations between spherical polar coordinates and the spherical harmonics.

One may write the above-stated expressions in terms of the electron momentum components parallel and perpendicular to the laser-field polarization. In this case, equation (6.13) reads

$$V_{\mathbf{p}_2 e}^{(2p)} \sim \frac{\sqrt{\left[\tilde{p}_2(t)_{\parallel}\right]^2 + \mathbf{p}_{2\perp}^2}}{\left(2E_{2e} + \left[\tilde{p}_2(t)_{\parallel}\right]^2 + \mathbf{p}_{2\perp}^2\right)^2} \beta(\tilde{\mathbf{p}}_2(t)). \tag{6.16}$$

In $\beta(\tilde{\mathbf{p}}_2(t))$, the angles $\theta_{\tilde{p}_2}$ and $\varphi_{\tilde{p}_2}$ are given by

$$\theta_{\tilde{p}_2} = \arccos\left[\tilde{p}_2(t)_{\parallel} / \sqrt{\left[\tilde{p}_2(t)_{\parallel}\right]^2 + \mathbf{p}_{2\perp}^2}\right] \tag{6.17}$$

and $\varphi_{\tilde{p}_2} = \arccos[\tilde{p}_2(t)_x / \tilde{p}_2(t)_{\perp}]$, respectively. In equation (6.14), $\kappa^2 = (k - p_{1\parallel})^2 + \mathbf{p}_{1\perp}^2$ and the angles θ_κ and φ_κ read

$$\theta_\kappa = \arccos\left[\left(k - p_{1\parallel}\right) / \sqrt{(k - p_{1\parallel})^2 + \mathbf{p}_{1\perp}^2}\right] \tag{6.18}$$

and $\varphi_\kappa = \arccos[p_{1x}/p_{1\perp}]$, respectively. This angular dependence will be washed out when the transverse momentum components are integrated over (see section 3.3.3).

6.1.3 Excitation $3p \to 4s$ and $3p \to 4p$

Finally, we will assume that the second electron, initially in $3p$, will be excited either to the $4s$ or to the $4p$ state. Like the procedure adopted in the previous section, we will consider a coherent superposition of the $3p_x$, $3p_y$ and $3p_z$ states for the initial state of the electron, i.e.,

$$\left|\psi_{3p}^{(2)}\right\rangle = \frac{1}{\sqrt{3}}\left(\left|\psi_{3p_x}^{(2)}\right\rangle + \left|\psi_{3p_y}^{(2)}\right\rangle + \left|\psi_{3p_z}^{(2)}\right\rangle\right). \tag{6.19}$$

If the electron is excited to the $4s$ state, the excitation prefactor $V_{\mathbf{p}_1 e,\mathbf{k}g}^{(3p\to 4s)}$ will exhibit an angular dependence given by $\beta(\kappa)$, and the tunneling prefactor $V_{\mathbf{p}_2 e}^{(4s)}$ will not depend on the angular variables. Both prefactors also have a radial dependence on $\tilde{p}_2(t)$ or κ. If, however, the electron is excited to the $4p$ state, one must take the final state as

$$\left|\psi_{4p}^{(2)}\right\rangle = \frac{1}{\sqrt{3}}\left(\left|\psi_{4p_x}^{(2)}\right\rangle + \left|\psi_{4p_y}^{(2)}\right\rangle + \left|\psi_{4p_z}^{(2)}\right\rangle\right), \tag{6.20}$$

i.e., as a coherent superposition of $4p_x$, $4p_y$ and $4p_z$. In this case, the angular dependence of $V_{\mathbf{p}_2 e}$ will be embedded in $\beta(\tilde{\mathbf{p}}_2(t))$. The angular dependence of $V_{\mathbf{p}_1 e,\mathbf{k}g}^{(3p\to 4p)}$ will be more complex and will involve the sum of the orbital angular momenta of the two electronic bound states involved. Due to the higher quantum numbers involved, the prefactors

are messier than those in the previous sections and will not be written down explicitly. They can, however, be obtained from the general expressions in Appendix C.

6.1.4 Bound-state Singularity

The simplest scenario is if all prefactors are nonsingular, such as in the velocity-gauge formulation of the SFA. In this case, they will contribute to the electron momentum distributions as $|V_{\mathbf{p}_2 e}|^2$ and $|V_{\mathbf{p}_1 e,\mathbf{k}g}|^2$.

In the length-gauge SFA, however, the exponentially decaying bound states of the prefactors (3.45) and (3.43) exhibit singularities, due to the saddle-point equations (4.4) and (4.7). This is due to the fact that these prefactors will be inversely proportional to $\left([\mathbf{k}+\mathbf{A}(t'')]^2+2E_{1g}\right)^n$ and $\left([\mathbf{p}_2+\mathbf{A}(t)]^2+2E_{2e}\right)^m$, where n, m are integers. For the problem addressed in this specific work, however, only the prefactor $V_{\mathbf{p}_2 e}$ will influence the shape of the electron momentum distributions. This is a consequence of the fact that it gives the final momentum $\mathbf{p}_2$ of the second electron at the detector. The prefactor $V_{\mathbf{k}g}$, in contrast, determines the intermediate momentum $\mathbf{k}$, which will change to $\mathbf{p}_1$ after recollision. Hence, it will only affect the distributions quantitatively. Therefore, to first approximation, one can consider equation (3.45) as constant. A similar problem for the electron-impact ionization mechanism in NDSI has been discussed in detail in [74].

To overcome the singularity in $V_{\mathbf{p}_2 e}$, one needs to embed this prefactor into the action, which now reads

$$\tilde{S}(\mathbf{p}_1,\mathbf{p}_2,\mathbf{k},t,t',t'') = S(\mathbf{p}_1,\mathbf{p}_2,\mathbf{k},t,t',t'') - i\ln V_{\mathbf{p}_2 e}. \tag{6.21}$$

This will lead to modifications in the saddle-point equation $\partial_t \tilde{S}(\mathbf{p}_1,\mathbf{p}_2,\mathbf{k},t,t',t'')$, which is now given by

$$[\mathbf{p}_2+\mathbf{A}(t)]^2 = -2E_{2e} + i\partial_t \ln V_{\mathbf{p}_2 e}. \tag{6.22}$$

The main consequence of such a modification is that the drift velocity of the second electron is no longer pure imaginary. This will lead to a splitting in the ionization time t for each orbit, as compared to the non-modified case. Depending on the velocity in question, the barrier the electron must tunnel through in order to reach the continuum will either widen or narrow. This means that, with regard to the non-modified action, $\mathrm{Im}[t]$ will either increase or decrease.

This singularity, however, is present only in the radial part of this prefactor. Therefore, the angular parts are still slowly varying, and may be treated as above. The radial part of the prefactor, however, must be incorporated in the action.

6.2 Results

In this section, we will compute electron momentum distributions employing equation (3.50) and integrating the transition amplitude (see 3.3.3) over the azimuthal angles φ_{p_n} and, unless otherwise stated, we just consider $V_{\mathbf{k}g}$ as constant. We will now briefly discuss how the prefactors $V_{\mathbf{p}_2 e}$ and $V_{\mathbf{p}_1 e,\mathbf{k}g}$ behave with regard to the integration over φ_{p_n}. Obviously, if the second electron is excited from an s state to an s state, the prefactors $V_{\mathbf{p}_2 e}$ and $V_{\mathbf{p}_1 e,\mathbf{k}g}$ do not depend on this parameter. However, if a transition from or to a p state is considered there will be an angular dependence in such prefactors.

For instance, tunneling ionization from a p state would lead to the argument $\beta(\tilde{\mathbf{p}}_2(t))$ in equation (6.13). If excitation from an s state to a p state or vice versa takes place, the angular dependence of the prefactor $V_{\mathbf{p}_1 e,\mathbf{k}g}$ is given by $\beta(\kappa)$ in equation (6.14)). When integrated over the azimuthal angles φ_{p_n}, $|\beta(\kappa)|^2$ and $|\beta(\mathbf{p}_2)|^2$ will yield 2π, so that the angular dependence of these prefactors can be neglected. If, however, states of higher orbital quantum numbers are involved, or if the initial and excited bound states of the second electron are p states, this dependence will be more complex.

We will now investigate how the shape of the bound state to which the second electron is excited is imprinted on the electron momentum distributions. We will also employ different gauges and types of electron-electron interaction. Explicitly, we will assume that the second electron is either excited by a contact-type interaction $V_{12}^{(\delta)}(\mathbf{r}_1 - \mathbf{r}_2) = \delta(\mathbf{r}_1 - \mathbf{r}_2)$ or by a long-range, Coulomb type interaction $V_{12}^{(C)}(\mathbf{r}_1 - \mathbf{r}_2) = 1/(\mathbf{r}_1 - \mathbf{r}_2)$. In the former case, $V_{12}^{(\delta)}(\mathbf{p}_1 - \mathbf{k}) = const.$, while in the latter case $V_{12}^{(C)}(\mathbf{p}_1 - \mathbf{k}) \sim 1/(\mathbf{p}_1 - \mathbf{k})^2$. We are considering these two types of interaction in order to make an assessment of the role of the Coulomb tail in the RESI mechanism. In electron-impact ionization, for instance, the long-range nature of the Coulomb interaction leads to a V-shaped structure [10, 71, 74, 76, 77].

In order to perform a direct comparison, we will take the same parameters as in figure 5.8, but incorporate the prefactors $V_{\mathbf{p}_1 e,\mathbf{k}g}^{(1s\to 2s)}$ and $V_{\mathbf{p}_2 e}^{(2s)}$, or $V_{\mathbf{p}_1 e,\mathbf{k}g}^{(1s\to 2p)}$ and $V_{\mathbf{p}_2 e}^{(2p)}$, corresponding to the $1s \to 2s$ or $1s \to 2p$ excitation with subsequent tunneling, respectively.

In figure 6.1, we consider the lowest intensity in figure 5.8 and the velocity gauge. If the electron is excited to the $2s$ state [figure 6.1.(a)], we observe four spots which are slightly elongated along the $p_{n\parallel}$ axis. Hence, in comparison to its constant prefactor counterpart, i.e., figure 5.8.(a), there was a narrowing. This narrowing is caused by the interplay of two features in the prefactor $V_{\mathbf{p}_2 e}^{(2s)}$. First, this prefactor exhibits two symmetric nodes, which, for vanishing transverse momentum are located at $p_{2\parallel} = \pm\sqrt{U_p}$. As the transverse momentum increases, these minima move towards vanishing parallel momenta. Second, $V_{\mathbf{p}_2 e}^{(2s)}$ decreases very steeply with transverse momenta $\mathbf{p}_{2\perp}$. Hence,

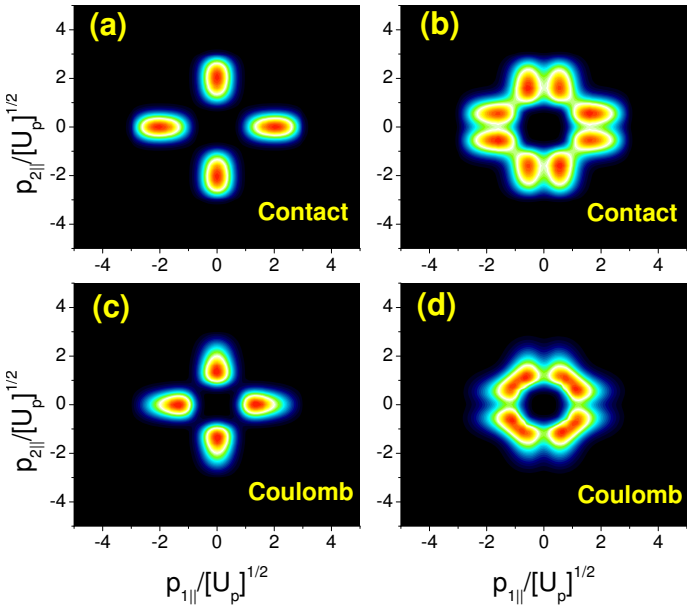

FIGURE 6.1: Velocity-gauge electron momentum distributions for helium ($E_{1g} = 0.97$ a.u., $E_{2g} = 2$ a.u. and $E_{2e} = 0.5$ a.u.) in a linearly polarized, monochromatic field of frequency $\omega = 0.057$ a.u. and intensity $I = 2.16 \times 10^{14}$ W/cm^2. In panels (a) and (c), the first electron has been excited to $2s$, while in panels (b), and (d) it has been excited to $2p$. The interaction employed is indicated in the figure. The contour plots have been normalized to the maximum probability in each panel.

upon integration over this parameter, the main contributions will be caused by small values of $\mathbf{p}_{2\perp}$ and will vanish near $p_{2\|} = \pm\sqrt{U_p}$.

If, on the other hand, one assumes that the second electron is excited to $2p$, there is both a broadening in the distributions and a splitting in their peaks. These features are depicted in figure 6.1.(b). The splitting occurs at the axis $p_{n\|} = 0, n = 1, 2$, and is caused by the fact that $V_{\mathbf{p}_2 e}$ exhibits a very pronounced node at vanishing momenta, i.e., exactly where one expects Im$[t]$ to be minimum and the yield to be maximum. This has been verified by a direct inspection of the radial dependence of equation (6.13), and omitting the $V_{\mathbf{p}_2 e}$ prefactor in our computations. The latter procedure caused the additional minima to disappear (not shown). The broadening in the distributions as compared to the $1s \to 2s$ case is a consequence of the much slower decrease in $V^{(2p)}_{\mathbf{p}_2 e}$ with increasing transverse momentum $p_{2\perp}$ and of the absence of the nodes at $p_{2\|} = \pm\sqrt{U_p}$. There are also additional nodes at the diagonal $p_{1||} = p_{2||}$ and at the anti-diagonal $p_{1||} = -p_{2||}$ of the $p_{1||}p_{2||}$ plane.

In this intensity regime, there seems to be little difference in the shapes of the distributions if the electron is excited to the $2s$ state, regardless of whether the first electron interacts with its parent ion through a contact or a Coulomb interaction [figures 6.1.(a) and (c), respectively]. This is possibly caused by the fact that the prefactor $V^{(2s)}_{\mathbf{p}_2 e}$, due

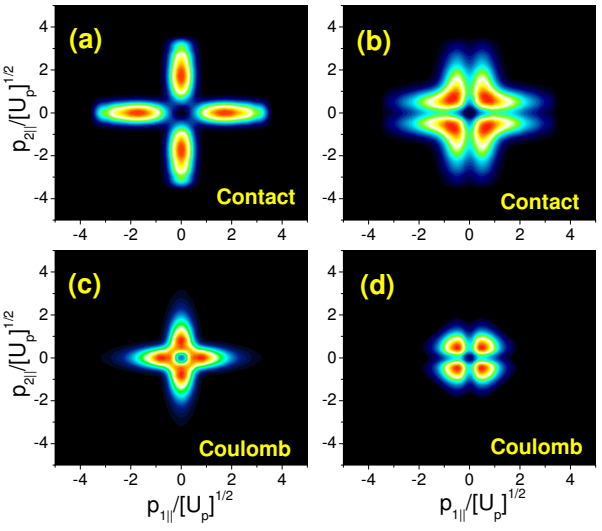

FIGURE 6.2: Velocity-gauge electron momentum distributions for the same parameters as in figure 6.1, but driving-field intensity $I = 3 \times 10^{14}$ W/cm^2. In panels (a) and (c), the first electron has been excited to $2s$, while in panels (b), and (d) it has been excited to $2p$. The interaction employed is indicated in the figure. The contour plots have been normalized to the maximum probability in each panel.

to its fast-decaying behavior, delimits a very narrow region in momentum space. This adds up to the very restrictive momentum constraints. In contrast, the effect of the Coulomb tail is much more critical if the electron is promoted to the $2p$ state. Indeed, for a Coulomb type interaction [figure 6.1.(d)], the splitting of the peaks at the axis $p_{n\|} = 0$ remain, but the nodes at $p_{1||} = p_{2||}$ and $p_{1||} = -p_{2||}$ disappear compared to their contact-interaction counterparts [figure 6.1.(b)]. This is caused by the fact that the former minima are a characteristic of the $V^{(2p)}_{\mathbf{p}_2 e}$ prefactor, whereas the latter are mainly determined by momentum-space effects. The Coulomb interaction introduces a further momentum bias, and washes out the latter nodes.

We will now discuss what happens if the intensity of the driving field is such that $3.17U_p > E_{2g} - E_{2e}$. These results are displayed in figure 6.2, for the highest intensity in figure (5.8). As expected, all distributions are much more elongated along the axis $p_{n\|} = 0$, as compared to the low-intensity case. The imprint, however, of the different bound states to which the second electron is excited and from which it subsequently tunnels are the same as in the below-threshold regime. Indeed, we notice that there is a narrowing in the distributions for the $1s \to 2s$ case [figure 6.2.(a) and (c)], and a splitting in the peaks at the four axis in the $1s \to 2p$ case [figures 6.2.(b) and (d)]. This is not surprising, as the prefactors $V^{(2s)}_{\mathbf{p}_2 e}$ and $V^{(2p)}_{\mathbf{p}_2 e}$ exhibit the same functional dependencies as before.

The shapes of distributions, however, change much more critically in this intensity regime, with regard to the type of electron-electron interaction, than for the intensity used in figure (6.1). For all cases, the distributions computed using the Coulomb-type interaction (figures 6.2.(c) and 6.2.(d)) are much more localized in the low-momentum regions than those computed with a contact-type interaction (see figures 6.2.(a) and 6.2.(b)). This is expected, as $V_{12}(\mathbf{p}_1 - \mathbf{k})$ favors low momenta for the former, while it is constant for the latter. Physically, this reflects the fact that rescattering of the first electron is now allowed to occur over an extensive region in momentum space. Hence, it does make a difference whether the second electron is excited by a long-range or zero-range interaction.

We will now perform an analysis of the electron-momentum distributions in the length gauge. In this case, the prefactor $V_{\mathbf{p}_2 e}$ governing the tunneling of the second electron exhibits a singularity, and must be incorporated in the action. The modifications in the action read, for the $2s$ and $2p$ bound states,

$$-i\partial_t \ln V_{\mathbf{p}_2 e}^{(2s)} = -i\frac{2E(t)\tilde{p}_2(t)_\parallel\left(\left[\tilde{p}_2(t)_\parallel\right]^2 + \mathbf{p}_{2\perp}^2 - 6E_{2e}\right)}{\chi_+(\tilde{\mathbf{p}}_2(t))\chi_-(\tilde{\mathbf{p}}_2(t))}, \tag{6.23}$$

and

$$-i\partial_t \ln \tilde{V}_{\mathbf{p}_2 e}^{(2p)} = i\frac{E(t)(\mathbf{p}_{2\perp}^2 + 2E_{2e} - 3\left[\tilde{p}_2(t)_\parallel\right]^2)}{\tilde{p}_2(t)_\parallel\left(\left[\tilde{p}_2(t)_\parallel\right]^2 + \mathbf{p}_{2\perp}^2 + 2E_{2e}\right)}, \tag{6.24}$$

respectively, with
$\chi_\pm(\tilde{\mathbf{p}}_2(t)) = \left(\left[\tilde{p}_2(t)_\parallel\right]^2 + \mathbf{p}_{2\perp}^2 \pm 2E_{2e}\right)$ and $E(t) = -\partial_t A(t)$.

For each orbit, the tunneling time of the second electron will split into two values, compared to the non-modified action. This has particularly important consequences as far as Im$[t]$ is concerned, since it provides a rough measure of the width of the barrier through which the second electron tunnels. Physically, this means there will be one set of orbits for which the potential barrier, effectively, will be widened, and another one for which it will be narrowed.

In figures 6.3, we present the contributions of each of the orbits resulting from this splitting for a final $2s$ state, for two different driving-field intensities. For simplicity, in order to single out the effect of the modified action, we took the rescattering prefactor $V_{\mathbf{p}_1 e,\mathbf{k}g}$ to be constant.

In general, the distributions differ quantitatively by a factor between 1.5 and 1.7, depending on whether Im$[t]$ decreased [figures 6.3(a) and (c)] or increased [figures 6.3(b) and (d)]. This shows that the splitting in this quantity is small, and therefore both contributions are comparable.

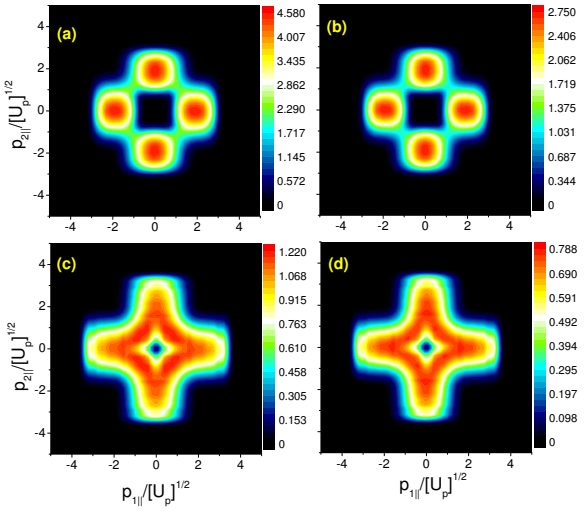

FIGURE 6.3: Length-gauge electron momentum distributions for helium in a linearly polarized, monochromatic field. Throughout, we assumed $V_{\mathbf{p}_1 e,\mathbf{k}g} = const.$, V_{12} to be a contact-type interaction, and incorporated $V^{(2s)}_{\mathbf{p}_2 e}$ in the action. Panels (a) and (c) correspond to the trajectories for which the barrier has been narrowed by the modifications in the action, while Panels (b) and (d) correspond to those for which it has been widened. The upper and lower panels correspond to driving field intensities $I = 2.16 \times 10^{14}$ W/cm^2 and $I = 3 \times 10^{14}$ W/cm^2, respectively. In order to perform a quantitative comparison, we are providing the explicit values for the NSDI yield. In the upper panels, these values are being multiplied by 10^{17} and 10^{16}, respectively.

Furthermore, the distributions displayed in figures 6.3 are strikingly similar to those observed in figure 5.8 (see panels (a) and (c) therein), for which only constant prefactors have been considered. Indeed, the width of all distributions, along the axis, is determined by the direct ATI cutoff, i.e., $-2\sqrt{U_p} \leq p_{n\parallel} \leq 2\sqrt{U_p}$. At first sight, this is unexpected, as we assume that the second electron is tunneling from a $2s$ state. As previously discussed, the prefactor $V^{(2s)}_{\mathbf{p}_2 e}$ exhibits a node in $p_{2\parallel} = \pm\sqrt{U_p}$, which leads to a narrowing of the distributions along the $p_{n\parallel}$ axis. An inspection of equation (6.7) also suggests that, were it not for its singularity, the length-gauge prefactor would be very similar to the velocity-gauge prefactor. This is a consequence of the fact that the second electron is leaving when the field $E(t)$ is near its maximum. For a monochromatic field, this implies that the vector potential $A(t)$ practically vanishes.

One should note, however, that we are considering only the individual contributions from each of the orbits originating from the modification of the action. It is very likely that, in order to recover the structure determined by the prefactor $V^{(2s)}_{\mathbf{p}_2 e}$, one must consider the coherent superposition of all the orbits originating from the splitting of Im$[t]$ when computing the yield. Since these contributions are comparable, one expects the above-mentioned nodes to be recovered due to quantum-interference effects.

In order to clarify this issue further, we consider a test case in which Gaussian bound states

$$\psi(\mathbf{r}_\alpha) = \left(\frac{E_\alpha}{\pi}\right)^{3/2} \exp\left[-E_\alpha r_\alpha^2\right], \tag{6.25}$$

where $E_\alpha = E_{1g}, E_{2g}$ and E_{2e} were taken in order to compute the prefactors $V_{\mathbf{k}g}, V_{\mathbf{p}_2 e}$ and $V_{\mathbf{p}_1 e,\mathbf{k}g}$. Due to the choice of wavefunction, the prefactors $V_{\mathbf{p}_2 e}$ and $V_{\mathbf{k}g}$ are no longer singular in the length gauge.

The explicit expression for the ionization prefactors reads

$$V_{\tilde{\mathbf{p}}\zeta} = 2\left(\frac{E_\alpha}{\tilde{p}}\right) \exp[-\frac{\tilde{p}^2}{4E_\alpha}]\text{erfi}\left[\frac{\tilde{p}}{2\sqrt{E_\alpha}}\right], \tag{6.26}$$

where erfi indicates the imaginary error function $\text{erfi}[z] = \text{erf}[iz]/iz$, $\tilde{p} = k(t'')$ or $p_2(t)$, $\zeta = g$ or e and $E_\alpha = E_{1g}$ or E_{2e}. In the length gauge, $p_2(t) = p_2 + A(t)$ and $k(t'') = k + A(t'')$, while in the velocity gauge $p_2(t) = p_2$ and $k(t'') = k$. The rescattering prefactor $V_{\mathbf{p}_1 e,\mathbf{k}g}$ is given by

$$\begin{aligned} V_{\mathbf{p}_1 e,\mathbf{k}g} \quad = \quad & \left[\frac{E_{2e}E_{2g}}{\pi(E_{2e}+E_{2g})}\right]^{3/2} \exp\left[-\frac{(\mathbf{p}_1-\mathbf{k})^2}{4(E_{2e}+E_{2g})}\right] \\ & \times V_{12}(\mathbf{p}_1-\mathbf{k}). \end{aligned} \tag{6.27}$$

This prefactor will be the same for both velocity and length gauges.

Figure 6.4 exhibits the results obtained employing the prefactors (6.26) and (6.27) in the velocity and length gauges [panels (a) and (b), respectively]. The figure shows nearly identical electron-momentum distributions. This is in agreement with the previous discussion.

6.2.1 Comparison with Experiments

We will now perform a direct comparison with the results in reference [86]. In particular, in this reference, the distributions encountered have been modeled employing the electron-impact ionization physical mechanism and a modified ionization threshold for the second electron. Apart from that, however, in view of the driving-field intensities involved, one expects recollision-excitation tunneling to be present.

For that purpose, we will consider argon and the same laser-field parameters as in reference [86] (c.f. figure 2 therein). We will assume, however, that, when the first electron recollides, it excites the second electron from the $3p$ state either to the $4s$ or to the $4p$ state. Therefore, we took the velocity gauge, and assumed that the first electron interacts with the ion by a Coulomb or contact interaction.

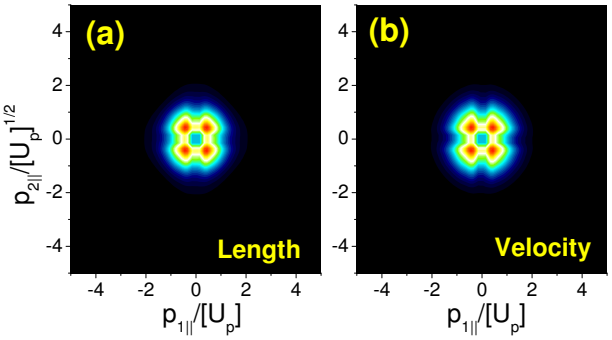

FIGURE 6.4: Electron momentum distributions computed with Gaussian bound-state wavefunctions for the first and second electron, in the velocity and length gauge (panels (a) and (b), respectively). Throughout, we considered that the second electron is excited by a Coulomb-type interaction, the same bound-state energies as for helium and a driving-field intensity $I = 3 \times 10^{14}$ W/cm^2. The contour plots have been normalized to the maximum probability in each panel.

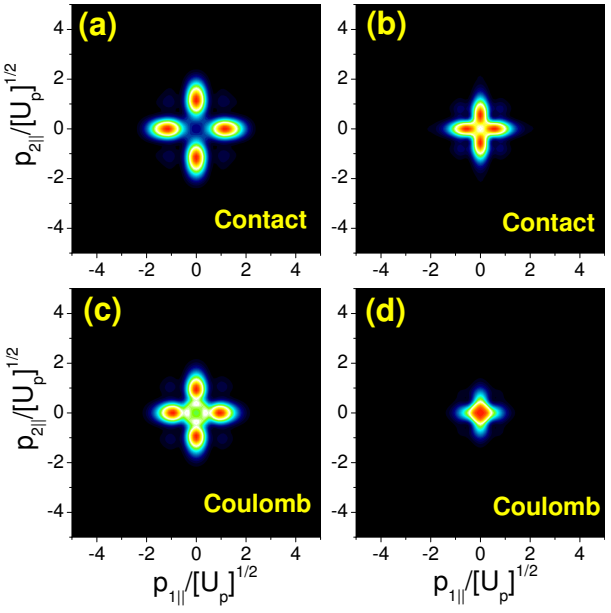

FIGURE 6.5: Velocity-gauge electron momentum distributions for Argon in a linearly polarized, monochromatic field of frequency $\omega = 0.057$ a.u. The electron is excited from $3p$ to $4s$, i.e., $E_{1g} = 0.58$ a.u., $E_{2g} = 1.02$ a.u. and $E_{2e} = 0.40$ a.u. in our calculations. The laser-field intensity in panels (a) and (c), and panels (b) and (d) is $I = 9 \times 10^{13}$ W/cm^2 and $I = 1.5 \times 10^{14}$ W/cm^2, respectively. The type of interaction V_{12} taken is indicated in the figure. The contour plots have been normalized to the maximum probability in each panel. We have verified, however, that the highest yields on left-hand panels are between one and a half and two orders of magnitude smaller than those on the right-hand side.

The results for the $3p \to 4s$ excitation are presented in figure 6.5. An overall feature in the distributions are two main maxima along the $p_{n\parallel}$, $n = 1, 2$, axis. These features are mainly caused by the $V^{(4s)}_{\mathbf{p}_2 e}$ prefactor for the tunnel ionization of the second electron, which decays very rapidly with increasing transverse momenta and exhibit nodes near $p_{2\parallel} = \pm 0.5\sqrt{U_p}$. In general, we have verified that this prefactor determines the shape of the electron-momentum distributions. Secondary maxima, around one order of magnitude smaller, occur due to the rescattering prefactor $V^{(3p\to 4s)}_{\mathbf{p}_1 e,\mathbf{k}g}$. This prefactor exhibits an annular shape around $p_{1\parallel} = p_{2\parallel} = 0$.

The existing experiments, however, do not lead to distributions concentrated along the axis of the $p_{1\parallel}p_{2\parallel}$ plane. The results for helium in the previous section suggest that a p state may lead to broader distributions. For that reason, we will assume that, instead, the second electron is excited to the $4p$ state.

Figure 6.6 depicts the electron-momentum distributions for Argon under the assumption that the electron was excited from $3p$ to $4p$. All distributions in the figure exhibit four main maxima, which are broader than those in figure 6.5 and almost split at the axis $p_{n\parallel} = 0$. These maxima are mainly determined by the prefactor $V^{(4p)}_{\mathbf{p}_2 e}$, which has a node at the axis for low transverse momenta and nodes around $p_{2\parallel} = \pm\sqrt{U_p}$ across a wide transverse-momentum range. Apart from that, the prefactors $V^{(3p\to 4p)}_{\mathbf{p}_1 e,\mathbf{k}g}$ decay more slowly with regard to the transverse momenta. This implies that, upon integration, a larger momentum region will be contributing to the NSDI yields. As in the previous case, this prefactor also leads to secondary maxima (see figure 6.6.(c) and (d) for concrete examples). In all cases, both in figures 6.5 and 6.6, a Coulomb-type interaction mainly introduces a bias towards lower momenta.

Despite the above-mentioned broadening, the electron-momentum distributions in figure 6.6 are still considerably narrower than those observed in reference [86]. Within our framework, this constraint is imposed by the $V^{(4p)}_{\mathbf{p}_2 e}$ prefactor. In fact, we have verified that, for large principal quantum number, this prefactor always exhibits nodes at lower absolute momenta than the ATI cutoff of $p_{2\parallel} = 2\sqrt{U_p}$. In fact, if $V_{\mathbf{p}_2 e}$ is taken to be constant, the distributions become considerably broader and a better agreement with the experiments is obtained. This is shown in figures 6.7, as ring-shaped distributions with four symmetric maxima at $p_{1\parallel} = p_{2\parallel}$ and $p_{1\parallel} = -p_{2\parallel}$. Such maxima are mainly determined by the $V^{(3p\to 4p)}_{\mathbf{p}_1 e,\mathbf{k}g}$ prefactor. One should note, however, that this procedure is inconsistent from a theoretical perspective: Since the electron has been excited to the $4p$ state, it should subsequently tunnel from it. Hence, the appropriate prefactor must be taken. Furthermore, due to external field distortion the $4p$ state might be over the barrier, which may not provide any nodal structures.

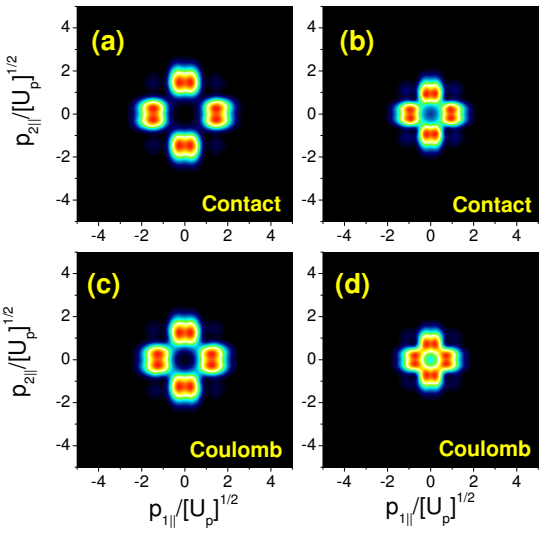

FIGURE 6.6: Velocity-gauge electron momentum distributions for argon in a linearly polarized, monochromatic field of frequency $\omega = 0.057$ a.u. The electron is excited from $3p$ to $4p$, i.e., $E_{1g} = 0.58$ a.u., $E_{2g} = 1.02$ a.u. and $E_{2e} = 0.31$ a.u. in our calculations. The laser-field intensity in panels (a) and (c), and panels (b) and (d) is $I = 9 \times 10^{13}$ W/cm^2 and $I = 1.5 \times 10^{14}$ W/cm^2, respectively. The type of interaction V_{12} taken is indicated in the figure. The contour plots have been normalized to the maximum probability in each panel. We have verified, however, that the highest yields on left-hand panels are between one and two orders of magnitude smaller than those on the right-hand side.

Nonetheless, the procedure of removing the $V_{\mathbf{p}_2 e}$ prefactor appears to mimic to some extent what happens in a real-life situation, for which the bound states exhibit ac Stark shifts. The first electron returns near a field crossing. Hence, at the rescattering time t', these shifts will only be a small perturbation and are not expected to influence the distributions significantly. The second electron, however, tunnels close to a field maximum. This means that, in this case, the Stark shifts will be more prominent and will cause a broadening in the electron momentum distributions. A rough, ad hoc way of verifying this is to introduce a time-dependent excited state energy according to the procedure described in reference [178]. Such an approach has also been adopted in [86] for electron-impact ionization. A rigorous way of incorporating these shifts, however, is far more challenging.

6.3 Conclusions

Our analysis of the rescattering-excitation ionization (RESI) mechanism shows that the NSDI electron momentum distributions depend on the interplay between the relevant

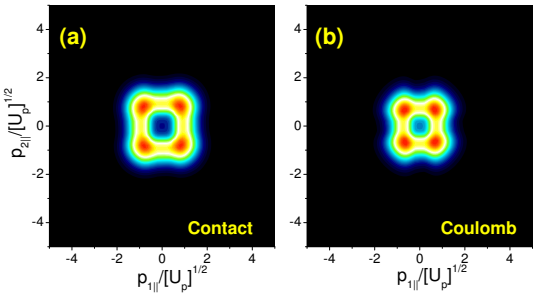

FIGURE 6.7: Velocity-gauge electron momentum distributions for argon in a linearly polarized, monochromatic field of frequency $\omega = 0.057$ a.u. and intensity $I = 1.5 \times 10^{14}$ W/cm^2. The electron is excited from $3p$ to $4p$. We have taken the prefactor $V_{\mathbf{p}_2,e}$ to be constant. The type of interaction V_{12} is indicated in the figure. The contour plots have been normalized to the maximum probability in each panel.

momentum-space regions, the type of interaction exciting the second electron, and the spatial dependence of the bound states involved.

We have observed that the bound states involved in the process leave very distinct fingerprints on the electron momentum distributions. This is particularly true for the bound state of the second electron, prior and subsequently to excitation. In fact, the widths of the distributions, their shapes and the number of maxima present will strongly depend on the principal and orbital quantum numbers of the bound states involved.

In contrast, the type of interaction V_{12} by which the second electron is excited influences such distributions in a less drastic way. Indeed, a long-range, Coulomb interaction mainly introduces a bias towards lower momenta, as compared to a contact-type interaction.

A very important observation is that all distributions encountered in this work are equally spread over the four quadrants of the $p_{1\|}p_{2\|}$ plane. Under no circumstances have we found electron momentum distributions concentrated only on the second and fourth quadrant of this plane, as reported in the literature [13, 109, 112–114].

Within our framework, the above-stated symmetry can immediately be inferred from equation (3.49). Nonetheless, one could argue that our approach does not include the residual binding potential in the electron propagation in the continuum. Recent results, however, from a classical-trajectory computation in which the Coulomb potential has been incorporated, also revealed the same symmetry if only the RESI mechanism is singled out [111] (see figures. 3.(b) and 4.(b) in [111]). This is a strong hint that our results are not an artifact of the strong-field approximation.

Hence, we suspect that, in the existing literature, the contributions from the RESI mechanism to nonsequential double ionization also equally occupy the four quadrants of the $p_{1\parallel}p_{2\parallel}$ plane. They may, however, be difficult to extract, as explained below.

In many situations addressed in the literature, the driving-field intensity is high enough for electron-impact ionization to occur. This means that this latter NSDI mechanism is also present, and fills the first and third quadrant of the $p_{1\parallel}p_{2\parallel}$ plane. Since, in many ab initio models, the different rescattering mechanisms are difficult to disentangle, the contributions from electron-impact ionization possibly obscure those from RESI in this region. In the second and fourth quadrant of the parallel momentum plane, the former contributions are absent and those from RESI can be more easily identified. In our approach, electron-impact ionization is absent from the start. Hence, we can study the RESI process separately, and assess all its consequences.

Furthermore, in several classical computations, one tries to mimic the RESI mechanism by considering, instead, electron impact ionization with a time delay between the rescattering of the first electron and the rescattering of the second electron. This is a completely different physical process, which populates only the second and the fourth quadrants of the parallel momentum plane [13, 109, 112–117].

In general, the RESI mechanism gets more prominent as the driving-field intensity is far below the ionization threshold, so that the second electron may no longer be provided with enough energy to overcome the second ionization potential. Alternatively, if the pulse is long, one also expects RESI to be more prominent [70]. Otherwise, electron-impact ionization will dominate.

An example of the former scenario can be found in reference [86] (see figure 2 therein), for NSDI around the electron-impact ionization threshold. For the higher driving-field intensity, one may identify two elongated shapes along $p_{1\parallel} = p_{2\parallel}$ superposed to a more symmetric structure. These shapes are a signature of the electron-impact ionization mechanism. As the intensity decreases, this process gets less and less prominent and RESI dominates. Consequently, the distributions become symmetric, and equally occupy the four quadrants of the parallel momentum plane. In fact, ring-shaped distributions centered around $p_{1\parallel} = p_{2\parallel} = 0$ have been observed experimentally for this intensity region [84–86].

Our results are far more localized near the $p_{n\parallel} = 0$ axis than the experimental findings. This discrepancy may be due to the following reasons. First, for higher intensities employed in reference [86], collisional excitation may take place not only to the $4s$ or to the $4p$ state, but also to highly lying states, or to a coherent superposition of excited

states. To take this into account may be needed in order to reproduce the experimental data.

Second, at the relevant driving-field intensities, one expects the excited states to be distorted by the field, and the propagation of the electron in the continuum near the core to be influenced by the residual ionic potential. This implies that a semi-analytical treatment beyond the strong-field approximation is necessary (see, e.g., [83, 94, 95, 149] for other phenomena and the electron-impact ionization case, respectively). The Stark shift of the excited bound state seems to be particularly important, due to the fact that the second electron leaves close to a field maximum. In fact, a computation with a time-dependent energy for the excited bound state improves the agreement between theory and experiment, especially if the electron is leaving from a $4p$ state. One should note, however, that a rigorous treatment of such features is very demanding, and will not be performed in this work.

Finally, the results obtained in this chapter show that the dynamics of the second electron have a huge influence in the shapes of the electron-momentum distributions. A suppression or enhancement in its tunnel ionization would lead to an overall suppression or enhancement in the yield. Furthermore, changes in its ionization time would affect its most probable momentum, and therefore the peaks of the electron momentum distributions. Apart from that, depending on the shape of the excited state wavefunction, there may be nodes in the corresponding prefactors, which may cause the distributions to broaden or narrow. This means that, in principle, the shapes of the electron-momentum distributions can be manipulated by an adequate driving-field choice and by preparing the first electron in a suitable superposition of states.

Chapter 7

Electron-impact Ionization in Diatomic Molecules: Quantum-interference Effects, Alignment and the Orbital Symmetry

In this chapter we address the influence of the orbital symmetry and of the molecular alignment with respect to the laser-field polarization on laser-induced nonsequential double ionization. We work within the strong-field approximation and assume that the second electron is dislodged by electron-impact ionization (see 2.2.1), and also consider the classical limit of this model. We show that the electron-momentum distributions exhibit interference maxima and minima due to the electron emission at spatially separated centers. The interference patterns survive the integration over the transverse momenta for a small range of alignment angles, and are sharpest for parallel-aligned molecules. Due to the contributions of transverse-momentum components, these patterns become less defined as the alignment angle increases, until they disappear for perpendicular alignment. This behavior influences the shapes and the peaks of the electron momentum distributions. This work has been published in [2].

The main motivation behind this work lies on the fact that recent NSDI experiments on diatomic molecules have shown that the shapes of the electron momentum distributions depend on the symmetry of the highest occupied molecular orbital [13, 84]. This holds even if the molecular sample is randomly aligned with respect to the laser-field polarization [84]. Indeed, in [84], very distinct electron momentum distributions were observed

for N_2 and O_2, as functions of the electron momentum components $p_{n\parallel}$ $(n = 1, 2)$ parallel to the laser-field polarization. For the former species, elongated maxima along the diagonal $p_{1\parallel} = p_{2\parallel}$ were reported, while, for O_2, the distributions exhibit a prominent maximum in the region of vanishing parallel momenta, and are quite broad along the direction $p_{1\parallel} = -p_{2\parallel} + const.$ This has been confirmed by theoretical computations within a classical framework, which reproduced some of the differences in the yields.

Subsequently, it was found that the peak momenta and the shape of the N_2 electron-momentum distributions changed considerably with the alignment angle of the molecules, with respect to the laser-field polarization [13]. Specifically, for parallel alignment, a roughly 40% larger peak momenta along the diagonal $p_{1\parallel} = p_{2\parallel}$ was observed, as compared to the perpendicular case. Furthermore, for perpendicular alignment, a larger number of events in the second and fourth quadrant of the momentum plane $(p_{1\parallel}, p_{2\parallel})$ was reported. In [13], these events were attributed to excitation-tunneling mechanisms.

Despite the above-mentioned investigations, NSDI in molecules has been considerably less studied than HHG or ATI, possibly due to the fact that it is far more difficult to measure, or to model (for a review on this subject see [120] and the discussions in the previous chapters). In principle, since the physical mechanisms responsible for NSDI are similar to those behind HHG and ATI, one would expect that this phenomenon can also be used to retrieve information about the target. For instance, it is very likely that there will be quantum interference due to photoelectron emission at different centers in the molecule. Apart from that, since the type of the electron-electron interaction influences the shape of the electron momentum distributions considerably, one expects that NSDI will provide more dynamical information than the other phenomena.

This chapter is organized as follow: in section 7.1, we obtain the specific prefactors for a diatomic molecule, simplifying the geometry of the molecular orbitals by just considering hydrogenic molecular orbitals. We compute transition amplitude (3.33) using the saddle-point approximation to obtain electron momentum distributions of N_2, for angle-integrated (7.2.1), and aligned molecules (7.2.2). Specifically, we investigate the influence of the orbital symmetry and of the alignment angle on the NSDI electron momentum distributions, and whether, within our framework, the features reported in [84] and [13] are observed. Furthermore, we address the question of whether well-defined interference patterns such as those observed in ATI or HHG computations may also be obtained for NSDI, and, if so, under which conditions. Finally, in section 7.3, we state the main conclusions of this chapter.

7.1 Diatomic Molecules

We will now consider the specific case of diatomic molecules. For simplicity, we will assume frozen nuclei, the linear combination of atomic orbitals (LCAO) approximation, and homonuclear molecules. This very simplified model has the main advantage of allowing a transparent picture of the physical mechanisms behind the interference patterns. Explicitly, the molecular bound-state wave function for each electron is

$$\psi_0^{(n)}(\mathbf{r}_n) = C_\psi \left[\phi_0^{(n)}(\mathbf{r}_n - \mathbf{R}/2) + \epsilon\phi_0^{(n)}(\mathbf{r}_n + \mathbf{R}/2)\right] \tag{7.1}$$

where $n = 1, 2$, $\epsilon = \pm 1$, and $C_\psi = 1/\sqrt{2(1 + \epsilon S(\mathbf{R})}$, with

$$S(\mathbf{R}) = \int \left[\phi_0^{(n)}(\mathbf{r}_n - \mathbf{R}/2)\right]^* \phi_0^{(n)}(\mathbf{r}_n + \mathbf{R}/2) d^3r. \tag{7.2}$$

The positive and negative signs for ϵ correspond to symmetric and antisymmetric orbitals, respectively. The binding potential of this molecule, as seen by each electron, is given by

$$V(\mathbf{r}_n) = V_0(\mathbf{r}_n - \mathbf{R}/2) + V_0(\mathbf{r}_n + \mathbf{R}/2), \tag{7.3}$$

where V_0 corresponds to the binding potential of each centre in the molecule.

The above-stated assumptions lead to

$$V_{\mathbf{k}0}^{(s)} = -\frac{2C_\psi}{(2\pi)^{3/2}} \cos[\tilde{\mathbf{k}}(t') \cdot \mathbf{R}/2] \mathcal{I}(\tilde{\mathbf{k}}(t')) \tag{7.4}$$

or

$$V_{\mathbf{k}0}^{(a)} = -\frac{2iC_\psi}{(2\pi)^{3/2}} \sin[\tilde{\mathbf{k}}(t') \cdot \mathbf{R}/2] \mathcal{I}(\tilde{\mathbf{k}}(t')), \tag{7.5}$$

for the symmetric and antisymmetric cases, respectively, with

$$\mathcal{I}(\tilde{\mathbf{k}}(t')) = \int d^3r_1 \exp[i\tilde{\mathbf{k}}(t') \cdot \mathbf{r}_1] V_0(\mathbf{r}_1) \phi_0^{(1)}(\mathbf{r}_1). \tag{7.6}$$

Thereby, we have neglected the integrals for which the binding potential $V_0(\mathbf{r})$ and the bound-state wave function $\phi_0^{(1)}(\mathbf{r})$ are localized at different centers in the molecule. We have verified that the contributions from such integrals are very small for the parameter range of interest, as they decrease very quickly with the internuclear distance.

Equations (7.4) and (7.5) do not play a significant role in the appearance of well-defined interference patterns. This is due to the fact that the times t' at which the electron is emitted lie near the peak field of the laser field. In other words, the electron trajectories relevant to the momentum distributions start near the times for which the electric field is maximum. For those most important trajectories, the range of $k(t')$ is so limited that

the term $\cos(\mathbf{k}(t')\cdot\mathbf{R}/2)$ does not cross zero. In fact, we verified that the prefactor $V_{\mathbf{k}0}$ has no influence on the interference patterns (not shown).

Assuming that the electron-electron interaction depends only on the difference between the coordinates of both electrons, i.e., $V_{12}=V_{12}(\mathbf{r}_1-\mathbf{r}_2)$, one may write the prefactor $V_{\mathbf{p}_n\mathbf{k}}$ as

$$V^{(s)}_{\mathbf{p}_n\mathbf{k}}=\frac{2C_\psi}{(2\pi)^{9/2}}V_{12}(\mathbf{p}_1-\mathbf{k})\cos[\mathcal{P}(t)\cdot\mathbf{R}/2]\varphi_0^{(2)}(\mathcal{P}(t)) \tag{7.7}$$

or

$$V^{(a)}_{\mathbf{p}_n\mathbf{k}}=\frac{2iC_\psi}{(2\pi)^{9/2}}V_{12}(\mathbf{p}_1-\mathbf{k})\sin[\mathcal{P}(t)\cdot\mathbf{R}/2]\varphi_0^{(2)}(\mathcal{P}(t)), \tag{7.8}$$

with $\mathcal{P}(t)=\tilde{\mathbf{p}}_1(t)+\tilde{\mathbf{p}}_2(t)-\tilde{\mathbf{k}}(t)$, for symmetric and antisymmetric orbitals, respectively. Thereby,

$$\varphi_0^{(2)}(\mathcal{P}(t))=\int d^3r_2\exp[i\mathcal{P}(t)\cdot\mathbf{r}_2]\phi_0^{(2)}(\mathbf{r}_2), \tag{7.9}$$

and

$$V_{12}(\mathbf{p}_1-\mathbf{k})=\int d^3rV_{12}(\mathbf{r})\exp[i(\mathbf{p}_1-\mathbf{k})\cdot\mathbf{r}], \tag{7.10}$$

with $\mathbf{r}=\mathbf{r}_1-\mathbf{r}_2$. Specifically, in the velocity and length gauges, the argument in equations (7.7), (7.8) is given by $\mathcal{P}(t)=\mathbf{p}_1+\mathbf{p}_2-\mathbf{k}$ and $\mathcal{P}(t)=\mathbf{p}_1+\mathbf{p}_2-\mathbf{k}+\mathbf{A}(t)$, respectively.

The interference patterns studied in this work are caused by the pre-factors $V_{\mathbf{p}_n\mathbf{k}}$. Explicitly, the two-centre interference condition defined by $V_{\mathbf{p}_n\mathbf{k}}$ gives the extrema

$$\left[\tilde{\mathbf{p}}_1(t)+\tilde{\mathbf{p}}_2(t)-\tilde{\mathbf{k}}(t)\right]\cdot\mathbf{R}=n\pi. \tag{7.11}$$

For symmetric, highest occupied molecular orbitals, even and odd numbers in equation (7.11) denote maxima and minima, respectively, whereas in the antisymmetric case the situation is reversed (i.e., even and odd n give minima and maxima, respectively). This equation will be discussed in more detail in section (7.2.2).

The structure of the highest occupied molecular orbital is embedded in equations (7.4)-(7.8). The simplest way to proceed is to consider these prefactors and the single-centre action (3.34). The multiple integral in (3.33) will be solved using saddle-point methods.

Using the saddle-point equations (4.1)-(4.3), the transition amplitude is then computed by means of a uniform saddle-point approximation (As it was discussed in Chapter 4). A more rigorous approach would be to incorporate the prefactors (7.7) or (7.8) in the action. This would lead to modified saddle-point equations, in which the structure of the molecule, in particular scattering processes involving one or two centers, are taken into account. Recently, however, in the context of HHG, it has been verified that, unless

the internuclear distances are of the order of the electron excursion amplitude, both procedures yield practically the same results [179, 180]. Therefore, for simplicity, we will restrict our investigation to single-atom saddle-point equations (4.4)-(4.6), together with the two-centre prefactors (7.7) or (7.8).

7.2 Results

We compute electron momentum distributions, as functions of the momentum components $(p_{1\parallel}, p_{2\parallel})$ parallel to the laser-field polarization, as discussed in 3.3.3. In particular, we investigate how the symmetry of the molecular orbitals influence the electron momentum distributions. Furthermore, we integrate over the transverse momenta as well as considering situations for which the transverse momenta are resolved. For the latter case, the integrals in (3.50) are dropped.

The above-stated distribution may also be mimicked employing a classical ensemble computation, in which a set of electrons are released with vanishing drift momentum and weighed with the quasi-static rate

$$R(t') \sim |E(t')|^{-1} \exp\left[-2(2|E_{01}|)^{3/2}/(3|E(t')|)\right]. \tag{7.12}$$

Subsequently, these electrons propagate in the continuum following the classical equations of motion in the absence of the binding potential. Finally, some of them return and release a second set of electrons. Explicitly, this distribution is given by

$$F^{cl}(p_{1\parallel}, p_{2\parallel}) = \iint d^2p_{1\perp} d^2p_{2\perp} F^{cl}(\mathbf{p}_1, \mathbf{p}_2), \tag{7.13}$$

with

$$\begin{aligned} F^{cl}(\mathbf{p}_1, \mathbf{p}_2) = \quad & \int dt' R(t') |V_{\mathbf{p}_n \mathbf{k}}|^2 |V_{\mathbf{k}0}|^2 \\ & \delta\left(\sum_{i=1}^{2} \frac{[\mathbf{p}_i + \mathbf{A}(t)]^2}{2} + |E_{02}| - E_{\mathrm{r}}(t)\right), \end{aligned} \tag{7.14}$$

where $E_{\mathrm{r}}(t) = [\mathbf{k}+\mathbf{A}(t)]^2/2$ is the kinetic energy of the first electron upon return (see [75] for details). One should note that the argument in equation (7.14) is just equation (4.3), which expresses conservation of energy following rescattering. This argument implicitly depends on t', since both start and return times are inter-related. If the laser-field intensity is far above the threshold, i.e., if the classically allowed region is large, both approaches yield very similar results [175].

7.2.1 Angle-integrated Distributions

As a first step, we will discuss angle-integrated electron momentum distributions from equation (3.33), for different gauges and orbital symmetry. To a first approximation, we will assume that the second electron is dislodged by the contact-type interaction

$$V_{12}(\mathbf{r}_1 - \mathbf{r}_2) = \delta(\mathbf{r}_1 - \mathbf{r}_2), \tag{7.15}$$

and that the electrons are bound in $1s$ states. These assumptions have been employed in [84], and led to a reasonable degree of agreement with the experimental data. In this case, the prefactor $V_{12}(\mathbf{p}_1 - \mathbf{k}) = const.$ in (7.7)-(7.8), and the Fourier transform of the initial wave function of the second electron reads

$$\varphi_0^{(2)}(\mathcal{P}(t)) \sim \frac{1}{[2E_{02} + \mathcal{P}(t)^2]^2}. \tag{7.16}$$

The prefactors $V_{\mathbf{k}0}$ and $V_{\mathbf{p}_n\mathbf{k}}$ agree with the results in [84], for which the velocity gauge was taken.

We will consider the ionization potentials and equilibrium internuclear distance of N_2, and laser-field intensities well within the experimental range. To a first approximation, we will model the highest-occupied molecular orbital of N_2 using the symmetric prefactor (7.7). In order to facilitate a direct comparison, we will also include the antisymmetric prefactor (7.8), and the single-atom case, for which $V_{\mathbf{p}_n\mathbf{k}} \sim V_{12}(\mathbf{p}_1 - \mathbf{k})\varphi_0^{(2)}(\mathcal{P}(t))$, and employ the same molecular and field parameters for all cases.

Figure 7.1 depicts the above-mentioned distributions. In general, even though different gauges and orbital symmetry lead to very distinct prefactors, the shapes of the distributions are very similar. This is due to the fact that the momentum region for which the transition amplitude (3.33) has a classical counterpart is relatively small. Indeed, we have verified that, for vanishing transverse momenta $p_{1\perp} = p_{2\perp} = 0$, this region starts slightly below $\pm\sqrt{U_p}$, and extends to almost $\pm 3\sqrt{U_p}$. This is the case for which the classically allowed region is the most extensive, so that below $\pm\sqrt{U_p}$ the contributions to the yield are negligible. Hence, the maxima and the shapes of these distributions are determined by the interplay between phase-space effects and the prefactor (7.16).

In the length gauge, equation (7.16) is very large near $p_{1\parallel} + p_{2\parallel} = \pm 1.5\sqrt{U_p}$, while in the velocity gauge this holds for $p_{1\parallel} + p_{2\parallel} = \pm 0.5\sqrt{U_p}$. This is in agreement with the features displayed in figure 7.1. In fact, a closer inspection of the length-gauge distributions shows that they exhibit slightly larger maxima, near $p_{1\parallel} = p_{2\parallel} = \pm 1.5\sqrt{U_p}$, and are broader along $p_{1\parallel} = -p_{2\parallel}$ than their velocity-gauge counterparts. In the velocity gauge, since the peak of the prefactor lies outside the classically allowed region, we expect that the yield

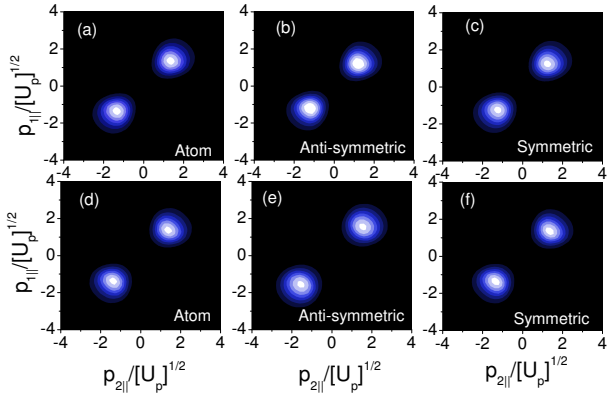

FIGURE 7.1: Angle-integrated electron momentum distributions as functions of the momentum components $(p_{1\|}, p_{2\|})$ parallel to the laser-field polarization, computed using the contact-type interaction (7.15). The field intensity and frequency have been taken as $I = 1.5 \times 10^{14}$ W/cm^2, and $\omega = 0.057$ a.u., respectively, and the ionization potentials $E_{01} = 0.573$ a.u. and $E_{02} = 0.997$ a.u. correspond to N_2 at the equilibrium internuclear distance $R = 2.068$ a.u. The upper and lower panels have been calculated in the velocity and the length gauge, respectively. Panels (a), and (d) correspond to the single atom case, panels (b) and (e) to the antisymmetric prefactors (7.4) and (7.7), and panels (c) and (f) to the symmetric prefactors (7.5) and (7.8).

will be maximal near the smallest momentum values which have a classical counterpart. This agrees with figures 7.1(a)-(c), which exhibit peaks slightly above $\pm\sqrt{U_p}$.

In figure 7.1, one also notices that the distributions are nearly identical in the single-atom and molecular case. This is possibly due to the fact that the distributions are being angle-integrated. Apart from that, we have verified that, within the classically allowed region, there is at most a single interference minimum. This may additionally contribute for the lack of well-defined interference patterns.

7.2.2 Interference Effects

For the above-stated reasons, in order to investigate whether interference patterns are present in the NSDI electron momentum distributions, we will proceed in many ways. First, we will increase the classically allowed momentum region, and hence the radius of the hypersphere given by equation (5.2). For that purpose, we will increase the intensity of the driving laser field. Second, in this section, we will consider aligned molecules, as it is not clear whether integrating over the alignment angle washes the interference patterns out. One should note that, for the parameters considered in this work, the De Broglie wavelength of the returning electron is much larger than the equilibrium internuclear distance of N_2.

Finally, in order to disentangle the influence of the prefactor which accounts for the two-centre interference from that of $\varphi_0^{(2)}(\mathcal{P}(t))$, we make the further assumption that V_{12} is placed at the position of the ions. Without this assumption, prefactor (7.16) corresponding to the contact interaction depends on the final electron momenta, and thus introduces a bias in the distributions. This may obscure any effects caused solely by the molecular prefactors.

Explicitly, this reads

$$V_{12} = \delta(\mathbf{r}_1 - \mathbf{r}_2)\left[\delta(\mathbf{r}_2 - \mathbf{R}/2) + \delta(\mathbf{r}_2 + \mathbf{R}/2)\right]. \tag{7.17}$$

Such an interaction has been successfully employed in the single-atom case, and led to "balloon-shaped" distributions peaked near $p_{1\parallel} = p_{2\parallel} = \pm 2\sqrt{U_p}$. Such distributions exhibited a reasonable degree of agreement with the experiments [75]. This choice of V_{12} yields $\varphi_0^{(2)}(\mathcal{P}(t)) = const$, in addition to $V_{12}(\mathbf{p}_1 - \mathbf{k}) = const$. Hence, apart from effects caused by the integration over momentum space, the shape of the distributions will be mainly determined by the cosine or sine factor in equations (7.7) or (7.8). The former and the latter case correspond to the symmetric or antisymmetric case, respectively. The explicit interference maxima and minima are given by equation (7.11).

We will now perform a more detailed analysis of such interference condition. In terms of the momentum components $p_{i\parallel}$, or $p_{i\perp}$ $(i = 1, 2)$, parallel or perpendicular to the laser-field polarization, this condition may be written as $\cos\left[\zeta R/2\right]$ or $\sin\left[\zeta R/2\right]$, in terms of the argument ζ. Explicitly, this argument is given by

$$\zeta = \zeta_\parallel + \zeta_\perp, \tag{7.18}$$

with

$$\zeta_\parallel = \left[\sum_{i=1}^{2} p_{i\parallel} - k(t)\right]\cos\theta \tag{7.19}$$

and

$$\zeta_\perp = p_{1\perp}\sin\theta\cos\varphi + p_{2\perp}\sin\theta\cos(\varphi + \alpha). \tag{7.20}$$

In the above-stated equations, θ gives the alignment angle of the molecule, φ corresponds to the angle between the perpendicular momentum $\mathbf{p}_{1\perp}$ and the polarization plane, and α represents the angle between both perpendicular momentum components. Since we are dealing with non-resolved transverse momenta, we integrate over the latter two angles. In the velocity and in the length gauge, $k(t) = k$ and $k(t) = k - A(t)$, respectively. Interference extrema will then be given by the condition

$$(\zeta_\perp + \zeta_\parallel)R = n\pi. \tag{7.21}$$

For a symmetric linear combination of atomic orbitals, even and odd n correspond to interference maxima and minima, respectively, whereas, in the antisymmetric case, this condition is reversed.

An inspection of equations (7.19) and (7.20), together with the above-stated condition, provides an intuitive picture of how the interference patterns change with the alignment angle θ. For parallel alignment, the only contributions to such patterns will be due to $\zeta_{\parallel}$. In this particular case, the interference condition may be written as

$$p_{1\parallel} + p_{2\parallel} = \frac{n\pi}{R\cos\theta} + k(t), \tag{7.22}$$

where $\cos\theta = 1$. Equation (7.22) implies the existence of well-defined interference maxima or minima, which, to first approximation, are parallel to the anti-diagonal $p_{1\parallel} = -p_{2\parallel}$. This is only an approximate picture, as k, according to the saddle-point equation (4.5), is dependent on the start time t' and on the return time t. Furthermore, since t' and t also depend on the transverse momenta of the electrons (see [16] for a more detailed discussion), equation (7.22) is influenced by such momenta. Finally, in the length gauge, there is an additional time dependence via the vector potential $\mathbf{A}(t)$ at the instant of rescattering.

As the alignment angle increases, the contributions from the term $\zeta_{\perp}$ related to the transverse momenta start to play an increasingly important role in determining the interference conditions. The main effect such contributions have is to weaken the fringes defined by equation (7.22), until, for perpendicular alignment, the fringes completely vanish and the electron momentum distributions resemble those obtained for a single atom. This can be readily seen if we consider the interference condition for $\theta = \pi/2$, which is

$$p_{1\perp}\cos\varphi + p_{2\perp}\cos(\varphi + \alpha) = \frac{n\pi}{R}. \tag{7.23}$$

Equation (7.23) gives interference conditions which do not depend on $k(t)$, and which vary with the angles φ and α. As one integrates over the latter parameters, which is the procedure adopted for distributions with non-resolved transverse momentum, any structure which may exist in equation (7.23) is washed out.

In figure 7.2, we display electron momentum distributions computed in the velocity gauge for the highest symmetric occupied molecular orbital and various alignment angles. The symmetric case is of particular interest, since, recently, NSDI electron momentum distributions have been measured for aligned N_2 molecules [13]. For parallel alignment, interference fringes parallel to the anti-diagonal $p_{1\parallel} = -p_{2\parallel}$ can be clearly seen, according to equation (7.22). For small alignment angles, such as that in figure 7.2(b), the maxima and minima start to move towards larger parallel momenta. Furthermore, there exists an

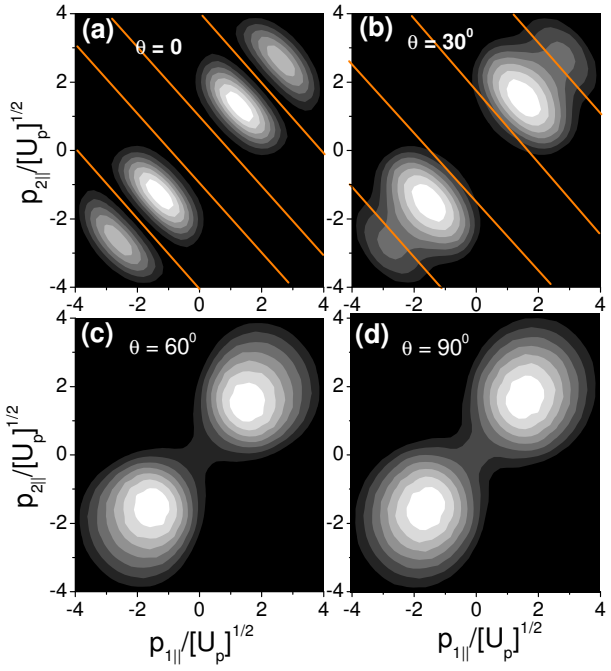

FIGURE 7.2: Electron momentum distributions as functions of the parallel momenta $(p_{1\parallel}, p_{2\parallel})$, for several alignment angles. We consider the velocity gauge, symmetric orbitals, and driving-field intensity $I = 5 \times 10^{14}$ W/cm^2. The remaining field and molecular parameters are the same as in the previous figure. The position of the interference minima, estimated by assuming that the first electron returns at a field crossing, are indicated by the lines in the figure. Panel (a), (b), (c) and (d) correspond to alignment angles $\theta = 0, \theta = 30^0$, $\theta = 60^0$ and $\theta = 90^0$, respectively.

increase in the momentum difference between consecutive maxima or minima, and the interference fringes become less defined. This is due to the fact that the term $\zeta_\perp$, which washes out the interference patterns, gets increasingly prominent. For large alignment angles, such as that in figure 7.2(c), the contributions from this term are very prominent and have practically washed out the two-centre interference. Finally, for perpendicular alignment, the distributions resemble very much those obtained for the single-atom case, i.e., circular distributions peaked at $p_{1\parallel} = p_{2\parallel} = \pm 2\sqrt{U_p}$ (c.f. Refs. [74, 75] for details). This is expected, since the term responsible for the two-centre interference lets fringes vanish for $\theta = 90^0$.

The fringes in figure (7.2) exhibit a very good qualitative agreement with the interference conditions derived in this section. Furthermore, the figure shows that, for some alignment angles, the patterns caused by the two-centre interference survive the integration over the transverse momentum components. It is not clear, however, how well the position of the fringes agree with equation (7.22) quantitatively, and if it is possible to provide simple estimates for these maxima and minima. Apart from that, it is not an

obvious fact that the patterns survive the integration over the transverse momentum, and one should understand why this happens.

In particular, the role of the intermediate momentum of the first electron will be analyzed subsequently. According to the return condition (4.5), this quantity depends on the start and return times of the first electron. Furthermore, in the length gauge, the interference condition also depends on the vector potential $\mathbf{A}(t_1)$ at the return time of the first electron. For each pair $(p_{1\parallel}, p_{2\parallel})$, the emission and return times are strongly dependent on the transverse momenta [16]. Apart from that, physically, there are several orbits along which the first electron may return, which occur in pairs. Hence, there exist several possible values for k. In practice, only the two shortest orbits contribute significantly to the yield. The contributions from the remaining pairs are strongly suppressed due to wave-packet spreading. However, this still means that the intermediate momentum, and therefore the position of the maxima and minima, has two possible values, which depend on the start and return times, and also on the final momentum components.

We have made a rough estimate of the position of these patterns for parallel alignment, in the velocity and length gauges, along the diagonal $p_{1\parallel} = p_{2\parallel} = p_{\parallel}$. This estimate is given in Table 7.1. For symmetric highest occupied molecular orbitals, the even and odd numbers denote maxima and minima, respectively, while for antisymmetric orbits this role is reversed. Thereby, we assumed that the first electron leaves at peak field and returns at a field crossing[1]. This gives $|k| \simeq \sqrt{U_p}/(0.75\pi)$ in the saddle-point equation (4.2). Furthermore, in the length-gauge estimate, we took $|A(t)| \simeq 2\sqrt{U_p}$. We have verified that both quantities are negative for the orbits in question.

These estimates agree reasonably well with the electron momentum distributions along $p_{1\parallel} = p_{2\parallel} = p_{\parallel}$. These distributions are depicted in figure (7.3) for several alignment angles, the velocity gauge, and the highest symmetric occupied molecular orbitals. The positions of the minima, for each angle, are indicated in the figure. These minima have been computed employing equation (7.22) and the above-stated estimate for k. For parallel alignment [figure 7.3(a)], the position of the extrema agree relatively well with Table 7.1. This suggests that the intermediate momentum of the first electron, upon return, can be approximated by its value at the field crossing. As the alignment angle increases, the patterns become increasingly blurred until they are eventually washed out by the contributions of $\zeta_{\perp}$. For instance, for $\theta = 30^0$ [figure 7.3(b)], one may still identify a change of slope in the distributions, at the momentum for which the minima $n = 3$ is expected to occur. For $\theta = 60^0$, however, the term $\zeta_{\perp}$ has already washed out the interference patterns. Indeed, in figure 7.3(c), there is no evidence of interference

[1]Note that is a rather crude approximation. Strictly speaking, the electron leaves after the field maximum in order to return near a crossing (for details see [16]).

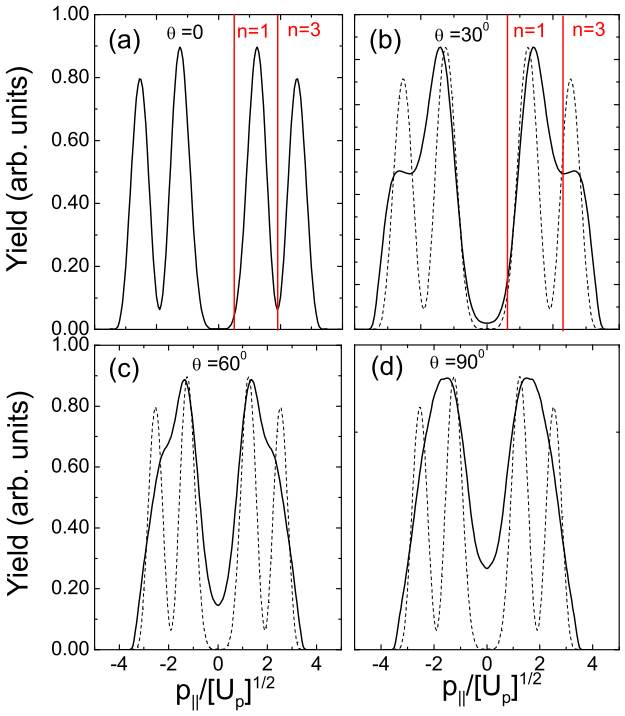

FIGURE 7.3: Electron momentum distributions for parallel momenta $p_{1\parallel} = p_{2\parallel} = p_\parallel$, non-resolved transverse momenta and several alignment angles. We consider the velocity gauge, symmetric orbitals, and the same molecule and field parameters as in the previous figure. The position of the interference minima, estimated by assuming that the first electron returns at a field crossing, are indicated by the vertical lines in the figure. Panel (a), (b), (c) and (d) correspond to alignment angles $\theta = 0, \theta = 30^0$, $\theta = 60^0$ and $\theta = 90^0$, respectively. For comparison, the yield for $\theta = 0$ are indicated as the dashed lines in the figure. To facilitate the comparison, the yields have been normalized to the same peak values.

patterns. Finally, for perpendicular alignment, the distributions resemble very much those obtained in the single-atom case, as shown in [figure 7.3(d)].

In order to investigate the behavior of the intermediate momentum k with respect to $p_{n\perp}(n = 1, 2)$, we will compute electron momentum distributions keeping the absolute values of the transverse momenta fixed. For simplicity, we will take $\theta = 0$ and parallel momenta along the diagonal, i.e., $p_{1\parallel} = p_{2\parallel} = p_\parallel$. These distributions are displayed in figure 7.4. In this case, there exists a region of parallel momenta for which the yield is oscillating, between the maximum and the minimum parallel momentum. These oscillations are due to the quantum interference between the two shortest possible orbits along which the first electron may return. These orbits constitute the pair that has

Extrema	Parallel momentum $p_{\parallel}/[U_p]^{1/2}$	
Order n	velocity gauge	length gauge
1	0.513	1.513
2	1.239	2.239
3	1.964	2.964
4	2.689	3.689

TABLE 7.1: Electron momenta corresponding to the interference maxima and minima given by equation (7.22), in the velocity and length gauges, for a parallel-aligned molecule, for the same field and molecule parameters as in figure 7.3. The parallel momenta $p_{\parallel}$ were taken to be along the diagonal $p_{1\parallel} = p_{2\parallel}$ in the momentum plane, and the transverse momenta are assumed to be vanishing. If the highest occupied molecular orbital is approximated by a symmetric combination of atomic orbitals, the maxima and minima are denoted by even and odd number, while in the antisymmetric case, this role is reversed, i.e., odd and even numbers denote maxima and minima, respectively.

been employed in the computations performed in this work. The larger the transverse momenta are, the less extensive this region is. This is expected according to equation (5.1), which delimits this region (for details see reference [16]).

Apart from these oscillations, figure (7.4) also exhibits the maxima and minima caused by the spatial two-centre interference. The figure shows that the position of such patterns is very robust with respect to the choice of $p_{\perp n}$, $n = 1, 2$. Indeed, both maxima and minima remain at practically the same positions, if different transverse momenta are taken. For this reason, such patterns survive if one integrates over the transverse momenta. In contrast, the oscillations due to the temporal interference get washed out. For the parameters employed in the figure, we have verified reasonable agreement between the second minimum and Table 1. The first minimum is to a large extent washed out by the contributions of the events displaced by a half-cycle, i.e., which are related to the transition amplitude M_L.

Interference fringes parallel to $p_{1\parallel} = -p_{2\parallel}$ are also present in the length gauge, and for antisymmetric orbitals. This is shown in the upper panels of figure 7.5, for a parallel alignment angle. In fact, the main difference as compared to the symmetric, velocity-gauge case, is the position of their interference patterns, in agreement with equation (7.22). There is also some blurring in the patterns, in the length gauge, possibly caused by the fact that the vector potential $\mathbf{A}(t)$ depends on the return time t. This latter quantity is different for different transverse momenta. The patterns, however, can also be clearly identified in this gauge. In all cases, however, there is no evidence of a straightforward connection between an enhancement or suppression of the yield in the low-momentum region and the symmetry of the orbital. For instance, in the velocity

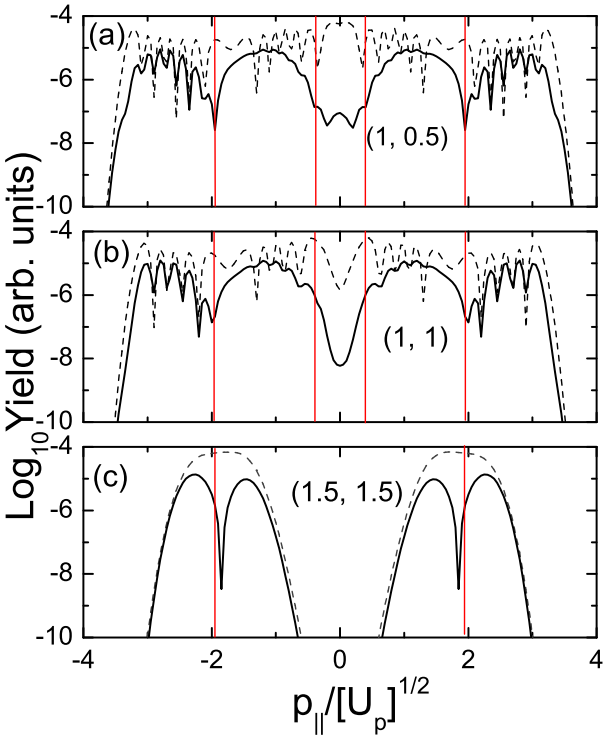

FIGURE 7.4: Electron momentum distributions for resolved transverse momenta, as functions of the parallel momentum $p_{1\parallel} = p_{2\parallel} = p_\parallel$, for alignment angle $\theta = 0$. We consider the velocity gauge, symmetric orbitals, and the same molecule and field parameters as in the previous figure. For comparison, the corresponding single-atom distributions are presented as the dashed lines in the figure. The interference minima according to Table 1 are indicated by the vertical lines in the figure. The numbers in the figure indicate the transverse momentum components $(p_{1\perp}, p_{2\perp})$ in units of $\sqrt{U_p}$.

gauge, the yield is enhanced if the orbital is antisymmetric. The length-gauge distributions, on the other hand, exhibit a suppression in that region regardless of the orbital symmetry.

In the lower panels of figure 7.5, we display the distributions along $p_{1\parallel} = p_{2\parallel} = p_\parallel$. Similarly to the velocity-gauge, symmetric case, the minima and maxima of the distributions roughly agree with Table 1. In fact, the even numbers in this table roughly give the position of the minima in figure 7.5(e) and (f), which correspond to antisymmetric orbitals, while the odd numbers approximately yield the minima in figure 7.5(d), which display the length-gauge, symmetric case. Specifically for the length-gauge distributions [figure 7.5(d) and (e)], there is an overall displacement of roughly $2\sqrt{U_p}$ in the position of the patterns. This is consistent with the modified interference conditions in this case.

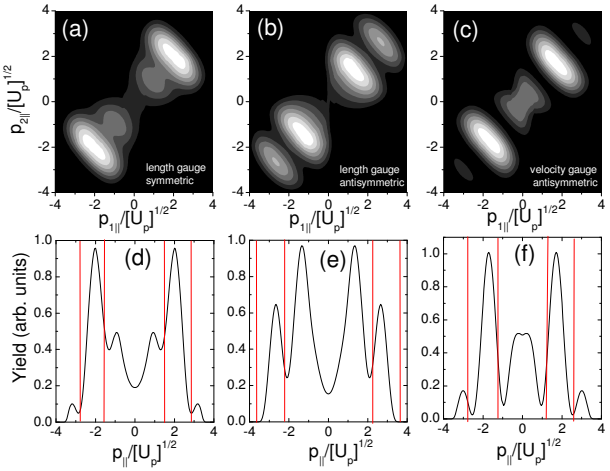

FIGURE 7.5: Electron momentum distributions for a parallel-aligned molecule ($\theta = 0$), different orbital symmetries and gauges. The upper and lower panels give the contour plots as functions of the parallel momenta, and the distributions along $p_{1\|} = p_{2\|} = p_\|$, respectively. We integrate over the transverse momenta, and employ the same molecule and field parameters as in the previous figures. The interference minima according to Table 1 are indicated by the vertical lines in the figure. Panel (a) and (d), (b) and (e), and (c) and (f) correspond to symmetric orbitals in the length gauge, antisymmetric orbitals in the length gauge and antisymmetric orbitals in the velocity gauge, respectively. For panels (d), (e) and (f), the units in the vertical axis have been chosen so that their upper values are unity (the original values have been divided by 0.016, 0.01 and 0.04, respectively).

7.2.3 The Classical Limit

In the following, we perform a comparison between the S-Matrix computation and its classical limit. In the single-atom case, both computations led to very similar results, unless the driving-field intensity is close to the threshold intensity [175]. At this intensity, the kinetic energy upon return is just enough to make the second electron overcome the ionization potential. Therefore, since the intensity used in most figures is far above the threshold intensity, one would expect similar results.

In figure 7.6, we display differential momentum distributions as functions of the parallel momentum components, computed employing the classical model. This is the classical counterpart of figure 7.2, in which the quantum mechanical distributions are depicted for the same parameters. Indeed, for all alignment angles depicted, the classical and quantum-mechanical distributions look very similar. Hence, even though the two-centre interference is an intrinsically quantum mechanical effect, it can be mimicked to a very large extent within a classical model. There is also a good quantitative agreement between the positions of the minima and maxima in both classical and quantum mechanical cases. This is shown in figure 7.7, for parallel momenta $p_{1\|} = p_{2\|} = p_\|$, and several

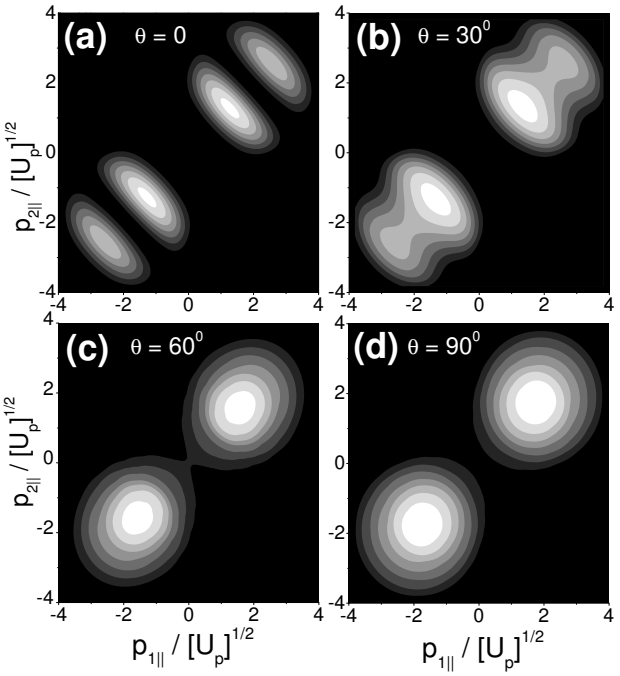

FIGURE 7.6: Electron momentum distributions for highest symmetric occupied molecular orbitals and several alignment angles, as functions of the parallel momentum components $(p_{1\parallel}, p_{2\parallel})$, computed in the velocity gauge using the classical model for the same field and molecular parameters as in Fig. 7.2. Panels (a), (b), (c) and (d) correspond to $\theta = 0$, $\theta = 30^0$, $\theta = 60^0$, and $\theta = 90^0$, respectively.

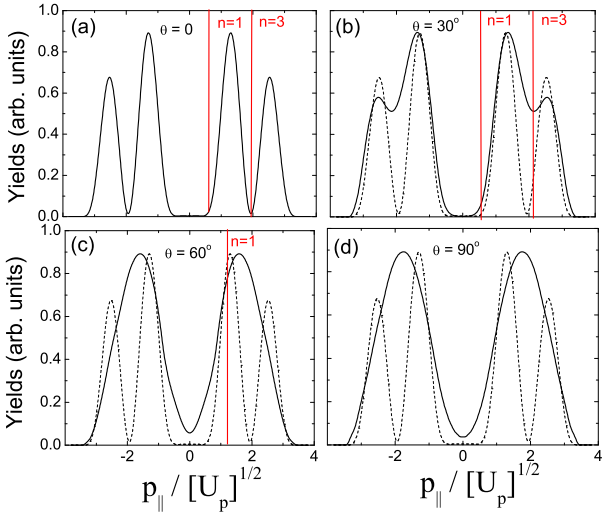

FIGURE 7.7: Electron momentum distributions for highest symmetric occupied molecular orbitals and several alignment angles, along $p_{1\parallel} = p_{2\parallel} = p_{\parallel}$, computed in the velocity gauge using the classical model for the same field and molecular parameters as in Fig. 7.3. Panels (a), (b), (c) and (d) correspond to $\theta = 0$, $\theta = 30^0$, $\theta = 60^0$, and $\theta = 90^0$, respectively.

alignment angles. For $\theta = 0$ and $\theta = 30^0$ [figures 7.7(a) and 7.7(b), respectively], the maxima and minima agree very well with those in figure 7.3. The main difference, with regard to the quantum-mechanical case, is that, for large alignment angles, the classical distributions are more localized than their quantum-mechanical counterparts, especially in the low momentum regions. For instance, in figure 7.7(d), the yield is much lower near $p_{\parallel} = 0$, as compared to the outcome of the S-Matrix computation [figure 7.3(d)]. This discrepancy is possibly due to the fact that the classical model underestimates contributions to the yield near the boundary of the classically allowed region.

7.3 Conclusions

In this work, we addressed two aspects of non-sequential double ionization of diatomic molecules: the influence of the symmetry of the highest occupied molecular orbital, and of the alignment angle, on the differential electron momentum distributions. We considered the physical mechanism of electron-impact ionization, within the strong-field approximation, and very simple models for the highest occupied molecular orbitals, within the LCAO and frozen nuclei approximations.

For angle-integrated electron momentum distributions, we have shown that, for driving-field intensities within the tunneling regime and compatible with existing experiments [84], the distributions computed with symmetric and antisymmetric orbitals (prefactors 7.7) and (7.8), respectively), or different gauges, look practically identical. This is due to the fact that, if only electron-impact ionization is taken into account, the momentum region for which this process has a classical counterpart is too small to allow the corresponding pre-factors to have a significant influence. At first sight, this is in contradiction with the experimental findings and computations in [84]. Therein, a broadening parallel the anti-diagonal direction has been reported only for the anti-symmetric case, while, for a symmetric combination of atomic orbitals, an elongation in the direction $p_{1\parallel} = p_{2\parallel}$ was observed. One should note, however, that, in [84], an effective, time-dependent second ionization potential $E_{02}(t) = E_{02} - 2\sqrt{2|E(t)|}$ is used [86]. This feature has not been incorporated in the present computations. It has the effect of increasing the classically allowed momentum region and introducing an additional time dependence in the prefactors and the action.

We also made a detailed assessment of the interference effects due to the fact that electron emission may occur from two spatially separated centers. In order to disentangle the interference effects from those caused by the prefactor $\varphi_0^{(2)}(\mathcal{P}(t))$, we assumed that the second electron was dislodged by a contact-type interaction at the position of the ions. We observed interference fringes in the electron momentum distributions, along $p_{1\parallel} =$

$-p_{2\parallel} + const$ for all gauges and orbital symmetries. These fringes are most pronounced if the molecule is aligned parallel to the laser-field polarization. As the alignment angle increases, it gets washed out by the term (7.23), which, for angle-integrated momenta, is essentially isotropic in the perpendicular momentum plane. Consequently, the peaks of the distributions shift towards higher momenta, and their shapes resemble more and more those obtained for the same type of interaction in the single-atom case. We also found that the prominence of such peaks will depend on the integration over the electron transverse momenta, so that some maxima may be more prominent than others.

Interestingly, we are able to observe changes in the peak momenta of the distributions, as the alignment is varied, even if a single physical mechanism, namely electron-impact ionization, is considered. These changes are caused by the two-centre interference effects. This complements recent results, in which different types of collisions and double-ionization mechanisms are associated with changes in the peaks of NSDI distributions, within the context of molecules [13, 113]. Finally, for laser-field intensities within the tunneling regime, the distributions obtained including only electron-impact ionization are far more localized than those reported experimentally, and the differences between different gauges and orbital symmetries are barely noticeable. In order to assess such effects, it was necessary to consider much higher intensities, for which other physical mechanisms, such as multiple electron recollisions, would also be expected to play a role [113]. These discrepancies may be due to the fact that we are not including the physical mechanism in which the first electron, upon return, promotes the second electron to an excited state, from which it subsequently tunnels out.

Chapter 8

Excitation, Two-centre Interference and the Orbital Geometry in Molecular NSDI

Recently, several studies have found that the core dynamics, in particular excitation, is important for high-harmonic generation in molecules [34, 181, 182]. This may also be true for nonsequential double ionization. Indeed, we have shown in Chapter 6 that, for the RESI mechanism, the shape of the electron momentum distributions depends very strongly on the initial and excited bound states of the second electron [3, 4], in fact far more critically than for electron-impact ionization [74]. If this is the case already for single atoms, one expects this dependence to be even more critical for molecules.

Apart from that, the geometry of the molecular orbitals and the molecular alignment with respect to the laser-field polarization, as discussed in the previous chapter, affect the shapes of the electron momentum distributions in NSDI. In our previous study (Chapter 7 or [2]), however, the geometry of the molecular orbitals involved has been simplified to a great extent. In fact, the HOMO was approximated by a linear combination of $1s$ orbitals. This implies that important features such as the spatial dependence of the orbitals, the presence of nodal planes or s p mixing were ignored.

To some extent, these simplifying assumptions can be made for electron-impact ionization and one may still gain useful information about the molecular structure. For instance, in the previous chapter we addressed the influence of the orbital symmetry and the molecular alignment with respect to the laser-field polarization on NSDI of diatomic molecules for this mechanism. We showed that the electron momentum distribution exhibit interference maxima and minima due to electron emission at spatially

separated centers. Such fringes were positioned at $p_{1||} + p_{2||} = const.$, i.e., parallel to the anti diagonal of the plane spanned by the electron momentum components $p_{n\|}$ parallel to the laser-field polarization. They were sharpest if the molecule was aligned along the direction of the field, i.e., for vanishing alignment angle. As this angle increased, the fringes got increasingly blurred until they were completely washed out for perpendicular alignment.

For RESI we expect a more critical dependence with regard to the geometry of the bound-state wavefunctions, not only because the excitation process strongly depends on them, but also due to the fact that the second electron is reaching the continuum by tunneling. It is by now well known that this ionization mechanism is strongly influenced by the presence of nodal planes or the directionality of a particular molecular orbital. For instance, for HHG the nodal plane of a π state suppresses tunnel ionization when it coincides with the polarization axis [34, 181–184]. Hence, it is not justifiable, not even as a first approximation, to employ linear combinations of $1s$ orbitals.

In this chapter, we perform a systematic analysis of quantum-interference effects in NSDI of diatomic molecules considering the RESI mechanism. We construct a semi-analytical model, in which an electron tunnels from the HOMO of a neutral molecule and rescatters with the HOMO of its singly ionized counterpart. Thereby, the second electron is excited to the lowest unoccupied molecular orbital (LUMO). We investigate the influence of such orbitals and of the alignment angle on the NSDI electron momentum distributions. Specifically we choose species for which these orbitals have different geometries and parities, such as π_g, π_u, σ_g, σ_u. Furthermore, we address the question of whether well-defined interference patterns such as those observed in ATI or HHG computations may also be obtained for NSDI in the context of the RESI mechanism, and, if so, under what conditions. These are complementary studies to those performed in Chapters 5 and 6, where we showed that, for single atoms, the shape of the electron momentum distributions carry information about the bound state from which the second electron leaves and the state to which it is excited.

This chapter is organized as follows. In Section 8.1, we discuss the expression for the specific prefactors for a diatomic molecule using Gaussian orbital basis sets. Furthermore, we derive a general two-centre interference condition for the RESI mechanism (8.2). Subsequently, in section 8.3, we compute electron momentum distributions of Li_2 and N_2 for several molecular alignment angles (8.3.1), and molecular orbitals (8.4). Finally, we state the main conclusions of this chapter (8.5).

8.1 Prefactors

In this work, we assume frozen nuclei and a linear combination of atomic orbitals (LCAO) to construct approximate wave functions for the diatomic molecules. This implies that the molecular bound-state wave function for each electron is given by

$$\psi^{(n)}(\mathbf{r}_n) = \sum_{\alpha,l\alpha} c_\alpha[\phi_\alpha^{(n)}(\mathbf{r}_n + \mathbf{R}/2) + (-1)^{l_\alpha+\lambda_\alpha}\phi_\alpha^{(n)}(\mathbf{r}_n - \mathbf{R}/2)] \tag{8.1}$$

where R and l_α denote the internuclear separation and the orbital quantum numbers, respectively. The index $n = 1, 2$ refers to the electron in question. The index $\lambda_\alpha = 0$ applies to gerade symmetry and $\lambda_\alpha = 1$ to ungerade symmetry. The binding potential of this molecule, as seen by each electron, is given by

$$V_\varkappa(\mathbf{r}_n) = \mathcal{V}_\varkappa(\mathbf{r}_n - \mathbf{R}/2) + \mathcal{V}_\varkappa(\mathbf{r}_n + \mathbf{R}/2) \tag{8.2}$$

where the subscript $\varkappa = 0$ or ion refers either to the neutral molecule or to its ionic counterpart, respectively, and $\mathcal{V}_\varkappa(\mathbf{r}_n) = Z_{eff}/r_n$ is the potential at each centre in the molecule.

In this work, the wave function $\phi_\alpha^{(n)}$ is approximated by a Gaussian basis set,

$$\phi_\alpha^{(n)}(\mathbf{r}_n) = \sum_j b_j^{(n)} x^{l_\alpha} y^{l_\alpha} z^{l_\alpha} \exp[\zeta_j \mathbf{r}^2] \tag{8.3}$$

The coefficients b_j and c_α and the exponents ζ_j can be extracted either from existing literature or from quantum chemistry codes. We compute these coefficients using GAMESS-UK [1]. In our basis set, we take only s and p states. This means that, in all the expressions that follow, l_α and l_β are either 0 or 1.

Based on above-stated assumptions, the RESI prefactors (3.46) and (3.43) will have the following forms

$$\begin{aligned} V_{\mathbf{p}_1 e,\mathbf{k}g} &= \frac{V_{12}(\mathbf{p}_1 - \mathbf{k})}{(2\pi)^{3/2}} \sum_\alpha \sum_\beta [e^{i(\mathbf{p}_1-\mathbf{k})\cdot\mathbf{R}/2} \\ &\quad + (-1)^{l_\alpha+l_\beta+\lambda_\alpha+\lambda_\beta} e^{-i(\mathbf{p}_1-\mathbf{k})\cdot\mathbf{R}/2}]\mathcal{I}_1, \end{aligned} \tag{8.4}$$

where

$$\mathcal{I}_1 = \int d^3r_2 e^{-i(\mathbf{p}_1-\mathbf{k})\cdot\mathbf{r}_2}\phi_\alpha^{(2)}(\mathbf{r}_2)^*\phi_\beta^{(2)}(\mathbf{r}_2) \tag{8.5}$$

and

$$V_{\mathbf{p}_2 e} = \frac{4\pi}{(2\pi)^{3/2}}\sum_\alpha \left[e^{i\tilde{\mathbf{p}}_2\cdot\mathbf{R}/2} + (-1)^{l_\alpha+\lambda_\alpha}e^{-i\tilde{\mathbf{p}}_2\cdot\mathbf{R}/2}\right]\mathcal{I}_2, \tag{8.6}$$

where

$$\mathcal{I}_2 = \int d^3r_2 \mathcal{V}_0(\mathbf{r}_2)e^{-i\tilde{\mathbf{p}}_2\cdot\mathbf{r}_2}\phi_\alpha^{(2)}(\mathbf{r}_2). \tag{8.7}$$

In general, the form factor (3.44) does not affect the shape of the electron-momentum distributions. This is particularly true when the first electron tunnels from an orbital with no nodal planes, such as a σ_g orbital [2]. However, one has to be careful when the electron tunnels from any orbital with at least one nodal plane, such as a π orbital, as this would lead to a suppression of ionization for specific alignment angles.

In the following, we will rewrite the above equations in terms of the electron-momentum components $p_{n\parallel}$ and $\mathbf{p}_{n\perp}$ parallel and perpendicular to the laser-field polarization. Physically, we are dealing with a diatomic molecule whose main axis is rotated by an angle θ with respect to the direction of the laser-field polarization. Hence, we are dealing with two frames of references, i.e., the molecular frame of reference and the laser field frame of reference. The electron momenta in terms of their parallel and perpendicular components with regard to the laser-field polarization read

$$\mathbf{p}_n = p_{n||}\hat{e}_{z'} + p_{n\perp}\cos\varphi\hat{e}_{x'} + p_{n\perp}\sin\varphi\hat{e}_{y'}, \tag{8.8}$$

where we assumed that the laser field is polarized along the z' axis, the coordinates x' and y' define the plane perpendicular to the laser-field polarization and φ is the azimuthal angle. In order, however, to compute the momentum-space wavefunctions for this molecule, we need the momentum coordinates in the frame of reference of the molecule. The molecular coordinates x, y and z can be obtained by a coordinate rotation around the x axis. In this case, the momenta of the electrons in terms of the parallel and perpendicular components in this latter frame of reference will be

$$\begin{aligned}\mathbf{p}_n &= (p_{n||}\cos\theta + p_{n\perp}\sin\theta\sin\varphi)\hat{e}_z + p_{n\perp}\cos\varphi\hat{e}_x \\ &\quad + (p_{n\perp}\cos\theta\sin\varphi - p_{n||}\sin\theta)\hat{e}_y.\end{aligned} \tag{8.9}$$

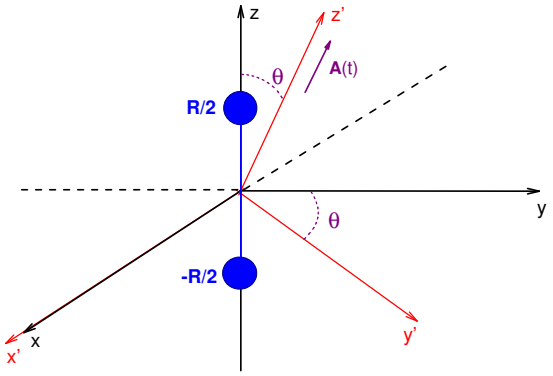

FIGURE 8.1: Schematic representation of the molecule and laser field frames of reference, represented by the black and red sets of axis x, y, z and x', y', z' respectively. The two centers of the molecule are separated by R along the z axis of the molecule, and their positions are indicated by the blue circles in the figure. The field $\mathbf{A}(t)$ is polarized along the z' axis, and θ shows the alignment angle of the molecule with respect to the laser field.

This implies that the momentum components p_{nx}, p_{ny} and p_{nz} are defined by equation (8.9) and that

$$\mathbf{p}_n \cdot \mathbf{R}/2 = (p_{n||} \cos\theta + p_{n\perp} \sin\theta \sin\varphi)R/2. \tag{8.10}$$

A schematic representation of both the field molecular sets of coordinates is presented in figure (8.1). Below, we provide the explicit expressions for the integrals $\mathcal{I}_n (n = 1, 2)$ in the prefactors (8.4) and (8.6), for the specific types of orbitals employed in this work.

8.1.1 Excitation $\sigma \to \sigma$

If the second electron is excited from a σ to a σ orbital, both integrals will have the forms

$$\begin{aligned} \mathcal{I}_1 &= \sum_{j,j'} \frac{b_j^{(1)} b_{j'}^{(1)} \pi^{3/2} (-i)^{l_\alpha + l_\beta}}{2^{l_\alpha + l_\beta} (\zeta_j + \zeta_{j'})^{3/2 + l_\alpha + l_\beta}} \\ &\quad \times \exp[-\frac{(\mathbf{p}_1 - \mathbf{k})^2}{4(\zeta_j + \zeta_{j'})}] . \Upsilon(l_\alpha, l_\beta) \end{aligned} \tag{8.11}$$

where

$$\Upsilon(l_\alpha, l_\beta) = \begin{cases} 1, & l_\alpha + l_\beta = 0 \\ (\mathbf{p}_1 - \mathbf{k})_z, & l_\alpha + l_\beta = 1 \\ 2(\zeta_j + \zeta_{j'}) - (\mathbf{p}_1 - \mathbf{k})_z, & l_\alpha + l_\beta = 2 \end{cases}, \tag{8.12}$$

and

$$\mathcal{I}_2 = \sum_{,j'} b_{j'}^{(2)} (-i)^{l_\beta} G(l_\beta), \tag{8.13}$$

where

$$G(l_\beta) = \begin{cases} 2\sqrt{\pi} I_r^{(l_\alpha=0)}, l_\beta = 0 \\ (\tilde{p}_{2z}/p_2)\, I_r^{(l_\alpha=1)}, l_\beta = 1. \end{cases} \tag{8.14}$$

In equation (8.14), $I_r^{(l_\alpha=0)}$ and $I_r^{(l_\alpha=1)}$ indicate the radial integrals

$$I_r^{(l_\alpha)} = \int_0^\infty r^{l_\beta+1} j_{l_\beta}(\tilde{p}_2 r) \exp[-\zeta_j r^2] dr. \tag{8.15}$$

8.1.2 Excitation $\sigma \to \pi$

We also consider that the second electron is excited to either a π_u or a π_g orbital. In this case, since these orbitals are degenerate, one must consider a coherent superposition of the π_x and π_y orbitals. This gives

$$\begin{aligned} \mathcal{I}_1 = \sum_{j,j'} b_j^{(1)} b_{j'}^{(1)} \pi^{3/2} \Big[(-i(\mathbf{p}_1 - \mathbf{k})_y)^{l_\beta} + (-i(\mathbf{p}_1 - \mathbf{k})_x)^{l_\beta} \Big] \\ \frac{(-i(\mathbf{p}_1 - \mathbf{k})_z)^{l_\alpha}}{2^{l_\alpha+l_\beta} (\zeta_j + \zeta_{j'})^{3/2+l_\alpha+l_\beta}} \exp[-\frac{(\mathbf{p}_1 - \mathbf{k})^2}{4(\zeta_j + \zeta_{j'})}]. \end{aligned} \tag{8.16}$$

One should note that, if the electron is excited from a π to a σ orbital, $\mathcal{I}_1$ will also have this form. In the second prefactor,

$$\mathcal{I}_2 = \sum_{,j'} b_{j'}^{(2)} (-i)^{l_\beta} \left[\frac{(\tilde{\mathbf{p}}_{2y})^{l_\beta} + (\tilde{\mathbf{p}}_{2x})^{l_\beta}}{\tilde{p}_2} \right] I_r^{(l_\beta)}, \tag{8.17}$$

with $l_\beta = 1$.Throughout, $(\mathbf{p}_1 - \mathbf{k})_\varkappa$, with $\varkappa = x, y, z$ are defined according to equation (8.9).

8.2 Interference Condition

Here, we provide a general interference condition, which takes into account the structure of the orbitals. This includes $s-$ and p mixing and the orbital parity. The expressions

that follow are easily derived if the exponentials in equations (8.4) and (8.6) are expanded in terms of trigonometric functions. In this case, the prefactor (8.4) can be written as

$$V_{\mathbf{p}_1 e,\mathbf{k}g} = \frac{V_{12}(\mathbf{p}_1 - \mathbf{k})}{(2\pi)^{3/2}} \sum_{\alpha} \sum_{\beta} \sqrt{C_+^2 - C_-^2}\, \sin[\xi_1 + (\mathbf{p}_1 - \mathbf{k}) \cdot \mathbf{R}/2]\mathcal{I}_1, \tag{8.18}$$

with

$$\xi_1 = \arctan[\frac{-iC_+}{C_-}] \tag{8.19}$$

and

$$C_\pm = 1 \pm (-1)^{l_\alpha + l_\beta + \lambda_\alpha + \lambda_\beta}. \tag{8.20}$$

A similar procedure for high-order harmonic generation has been adopted in [183]. Interference minima are present if

$$\xi_1 + (\mathbf{p}_1 - \mathbf{k}) \cdot \mathbf{R}/2 = m\pi \tag{8.21}$$

where m is an integer. Similarly, interference maxima are obtained for

$$\xi_1 + (\mathbf{p}_1 - \mathbf{k}) \cdot \mathbf{R}/2 = (2m+1)\pi/2. \tag{8.22}$$

We will focus on the minima given by equation (8.21) as they are much easier to observe. If this equation is written in terms of the electron momentum component $(\mathbf{p}_1 - \mathbf{k})_z$ parallel to the molecular axis, we find

$$\left[(p_{1||} - k)\cos\theta + p_{1\perp}\sin\theta\sin\varphi\right] R/2 = m\pi - \xi_1. \tag{8.23}$$

The above equation shows that the parallel momentum component $p_{1||}$ will lead to well-defined interference fringes approximately at

$$p_{1||} = \frac{2(m\pi - \xi_1)}{R\cos\theta} + k. \tag{8.24}$$

This means that, in the $p_{1||}p_{2||}$ plane, these minima will be at $p_{1||} = const.$, i.e., parallel to the $p_{1||}$ axis. When the azimuthal angle is integrated over, the perpendicular component $p_{1\perp}$ will mainly cause a blurring in such fringes. Extreme limits will be found for the alignment angle $\theta = 0$, with sharp, two-centre patterns, and $\theta = 90°$, when they get washed out.

Following the same line of argument,

$$V_{\mathbf{p}_2 e} = \frac{4\pi}{(2\pi)^{3/2}} \sum_{\alpha} \sqrt{D_+^2 - D_-^2}\, \sin[\xi_2 + \tilde{\mathbf{p}}_2 \cdot \mathbf{R}] \mathcal{I}_2 \tag{8.25}$$

with

$$\xi_2 = \arctan[\frac{-iD_+}{D_-}] \tag{8.26}$$

and

$$D_\pm = 1 \pm (-1)^{l_\beta + \lambda_\beta} \quad . \tag{8.27}$$

Interference minima are present for (8.6) if

$$\xi_2 + \tilde{\mathbf{p}}_2 \cdot \mathbf{R} = m\pi. \tag{8.28}$$

Likewise, there will be interference fringes for

$$\tilde{p}_{2||} = \frac{2(m\pi - \xi_2)}{R\cos\theta}, \tag{8.29}$$

i.e., parallel to the $p_{2||}$ axis in the plane spanned by the parallel momentum components $p_{1||}, p_{2||}$. In the velocity and the length gauges, $\tilde{p}_{2||} = p_{2||}$ and $p_{2||} + A(t)$, respectively. Since, however, $A(t) \simeq 0$ for the electron tunneling time, in practice there will be very little difference. The perpendicular momentum components will lead to a blurring in the fringes.

8.3 Results

Following the same line of argument as in section (3.3.3), we compute electron momentum distributions, as functions of the momentum components $(p_{1\|}, p_{2\|})$ parallel to the laser-field polarization.

In the following, we compute electron momentum distributions for Li_2 and N_2. We assume that the first electron leaves from the neutral species and rescatters with the singly ionized molecule, i.e., Li_2^+ or N_2^+, respectively. For all cases, we assume that the electron-electron interaction is of contact type, i.e., $V_{12} = \delta(\mathbf{r}_1 - \mathbf{r}_2)$. This will avoid a further momentum bias in the electron-electron distributions as it leads to $V_{12}(\mathbf{p}_1 - \mathbf{k}) = const$ and allow us to investigate the influence of the target structure alone. For a long-range potential, $V_{12}(\mathbf{p}_1 - \mathbf{k})$ would be momentum dependent.

8.3.1 Interference Effects and the Influence of $s-$ and $p-$ Mixing

We will commence by investigating whether the interference conditions derived in section (8.2) hold. For that purpose, we must have non-negligible tunneling ionization for parallel-aligned molecules, as this is the situation for which the fringes are expected to be sharpest. Hence, one must consider a target for which neither HOMO nor the LUMO exhibits nodal planes along the internuclear axis. Therefore, we assume that the first electron rescatters inelastically with Li_2^+, exciting the second electron from its HOMO ($2\sigma_g$) to its LUMO ($2\sigma_u$). In order to get a clear picture of conditions (8.21) and (8.28), we must investigate the corresponding prefactors individually.

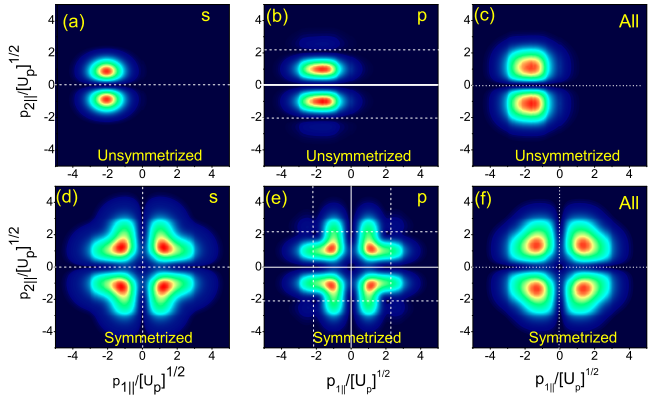

FIGURE 8.2: Electron-momentum distributions for NSDI in Li_2 ($E_{1g} = 0.18092040$ a.u.,$E_{2g} = 0.43944428$ a.u. and $E_{2e} = 0.12481836$ a.u.) considering only the RESI mechanism, as functions of the momentum components parallel to the laser-field polarization, obtained considering $V_{\mathbf{p}_2 e}$ according to equation (3.43) and $V_{\mathbf{p}_1 e,\mathbf{k}g} = const.$ We consider zero alignment angle, driving-field intensity $I = 4.6 \times 10^{13}$ W/cm^2 and $\omega = 0.057$ a.u. respectively. Panels (a) to (c) display only the contribution from the orbits starting in the first half cycle of the field, while in panels (d) to (f) the distributions have been symmetrized to account for the electron orbits starting in the other half cycle and for electron indistinguishability. The left, middle and right panels correspond to the contributions of the s, p and all states used in the construction of the σ_u LUMO, respectively. The solid, dashed and short dashed lines show the position of minima due to the two centre interferences, node of the wavefunction and mixed cases, respectively. The contour plots have been normalized to the maximum probability in each panel.

In figure 8.2, we depict the above-mentioned electron-momentum distributions for the alignment angle $\theta = 0$. We consider $V_{\mathbf{p}_1 e,\mathbf{k}g} = const.$ and focus on the influence of $V_{\mathbf{p}_2 e}$ alone. We take either the individual contributions of s and p states or the combination of both for $2\sigma_u$. For clarity, in the upper panels, we also exhibit the distributions obtained without symmetrizing with respect to the momentum exchange and electron start times. For all cases, the two-centre fringes in figure 8.2 are parallel to $p_{2||} = const.$, in agreement with the second interference condition derived in section 8.2.

For pure s or p states and $\lambda_\alpha = 1$, which is the case for a σ_u orbital, this condition can be further simplified. It reduces to

$$\sin[\tilde{\mathbf{p}}_2 \cdot \mathbf{R}/2] = 0, \tag{8.30}$$

for s states, and

$$\cos[\tilde{\mathbf{p}}_2 \cdot \mathbf{R}/2] = 0 \tag{8.31}$$

for p states. This implies that, for the former, we expect minima at $\tilde{\mathbf{p}}_2 \cdot \mathbf{R} = 2m\pi$, while for the latter they should occur at $\tilde{\mathbf{p}}_2 \cdot \mathbf{R} = (2m+1)\pi$. The position of such minima can also be determined analytically by considering that the second electron tunnels at the peak of the laser field, i.e., at $= \omega\pi/2$. The dashed lines in the figure show that the position of these minima exhibit a very good agreement with this simple estimate. Physically, this good agreement may be attributed to the fact that the second electron tunnels most probably at this time.

For the s states the two-centre interference gives a sharp minimum at $p_{2\parallel} = 0$ (figure 8.2 (a) and (d)), while for the p states these patterns are located near $p_{2\parallel} = \pm 3\sqrt{U_p}$ (figure 8.2 (b) and (e)). In the $p-$state case the distribution has another minimum at $p_{2\parallel} = 0$, which comes from the fact the p wavefunctions have a node at vanishing momentum. This causes a suppression in the transition amplitude. If the contributions of both s and p states are considered, the minima in the high-momentum region due to the two-centre interference seen for the p states vanish, but the minimum at $p_{2\parallel} = 0$ survives. This is shown in figure 8.2.(c) and (f) for unsymmetrized and symmetrized distributions, respectively.

One should note, however, that for parallel-aligned molecules, both the two-centre minimum for the s states and the minimum caused by the node in the p states occur at the same momentum, i.e., at $p_{2\parallel} = 0$. Hence, when s p mixing is included both mechanisms contribute to the suppression at the axes $p_{n\parallel} = 0$ seen in figures 8.2.(c) and (f). We will now investigate the behavior of this node when the alignment angle is varied. Since for Li_2 both the LUMO and the HOMO exhibit distinct shapes and symmetries one can expect significant changes in the electron-momentum distributions when this parameter is modified.

Hence, in figure 8.3, we consider the same prefactors as in the previous case, but alignment angles $\theta = 45^0$ and 90^0. The figure shows that the patterns caused by the electron emission at spatially separated centres gets washed out for such angles. This is due to the momentum components perpendicular to the laser-field polarization, and can be

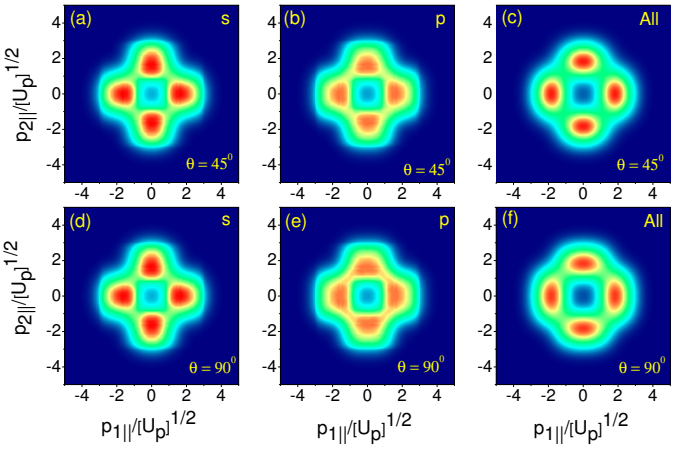

FIGURE 8.3: Electron-momentum distributions for RESI in Li_2 as functions of the electron momentum components parallel to the laser-field polarization considering $V_{\mathbf{p}_1 e,\mathbf{k}g} = const$ and $V_{\mathbf{p}_2 e}$ according to equation (3.43), for alignment angles $\theta = 45^0$ (panels (a) to (c)), and 90^0 (panels (d) to (f)). The remaining parameters are the same as in the previous figures. The solid lines show the position of minima due to the node of the one-centre wavefunction. From left to right, we considered the contributions of the s, p and all states used in the construction of the LUMO. All panels have been symmetrized with regard to the electron orbits and indistinguishability. The contour plots have been normalized to the maximum probability in each panel.

seen very clearly in figure 8.3, where the s contributions are displayed for $\theta = 45°$. Already for this angle the interference minima at the axes $p_{\parallel} = 0$ are absent. The minima caused by the node of the p wavefunctions also vanish, as shown in Fig. 8.3.(b). This is caused by the fact that, in momentum space, these wavefunctions are proportional to $G(l_\beta = 1)$ (see equation (8.14)). This function contains components of $\mathbf{p}_2$ both parallel and perpendicular to the laser field polarization, and the contributions from the latter wash out the minimum. Obviously, this situation persists when s p mixing is included (see figure 8.3.(c)).

For $\theta = 90°$, only the components $p_{2\perp}$ contribute, and the electron momentum distributions are determined by the momentum-space integration alone. As a result, they reflect the momentum-space constraints for the RESI mechanism. These constraints lead to electron momentum distributions peaked at $(p_{i\parallel}, p_{j\parallel}) = (\pm 2\sqrt{U_p}, 0)$, with $i, j = 1, 2$ and $i \neq j$ and with widths $2\sqrt{U_p}$, and have been explicitly written in [3, 4]. This holds both for the s, p and mixed case (Figs. 8.3.(d), (e) and (f), respectively).

We will now focus on the interference condition determined by the excitation prefactor (3.44). With this objective, we will keep $V_{\mathbf{p}_2 e} = const.$ and investigate the influence of $V_{\mathbf{p}_1 e,\mathbf{k}g}$ alone, starting from vanishing alignment angle. Once more, we will study

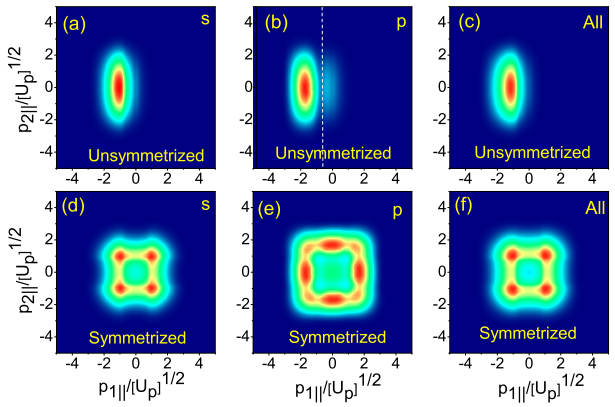

FIGURE 8.4: RESI electron-momentum distributions for Li_2 considering $V_{\mathbf{p}_2 e} = const.$ and $V_{\mathbf{p}_1 e, \mathbf{k} g}$ according to equation (8.4), for $\theta = 0$. The field and molecular parameters are the same as in the previous figure. The upper panels display only the contribution from the sets of orbits starting in the first half cycle of the laser field. In the lower panels the distributions have been symmetrized in order to account for the orbits starting in the other half cycle of the field, and for electron indistinguishability. The left, middle and right panels display the contributions from s, p and all states composing the HOMO and the LUMO, respectively. The dashed line shows the position of the two-centre interference minimum. The contour plots have been normalized to the maximum probability in each panel.

the contributions of the s and p states, and the overall distributions. The interference condition and also the wavefunctions in the excitation prefactor now incorporate the HOMO and the LUMO (see equation (3.44)). For Li_2^+, the former and the latter are a gerade and an ungerade orbital, so that $\lambda_\alpha = 0$ and $\lambda_\beta = 1$ in equation(8.21). For a pure s states, $l_\alpha = l_\beta = 0$ and for a pure p states, $l_\alpha = l_\beta = 1$. This will lead to the simplified interference condition

$$\sin[(\mathbf{p}_1 - \mathbf{k}) \cdot \mathbf{R}/2] = 0 \tag{8.32}$$

for both. Hence, one expects a minimum close to vanishing parallel momenta in the pure cases. When s p mixing is included, however, different angular momenta will also be coupled and the general interference condition must be considered.

The electron momentum distributions obtained in this way are shown in figure 8.4, for both symmetrized and unsymmetrized distributions (upper and lower panels, respectively). For most distributions in the figure, we do not observe clear minima. This holds both for those caused by the two centre interference and by the node of the wavefunctions at the ions. We only observe a two centre minimum if we consider the individual contributions of the p states, and do not symmetrize the distributions (see figure 8.4.(b)). This is due to the fact that, for the parameters considered in this work, the two-centre

minimum according to condition (8.24) lies at or beyond the boundary of the momentum region for which rescattering of the first electron has a classical counterpart. The centre of this region is roughly at $p_{1||} \simeq 2\sqrt{U_p}$ and its extension is determined by the difference between the maximal electron kinetic energy upon return and the excitation energy $E_{2g} - E_{2e}$, as discussed in Chapter 6.

Apart from that, s p mixing will lead to a blurring of this minimum, as it couples states with different angular momenta. Symmetrization introduces other events, either due to the electron indistinguishability or displaced by half a cycle, and obscures this minimum further, as shown in the lower panels of the figure.

$$\cos[(\mathbf{p}_1 - \mathbf{k}) \cdot \mathbf{R}/2] = 0. \tag{8.33}$$

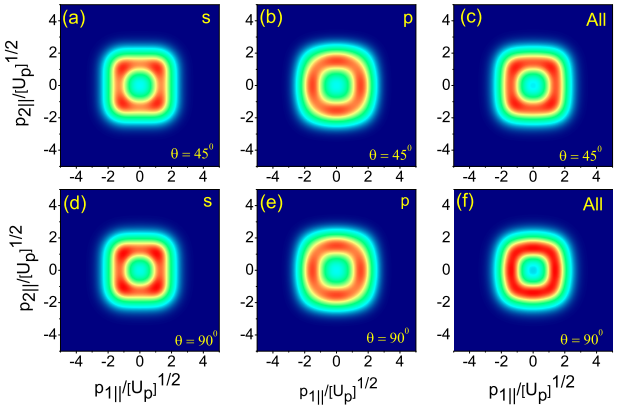

FIGURE 8.5: Electron-momentum distributions for RESI in Li_2 as functions of the electron-momentum components parallel to the laser-field polarization considering $V_{\mathbf{p}_2 e} = const.$ and $V_{\mathbf{p}_1 e, \mathbf{k}g}$ according to equation (8.4), for alignment angles $\theta = 45^0$ and 90^0 (upper and lower panels, respectively). All distributions have been symmetrized to account for the orbits starting in the other half cycle of the field, and for electron indistinguishability. The left, middle and right panels display the contributions from s, p and all states composing the HOMO and the LUMO, respectively. The contour plots have been normalized to the maximum probability in each panel.

If the alignment angle is varied, incorporating only the excitation prefactor $V_{\mathbf{p}_1 e, \mathbf{k}g}$ will lead to ring-shaped distributions. This can be observed in all panels of figure 8.5, regardless of whether only p, s or all basis states employed in the construction of the HOMO and LUMO are taken. This behavior may be attributed to the fact that the explicit expression for the prefactor $V_{\mathbf{p}_1 e, \mathbf{k}g}$ incorporates both the HOMO and the LUMO. Hence, upon integration over the transverse momenta, the wavefunction-specific features gets was out.

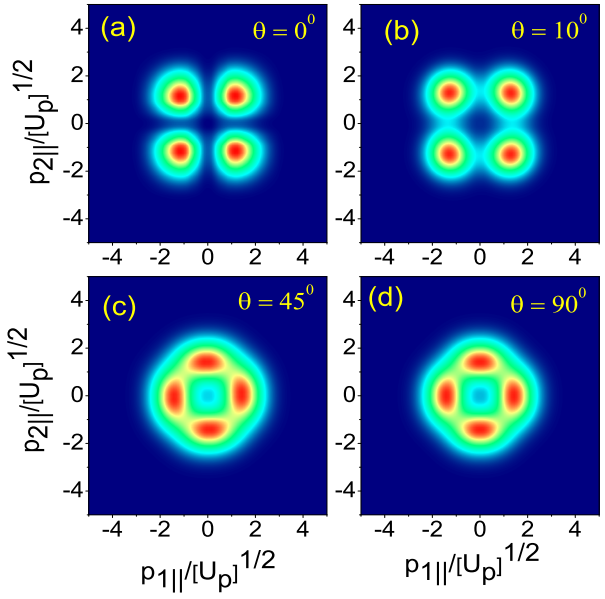

FIGURE 8.6: Electron-momentum distributions for Li_2 as functions of the parallel momenta $(p_{1\parallel}, p_{2\parallel})$ considering all prefactors, for different alignment angles. Panel (a), (b),(c) and (e) correspond the alignment angle θ= 0, 10, 45 and 90 degrees, respectively. The contour plots have been normalized to the maximum probability in each panel, and the field and molecular parameters are the same as in the previous figures.

In figure 8.6, we incorporate both prefactors $V_{\mathbf{p}_2 e}$ and $V_{\mathbf{p}_1 e,\mathbf{k}g}$ and vary the alignment angle. The main conclusion to be drawn from the figure is that the prefactor $V_{\mathbf{p}_2 e}$ plays the dominant role in determining the shapes of the electron momentum distributions. This can be observed by a direct comparison of figure 8.6.(a) with figure 8.2.(f), for vanishing alignment angle. The distributions in both figures exhibit similar shapes and minima at the axes $p_{n||} = 0$, and are very different from those obtained if only the recollision-excitation prefactor is included (see figure 8.4(f)). The main effect of the excitation prefactor $V_{\mathbf{p}_1 e,\mathbf{k}g}$ is to alter the widths of the distributions. This situation persists for larger angles, such as $\theta = 45°$ and $\theta = 90°$, as a comparison of figure 8.6.(c) and (d), with figure 8.3.(c) and (f) shows. In all such figures, the nodes at the axis determined by the two-centre interference minima are washed out. In this context, one should notice that the two-centre interference effects are already much less prominent for an alignment angle as small as $\theta = 10°$. This is explicitly shown in figure 8.6.(b).

8.4 Molecular Orbital Signature

In the previous section, we dealt exclusively with σ orbitals. Spatially, such orbitals are localized along the internuclear axis, and do not exhibit nodal planes for vanishing

alignment angle. A legitimate question is, however, how the shape of the molecular orbital to which the second electron is excited is imprinted on the electron momentum distributions. From other strong-field phenomena, it is well-known that the presence of nodal planes may suppress the yield considerably [182, 183].

For that reason, we will now compute electron momentum distributions for N_2. The first electron will be ripped out from the HOMO, which is also $3\sigma_g$ orbital. However, upon return, it will excite the second electron to the LUMO, which is a π_g orbital. A π_g orbital has gerade symmetry and exhibits two nodal planes, which will be oriented along the laser-field polarization for parallel and perpendicular-aligned molecules.

Figure 8.7 shows electron momentum distributions for N_2 for alignment angles of zero and 90 degrees. Here, both prefactors $V_{\mathbf{p}_2 e}$ and $V_{\mathbf{p}_1 e,\mathbf{k}g}$ are incorporated in the computation. As was discussed in the previous section, one could expect sharp two-centre interference minima along the axes $p_{n||} = 0$ for zero alignment angle. This is confirmed by figure 8.7(a), which shows a clear minima along the axes $p_{n||} = 0$, similar to Li_2 (figure 8.6(a)). In comparison to figure 8.6(a), however, these minima are wider. This is very likely due to the fact that the nodal plane parallel to the internuclear axis also contributes to the emergence of these minima. Figure 8.6(b), for alignment angle $\theta = 90°$, confirms that the nodal planes of the π_g wavefunction leave a strong imprint in the RESI distributions. In the figure, the suppression along the axis $p_{n||} = 0$ can only be attributed to the nodal plane perpendicular to internuclear axis. In fact, from the interference conditions derived in section 8.3.1 and the results obtained in the previous chapter we expect the interference patterns due to the electron emission at specially separated centres to wash out completely for an alignment angle of $\theta = 90°$. Therefore, the minima present in figure 8.7(b) come from nodes of the π_g wavefunction.

The computations in chapter show that the electron momentum distributions of N_2 and Li_2 will have different shapes as we vary the molecular alignment angle with respect to the laser polarization direction. Thus RESI can be used a powerful tool to probe the molecular orbitals of the target.

8.5 Conclusions and Outlook

In this chapter we address the influence of the molecular orbital geometry and of the molecular alignment with respect to the laser-field polarization on laser-induced nonsequential double ionization of N_2 and Li_2. We focus on the recollision excitation with subsequent tunneling ionization (RESI) mechanism, in which the first electron, upon return, promotes the second electron to an excited state, from where it subsequently

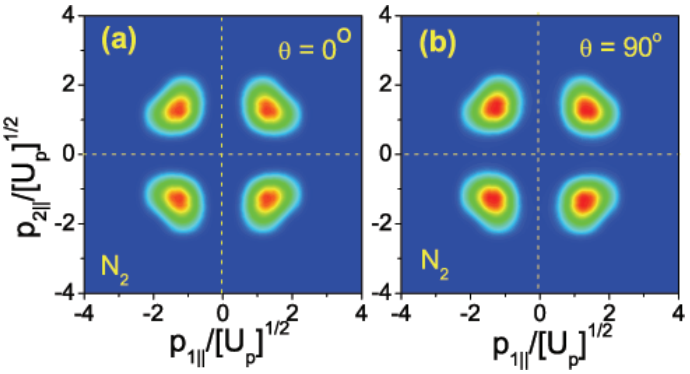

FIGURE 8.7: Electron-momentum distributions for N_2 (E_{1g} = 0.63485797 a.u., E_{2g} = 1.12657012 a.u. and E_{2e} = 0.26871290 a.u.) as functions of the parallel momenta $(p_{1\parallel}, p_{2\parallel})$ considering all prefactors, for alignment angles θ= 0 and 90, panel (a) and (b), respectively. We consider a driving-field intensity $I = 1.25 \times 10^{14}$ W/cm^2 and ω = 0.057 a.u. The contour plots have been normalized to the maximum probability in each panel.

tunnels. We assumed the nuclei to be frozen and constructed the molecular wave function using Gaussian basis sets within the LCAO approximation.

In Li_2, for zero alignment angle the influence of $V_{\mathbf{p}_2 e}$ alone gives sharp minima at $p_{n\parallel} = 0$ due to the electron emission at spatially separated centre and node of the p state. These patterns disappear for alignment angle $\theta = 45°$ and 90°. On the other hand, by considering only the influence of $V_{\mathbf{p}_1 e,\mathbf{k}g}$ we almost do not observe any minima for zero alignment. This is due to the fact that, for the parameters considered in this work, the two-centre minimum according to condition (8.24) lies at or beyond the boundary of the momentum region for which rescattering of the first electron has a classical counterpart. In this case, by varying the alignment angle we will get ring-shaped distributions.

By incorporating both prefactors $V_{\mathbf{p}_2 e}$ and $V_{\mathbf{p}_1 e,\mathbf{k}g}$, the minima at $p_{n\parallel} = 0$ survive for zero alignment angle. This indicates that the prefactor $V_{\mathbf{p}_2 e}$ plays the dominant role in determining the shapes of the electron momentum distributions. This conclusion become more solid if we compare figure 8.6.(a) with figure 8.2.(f), for vanishing alignment angle. Furthermore, the computations show that the excitation prefactor $V_{\mathbf{p}_1 e,\mathbf{k}g}$ just alters the widths of the distributions. The patterns caused by the two-centre interference get washed out as the alignment angle varies. They become less defined for an alignment angle as small as $\theta = 10°$.

For zero alignment angle, the electron momentum distributions of N_2 shows a sharp minima around $p_{n\parallel} = 0$ due to the electron emission at specially separated centers and nodes of the wave function. In contrast to Li_2, minima survive even when molecule is aligned perpendicular to the laser field polarization direction. It is clear that at $\theta = 90°$ the nodal plane of the wave function are responsible for occurring of these patterns.

The computation of RESI for N_2 and Li_2 show that the molecular orbital signature is embedded in the the electron momentum distributions and it is reveal itself as we vary the alignment angle. Furthermore, it indicates that the RESI can be an appropriate tool for retrieving information about the molecular structure.

In order to understand the role of nodal plane in the electron momentum distributions, one needs to investigate the N_2 at various angles such as $\theta = 30°$, $45°$ and $60°$. In addition, It would be very useful if one studies the electron momentum distributions of Li_2 under the assumption that the second electron is excited to a π_u orbital, which is the second lowest unoccupied orbital in Li_2^+. This orbital has ungerade symmetry and exhibits a single nodal plane at the internuclear axis, which will be parallel to the laser-field polarization for vanishing alignment angle. This single nodal plane will give a more complete picture about the influence of the wavefunction structure on the electron-momentum distributions. The above-mentioned investigations, for a wide range of alignment angles are currently being performed by us.

Chapter 9

Beyond the Strong-field Approximation: a Coulomb-corrected S-Matrix Approach for Direct Above-threshold Ionization

Since the early days of strong-field laser physics, the strong-field approximation has been applied to a wide range of phenomena, such as above threshold ionization, high order harmonic generation and laser-induced nonsequential double ionization. The strong-field approximation is a very powerful approach, and has played a major role in the quantum mechanical description of strong-field phenomena such as laser-induced rescattering or recombination processes between an electron and its parent ion. It was decisive in explaining a multitude of features in strong-field phenomena, such as the plateau and the cutoff for HHG and ATI [159, 162] and "the knee" in the NSDI yield [152], and hence helped establish many of the current paradigms in this field. This was made possible due to the very clear physical interpretation provided by this approach, as discussed in Chapter 2 and 3.

The SFA, however, suffers from several drawbacks:

- *The strong-field approximation neglects the Coulomb potential when the electron propagate in the continuum, approximating the continuum states by field-dressed plane waves, i.e., Volkov states [147].* This means that, physically, effects such as Coulomb focusing are not incorporated. This implies that the spread of the

returning electronic wavepacket is overestimated in the SFA [185]. Apart from that, it has been recently shown that, within the SFA, field-dressed momentum conservation leads to the neglect of several types of electron trajectories, which are important, for instance, for describing the recently observed energy structure in ATI [80]. In addition, this approximation fails to describe symmetry breaking in photoelectron spectra. For instant, if one place the detectors along the polarization of the laser field, then the left and the right detectors observe different numbers of electrons (more detail can be found in reference [94]).

- *The strong-field approximation is not gauge invariant.* This drawback appears as a consequence of the fact that the series 3.7 and 3.9 are mixed (see, e.g., [186] for a discussion of this issue), and is particularly problematic for extended systems such as molecules. In this latter case, the interference patterns due to the high-order harmonic or photoelectron emission at spatially separated centers are strongly influenced by the choice of gauge. For a detailed discussion of the gauge influence on the interference patterns of HHG in diatomic molecule see, e.g., [180, 187].

- *In the strong-field approximation, the continuum and the bound states are not orthogonal.* This is a further consequence of approximating the continuum by Volkov waves. This lack of orthogonality leads to artifacts which mask the above-mentioned interference patterns for HHG in molecules. It also causes problems as far as the translational invariance of SFA transition amplitudes are concerned [170].

- *There are no clear convergence criteria for the strong-field approximation.* When iterating the Dyson equation and constructing a perturbative series around either the laser field or the binding potential, one may establish clear convergence criteria for both. In the strong-field approximation, however, as, formally, these series are mixed, the convergence criteria are not clear.

- *The strong-field approximation does not account for the distortions caused by the field on the bound states.* This is particularly problematic for highly lying states, or for electron start times close to the field peak. For instance, in Chapter 6 it was argued that this may lead to the lack of agreement between the experimental results of NSDI of argon and the SFA computations.

To develop, however, a semi-analytic approach which goes beyond the strong-field approximation is a highly demanding task, and, up to the present time, only two research groups worldwide have succeeded in tackling this challenge (O. Smirnova and her co-workers [94, 95, 188] and D. Bauer and his co-workers [149, 189]). This is discussed in more details in section 9.3.

The approach discussed in this chapter is being developed with the subsequent intention of being applied to RESI. Since this mechanism is related to electron-electron correlation near the ionization threshold, and also to excitation, we expect the interplay between the Coulomb potential and the laser field to play a significant role.

As was shown in the previous chapters, the RESI mechanism may be understood as two subsequent ATI-like processes:

1. A rescattered ATI-like process for the first electron
2. Direct above-threshold ionization for the tunnel ionization of the second electron.

A realistic strategy to follow would be first to implement the Coulomb correction on the simplest processes in RESI (direct ATI), and then deal with the more complicated process (rescattered ATI).

In this chapter, the influence of the Coulomb potential on direct ATI is investigated. The Coulomb potential's influence is incorporated in a semi-analytical approach, which is constructed around the strong-field approximation. The main assumptions involved in this approach are discussed in section 9.1. In this Section, we also show that they lead to an ATI transition amplitude very similar to that found in [94, 188]. Subsequently, in section 9.2, we discuss the saddle-point equations obtained from that expression, with emphasis on the effects of the Coulomb potential on the electron motion in the continuum, and on the phase shifts introduced by the Coulomb continuum states at the instant of ionization and when the electron reaches the detector. The relation between the saddle-point equations and the classical equations of motion of an electron is addressed in section 9.3. This discussion is followed by a brief analysis of how to treat the tunnel ionization process (section 9.4). This should include an adequate choice for the initial momenta and the tunnel exit, i.e., the point in space for which the electron reaches the continuum. Finally, in section 9.5, we close the chapter by discussing our preliminary results and conclusions on this topic, and what should be next steps in order to bring about the full implementation of the Coulomb-corrected approach developed in this chapter.

9.1 Coulomb-corrected Transition Amplitude

In this section, the residual binding potential is incorporated in a semi-analytic, S-matrix model for the specific case of direct ATI. In this work, one of the main assumption of the strong-field approximation is still maintained. In this approximation, the laser

field interaction with an atom is neglected when the electrons are bound to atoms or molecules. In direct above-threshold ionization, at the time t', an electron leaves the atom from a bound state $|\varphi_b(t')\rangle$ and reaches the detector without scattering with a final state of $|q\rangle$.

By using the S-matrix (3.14), the transition amplitude of the system becomes

$$c_q(t) = -i \int_{-\infty}^{t} dt' \, \langle q| \, U(t,t') H_I(t') \left|\varphi_b(t')\right\rangle . \tag{9.1}$$

This is the well-know expression for the direct ATI transition amplitude, where H_I is the interaction of the atom with the laser field, and $U(t,t')$ the time evolution operator related to the full Hamiltonian of the system.

On cannot exactly solve equation (9.1) because the full time evolution operator cannot be computed exactly. However, this operator can be approximated in a way such that the computations can be simplified considerably if one proceeds as follows. As a starting point, we will write this operator in the Kramers-Henneberger gauge [190, 191]. This gives

$$U_{KH}(t,t') = \exp[-i\frac{\widehat{\mathbf{p}}}{2}(t-t') - i\int_{t'}^{t} V(\widehat{\mathbf{r}} - \alpha(\tau))d\tau)], \tag{9.2}$$

where $\widehat{\mathbf{r}}$ and $\widehat{\mathbf{p}}$ denote the position and momentum operator, respectively. The electron excursion amplitude is given by

$$\alpha(\tau) = \int^{\tau} \mathbf{A}(\xi) d\xi. \tag{9.3}$$

In equation (9.2), the coupling of the system with the external laser field is embedded in the binding potential $V(\widehat{\mathbf{r}} - \alpha(\tau))$, where in the case of a vanishing binding potential, the free particle Hamiltonian is obtained. The time-evolution operator (9.2) cannot be written in terms of a product, as the operators involved do not commute. In fact, the Baker-Campbell-Hausdorff formula states that for two non-commuting operators $\widehat{A}$ and $\widehat{B}$

$$\exp(\widehat{A})\exp(\widehat{B}) = \exp(\widehat{C}), \tag{9.4}$$

where

$$\widehat{C} = \widehat{A} + \widehat{B} + \frac{1}{2}[\widehat{A},\widehat{B}] + \frac{1}{12}([\widehat{A},[\widehat{A},\widehat{B}]] + [[\widehat{A},\widehat{B}],\widehat{B}]) + ... \tag{9.5}$$

For the specific cases of

$$\widehat{A} = -i\frac{\widehat{\mathbf{p}}}{2}(t-t') \tag{9.6}$$

and

$$\widehat{B} = -i \int_{t'}^{t} V(\widehat{\mathbf{r}} - \alpha(\tau))d\tau), \tag{9.7}$$

one may show that these commutators depend on the spatial derivatives of the binding potential. Without loss of generality, one may analyze this behaviour by checking the commutators between $\widehat{\mathbf{p}}^2$ and $V(\widehat{\mathbf{r}})$. The first-order commutator involving these operator reads

$$[\widehat{\mathbf{p}}^2, V(\widehat{\mathbf{r}})] = i\widehat{\mathbf{p}}.\nabla V(\widehat{\mathbf{r}}) + i\nabla V(\widehat{\mathbf{r}}).\widehat{\mathbf{p}}, \tag{9.8}$$

and, similarly, the higher-order commutators depend on the higher spatial derivatives of the electron binding potential.

However, under the assumption that the binding potential varies slowly, on can neglect all commutators. Thus we can approximate (9.2) by the product

$$U_{KH}(t,t') \sim \exp[-i\frac{\widehat{\mathbf{p}}^2}{2}(t-t')] \exp[-i \int_{t'}^{t} V(\widehat{\mathbf{r}} - \alpha(\tau))d\tau)]. \tag{9.9}$$

We will now assume that, to first approximation, the binding potential may be neglected when defining the coordinate $\mathbf{r}$. In the Kramers-Henneberger gauge, this implies that one can approximate the electron coordinate associated with the position operator as

$$\mathbf{r}_{_{FF}}(\mathbf{p},\tau,t') = \mathbf{r}_0 + \mathbf{p}(\tau - t'), \tag{9.10}$$

where $\mathbf{r}_0$ denotes the initial coordinate of the electron. This is nothing but the coordinate of a free electron as a function of time.

In the context of this thesis, however, the desired gauge is the length gauge. Therefore one needs to transform (9.2) into the length-gauge time evolution operator. By applying the required transformation, we will have

$$\begin{aligned} U_L(t,t') \quad = \quad & \exp[-i \int_{t'}^{t} \frac{\mathbf{A}^2(\tau)}{2} d\tau] \exp[-i\mathbf{A}(t).\widehat{\mathbf{r}}] \exp[-i\widehat{\mathbf{p}}.\alpha(t)] \\ & U_{KH}(t,t') \exp[-i\widehat{\mathbf{p}}.\alpha(t')] \exp[-i\mathbf{A}(t').\widehat{\mathbf{r}}], \end{aligned} \tag{9.11}$$

By using closure relations in $\mathbf{r}$ and $\mathbf{p}$ and applying the length gauge time evolution operator U_L, equation (9.1) becomes

$$c_q(t) = -i \int_{-\infty}^{t} dt' \int d^3p \int d^3r < \mathbf{q}|\mathbf{r} >< \mathbf{r}|U_L(t,t') \left|\mathbf{p} + \mathbf{A}(t')\right\rangle < \mathbf{p}+\mathbf{A}(t')| \; H_I(t') \left|\varphi_b(t')\right\rangle, \tag{9.12}$$

where $\mathbf{r}$ and $\mathbf{p}$ denote the intermediate coordinate and the intermediate momentum of the electron, respectively. Due to the presence of the binding potential, the field-dressed momentum of the system is not conserved. Thus, the final momentum $\mathbf{q}$ is not the same as the intermediate momentum $\mathbf{p}$. This fact has been first observed and discussed systematically in [188], in a slightly different context, namely that of laser-induced XUV ionization.

By inserting (9.11) into (9.12) we obtain

$$< \mathbf{r}|U_L(t,t') \left|\mathbf{p} + \mathbf{A}(t')\right\rangle = \exp[i\mathbf{A}(t).\mathbf{r}] \exp[-i(\Phi_v(t,t') + \Phi_c(t,t'))] < \mathbf{r}|\mathbf{p} >, \quad (9.13)$$

with

$$\Phi_v(t,t') = \frac{1}{2}\int_{t'}^{t} d\tau [\mathbf{p} + \mathbf{A}(\tau)]^2 \quad (9.14)$$

and

$$\Phi_c(t,t') = \int_{t'}^{t} d\tau \mathbf{V}(\mathbf{r}_L(\tau)), \quad (9.15)$$

where(9.14) and (9.15) are the phases which the electron obtains along its trajectory in the continuum. The laser field and the presence of the Coulomb potential in the continuum give a Volkov phase $\Phi_v(t,t')$ and a Coulomb phase $\Phi_c(t,t')$, respectively, to the electron. The coordinate $\mathbf{r}_L$ is defined as

$$\mathbf{r}_L(\mathbf{p},\tau,t') = \mathbf{r}_0 + \int_{t'}^{\tau} dt'' [\mathbf{p} + \mathbf{A}(t'')]. \quad (9.16)$$

At the time t'', the electron tunnels from tan initial coordinate $\mathbf{r}_0$. We will refer to this coordinate as the "tunnel exit".

Apart from taking into account the influence of the Coulomb potential along the electron trajectory, it is also necessary to account for the presence of the Coulomb potential at the instant of ionization and at the detector [94, 95]. Following the procedure suggested in these references, we define the initial continuum states and the asymptotic states of the electron using Coulomb scattering waves. This assumption yields

$$< \mathbf{r}|\mathbf{p} >= \frac{1}{(2\pi)^{3/2}} \exp[i\mathbf{p}\cdot\mathbf{r}] \exp[-i\Phi_p(\mathbf{r})] \quad (9.17)$$

and

$$< \mathbf{q}|\mathbf{r} >= \frac{1}{(2\pi)^{3/2}} \exp[-iq\cdot\mathbf{r}] \exp[i\Phi_q(\mathbf{r})], \tag{9.18}$$

where Φ_p is the phase related to the distortion due to the Coulomb potential near the core, and Φ_q is the phase related to the distortion at the end of the pulse. These phases are defined as

$$\Phi_p = \exp[\int_{+\infty}^{t'} d\tau \mathbf{r}_{_{FF}}(\mathbf{p}, \tau, t')] \tag{9.19}$$

and

$$\Phi_q = \exp[\int_{+\infty}^{t} d\tau \mathbf{r}_{_{FF}}(\mathbf{q}, \tau, t)]. \tag{9.20}$$

By considering equations (9.13) - (9.20) and the fact that $|\varphi_b(t')\rangle = \exp[I_p t']\,|\varphi_b\rangle$, the transition amplitude reads

$$c_q(t) = \frac{-i}{(2\pi)^3} \int_{-\infty}^{t} dt' \int d^3p \int d^3r \exp[iS_c(\mathbf{q}, \mathbf{p}, \mathbf{r}, \mathbf{t}')] < \mathbf{p} + \mathbf{A}(t')|\ H_I(t')\,|\varphi_b\rangle\,, \tag{9.21}$$

with the action

$$\begin{aligned} S_c(\mathbf{q}, \mathbf{p}, \mathbf{r}, \mathbf{t}') \quad = \quad & (\mathbf{p}-\mathbf{q}).\mathbf{r} - \frac{1}{2}\int_{t'}^{t} d\tau[\mathbf{p} + \mathbf{A}(t')]^2 - \int_{t'}^{t} d\tau \mathbf{V}(\mathbf{r}_{_L}(\tau)) + \int_{+\infty}^{t'} d\tau \mathbf{V}(\mathbf{r}_{_{FF}}(\mathbf{p}, \tau, t')) \\ & - \int_{+\infty}^{t} d\tau \mathbf{V}(\mathbf{r}_{_{FF}}(\mathbf{q}, \tau, t')) + I_p t', \end{aligned} \tag{9.22}$$

where I_p is the ionization potential.

One may identify two key "ingredients" in equation (9.21): 1) the prefactor which denotes the matrix element between a bound state $|\varphi_b(t')\rangle$ and a continuum state $< \mathbf{p} + \mathbf{A}(t')|$, coupled by the interaction Hamiltonian H_I at the ionization time t'; 2) the action which corresponds to the phase acquired by the electron from the tunnel time t' to the detecting time t. The transition amplitude in (9.21) is identical to that obtained using the Volkov-Coulomb Eikonal approximation developed in [94, 188]. In this approach, a field-dressed Wentzel-Kramers-Brillouin (WKB) approximation is developed in order to incorporate the binding potential in the continuum. The field-free counterpart is valid if the Coulomb potential varies smoothly. In our derivation this assumption is implicit in the neglect of the commutators (9.8) in order to obtain (9.9).

The Volkov-Coulomb Eikonal approximation developed in [94, 188] has mostly been used in laser-induced XUV ionization, especially if the saddle-point approximation has been employed (as in reference [188]). In this case, an electron is ejected in the continuum by a high-frequency photon from an additional XUV pulse and reaches the detector without rescattering. In the saddle-point framework, the calculation of the corresponding

transition amplitude is considerably simplified, as the ionization time t' will be real in the saddle-point equations.

For above threshold ionization, however, the situation is more complicated, as the electron reaches the continuum by tunneling ionization. This implies that there is no real solution for the saddle-point equation describing ionization. This will lead to a complex ionization time, which will bring several difficulties. For instance, a complex ionization time will render the other intermediate variables complex. In the present context, this will lead to branches in the saddle-point equations. Apart from that, it will be necessary to find appropriate physical criteria in order to define the tunnel exit.

By neglecting the Coulomb potential ($V(\mathbf{r}) = 0$) in (9.21), the strong-field approximation transition amplitude for direct ATI is recovered. In this case, the integral over the electron coordinate $\mathbf{r}$ reduces to

$$\frac{1}{(2\pi)^{3/2}} \int d^3r \exp[i(\mathbf{p}-\mathbf{q}).\mathbf{r}] = \delta(\mathbf{p}-\mathbf{q}). \tag{9.23}$$

Consequently, the transition amplitude (9.21) may be written as

$$c_q^{SFA}(t) = \frac{-i}{(2\pi)^{3/2}} \int_{-\infty}^{t} dt' \exp[iS_c^{SFA}(\mathbf{q},\mathbf{t}')] < \mathbf{q} + \mathbf{A}(t')| \; H_I(t') \left|\varphi_b(t')\right\rangle, \tag{9.24}$$

with the action

$$S_{SFA}(\mathbf{q},\mathbf{t}') = -\frac{1}{2}\int_{t'}^{t} d\tau[\mathbf{q}+\mathbf{A}(t')]^2 + I_p t'. \tag{9.25}$$

By comparing the transition amplitude (9.21) and (9.24), several differences can be identified. In the strong-field approximation transition amplitude for direct ATI (9.24), the field-dressed momentum is conserved. It means the initial momentum $\mathbf{p}$ and the final momentum $\mathbf{q}$ are the same ($\mathbf{p} = \mathbf{q}$). Therefore, one just needs to integrate the transition amplitude upon the tunneling time t'. In the Coulomb-corrected approach, the binding potential acts upon the momentum of the electron in the course of its trajectory and introduces the phase (9.15). As a direct consequence, beyond the SFA, the transition amplitude must also be integrated over the intermediate electron momentum $\mathbf{p}$ and the intermediate electron coordinate $\mathbf{r}$. Furthermore, in the SFA transition amplitude the phases (9.19) and (9.20) are not present. Physically, this means that, in the absence of the binding potential, the electron continuum states are described by plane waves. However, in the presence of Coulomb potential there is a distortion near the core. In addition, in the Coulomb-corrected approach, at the end of the pulse the asymptotic continuum state is a Coulomb scattering state instead of a plane wave.

9.2 Saddle-point Equations

We employ saddle-point methods to compute the transition amplitude in (9.21). The saddle-point equations are obtained from the conditions $\partial S_c(\mathbf{q},\mathbf{p},\mathbf{r},t')/\partial t' = 0, \partial S_c(\mathbf{q},\mathbf{p},\mathbf{r},t')/\partial \mathbf{r} = \mathbf{0}$ and $\partial S_c(\mathbf{q},\mathbf{p},\mathbf{r},t')/\partial \mathbf{p} = \mathbf{0}$ and are, respectively

$$\frac{1}{2}[\mathbf{p}+\mathbf{A}(t')]^2 = -\mathbf{V}(\mathbf{r}_{_L}(t')) - [\mathbf{p}+\mathbf{A}(t')]\int_{+\infty}^{t'} d\tau \nabla_{\mathbf{r}}\mathbf{V}(\mathbf{r}_{_{FF}}(\mathbf{p},\tau,t')) - I_p, \tag{9.26}$$

$$\begin{aligned}(\mathbf{p}-\mathbf{q}) - \int_{t'}^{t} d\tau \nabla_{\mathbf{r}}\mathbf{V}(\mathbf{r}_{_L}(\tau)) + \int_{+\infty}^{t'} d\tau \nabla_{\mathbf{r}}\mathbf{V}(\mathbf{r}_{_{FF}}(\mathbf{p},\tau,t')) \\ - \int_{+\infty}^{t} d\tau \nabla_{\mathbf{r}}\mathbf{V}(\mathbf{r}_{_{FF}}(\mathbf{q},\tau,t')) = 0,\end{aligned} \tag{9.27}$$

$$\begin{aligned}-\mathbf{r} + \int_{t'}^{t} d\tau [\mathbf{p}+\mathbf{A}(t')] + \mathbf{r}_0 + \int_{t'}^{t} d\tau (\tau - t')\nabla_{\mathbf{r}}\mathbf{V}(\mathbf{r}_{_L}(\tau)) + \int_{+\infty}^{t'} d\tau (\tau - t')\nabla_{\mathbf{r}}\mathbf{V}(\mathbf{r}_{_{FF}}(\mathbf{p},\tau,t')) \\ - \int_{+\infty}^{t} d\tau (\tau - t')\nabla_{\mathbf{r}}\mathbf{V}(\mathbf{r}_{_{FF}}(\mathbf{q},\tau,t')) = 0.\end{aligned} \tag{9.28}$$

Equation (9.26) corresponds to the conservation of energy at the time t', when the electron tunnels through the barrier at the coordinate $\mathbf{r}(t') = \mathbf{r}_0$. The right hand side of this equations gives the kinetic energy of the electron in the continuum. For the SFA, we would have just I_p in the right hand side of the equation, while the corrected approach introduced the remaining terms, which are distortions due to the Coulomb potential. The solution of equation (9.26) is complex, since tunneling has no classical counterpart. Therefore, within the saddle-point framework, the intermediate momentum $\mathbf{p}$ and electron coordinates $\mathbf{r}$ are also complex.

Equation (9.27) shows that the electron momentum is no longer conserved, as compared to the SFA. The net force $\nabla_{\mathbf{r}} V(\mathbf{r}_{_L}(t))$ acts on the electron along its trajectory from the tunnel exit $\mathbf{r}_0$ to the detector and alter the electron momentum in the continuum. The remaining terms are related to the phase distortions at the tunneling time t' and at the end of the pulse, i.e. when the electron reaches the detector. The intermediate momentum $\mathbf{p}$ and the electron momentum $\mathbf{q}$ at the detector become the same if $V \to 0$. Thus the electron momentum of the system will be conserved in the SFA.

Equation (9.28) provides the electron coordinate as function of time. Furthermore, this equation can be directly related to the classical equation of motion of an electron under the influence of the laser field and the binding potential. By finding the solutions of the

saddle-point equations, the transition amplitude can be approximated as

$$c_q(t) \simeq \sum_s (2\pi i)^{7/2} \frac{< \mathbf{p}_s + \mathbf{A}(t'_s)|\ H_I(t'_s)\,|\varphi_b\rangle}{\sqrt{\det S''_c(\mathbf{q}, \mathbf{p}_s, \mathbf{r}_s, t'_s)}} \exp[-iS_c(\mathbf{q}, \mathbf{p}_s, \mathbf{r}_s, t'_s)], \tag{9.29}$$

where the index s runs over the relevant saddle points and $\det S''_c(\mathbf{q}, \mathbf{p}_s, \mathbf{r}_s, t'_s)$ is the 7×7 determinant of the second derivatives of the action with respect to $\mathbf{p}$, $\mathbf{r}$ and t'.

The situation for the standard strong-field approximation is much simpler, as we have only one saddle-point equation which be integrated over t' equation (9.25). In this latter case, the saddle-point approximation for the direct ATI transition amplitude reads

$$c_{SFA}(t) \simeq \sum_s (2\pi i)^{1/2} \frac{< \mathbf{q} + \mathbf{A}(t'_s)|\ H_I(t')\,|\varphi_b\rangle}{\sqrt{\partial^2 S_{SFA}(\mathbf{q}, t'_s)/\partial t'^2}} \exp[-iS_{SFA}(\mathbf{q}, t'_s)]. \tag{9.30}$$

9.3 Classical Equations of Motion and the Eikonal Approximation

The saddle-point equations (9.26)-(9.28) are similar to those in [188], with the difference that we suppose that the electron is ionized by tunneling, while in [188] a short XUV pulse provides ionization mechanism. As a result, they deal with a real ionization time whereas in our case we have a complex ionization time, which makes the calculation more complicated. In the literature, however, a slightly different Coulomb-corrected version of the strong-field approximation has been applied to direct ATI [149, 189]. Therein, the classical equations of motion of an electron under the influence of the external field and the Coulomb potential are solved numerically. These results are used as the real parts of $\mathbf{r}$, $\mathbf{p}$ and t' in a modified action including the Coulomb phase (9.15), but not the terms (9.19) and (9.20) related to the Coulomb distortions at the ionization and detection times. Explicitly, the authors consider the equations

$$\frac{d\mathbf{v}}{d\tau} = -\mathbf{E}(\tau)\widehat{\mathbf{e}}_x - \nabla_{\mathbf{r}} \mathbf{V}(\mathbf{r}_L(\tau)), \tag{9.31}$$

where $\mathbf{E}(\tau)$ is a linearly polarized time-dependent electric field and

$$\frac{d\mathbf{r}}{d\tau} = \mathbf{v}. \tag{9.32}$$

Here, all the variables involved are real, and the initial condition $\mathbf{r}_0$ is a real tunnel exit adapted from [192]. Considering the initial velocity $\mathbf{v}(t') = \mathbf{p} + \mathbf{A}(t')$; the velocity at the detector $\mathbf{v}(t) = \mathbf{q} + \mathbf{A}(t)$ and integrating equation (9.31) in this time interval we obtain equation (9.27) without the surface terms (the last two terms in the right hand of

this equation). By inserting the velocities obtained from integration of equation (9.32) in (9.31), obtain

$$\mathbf{r} = \mathbf{r}_0 + \int_{t'}^{t} d\tau[\mathbf{p} + \mathbf{A}(t')] - \int_{t'}^{t}\int_{t'}^{\tau} dt'' \nabla_{\mathbf{r}} \mathbf{V}(\mathbf{r}(t'')). \tag{9.33}$$

If we approximate $\mathbf{r}(t'')$ by equation (9.16) and integrate by parts with regard to $''$), we obtain

$$\int_{t'}^{\tau} dt'' \nabla_{\mathbf{r}} \mathbf{V}(\mathbf{r}_L(t'')) \simeq (\tau - t')\nabla_{\mathbf{r}} \mathbf{V}(\mathbf{r}_{_L}(\tau)) - \int_{t'}^{\tau} dt'' \frac{\nabla_{\mathbf{r}} \mathbf{V}(\mathbf{r}_L(t''))}{dt''}. \tag{9.34}$$

If the last term in the above equation is neglected then (9.33) will have a form similar to the equation (9.28) without the surface terms. This latter approximation implies that the gradient of the binding potential varies smoothly in time and can be neglected. This is the assumption behind the Coulomb-Volkov eikonal approximation in [188] and in the approach employed in this work.

9.4 The Tunnel Exit

An important issue is the treatment of tunnel ionization, and how to define the point in space at which the electron reaches the continuum. This defines the initial conditions to be implemented in the Coulomb-corrected SFA. This problem does not occur for the SFA, as the influence of the potential is reduced to one point at $\mathbf{r} = 0$.

Tunneling beyond the SFA is considerably more difficult than if one is dealing, for instance, with laser-induced XUV ionization. In the latter case, the starting momenta are real. In contrast, for tunneling, in principle all variables are complex. In fact, one can only guarantee the reality of the final momentum $\mathbf{q}$ at the end of the pulse, as this is the observed quantity. Our tunnel exit is chosen such that

$$\mathbf{V}(\mathbf{r}_0) - \mathbf{r}_0 \cdot \mathbf{E}(t') = -I_p \tag{9.35}$$

Equation (9.35) states that the electron will tunnel at the specific value $\mathbf{r}_0$ of the electron coordinate such that the effective potential barrier determined by the binding potential is equal to the binding-state energy of the electron. This equation corresponds to the turning point condition for the binding potential in the presence of the external laser

field. Note that, since t' is complex, the coordinate r_0 fulfilling (9.35) is expected to be complex as well. One may now argue that the tunnel exit must be real. In fact both [188] and [149, 189] have considered a real tunnel exit based on reference [192], which assumes an electron starts its journey inside the potential barrier with some complex time and by the time of tunneling the imaginary part of the time vanishes, thus the electron is "born" with a real time in the continuum.

In our view, however, one may physically define a real tunnel exit, but in the context of the saddle-point method the tunnel exit is associated with a complex tunneling time. Thus, there is no guarantee that it will be real. Clearly, a complex solution for equation (9.35) has many branches. Hence, one must chose those branches that make physically sense. Apart from that, equation (9.35) has in principle many solutions, not all of which correspond to a tunnel exit.

9.5 Preliminary Results and Outlook

Photoelectron spectra will be computed by employing the approach discussed in the previous section. We will consider model atoms, bound by either short-range or long-range potentials, under the influence of a linearly polarized monochromatic field

$$\mathbf{E}(t) = \mathbf{E}_0 \sin(\omega t). \tag{9.36}$$

We will restrict the dynamics of the problem to one or two dimensions. In the latter case, our results will be compared to those obtained using the numerical solution of the time-dependent Schrödinger equation. In this case, we will consider QPROP, which is a free Schrödinger solver for atoms in intense laser field [193]. We will use a soft-core potential

$$\mathbf{V}(\mathbf{r}) = -\frac{C}{\sqrt{a^2 + r^2}}, \tag{9.37}$$

where a and C have been chosen such that the energy of its ground state matches that of hydrogen. In one or two dimensions, $r^{(1D)} = x, x \geq 0$ or $r^{(2D)} = \sqrt{x^2 + y^2}$, respectively. The tunnel exit is computed according to equation (9.35). We choose the tunnel exit as $(x; y) = (r_0, 0)$. This is a reasonable assumption for a linearly polarized field, even though the electronic wavepacket exhibits a non-vanishing width. Furthermore, we employe a hard-core potential to compute r_0, due to the fact that this provides a simple analytical solution. The explicit expression for the tunnel exit reads

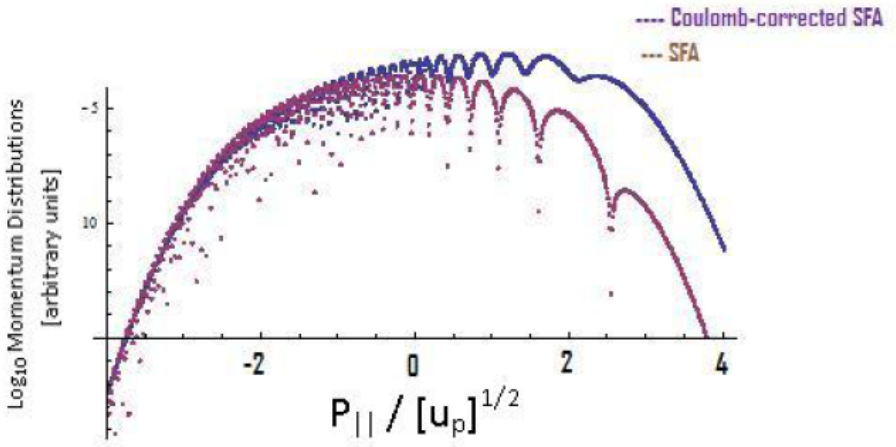

FIGURE 9.1: Transition amplitude of the Coulomb-corrected strong-field approximation in above-threshold ionization in comparison to the SFA by considering the surface terms. We consider a monochromatic field of intensity $I = 1.5\times10^{14}$ W/cm^2, frequency $\omega = 0.057$ a.u and transverse momenta $p_\perp = 0$ for a model atom, for which the electron tunnels from a ground state of energy $E_{1g} = 0.5$ a.u.

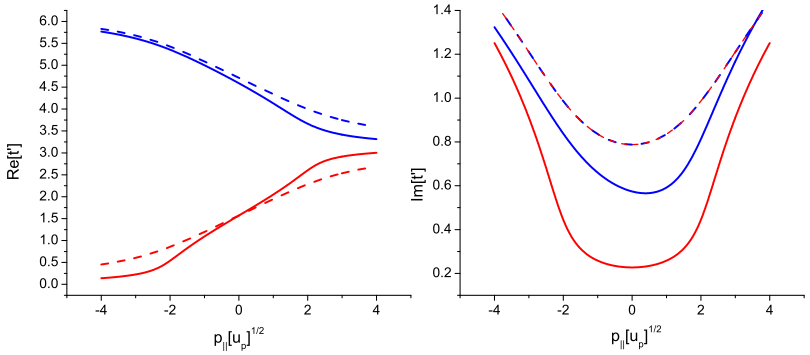

FIGURE 9.2: Tunneling times of the first electron, as functions of its parallel momentum $p_{||}$, for a monochromatic field of intensity $I = 1.5\times10^{14}$ W/cm^2 and frequency $\omega = 0.057$ a.u, for transverse momenta $p_\perp = 0$. The panel on the left-hand side and on the right-hand side give the real and the imaginary parts of the tunneling time t', respectively, with the blue lines show the long orbit and the red lines short orbits. In this specific figure, we consider a model atom, for which the electron tunnels from a ground state of energy $E_{1g} = 0.5$ a.u. The dashed and solid lines correspond to the the Coulomb-corrected S-Matrix approach and the SFA, respectively.

$$\mathbf{r}_0 = -\frac{I_p + \sqrt{I_p^2 - 4CE_0\sin(\omega t')}}{2E_0\sin(\omega t')}. \tag{9.38}$$

It is easy to show that this tunnel exit tends to infinity if the electric field vanishes, and decreases if the field is a maximum. The computation presented here is still very preliminary. So far the situation with the results is as follows:

- There is a code for the one-dimensional (1D) situation which works if only the surface terms are taken. If one includes changes along the trajectory, convergence is still poor. The former terms, however, indicate a phase shift for quantum interference patterns due to different ionization times in the yield, in comparison to the strong-field approximation. This is shown in figure 9.1 and agrees qualitatively with the results in [149].

- The one-dimensional calculation shows that the surface terms play an important role. This is particularly true for the surface term close to the core. This is expected as the binding potential is dominant in this region (see figure 9.2). Further investigation is required to find out how references [149, 189] could justify the neglect of this term.

- What tunnel exit to take is still a mystery. However, by using equation (9.35) for a one-dimensional Coulomb potential we have obtained four branches, two of which can be eliminated employing physical arguments. More detailed studies of the remaining branches are however missing.

- There are still several branches for the intermediate variables $\mathbf{r}$ and $\mathbf{p}$ in the saddle-point equations, which must be selected employing valid physical arguments.

- Recently, we computed ATI spectra from the numerical solution of the time-dependent Schrödinger equation employing QPROP [193]. These spectra will be used as a benchmark. However, in order to perform a direct comparison, we must implement a two or three-dimensional code for the approach described in this chapter. In this context, one should note that a one-dimensional model is not necessarily simpler to deal with. In fact, by taking a one-dimensional model we are forcing the electron to recollide from core if its momentum changes direction. This would imply a hard collision for which the binding potential would no longer vary smoothly and the present approach would break down. In contrast, in a two-dimensional model, the electron could possibly be deflected by the binding potential without colliding. This is in fact what happens in [80], for a wide class of trajectories.

Once the above issues are successfully dealt with, we intend to incorporate rescattering in the ATI transition amplitude, and, finally, bring those mechanisms together in RESI. In our view, this is a highly promising area of application for the Coulomb-corrected approach discussed here.

Chapter 10

Summary

This thesis addresses electron-electron correlation, excitation and quantum interference in the context of laser-induced nonsequential double ionization (NSDI). Its main emphasis is the recollision excitation with subsequential tunneling ionization (RESI) mechanism of NSDI. We drive the RESI transition amplitude and compute electron momentum distributions employing the strong-field approximation and saddle-point methods. This allows me to treat the problem analytically to a great extent. An analytical treatment is very important in order to obtain a transparent physical picture of this process. Therefore, we focus on potential attosecond imaging application and how RESI can be used to retrieve structural information about the atomic and molecular wavefunctions. Apart from that, we also address the specific issue of electron-impact ionization in diatomic molecules.

Chapters 1 and 2 place this work in a general context, by providing an overview of electron-electron correlation in strong laser field, and in particular of laser-induced nonsequential double ionization. Chapter 3 focuses on the theoretical aspects of the strong-field approximation. Starting from a general overview of the main concepts and assumptions behind it. Subsequently, by applying the SFA, the general transition amplitude of NSDI is derived for both electron-impact ionization and RESI. In Chapter 4, we briefly discuss the saddle-point methods employed in this thesis. Furthermore, it is illustrated when the saddle-point approximation needs to be replaced by the uniform approximation and how these two approximations relate to each other.

In Chapter 5, constraints for the parallel momentum components $p_{n||}(n = 1, 2)$ of electrons in the plane $p_{1\parallel}p_{2\parallel}$ are determined using the saddle-point equations. The saddle-point equations provide useful information on the momentum-space regions populated by the RESI and electron-impact ionization mechanisms. Furthermore, the constraints can be used as a tool for sketching the approximate shapes of the electron-momentum

distributions. It shows that RESI mechanism can be understood as a rescattered above-threshold ionization-like process (ATI) for the first electron, followed by direct ATI for the second electron. The shapes of the electron momentum distributions, are determined by the interplay between two different behaviors, associated with the collision of the first electron and the tunneling of the second electron. The momentum region determined by the tunnel ionization of the second electron from an excited state will be always restricted by the direct ATI cutoff. The relevant momentum region will not change regardless of the driving-field intensity, as this will always be a classically forbidden process. This also implies that one may define a threshold driving-field intensity for the RESI mechanism. This intensity is considerably lower than that necessary for the second ionization potential to be overcome by the second electron, i.e., for electron-impact ionization to occur.

Chapter 6 demonstrates that the RESI electron momentum distributions depends very critically on the bound state wave function and the type of electron-electron interaction. Furthermore, it shows that the bound states involved in the RESI process leave very distinct fingerprints on the electron momentum distributions. This is particularly true for the bound state of the second electron, prior and subsequent to excitation. In fact, the widths of the distributions, their shapes and the number of maxima present will strongly depend on the principal and orbital quantum numbers of the bound states involved. More importantly, the observations in this chapter show that all distributions encountered in this work are equally spread over the four quadrants of the $p_{1\|}p_{2\|}$ plane. Under no circumstances have we found electron momentum distributions concentrated only on the second and fourth quadrant of this plane, as reported in the literature [13, 109, 112–114].

In Chapters 7 and 8, we address NSDI for diatomic molecules. In these chapters, we investigate how molecular orbital symmetry [84] and the alignment angle of the molecules with respect to the laser-field polarization [13] affect the shapes of the electron momentum distributions. Chapter 7 deals with electron-impact ionization and Chapter 7 covers the RESI mechanism. The computations show that the electron-momentum distributions exhibit interference maxima and minima due to the electron emission at spatially separated centres. The interference patterns survive the integration over the transverse momenta for a small range of alignment angles, and are sharpest for parallel-aligned molecules. Due to the contributions of transverse-momentum components, these patterns become less defined as the alignment angle increases, until they disappear for perpendicular alignment. Explicitly, Chapter 8 demonstrates that the electron-momentum distributions exhibit interference maxima and minima, due to the molecular orbital geometry, such as nodes of the atomic wavefunction. Furthermore, the computation of RESI for N_2 and Li_2 show that the molecular orbital signature is embedded in the the

electron momentum distributions and it reveals itself as we vary the alignment angle. As a result, it indicates that the RESI can be an appropriate tool for retrieving information about the molecular structure.

In Chapter 9, we illustrates the Coulomb-corrected strong-field approximation by discussing the main challenges involved in this approach. For the sake of simplicity, the influence of the Coulomb potential on direct ATI (the simplest processes in RESI) is investigated. The Coulomb potential influence is incorporated in a semi-analytical approach, which is constructed around the strong-field approximation. Our preliminary results show that the surface term, which is related to the tunneling point close to the core, influence the ATI spectra and the electron ionization times considerably. This is expected as the binding potential is dominant in this region. This is, however, work in progress and several technical difficulties most be overcome. Once the Coulomb-corrected strong-field approximation of direct ATI is correctly implemented, we intend to incorporate rescattering in the ATI transition amplitude, and, finally, bring those mechanisms together in RESI. We expect these connections to play a major role, as, according to our previous results, RESI is quite sensitive with regard to the internal structure of the target involved.

Appendix A

Saddle-point Approximation

This appendix illustrates the derivation of the saddle-point approximation in (4.8). For the sake of simplicity, we start with a one-dimensional integral first for real variable and then in the complex plane. Subsequently, we extend the derivation for a two-dimensional integral. Finally, we provide the general equation for the multi-dimensional case in the complex plane. The derivations provided in here, are mainly based on Dr Carla Figueira de Morisson Faria's lecture notes and reference [194].

The saddle-point approximation in (4.8) is derived from asymptotic expansions of Laplace-type integrals. A one-dimensional Laplace-type integral reads

$$I = \int_a^b f(x) \exp(-\alpha s(x)) dx \tag{A.1}$$

When $\alpha \to \infty$ and $s(x)$ is real, the above integral decays exponentially or has nonoscillatory behavior. in this particular case, contour upon which this integral is computed is the real line or a subsection of it.

Here, the asymptotic expansion does not depend on the endpoints of the integration. Instead it depends entirely on the behavior of $s(x)$ and $f(x)$, in an arbitrarily small neighborhood of their global minimum (x_s) along the interval of integration. Thus, the entire integral in (A.1) can be approximated by considering the contribution from the vicinity of the stationary points, i.e $ds(x)/dx = 0$ on the integration contour. Furthermore, we assume that the integral does not have any singular point along the deformed contour, and second derivatives of $s(x)$, at the stationary points, are greater than zero ($s^{''}(x_s) > 0$). The contributions far from the extremum are negligible. Thus, the contour can be constructed almost like a Gaussian, when we move away from the vicinity of the stationary points. The latter correspond to maxima of the integrand, after deformation

of the original integration manifold. We apply Taylor series expansions on $s(x)$ about $x = x_s$. This leads to

$$s(x) \approx s(x_s) - \frac{(x - x_s)^2}{2} s''(x_s) \tag{A.2}$$

As a result, the (A.1) can be approximated as

$$I \approx f(x_s) \exp(-\alpha s(x_s)) I_0 \tag{A.3}$$

where

$$I_0 = \int_{-\infty}^{\infty} \exp(-\frac{\alpha(x - x_s)^2}{2} s''(x_s))) dx, \tag{A.4}$$

and $f(x) \approx f(x_s)$. This approximation is justifiable, since $f(x)$ is a slowly varying function comparing to $s(x)$. Equation (A.4) is a Gaussian integral. Thus, the approximated integral of (A.4) will have the following format:

$$I \approx f(x_s) \sqrt{\frac{2\pi}{\alpha s''(x_s)}} \exp(-\alpha s(x_s)) \tag{A.5}$$

Laplace's method can be extended further to approximate an integral in a complex plane. Let us assume that the contour integral in (A.1) is deformed in a complex plane, instead of the real axis, i.e.

$$I(\eta) = \int_C g(z) \exp(\eta s(z)) dz \tag{A.6}$$

Where $\eta \to \infty$, z is a complex variable, C a fixed contour in this plane, and $g(z)$ and $s(z)$ are analytic functions in some region that include C. As long as $s(z)$ stays in its analytical region, the value of the integral will not be affected by distorting the path. To elaborate the analytic condition of $s(z)$, we suppose

$$s(z) = u(x, y) + iv(x, y) \tag{A.7}$$

where complex variable $z = x + iy$. $u(x, y)$ and $v(x, y)$ are real functions. Since we are dealing with an analytic function, $s(z)$ has a well-defined derivative

$$\frac{ds(z)}{dz} = \lim_{\Delta z \to 0} \frac{s(z + \Delta z) - s(z)}{\Delta z} \tag{A.8}$$

In contrast to the function with real variable, Δz can approach zero from two independent directions (along the x axis or along the y axis). This means

$$\frac{\partial s(x, iy)}{\partial x} = \frac{\partial s(x + iy)}{\partial (iy)} \tag{A.9}$$

In terms of u and v, this leads to Cauchy-Riemann conditions

$$\begin{aligned} \frac{\partial u(x,y)}{\partial x} &= \frac{\partial v(x,y)}{\partial y}, \\ \frac{\partial u(x,y)}{\partial y} &= -\frac{\partial v(x,y)}{\partial x} \end{aligned} \tag{A.10}$$

Now, the second derivative of (A.9) will lead to a two-dimensional Laplacian equation, in which

$$\frac{\partial^2 u(x,y)}{\partial x^2} + \frac{\partial^2 u(x,y)}{\partial y^2} = \frac{\partial^2 v(x,y)}{\partial x^2} + \frac{\partial^2 v(x,y)}{\partial y^2} = 0, \tag{A.11}$$

which can be written as $\nabla^2 u = \nabla^2 v = 0$.

This result implies that, one can not have simultaneous maxima and minima in x and y. In fact, a minimum in x implies a maximum in y and vice versa. Hence, conditions A.10 lead to a saddle point in the complex plane. Furthermore, one can show that $\nabla u . \nabla v = 0$. This implies that the gradients of the real and imaginary parts are orthogonal. Thus, if we choose our contour along the steepest descent of $u(x, y)$, i.e. along ∇u , then, along the same contour, v is constant. Therefore, the contributions along this path are all in phase. One should note that a constant imaginary part for $s(z)$ does not guarantee that the chosen path is a steepest descent. Therefore one has to be careful with steepest ascents. In 1-D, one can choose the right contour considering above-mentioned criteria. In practice, for higher dimensions the situation is more difficult. Thus, in the multiple integrals computed in this work, trial-and-error has been used for finding the relevant steepest descent path.

Based on the above discussions, the real part of $s(z)$ in (A.6) determines the magnitude of the integrand, and its imaginary part determines the phase of the integrand. Therefore,

by choosing the contour integral through the saddle points along the steepest descent, the biggest contributions to the integral are all in phase. Like the Laplace-type integral (A.1), along this path, the integral has standard Gaussian form. In addition, the contribution of the integral away from the saddle point can be neglected, since $\eta \to \infty$. Now, we can approximate (A.6) carrying a Taylor series expansions on $s(z)$ about $z = z_s$. By following all the steps in Laplace-type integral (A.1), we will have

$$I(\eta) \approx g(z_s)\sqrt{\frac{2\pi}{\eta s''(z_s)}}\exp(-\eta s(z_s)) \tag{A.12}$$

Here, $g(z) \approx g(z_s)$, since $g(z)$ changes much more slowly than $\exp(\eta s(z))$.

Next, I discuss a case with two integration variables

$$I = \int\int f(x,y)\exp(-\alpha s(x,y))dxdy \tag{A.13}$$

By applying a Taylor expansion around x_s, y_s (the stationary points where first derivatives of $s(x,y)$ vanish), we will have

$$I \approx f(x_s,y_s)\exp(-\alpha s(x_s,y_s))\int_{-\infty}^{\infty}\int_{-\infty}^{\infty}\exp(-\alpha\chi)dxdy \tag{A.14}$$

where

$$\chi = A(x-x_s)^2 + B(y-y_s)^2) + 2C(x-x_s)(y-y_s) \tag{A.15}$$

where $A = \frac{1}{2}\frac{\partial^2 f(x,y)}{\partial x^2}$, $B = \frac{1}{2}\frac{\partial^2 f(x,y)}{\partial y^2}$ and $C = \frac{1}{2}\frac{\partial^2 f(x,y)}{\partial x \partial y}$ at $x = x_s$ and $y = y_s$

One can write (A.15) in matrix format of

$$(x-x_s, y-y_s)M\begin{pmatrix} x-x_s \\ y-y_s \end{pmatrix} \tag{A.16}$$

where $M = \begin{bmatrix} A & C \\ C & B \end{bmatrix}$

To eliminate the cross term in (A.15), we use a variable transformation to deform (A.14) to

$$I \approx f(x_s, y_s) \exp(-\alpha s(x_s, y_s)) \int_{-\infty}^{\infty} \int_{-\infty}^{\infty} \exp(-\alpha[E_1 p^2 + E_2 q^2]) dp dq \tag{A.17}$$

Since M is a diagonalizable matrix, we will have $\begin{bmatrix} A & C \\ C & B \end{bmatrix} = \begin{bmatrix} E_1 & 0 \\ 0 & E_2 \end{bmatrix}$, with $E_1 = A$ and $E_2 = \frac{1}{A}(AB - C^2)$.

The determinants of the two metrics are equal, thus $\det M = AB - C^2 = E_1 E_2$

By using the obtained results, the Gaussian part of the integral in(A.17) can be estimated as

$$I \approx f(x_s, y_s) \exp(-\alpha s(x_s, y_s)) \frac{\pi}{\alpha \sqrt{\det M}} \tag{A.18}$$

Consequently, one can estimate a Multidimensional integral of the format (A.17) at around a saddle point as

$$I(\eta) \approx (\frac{2\pi}{\eta})^{j/2} \frac{g(z_s)}{\sqrt{\det S''(z_s)}} \exp(-\eta S(z_s)) \tag{A.19}$$

where j corresponds to dimension of the integral. However, one has to be very careful to choose the right contour for this multidimensional integral. Using the techniques above with some trial and error attempts could help us to find these branches. This task is not always easy, especially when there are many branches around a given saddle point. Whatever branches we choose, we have to make sure it makes physical sense for the problem we are dealing with.

In the transition amplitude of NSDI, we are dealing with many saddle points. Thus, we need to sum the contributions from all the saddles (as it is shown in 4.8). One should note that in this thesis we use atomic units to represent all the equations. Thus, the coefficient of the actions (3.34) and (3.42), i.e. $1/\hbar$ is set to unity. Therefore, the assumption $\eta \to \infty$ is held, since $1/\hbar \to \infty$.

The saddle-point approximation is a very powerful technique for simplification of computations as it converts a multiple integrals to a simple one-dimension integral. Furthermore, for the physical processes like HHG, ATI and NSDI, it provides a space-time picture which gives us additional physical insight. For example, it allows us to investigate the interference processes which are a purely quantum mechanical concept. However,

this approximation is not valid when the domain of the integral contains a critical value. In this case, the valid expansion will be the uniform approximation. It is discussed in (4.3) and Appendix B.

Appendix B

Uniform Approximation

The standard saddle-point approximation is not valid when the domain of the integral contains a critical value. This occurs if we are dealing with asymptotic expansions of integrals with two nearby saddle points (coalescent saddle points), or when the saddle points are the singularities of the integral, or when the saddle points lie at an end point of the integral. To approximate the integral in this case, one needs to define an asymptotic expansion which remains valid even over a domain containing these critical values. Here, we look at a special case of the uniform approximation, which is valid for two coalescing or nearly coalescing simple saddle points. The derivations in this appendix are mainly based on Dr Carla Figueira de Morisson Faria's lecture notes and reference [194]. We will provide an adaption of the discussion in [194] and [172]. For simplicity, we will consider an integral of the form

$$I(\eta,\kappa) = \int_C f(z)\exp(\eta S(z;\kappa))dz \tag{B.1}$$

where $f(z)$ and $S(z;\kappa)$ are analytic functions in a connected domain, containing the contour C and the end points $z = \kappa_\pm$, with the critical value of $|\kappa_+ - \kappa_-| = 0$. By considering some reasonable criteria, we change the variable $z = z(t)$. The transformation is chosen such that the number of saddle points and their behaviour remain unaltered. In addition, the new expansion $\varphi(t,\kappa)$ should have a simpler form than $S(z;\kappa)$. Thus, one can have the simple form of

$$\varphi(t;\kappa) = S(z(t);\kappa) = -(\frac{t^3}{3} - \gamma^2 t) + \rho \tag{B.2}$$

We can determine γ and ρ by differentiating (B.2) with respect to t. Thus, we have

$$\dot{z} = \frac{dz}{dt} = (\frac{\gamma^2 - t^2}{S_z(z;\kappa)}) \tag{B.3}$$

To avoid any additional saddle point, $\dot{z}$ is required to be finite and nonzero. Therefore, we must have $t = \pm\gamma$ when $z = \pm\kappa$. By substituting these results to (B.2), and solving the second order simultaneous equations, we will have

$$\begin{aligned} \gamma^3 &= \frac{3}{4}\Delta S \\ \rho &= \frac{1}{2}\overline{S} \end{aligned} \tag{B.4}$$

here $\Delta S = S(\kappa_+;\kappa) - S(\kappa_-;\kappa)$ and $\overline{S} = S(\kappa_+;\kappa) + S(\kappa_-;\kappa)$. In equation (B.4) when $\kappa_+ \neq \kappa_-$, there are three solutions for γ. For a case $\gamma \neq 0$, we apply L'Hospital's rule in (B.3) to obtain

$$\dot{z}^2 = \mp\frac{2\gamma}{S_{zz}(\kappa_\pm;\kappa)}); \quad \text{with } t = \pm\gamma \text{ and } z = \kappa_\pm \tag{B.5}$$

In a case $\gamma = 0$ and $\kappa_+ = \kappa_-$, by applying L'Hospital's rule twice, we will have

$$\dot{z}^3 = \frac{-2}{S_{zzz}(\kappa_+;\kappa)}); \quad \text{with } t = 0 \text{ and } z = \kappa_+ \tag{B.6}$$

Thus, for each value of z, equation (B.2) defines three possible values of t, creating three branches of the inverse transformation. As a result, one needs to chose the right branch to keep the number of saddle points constant, as well as keeping their behavior unaltered. This problem can be solved by trial and error.

Under the transformation (B.2), one can write equation (B.1) as

$$I(\eta;\kappa) = \int_C F_0(t,\kappa)\exp(\eta\varphi(t;\kappa))dt + \varepsilon \tag{B.7}$$

where ε is asymptotically negligible, and

$$F_0(t;\kappa) = f(z(t))\frac{dz}{dt} \tag{B.8}$$

Furthermore, we need to expand F_0, in such that the derivation of the uniform expansion will be possible. To satisfy this condition, we set

$$F_0(t;\kappa) = \kappa_0 + \kappa_1 t + (t^2 - \gamma^2) H_0(t;\kappa) \tag{B.9}$$

with κ_0, κ_1 and H_0 are needed to be determined.

In the transformed domain, if H_0 is regular, then the last term in (B.9) vanishes at the two saddle points $t = \pm\gamma$. Therefor, we will have

$$\begin{aligned} \kappa_0 &= \frac{F_0(\gamma;\kappa) + F_0(-\gamma;\kappa)}{2} \\ \kappa_1 &= \frac{F_0(\gamma;\kappa) - F_0(-\gamma;\kappa)}{2\gamma} \end{aligned} \tag{B.10}$$

By inserting (B.9) and (B.2) into (B.7), we obtain

$$I(\eta;\kappa) \sim \int \exp(\eta\rho) \exp(-\eta(\frac{t^3}{3} - \gamma^2 t))(\kappa_0 + \kappa_1 t) dt + W_0(\eta;\kappa) \tag{B.11}$$

here

$$W_0(\eta;\kappa) \sim \int \exp(\eta\rho)(t^2 - \gamma^2) H_0(t;\kappa) \exp(-\eta(\frac{t^3}{3} - \gamma^2 t)) dt \tag{B.12}$$

The first term of (B.9) can be expressed in terms of the Airy function $Ai(x)$ and its derivative [194]. W_0 is integrated by parts. This leads to

$$I(\eta;\kappa) \sim 2\pi i \exp(\eta\rho)[\frac{\kappa_0}{\eta^{1/3}} Ai(\eta^{2/3}\gamma^2) + \frac{\kappa_1}{\eta^{2/3}} Ai'(\eta^{2/3}\gamma^2)] + W_1 \tag{B.13}$$

with

$$W_1(\eta;\kappa) = \int \exp(\eta\rho) H_1(t;\kappa) \exp(-\eta(\frac{t^3}{3} - \gamma^2 t)) dt \tag{B.14}$$

and $H_1(t;\kappa) = \frac{d}{dt} H_0(t;\kappa)$

Equation (B.14) can be computed iteratively, as it is an integral of the form (B.7). It can be proved that the asymptotic expansion (B.13) is uniformly valid, when the distance between two saddle points $\kappa_+ - \kappa_-$ is small.

For our concern problem, H_0 is regular in the transformed domain. Thus, the second term in (B.13) will be neglected.

In (B.13), the Airy function can be written in terms of Bessel functions

$$Ai(-z) = \frac{\sqrt{z}}{3}[J_{1/3}(\frac{2}{3}z^{3/2} + J_{-1/3}(\frac{2z^{3/2}}{3})] \tag{B.15}$$

$$A'i(z) = \frac{\sqrt{z}}{3}[J_{-2/3}(\frac{2}{3}(-z)^{3/2} - J_{2/3}(\frac{2}{3}(-z)^{3/2}] \tag{B.16}$$

By using these relationships and (B.4), we will have

$$\begin{aligned} I(\eta;\kappa) \sim\ & 2\pi i \exp(\eta_\rho) \\ & \{\frac{1}{3}(-1)^{1/2}\gamma\kappa_0[J_{1/3}((-1)^{3/2}\eta\Delta S) + J_{-1/3}((-1)^{3/2}\eta\Delta S)] \\ & \frac{1}{3}\gamma^2\kappa_1[J_{-2/3}((-1)^{3/2}\eta\Delta S) - J_{2/3}((-1)^{3/2}\eta\Delta S)]\} \end{aligned} \tag{B.17}$$

Here $(-1)^{1/2} = \exp(i\pi + 2m\pi)^{1/2}$ where m is an integer. Here, there are many branches, which is needed to be tested. By choosing the branch as $(-1)^{3/2} = -i$, and using (B.5), (B.8) and (B.10), we will have

$$\begin{aligned} I(\eta;\kappa) \sim\ & \sqrt{2\pi i\eta\Delta S/3}\exp(\eta\overline{S} + i\pi/4) \\ & \{(\frac{iA_1 - A_2}{2})[J_{1/3}(-i\eta\Delta S) + J_{-1/3}(-i\eta\Delta S)] \\ & (\frac{iA_2 - A_1}{2})[J_{-2/3}(-i\eta\Delta S) - J_{-2/3}(-i\eta\Delta S)]\} \end{aligned} \tag{B.18}$$

with

$$A_1 = \sqrt{2\pi/\eta}\frac{f(\gamma;\kappa_-)}{\sqrt{S_{zz}(\kappa_-;\kappa)}} \quad \text{and} \quad A_2 = \sqrt{2\pi/\eta}\frac{f(\gamma;\kappa_+)}{\sqrt{S_{zz}(\kappa_+;\kappa)}} \tag{B.19}$$

If two saddle points are well apart (large ΔS), then the saddle-point approximation of (A.12) is recovered from the uniform approximation (B.18). If the Bessel functions are expanded asymptotically

$$J_{\pm\vartheta}(z) \sim \sqrt{2/z\pi}\cos(z \mp \vartheta\pi/2 - \pi/4) \tag{B.20}$$

In the limit of large ΔS, by using the expansion (B.20), equation (A.12) is recovered from (B.18).

Appendix C

General Expressions for RESI Prefactors Employing Hydrogenic States

In this appendix, we provide the general expressions for the prefactors employed in this work related to hydrogenic states. We will make no simplifying assumption on the initial states of the first and second electron, and on the excited state to which the second electron is promoted, apart from the fact that they are given by hydrogenic wavefunctions. In order to compute the prefactors, we will employ the expansion

$$\begin{aligned} e^{-i\mathbf{q}\cdot\mathbf{r}_\alpha} &= 4\pi \sum_{l=0}^{\infty} \sum_{m=-l}^{l} (-i)^l j_l(qr_\alpha) \\ &\quad Y_l^m(\theta_{q_\alpha}, \varphi_{q_\alpha}) \left[Y_{l'}^{m'}(\theta_\alpha, \varphi_\alpha) \right]^*, \end{aligned} \tag{C.1}$$

where $\mathbf{q}$ denotes a generic momentum, $\mathbf{r}_\alpha$ the coordinate of the α^{th} electron, and $j_l(\cdot)$ the spherical Bessel functions of the first kind. This expression will be both used in the derivation of $V_{\mathbf{p}_2 e}$ and $V_{\mathbf{p}_1 e, \mathbf{k} g}$, together with the orthogonality relation

$$\int \left[Y_{l'}^{m'}(\theta_\alpha, \varphi_\alpha) \right]^* Y_l^m(\theta_\alpha, \varphi_\alpha) d\Omega = \delta_{ll'} \delta_{mm'}, \tag{C.2}$$

where Ω denotes the solid angle.

For the former prefactor, equation (3.43) reduces to

$$\begin{aligned} V_{\mathbf{p}_2 e} &\sim \iint \exp[-i(\tilde{\mathbf{p}}_2(t) \cdot \mathbf{r}_2)] R_{nl}(r_2) Y_l^m(\theta_2, \varphi_2) r_2 dr_2 d\Omega \\ &= 4\pi (-i)^l Y_l^m(\theta_{\tilde{p}_2}, \varphi_{\tilde{p}_2}) \mathcal{I}_1, \end{aligned} \tag{C.3}$$

with

$$\mathcal{I}_1 = \int_0^\infty r_2 R_{nl}(r_2) j_l(\tilde{p}_2(t) r_2) dr_2. \tag{C.4}$$

Similarly, equation (3.44) reads

$$V_{\mathbf{p}_1 e, \mathbf{k} g} \sim V_{12}(\mathbf{p}_1 - \mathbf{k}) \mathcal{I}_2, \tag{C.5}$$

with

$$\begin{aligned} \mathcal{I}_2 &= \int d^3 r_2 e^{i(\mathbf{k}-\mathbf{p}_1)\cdot \mathbf{r}_2} R_{n_e l_e}(r_2) \left[Y_{l_e}^{m_e}(\theta_2, \varphi_2) \right]^* \\ & \quad R_{n_g l_g}(r_2) Y_{l_g}^{m_g}(\theta_2, \varphi_2), \end{aligned} \tag{C.6}$$

where the indices g and e in the principal, orbital and magnetic quantum numbers refer to the ground and excited states, respectively.

We will now compute the radial integrals $\mathcal{I}_1$ and $\mathcal{I}_2$ explicitly. For that purpose, let us consider a generic Hydrogenic radial wavefunction

$$\begin{aligned} R_{nl}(r) &= C_{nl} r^l \exp[-\sqrt{2E_n} r] \\ & \quad \times \sum_{\nu=0}^{n-l-1} \frac{2^\nu (-1)^{\nu+1} (\sqrt{2E_n})^\nu}{\nu!(n-l-1-\nu)!(2l+1+\nu)!}, \end{aligned} \tag{C.7}$$

with

$$C_{nl} = -\left\{ \frac{(2\sqrt{2E_n})^{3+2l}(n-l-1)!}{2n\left[(n+l)!\right]^3} \right\}^{1/2} \left[(n+l)!\right]^2. \tag{C.8}$$

In the above-stated equations, E_n denotes the energy of the bound state to be studied, i.e., $n = 2g$ or $n = 2e$ for the ground or excited states of the second electron, respectively. Since we are performing a qualitative analysis, we will concentrate mostly on the functional form of $R_{nl}(r)$. The integral $\mathcal{I}_1$ present in the prefactor $V_{\mathbf{p}_2 e}$ can then be written as

$$\begin{aligned} \mathcal{I}_1 \propto & \sum_{\nu=0}^{n-l-1} \frac{(-1)^{\nu+1} 2^{\nu-1-l} (\sqrt{2E_n})^{-2-l}}{\nu!(n-l-1-\nu)!(2l+1+\nu)!} \frac{\Gamma\left[2+\nu+2l\right]}{\Gamma\left[3/2+l\right]} \\ & \times {}_2F_1\left(1+l+\frac{\nu}{2}, \frac{3+\nu}{2}+l, \frac{3}{2}+l, -\frac{[\tilde{p}_2(t)]^2}{2E_e}\right). \end{aligned} \tag{C.9}$$

The integral $\mathcal{I}_2$ in $V_{\mathbf{p}_1 e, \mathbf{k} g}$ is slightly more involved. It may be explicitly written as

$$\mathcal{I}_2 = 4\pi \sum_{l=0}^{\infty} \sum_{m=-l}^{l} (-i)^l Y_l^m(\theta_{q_\alpha}, \varphi_{q_\alpha}) \mathcal{I}_{2R} \mathcal{I}_{2\Omega}, \tag{C.10}$$

where

$$\mathcal{I}_{2R} = \int_0^\infty r_2^2 R_{n_g l_g}(r_2) R_{n_e l_e}(r_2) j_l(\kappa r_2) dr_2 \tag{C.11}$$

and

$$\mathcal{I}_{2\Omega} = \int Y_l^m(\theta_2, \varphi_2) \left[Y_{l_e}^{m_e}(\theta_2, \varphi_2)\right]^* Y_{l_g}^{m_g}(\theta_2, \varphi_2) d\Omega \tag{C.12}$$

give the radial and angular dependencies of such prefactors, respectively. The explicit expression for $\mathcal{I}_2$ is then

$$\begin{aligned}\mathcal{I}_2 \;=\; & 4\pi \sum_{l=|l_g-l_e|}^{l_g+l_e} \sum_{m=-l}^{l} (-i)^l (-1)^{m_e} Y_l^m(\theta_\kappa, \varphi_\kappa) \sqrt{\frac{(2l_g+1)\,(2l_e+1)}{4\pi\,(2l+1)}} \\ & \times \langle l_g, l_e, 0, 0 \,|l, 0\rangle \, \langle l_g, l_e, m_g, -m_e \,|l, 0\rangle \, \mathcal{I}_{2R}.\end{aligned} \tag{C.13}$$

The radial integral $\mathcal{I}_{2R}$ is proportional to

$$\begin{aligned}\mathcal{I}_{2R} \;\propto\; & \sum_{\nu_g=0}^{n_g-l_g-1} \sum_{\nu_e=0}^{n_e-l_e-1} \frac{(-1)^{\nu_e+\nu_g+1} 2^{\nu_e+\nu_g-1-l} (\sqrt{2E_{2g}})^{\nu_g} (\sqrt{2E_{2e}})^{\nu_e} \left[\zeta(E_{2g}, E_{2e})\right]^{-3-\nu_e-\nu_g-l_e-l_g}}{\nu_e! \nu_g! (n_e-l_e-1-\nu_e)! (n_g-l_g-1-\nu_g)! (2l_e+1+\nu_e)! (2l_g+1+\nu_g)!} \\ & \frac{\Gamma\left[2+\lambda\right]}{\Gamma\left[3/2+l\right]} \left(\frac{\kappa^2}{\zeta^2(E_{2g}, E_{2e})}\right)^{l/2} {}_2F_1\left(\frac{3+\lambda}{2}, \frac{4+\lambda}{2}, \frac{3}{2}+l, -\frac{\kappa^2}{\zeta^2(E_{2g}, E_{2e})}\right),\end{aligned} \tag{C.14}$$

where $\lambda = \nu_e + \nu_g + l_e + l_g + l$ and $\zeta(E_{2g}, E_{2e})$ is defined according to equation (6.6). Note that the terms in equation (C.13) are only non-vanishing if $m = m_g - m_e$ and $l_1 + l_2 - l$ is even.

In the present work, apart from the case in which only s states are involved and the angular integrals are constant, one may identify the following cases. First, the second electron may be initially in a p state and be excited to an s state. In this case, $l = l_g = 1$ and $l_e = 0$. Second, if the electron is initially in an s state and is excited to a p state, then $l = l_e = 1$ and $l_g = 0$. Finally, if the second electron suffers a transition from a p state to another p state, in principle $l = 0, 1, 2$. Due to the constraints upon l for the Clebsch-Gordan coefficients, however, only the terms with $l = 0, 2$ will survive. Apart from that, the constraint upon m will impose further restrictions for m_e and m_g. The above-stated expressions, however, are applicable to generic hydrogenic states.

Appendix D

Interference of Electron Momentum Distributions

In this appendix, we provide an argument for neglecting the interference terms in equation (3.49). Explicitly, we wish to show that

$$\iint |M_R + M_L|^2 d^2p_{1\perp} d^2p_{2\perp} \simeq \iint |M_R|^2 + |M_L|^2 d^2p_{1\perp} d^2p_{2\perp} \tag{D.1}$$

The integrand in each of these transition amplitudes can be written as $\mathcal{F}_\xi(\mathbf{p}_1, \mathbf{p}_2, t, t', t'', \mathbf{k}) \exp[iS_\xi]$, where $\mathcal{F}_\xi(\mathbf{p}_1, \mathbf{p}_2, t, t', t'', \mathbf{k})$ is the product of all the prefactors involved, and ξ refers to the left or right peak. The corresponding electron orbits are displaced by half a cycle. Since the first and the second electron tunnel near $A(t'') = A(t) = 0$, $\mathcal{F}_R(\mathbf{p}_1, \mathbf{p}_2, t, t', t'', \mathbf{k}) \simeq \mathcal{F}_L(\mathbf{p}_1, \mathbf{p}_2, t, t', t'', \mathbf{k}) = \mathcal{F}(\mathbf{p}_1, \mathbf{p}_2, t, t', t'', \mathbf{k})$. For a linearly polarized monochromatic field, the action related to the orbits with the same momenta $\mathbf{p}_1, \mathbf{p}_2$will be $S_L = \alpha(\mathbf{p}_1, \mathbf{p}_2, t, t') + S_R$. Thereby,

$$\alpha(\mathbf{p}_1, \mathbf{p}_2, t, t') = \alpha_0(p_{1\parallel}, p_{2\parallel}, t, t') + \frac{\mathbf{p}_{1\perp}^2}{2} + \frac{\mathbf{p}_{2\perp}^2}{2},$$

where

$$\begin{aligned} \alpha_0(p_{1\parallel}, p_{2\parallel}, t, t') &= 2U_p + \frac{p_{1\parallel}^2}{2} + \frac{p_{2\parallel}^2}{2} + E_{1g} + E_{2g} \\ &\quad - \frac{2A_0}{\omega} \left[p_{1\parallel} \sin\left[\omega t'\right] + p_{2\parallel} \sin\left[\omega t\right] \right]. \end{aligned} \tag{D.2}$$

Hence,

$$\begin{aligned} |M_R + M_L|^2 &\simeq |\exp[iS_R]|^2 \mathcal{F}(\mathbf{p}_1, \mathbf{p}_2, t, t', t'', \mathbf{k}) \\ &\quad \times [2 + 2\cos[\frac{\alpha_0}{2} + \frac{\mathbf{p}_{1\perp}^2}{4} + \frac{\mathbf{p}_{2\perp}^2}{4}]]. \end{aligned} \tag{D.3}$$

The first term in equation (D.3) corresponds to the incoherent sum, while the second term gives the interference condition. If the prefactors are slowly varying their dependence with regard to the transverse momentum can be neglected to first approximation. Therefore, the dependence with regard to $\mathbf{p}_{n\perp}^2$ $(n = 1, 2)$ is mainly determined by the trigonometric function coming from the interference between the actions S_R and S_L. Upon integration over $p_{1\perp}^2$ and $p_{2\perp}^2$, they cause the interference terms to vanish. In practice this means that the contributions from the coherent term are small. If $F(\mathbf{p}_1, \mathbf{p}_2, t, t', t'', \mathbf{k}) = const$, this argument is exact.

Appendix E

Atomic Units

In this appendix, we provide the atomic units used in this thesis.

1. Mass(m): a.u. = 9.1×10^{-31} kg (electron mass)
2. Length(r_0): a.u. = $\hbar^2/me^2 = 0.53 \times 10^{-10}$ m (Bohr radius)
3. Charge(e): a.u. = 1.602×10^{-19} C (electron charge)
4. Frequency(ω_0): a.u. = 4.13×10^{-15} s^{-1}
5. Planck's constant/2π: a.u. = 6.5×10^{-22} Mev
6. Energy(E_0): a.u. = $e^2/r_0 = 27.2$ eV
7. Intensity (I_0): a.u. = $\epsilon_0 ce^2/2r_0^2 = 3.51 \times 10^{16}$ W/cm^2

Bibliography

[1] GAMESS-UK is a package of ab initio programs for more details see http://www.cfs.dl.ac.uk/gamess uk/index.shtnl, M. F. Guest, I. J. Bush, H. J. J. van Dam, P. Sherwood, J. M. H. Thomas, J. H. van Lenthe, R. W. A. Havenith, and J. Kendrick. *Mol. Phys*, **103**:719, (2005).

[2] C. Figueira de Morisson Faria, T. Shaaran, X. Liu, and W. Yang. *Phys. Rev. A*, **78**:043407, (2008).

[3] T. Shaaran and C. Figueira de Morisson Faria. *J. Mod. Opt.*, **57**:11, (2010).

[4] T. Shaaran, M.T. Nygren, and C. Figueira de Morisson Faria. *Phys. Rev. A*, **81**: 063413, (2010).

[5] T. Shaaran, B. B. Augsein, and C. Figueira de Morisson Faria. *Under preperation*, **xx**:xxx, (2010).

[6] T. Shaaran, C. Figueira de Morisson Faria, and M. Lewenstein. *Under preparation*, xx:xx, (2010).

[7] F. Krausz and M. Y. Ivanov. *Rev. Mod. Phys.*, **81**:163, (2009).

[8] B. Walker, B. Sheehy, L. F. DiMauro, P. Agostini, K. J. Schafer, and K. C. Kulander. *Phys. Rev. Lett.*, **73**:1227, (1994).

[9] R. Moshammer, B. Feuerstein, W. Schmitt, A. Dorn, C. D. Schroter, J. Ullrich, H. Rottke, C. Trump, M. Wittmann, G. Korn, K. Hoffmann, and W. Sandner. *Phys. Rev. Lett.*, **84**:447, (2000).

[10] A. Staudte, C. Ruiz, M. Schoffler, S. Schossler, D. Zeidler, Th. Weber, M. Meckel, D. M. Villeneuve, P. B. Corkum, A. Becker, and R. Dorner. *Phys. Rev. Lett.*, **99**: 263002, (2007).

[11] J. S. Parker, B. J. S. Doherty, K. T. Taylor, K. D. Schultz, C. I. Blaga, and L. F. DiMauro. *Phys. Rev. Lett.*, **96**:133001, (2006).

[12] Y. Liu, D. Ye, J. Liu, A. Rudenko, S. Tschuch, M. Dürr, M. Siegel, U. Morgner, Q. Gong, R. Moshammer, and J. Ullrich. *Phys Rev. Lett.*, **104**:173002, (2010).

[13] D. Zeidler, A. Staudte, A. B. Bardon, D. M. Villeneuve, R. Dorner, and P. B. Corkum. *Phys. Rev. Lett.*, **95**:203003, (2005).

[14] C. Figueira de Morisson Faria and X. Liu. *Journal of modern Optics*, Submitted: for publication, (2010).

[15] C. Figueira de Morisson Faria, D. B. Milosevic, and G. G. Paulus. *Phys. Rev. A*, **61**:063415, (2000).

[16] C. Figueira de Morisson Faria and W. Becker. *Laser Physics*, **13**:1196, (2003).

[17] V. P. Veiko: "Fundamentals of Laser Assisted Micro and Nanotechnologies". *(SPIE)*, Proceedings **6985**:242, (2008).

[18] C. La-O-Vorakiat, M. Siemens, M. M. Murnane, and H. C. Kapteyn. *Phys. Rev. Lett.*, **103**:257402, (2009).

[19] D. Polli, G. Grancini, J. Clark, M. Celebrano, T. Virgili, G. Cerullo, and G. Lanzani. *Advanced Materials*, **22**:3048, (2010).

[20] M. Yu. Kuchiev. *Phys. Rev. Lett.*, **99**:130404, (2007).

[21] R. Singhal, P. Norreys, and H. Habara. *Springer Series in Optical Sciences*, **134**: 519, (2008).

[22] R. Pohl and et al. *Nature*, **466**:213, (2010).

[23] H. Schwoerer. *Springer Topics in Applied Physics*, **96**:235, (2004).

[24] J. Seres, E. Seres, A. J. Verhoef, G. Tempea, C. Streli, P. Wobrauschek, V. Yakovlev, A. Scrinzi, C. Spielmann, and F. Krausz. *Nature*, **433**:596, (2005).

[25] D. Xiang, Z. Huang, and G. Stupakov. *Phys. Rev. ST Accel. Beams*, **12**:060701, (2009).

[26] U. Chakravarty, P. A. Naik, S. R. Kumbhare, and P. D. Gupta. *Journal of the Optical Society of Korea*, **13**:80, (2009).

[27] P. Salires and M. Lewenstein. *Measurement Science and Technology*, **12**:1818, (2001).

[28] P. Tzallas, E. Skantzakis, C. Kalpouzos, E. P. Benis, G. D. Tsakiris, and D. Charalambidis. *Nature Physics*, **3**:846, (2007).

[29] J. Yao, Y. Li, B. Zeng, H. Xiong, H. Xu, Y. Fu, W. Chu, J. Ni, X. Liu, J. Chen, Y. Cheng, and Z. Xu. *Phys. Rev. A*, **82**:023826, (2010).

[30] A. Pukhov and J. Meyer ter Vehn. *Phys. Rev. Lett.*, **76**:3975, (1996).

[31] C. Joshi and V. Malka. *New Journal of Physics*, **12**:045003, (2010).

[32] C. B. Schroeder and E. Esarey. *Phys. Rev. E*, **81**:056403, (2010).

[33] P. B. Corkum and F. Krausz. *Nature Physics*, **3**:381, (2007).

[34] O. Smirnova, Y. Mairesse, S. Patchkovskii, N. Dudovich, D. Villeneuve, P. B. Corkum, and M. Y. Ivanov. *Nature Physics*, **460**:972, (2009).

[35] M. Nisoli and G. Sansonea. *Progress in Quantum Electronics*, **33**:17, (2009).

[36] see e.g. M. Gavrila eds. *"Atoms in Intense Laser Fields"*, Advance in Atomic, Molecular and Optical Physics:Acadamic, London, (1992).

[37] M. Ferray, A. L'Huillier, X. F. Li, L. A. Lompre, G. Mainfray, and C. Manus. *J. Phys. B*, **21**:L31, (1988).

[38] X. F. Li, A. L'Huillier, M. Ferray, L. A. Lompre, and G. Mainfray. *Phys. Rev. A*, **39**:5751, (1989).

[39] G. G. Paulus, W. Nicklich, Huale XU, P. Lampropoulos, and H. Walther. *Phys. Rev. Lett.*, **72**:18, (1994).

[40] D. Strickland and G. Mourou. *Opt. Commun.*, **56**:219, (1985).

[41] P. A. Franken, A. E. Hill, C. W. Peters, and G. Weinreich. *Phys. Rev. Lett.*, **7**: 118, (1961).

[42] W. Kaiser and C. G. B. Garret. *Phys. Rev. Lett.*, **7**:229, (1961).

[43] see e.g. G. A. Mourou, C. P. J. Barty, and M. D. Perry. *Physics Today*, "Ultrahigh-Intensity Lasers":22, (1998).

[44] see e.g. B. C. Stuart, M. D. Perry, J. Miller, G. Tietbohl, S. Herman, J. A. Britten, C. Brown, D. Pennington, V. Yanovsky, and K. Wharton. *Opt. Lett.*, **22**:242, (1997).

[45] L. S. Brown and T. W. B. Kibble. *Phys. Rev.*, **133**:705, (1964).

[46] J. H. Eberly and A. Sleeper. *Phys. Rev.*, **176**:1570, (1968).

[47] A. Sarachik and E. S. Chappert. *Phys. Rev. D*, **1**:2738, (1970).

[48] A. Bgacov, M. Pont, and R. Shakeshaft. *Phys. Rev. A*, **48**:R4027, (1993).

[49] N. Kylstra, A. M. Ermolaev, and C. J. Joachain. *J. phys. B*, **30**:L449, (1997).

[50] U. W. Rathe, C. H. Keitel, M. Protopapas, and P. L. Knight. *J. phys. B*, **30**:L531, (1997).

[51] G. A. Mourou, T. Tajima, and S. V. Bulanov. *Rev. Mod. Phys.*, **78**:309, (2006).

[52] R. Kienberger, E. Goulielmakis, M. Uiberacker, A. Baltuska, V. Yakovlev, F. Bammer, A. Scrinzi, Th. Westerwalbesloh, U. Kleineberg, U. Heinzmann, M. Drescher, and F. Krausz. *Nature*, **427**:817, (2004).

[53] M. Drescher, M. Hentschel, R. Kienberger, M. Uiberacker, V. Yakovlev, A. Scrinzi, Th. Westerwalbesloh, U. Kleineberg, U. Heinzmann, and F. Krausz. *Nature*, **419**: 803, (2002).

[54] H. Kapteyn, O. Cohen, I. Christov, and M. Murnane. *Science*, **317**:775, (2007).

[55] A. Scrinzi, M. Y. Ivanov, R. Kienberger, and D. M. Villeneuve. *J. Phys. B*, **39**: R1, (2006).

[56] C. Guo. *Springer Series in Chemical Physics*, **84**:43, (2006).

[57] O. Smirnova, S. Patchkovskii, Y. Mairesse, N. Dudovich, D. Villeneuve, P. Corkum, and M. Y. Ivanov. *Phys. Rev. Lett.*, **063601**:102, (2009).

[58] D. A. Telnov and S. I. Chu. *Phys. Rev. A*, **041401**:79, (2009).

[59] C. A. Ullrich and E. K. U. Gross. *Comments At. Mol. Phys.*, **33**:211, (1997).

[60] X. M. Tong and Shih-I. Chu. *Phys. Rev. A*, **57**:452, (1998).

[61] P. B. Corkum. *Phys Rev Lett.*, **71**:1994, (1993).

[62] A. l'Huillier, L. A. Lompre, G. Mainfray, and C. Manus. *Phys. Rev. A*, **27**:2503, (1983).

[63] M. V. Ammosov, N. B. Delone, and V. P. Krainov. *Sov. Phys. JETP*, **64**:1191, (1986).

[64] D. N. Fittinghoff, P. R. Bolton, B. Chang, and K. C. Kulander. *Phys. Rev. Lett.*, **69**:2642, (1992).

[65] S. Augst, D. D. Meyerhofer, D. Strickland, and S. L. Chin. *Phys. Rev. A*, **49**:2174, (1994).

[66] S. Larochelle, A. Talebpour, and S. L. Chin. *J. Phys. B*, **30**:245, (1997).

[67] The. Weber, M. Weckenbrock, A. Staudte, L. Spielberger, O. Jagutzki, V. Mergel, F. Afaneh, G. Urbasch, M. Vollmer, H. Giessen, and R. Dorner. *Phys. Rev. Lett.*, **84**:443, (2000).

[68] Th. Weber, H. Giessen, M. Weckenbrock, G. Urbasch, A. Staudte, L. Spielberger, O. Jagutzki, and V. Mergel. *Nature*, **405**:658, (2000).

[69] B. Feuerstein, R. Moshammer, D. Fischer, A. Dorn, C. D. Schröter, J. Deipenwisch, J. R. Crespo Lopez-Urrutia, C. Höhr, P. Neumayer, J. Ullrich, H. Rottke, C. Trump, M. Wittmann, G. Korn, and W. Sandner. *Phys Rev Lett.*, **87**:043003, (2001).

[70] V. L. B. de Jesus, B. Feuerstein, K. Zrost, D. Fischer, A. Rudenko, F. Afaneh, C. D. Schroter, R. Moshammer, and J. Ullrich. *J. Phys. B*, **37**:L161, (2004).

[71] A. Rudenko, V. L. B. de Jesus, Th. Ergler, K. Zrost, B. Feuerstein, C. D. Schroter, R. Moshammer, and J. Ullrich. *Phys. Rev. Lett.*, **99**:263003, (2007).

[72] A. Talebpour, S. Larochelle, and S. L. Chin. *J. Phys. B*, **30**:L245, (1997).

[73] C. Cornaggia and Ph. Hering. *Phys. Rev. A*, **62**:023403, (2000).

[74] C. Figueira de Morisson Faria and M. Lewenstein. *J. Phys. B*, **38**:3251, (2005).

[75] C. Figueira de Morisson Faria, H. Schomerus, X. Liu, and W. Becker. *Phys. Rev. A*, **69**:043405, (2004).

[76] A. Emmanouilidou. *Phys. Rev. A*, **78**:023411, (2008).

[77] D. F. Ye, X. Liu, and J. Liu. *Phys Rev Lett.*, **101**:233003, (2008).

[78] X. Liu and C. Figueira de Morisson Faria. *Phys. Rev. Lett.*, **92**:133006, (2004).

[79] C. Figueira de Morisson Faria. *J. Phys. B*, **42**:105602, (2009).

[80] T. M. Yan, S. V. Popruzhenko, M. J. J. Vrakking, and D. Bauer. *Phys. Rev. Lett.*, **105**:253002, (2010).

[81] A. Becker and F. H. M. Faisal. *Phys. Rev. Lett.*, **89**:193003, (2002).

[82] S. P. Goreslavskii, S. V. Popruzhenko, R. Kopold, and W. Becker. *Phys. Rev. A*, **64**:053402, (2001).

[83] D. I. Bondar, W. K. Liu, and M. Y. Ivanov. *Phys. Rev. A*, **79**:023417, (2009).

[84] E. Eremina, X. Liu, H. Rottke, W. Sandner, M. G. SchäG. G. Paulus, H. Walther, R. Moshammer, and J. Ullrich. *Phys Rev. Lett.*, **92**:173001, (2004).

[85] Y. Liu, S. Tschuch, A. Rudenko, M. Siegel M. Dürr, U. Morgner, R. Moshammer, and J. Ullrich. *Phys Rev. Lett.*, **101**:053001, (2008).

[86] E. Eremina, X. Liu, H. Rottke, W. Sandner, A. Dreischuch, F. Lindner, F. Grasbon, G. G. Paulus, H. Walther, R. Moshammer, B. Feuerstein, and J. Ullrich. *J. Phys. B.*, **36**:3269, (2003).

[87] S. l. Haan, J. S. Van Dyke, and Z. S. Smith. *Phys. Rev. Lett.*, **101**:113001, (2008).

[88] R. Moshammer, J. Ullrich, B. Feuerstein, D. Fischer, A. Dorn, C. D. Schroter, J. R. Crespo Lopez-Urrutia, C. Hohr, H. Rottke, C. Trump, M. Wittmann, G. Korn, and W. J. Sandner. *J. Phys. B*, **36**:L113, (2003).

[89] J. Chen, J. Liu, L. B. Fu, and W. M. Zheng. *Phys. Rev. A*, **63**:011404(R), (2000).

[90] M. Lein, R. Velotta N. Hay, J. P. Marangos, and P. L. Knight. *Phys. Rev. Lett.*, **88**:183903, (2002).

[91] M. Spanner, O. Smirnova, P. B. Corkum, and M. Y. Ivanov. *J. Phys. B*, **37**:L243, (2004).

[92] T. Shaaran, H. Schomerus, and C. Figueira de Morisson Faria. *Under preparation*, xx:xx, (2011).

[93] D. Bauer and P. Mulser. *Phys. Rev. A*, **59**:569, (1999).

[94] O. Smirnova, M. Spanner, and M. Y. Ivanov. *J. Phys. B*, **39**:S323, (2006).

[95] O. Smirnova, M. Spanner, and M. Y. Ivanov. *Phys. Rev. A*, **77**:033407, (2008).

[96] C. Cornaggia and Ph. Hering. *J. Phys. B*, **31**:L503, (1998).

[97] C. Guo, M. Li, J. P. Nibarger, and G. N. Gibson. *Phys. Rev. A*, **58**:R4271, (1998).

[98] W. C. Liu, J. H. Eberly, S. L. Haan, and R. Grobe. *Phys. Rev. Lett.*, **83**:520, (1999).

[99] U. Eichmann, M. Dorr, H. Maeda, W. Becker, and W. Sandner. *Phys. Rev. Lett.*, **84**:3550, (2000).

[100] P. Dietrich, N. H. Burnett, M. Y. Ivanov, and P. B. Corkum. *Phys. Rev. A*, **50**: R3585, (1994).

[101] K. C. Kulander, J. Cooper, and K. J. Schafer. *Phys. Rev. A*, **51**:561, (1995).

[102] J. Ullrich, R. Moshammer, R. Dorner A. Dorn, L. Ph. Schmidt, and H. Schmidt-Bocking. *Rep. Prog. Phys.*, **66**:1463, (2003).

[103] M. Weckenbrock, D. Zeidler, A. Staudte, Th. Weber, M. Schoffler, M. Meckel, S. Kammer, M. Smolarski, O. Jagutzki, V. R. Bhardwaj, D. M. Rayner, D. M. Villeneuve, P. B. Corkum, and R. Dorner. *Phys. Rev. Lett.*, **92**:213002, (2004).

[104] M. Lein, E. K. U. Gross, and V. Engel. *Phys. Rev. Lett.*, **85**:4707, (2000).

[105] C. Figueira de Morisson Faria, X. Liu, W. Becker, and H. Schomerus. *Phys. Rev. A*, **69**:R012402, (2004).

[106] S. Baier, C. Ruiz, L. Plaja, and A. Becker. *Phys. Rev. A.*, **74**:033405, (2006).

[107] S. Baier, C. Ruiz, L. Plaja, and A. Becker. *Laser Phys.*, **17**:358, (2007).

[108] S. Baier, C. Ruiz, A. Becker, and L. Plaja. *Phys. Rev. A*, **78**:013409, (2008).

[109] S. L. Haan, L. Breen, A. Karim, and J. H. Eberly. *Phys. Rev. Lett.*, **97**:103008, (2006).

[110] J. S. Prauzner-Bechcicki, K. Sacha, B. Eckhardt, and J. Zakrzewski. *Phys Rev A*, **78**:013419, (2008).

[111] A. Emmanouilidou and A. Staudte. *Phys Rev A*, **80**:053415, (2009).

[112] Y. Li, J. Chen, S. P. Yang, and J. Liu. *Phys Rev A*, **76**:023401, (2007).

[113] J. Liu, D. F. Ye, J. Chen, and X. Liu. *Phys Rev. Lett.*, **99**:013003, (2007).

[114] D. F. Ye, J. Chen, and J. Liu. *Phys Rev. A*, **77**:013403, (2008).

[115] R. Panfili, J. H. Eberly, and S. L. Haan. *Opt. Express*, **8**:431, (2001).

[116] R. Panfili, S. L. Haan, and J. H. Eberly. *Phys. Rev. Lett.*, **89**:113001, (2002).

[117] P. J. Ho, R. Panfili, S. L. Haan, and J. H. Eberly. *Phys. Rev. Lett.*, **94**:093002, (2005).

[118] R. Kopold, W. Becker, H. Rottke, and W. Sandner. *Phys Rev Lett.*, **85**:3781, (2000).

[119] J. S. Prauzner-Bechcicki, K. Sacha, B. Eckhardt, and J. Zakrzewski. *Phys Rev. A*, **71**:033407, (2005).

[120] R. Dörner, Th. Weber, M. Weckenbrock, A. Staudte, M. Hattas, H. Schmidt-Böcking, R. Moshammer, and J. Ullrich. *Adv. At., Mol., Opt. Phys.*, **48**:1, (2002).

[121] I. I. Bondar, N. B. Delone, M. I. Dudich, and V. V. Suran. *J. Phys. B*, **21**:2763, (1988).

[122] V. Ayvazyan et al. *Phys. Rev. Lett.*, **88**:104802, (2002).

[123] V. Ayvazyan et al. *Eur. Phys. J. D*, **37**:297, (2006).

[124] Y. Nabekawa, H. Hasegawa, E. J. Takahashi, and K. Midorikawa. *Phys Rev. Lett.*, **94**:043001, (2005).

[125] R. Moshammer, Y. H. Jiang, L. Foucar, A. Rudenko, Th. Ergler, C. D. Schrter, S. Ldemann, K. Zrost, D. Fischer, J. Titze, T. Jahnke, M. Schffler, T. Weber, R. Drner, T. J. M. Zouros, A. Dorn, T. Ferger, K. U. Khnel, S. Dsterer, R. Treusch, P. Radcliffe, E. Plnjes, and J. Ullrich. *Phys. Rev. Lett.*, **98**:203001, (98).

[126] A. Rudenko, L. Foucar, M. Kurka, Th. Ergler, K. U. Khnel, Y. H. Jiang, A. Voitkiv, B. Najjari, A. Kheifets, S. Ldemann, T. Havermeier, M. Smolarski, S. Schssler, K. Cole, M. Schffler, R. Drner, S. Dsterer, W. Li, B. Keitel, R. Treusch, M. Gensch, C. D. Schrter, R. Moshammer, and J. Ullrich. *Phys. Rev. Lett.*, **101**: 073003, (2008).

[127] P. B. Corkum. *Phys. Rev. Lett.*, **71**:1994, (1993).

[128] D. B. Milosevic and W. Becker. *Phys. Rev. A*, **68**:065401, (2003).

[129] S. P. Goreslavksii and S. V. Popruzhenko. *Opt. Express*, **8**:395, (2001).

[130] L. B. Fu, J. Liu, and S. G. Chen. *Phys. Rev. A*, **65**:021406, (2002).

[131] J. Chen and C. H. Nam. *Phys. Rev. A*, **66**:053415, (2002).

[132] B. Feuerstein, R. Moshammer, and J. Ullrich. *J. Phys. B*, **33**:L823, (2000).

[133] R. Kopold, W. Becker, H. Rottke, and W. Sandner. *Phys. Rev. Lett.*, **85**:3781, (2000).

[134] J. S. Prauzner-Bechcicki, K. Sacha, B. Eckhardt, and J. Zakrzewski. *Phys Rev Lett.*, **98**:203002, (2007).

[135] D. F. Ye and J. Liu. *Phys Rev A*, **81**:043402, (2010).

[136] Y. Liu, S. Tschuch, A. Rudenko, M. Durr, M. Siegel, U. Morgner, R. Moshammer, and J. Ullrich. *Phys. Rev. Lett.*, **101**:053001, (2008).

[137] J. L. Chaloupka, J. Rudati, R. Lafon, P. Agostini, K. C. Kulander, and L. F. DiMauro. *Phys. Rev. Lett.*, **90**:033002, (2003).

[138] P. B. Lerner, K. J. LaGattuta, and J. S. Cohen. *Phys. Rev. A*, **49**:R12, (1994).

[139] D. A. Wasson and C. Koonin. *Phys. Rev. A*, **39**:5676, (1989).

[140] N. I. Shvetsov-Shilovski, S. P. Goreslavski, S. V. Popruzhenko, and W. Becker. *Phys. Rev. A*, **77**:063405, (2008).

[141] W. Quan, X. Liu, and C. Figueira de Morisson Faria. *J. Phys. B*, **42**:134008, (2009).

[142] M. S. Pindzola, D. C. Griffin, and C. Bottcher. *Phys. Rev. Lett.*, **66**:2305, (1991).

[143] D. R. Schultz, C. Bottcher, D. H. Madison, J. L. Peacher, G. Buffington, M. S. Pindzola, T. W. Gorczyca, P. Gavras, and D. C. Griffin. *Phys. Rev. A*, **50**:1348, (1994).

[144] D. G. Lappas and R. J. van Leeuwen. *Phys. Rev. B*, **31**:L249, (1998).

[145] L. V. Keldysh. *Sov. Phys. JETP*, **20**:1307, (1964).

[146] W. Gordon. *Z. Phys.*, **40**:117, (1926).

[147] D. M. Volkov. *Z. Phys.*, **94**:250, (1935).

[148] H. R. Reiss. *Phys. Rev. A*, **22**:1786, (1980).

[149] S. V. Popruzhenko and D. Bauer. *J. Mod. Opt.*, **55**:2573, (2008).

[150] H. R. Reiss. *Springer Series in Chemical Physics*, **89**:1, (2008).

[151] C. Figueira de Morisson Faria, X. Liu, and W. Becker. *Springer series in Chemical Physics*, **85**:65, (2007).

[152] A. Becker and F. H. M. Faisal. *J. Phys. B*, **29**:L197, (1996).

[153] A. Becker and F. H. M. Faisal. *Phys. Rev. A*, **59**:R1742, (1999).

[154] S. V. Popruzhenko, Ph. A. Korneev, S. P. Goreslavskii, and W. Becker. *Phys. Rev. Lett.*, **89**:023001, (2002).

[155] L. V. Keldysh. *Sov. Phys. JETP*, **23**:924, (1966).

[156] F. H. M. Faisal. *J. Phys. B*, **6**:L89, (1973).

[157] H. G. Muller. *Phys. Rev. A*, **60**:1341, (1999).

[158] M. Awasthi, Y. V. Vanne, A. Saenz, A. Castro, and P. Decleva. *Phys. Rev. A*, **77**: 063403, (2008).

[159] M. Lewenstein, P. Balcou, M. Y. Ivanov, A. LHuillier, and P. B. Corkum. *Phys. Rev. A*, **49**:2117, (1994).

[160] W. Becker, A. Lohr, M. Kleber, and M. Lewenstein. *Phys. Rev. A*, **56**:645, (1997).

[161] W. Becker, S. Long, and J. K. McIver. *Phys. Rev. A*, **50**:1540, (1994).

[162] A. Lohr, M. Kleber, R. Kopold, and W. Becker. *Phys. Rev. A*, **55**:R4003, (1997).

[163] A. Becker and F. H. M. Faisal. *Phys. Rev. Lett.*, **84**:3546, (2000).

[164] S. V. Popruzhenko and S. P. Goreslavskii. *J. Phys. B*, **34**:L239, (2001).

[165] F. H. M. Faisal and A. Becker. *Plenum Press*, New York:397, (1996).

[166] A. Becker and F. H. M. Faisal. *OPTICS EXPRESS*, **8**:383, (2001).

[167] A. Becker and F. H. M. Faisal. *J. Phys. B*, **32**:L335, (1999).

[168] A. Becker and F. H. M. Faisal. *J. Phys. B*, **38**:R1, (2005).

[169] A. Becker and F. H. M. Faisal. *Phys. Rev. A*, **50**:3256, (1994).

[170] O. Smirnova, M. Spanner, and M. Y. Ivanov. *J. Mod. Opt*, **54**:1019, (2007).

[171] C. Figueira de Morisson Faria, X. Liu, A. Sanpera, and M. Lewenstein. *Phys. Rev. A*, **70**:043406, (2004).

[172] C. Figueira de Morisson Faria, H. Schomerus, and W. Becker. *Phys. Rev. A*, **66**: 043413, (2002).

[173] R. Kopold, W. Becker, and M. Kleber. *Opt. Comm.*, **179**:39, (2000).

[174] M. V. Berry. *Proc. R. Soc. London A*, **7**:422, (1989).

[175] C. Figueira de Morisson Faria, X. Liu, and W. Becker. *J. Mod. Opt.*, **53**:193, (2006).

[176] R. Kopold. *PhD thesis*, Technical University:Munich, (2001).

[177] W. Becker W, A. Lohr, and M Kleber. *Quantum Semiclass. Opt.*, **7**:423, (1995).

[178] H. W. van der Hart and Keith Burnett. *Phys. Rev. A*, **62**:013407, (2000).

[179] C. C. Chirilă and M. Lein. *Phys. Rev. A*, **73**:023410, (2006).

[180] C. Figueira de Morisson Faria. *Phys. Rev. A*, **76**:043407, (2007).

[181] S. Hässler, J. Caillat, W. Boutu, C. Giovanetti-Teixeira, T. Ruchon, T. Auguste, Z. Diveki, P. Breger, B. Carré A. Maquet, R. Taïeb, and P. Salières. *Nat. Phys.*, **6**:200, (2010).

[182] C. Figueira de Morisson Faria and B. B. Augstein. *Phys. Rev. A*, **81**:043409, (2010).

[183] S. Odžak and D. B. Milošević. *Phys. Rev. A*, **79**:023414, (2009).

[184] E. Hijano, C. Serrat, G. N. Gibson, and J. Biegert. *Phys. Rev. A*, **81**:041401, (2010).

[185] T. Brabec, M. Y. Ivanov, and P. B. Corkum. *Phys. Rev. A*, **54**:R2551, (1996).

[186] A. Fring, V. Kostrykin, and R. Schrader. *J. Phys. B*, **29**:5651, (1996).

[187] D. Bauer, D. B. Miloevi, and W. Becker. *Phys. Rev. A*, **72**:023415, (2005).

[188] O. Smirnova, A. S. Mouritzen, S. Patchkovskii, and M. Y. Ivanov. *J. Phys. B*, **40**: F197, (2007).

[189] S. V. Popruzhenko, G. G. Paulus, and D. Bauer. *Phys. Rev. A*, **77**:053409, (2008).

[190] H. A. Kramers. *Collected Scientific papers*, North-Holland:Amsterdam, (1956).

[191] W. C. Henneberger. *Phys. Rev. Lett.*, **21**:838, (1968).

[192] A. M. Perelomov, V. S. Popov, and M. V. Terentev. *Sov. Phys. JETP*, **24**:207, (1967).

[193] D. Bauer and P. Koval. *Comp. Phys. Comm.*, **174**:396, (2006).

[194] N. Bleistein and R. Handelsman. *Asymptotic Expansions of Integrals*, Dover Publications, Inc.:New York, Section 2, (1986).